Title

A computational investigation on spatial and temporal dynamics of cAMP

Permalink

https://escholarship.org/uc/item/94z1z7x7

Author

Getz, Michael

Publication Date

2020

Peer reviewed|Thesis/dissertation

UNIVERSITY OF CALIFORNIA SAN DIEGO

A computational investigation on spatial and temporal dynamics of cAMP

A dissertation submitted in partial satisfaction of the

requirements for the degree

Doctor of Philosophy

in

Chemical Engineering

by

Michael Getz

Committee in charge:

Professor Padmini Rangamani, Chair
Professor Pradipta Ghosh, Co-Chair
Professor Yi Chen
Professor Jesse Jokerst
Professor Andrew McCulloch
Professor Sheng Xu
Professor Jin Zhang

2020

The dissertation of Michael Getz is approved, and it is acceptable in quality and form for publication on microfilm and electronically:

_____

_____

_____

_____

_____

_____
Co-Chair

_____
Chair

University of California San Diego

2020

iii

DEDICATION

To my Family, Teachers, and Friends who supported me and kept me learning.

EPIGRAPH

The whole of science is nothing more than a refinement of every day thinking.

It is for this reason that the critical thinking of the physicist cannot possibly be restricted to the

examination of concepts of his own specific field.

He cannot proceed without considering critically a much more difficult problem,

the problem of analyzing the nature of everyday thinking.

—Albert Einstein

TABLE OF CONTENTS

vii

LIST OF FIGURES

xi

as it may appear in ELife, Brian Tenner, Michael Getz, Brian Ross, Donya Ohadi, Christopher H. Bohrer, Eric Greenwald, Sohum Mehta, Jie Xiao, Padmini Rangamani, Jin Zhang, Spatially compartmentalized phase regulation in the Ca 2+ -cAMP-PKA oscillatory circuit. The dissertation author was the second author of this material.

Appendix **C**, in full, is a reprint of the material as it appears in M. C. Getz, J. A. Nirody, and P. Rangamani. Stability analysis in spatial modeling of cell signaling. 10(1):e1395. eprint: https://onlinelibrary.wiley.com/doi/pdf/10.1002/wsbm.1395. The dissertation author was the primary author of this material.

Appendix **D**, in full, is a reprint of the material as it appears in L. M. Stolerman, M. Getz, S. G. L. Smith, M. Holst, and P. Rangamani. Stability Analysis of a Bulk–Surface Reaction Model for Membrane Protein Clustering. 82(2):30. The dissertation author was the co-first author of this material.

2015   B. S. in Chemical Engineering, University of Illinois, Chicago

Fall 2016,Winter 2018   Graduate Teaching Assistant, University of California, San Diego

2020   Ph. D. in Chemical Engineering, University of California, San Diego

PUBLICATIONS

Getz, M, Jasmine, N, Rangamani, P (2018). Stability analysis in spatial modeling of cell signaling. WIREs Syst Biol Med, 10: null. doi: 10.1002/wsbm.1395

Getz, M, Swanson, L, Sahoo, D, Ghosh, P, and Rangamani, P (2019). A predictive computational model reveals that GIV/Girdin serves as a tunable valve for EGFR-stimulated Cyclic AMP Signals. MBoC, mbc.E18-10-0630.

Stolerman, L.M.*, Getz, M.*, Smith, S.G.L. et al. Stability Analysis of a Bulk–Surface Reaction Model for Membrane Protein Clustering. Bull Math Biol 82, 30 (2020). doi: 10.1007/s11538-020-00703-4

ABSTRACT OF THE DISSERTATION

A computational investigation on spatial and temporal dynamics of cAMP

by

Michael Getz

Doctor of Philosophy in Chemical Engineering

University of California San Diego, 2020

Professor Padmini Rangamani, Chair

Professor Pradipta Ghosh, Co-Chair

Signaling networks are spatiotemporally organized in order to sense diverse inputs from the extracellular space, process information, and carry out specific cellular tasks. Various hormones and growth factors stimulate target cells through second messenger pathways, which in turn regulate cellular phenotypes. Cyclic adenosine monophosphate (cAMP) is a ubiquitous

second messenger that facilitates numerous signal transduction pathways; its production in cells is tightly balanced by activation of adenylate cyclases (ACs), i.e. "sources," and phosphodiesterases (PDEs) that hydrolyze it, i.e. "sinks." Since cAMP regulates various cellular functions, including cell growth/differentiation, gene transcription/protein expression, and hormone secretion, this has been exploited for the treatment of numerous human diseases. Here, we discuss two methods of information encoding in the cAMP pathway– regulation of cellular cAMP through GIV/Girdin in cancers and spatiotemporal control of sources and sinks of cAMP in pancreatic β cells. In the first part, we describe a network-based compartmental model of non-canonical cAMP signaling which reveals that Guanine nucleotide Exchange Modulators (GEMs), such as GIV/Girdin, serve as "tunable valves" that cells may employ to finetune cellular levels of cAMP. In the second part, we model the spatiotemporal regulation of Ca^{2+}-cAMP in pancreatic β cells. Ca^{2+}, cAMP, and Protein Kinase A (PKA) exist in an oscillatory circuit characterized by a high degree of feedback allowing specific controls based on oscillation frequencies. We describe a novel mode of regulation within this circuit involving a spatial dependence of the relative phase between cAMP, PKA, and Ca^{2+}. We show nanodomain clustering of Ca^{2+}-sensitive adenylyl cyclases drives precisely in-phase cAMP oscillations with Ca^{2+} within the membrane nanodomain, whereas Ca^{2+}-sensitive phosphodiesterases maintain out-of-phase oscillations within the general plasma membrane outside of the nanodomain, providing a striking example and novel mechanism of cAMP compartmentation. Disruption of this precise in-phase relationship perturbs Ca^{2+} oscillations, suggesting that the relative phase within an oscillatory circuit can encode specific functional information. Thus, mathematical modeling of spatiotemporal dynamics of second messengers gives insight into their cellular function.

Chapter 1

The versatile cAMP, A balancing act between "Sources" and "Sinks".

For cells to properly react to their environment, cells must constantly sense their external environment and correctly relay them to the intracellular environment. While sensing is mediated by a myriad of cell-surface receptors, relaying such signals depends on protein scaffolding, enzymatic reactions and the production of second messengers, such as cyclic nucleotides [1,2]. Of the various cyclic nucleotides, the first to be identified was cyclic adenosine 3,5-monophosphate (cAMP), a universal second messenger used by diverse forms of life, such as unicellular bacteria, fungi, protozoans, and mammals. cAMP relays signals triggered by hormones, ion channels, metabolism, and neurotransmitters [reviewed in [3, 4]]. cAMP also binds and regulates other cAMP-binding proteins such as cyclic nucleotide gated channels, PKA, and Epac1. Intracellular levels of cAMP are regulated by the antagonistic action of two classes of enzymes: adenylyl cyclases (ACs) and cyclic nucleotide phosphodiesterases (PDEs). ACs are membrane-bound enzymes that utilize ATP to generate cAMP; the latter transmits signals from cell-surface receptors to second messengers. In contrast, PDEs are soluble enzymes and catalyze the degradation of

the phosphodiester bond resulting in the conversion of cAMP to AMP. Most ACs are activated downstream from G-protein-coupled receptors (GPCRs) by interactions with the α subunit of the Gs protein (Gαs). Gαs is released from heterotrimeric $\alpha\beta\gamma$ G-protein complexes following binding of agonist ligands to GPCRs and binds to and activates AC [5]. Alternatively, AC activity can be inhibited by ligands that stimulate GPCRs coupled to Gi and/or cAMP can be degraded by PDEs. PDE4, for instance, is activated by protein kinase A (PKA), a downstream effector of cAMP, resulting in a negative feedback loop between cAMP and PDE4s [6–9]. Thus, the level of cAMP in cells is a fine balance between synthesis by ACs, degradation by PDEs, and feedback through the PKA-PDE loop [3].

In some cell types, including neurons, cardiomyocytes, and pancreatic β cells, cAMP concentrations oscillate intracellularly [10, 11], and the oscillations encode dynamic signaling information (e.g. signal strength, duration, and target diversity) into parameters such as frequency and amplitude [12, 13]. This is perhaps best exemplified in the β cell where Ca^{2+}, cAMP, and the downstream cAMP-dependent kinase Protein Kinase A (PKA) constitute a highly-coordinated oscillatory circuit characterized by multiple feedback mechanisms [14–16] and is responsible for integrating metabolic and signaling information in order to regulate diverse functions [17]. In addition to temporal control, biochemical pathways are also spatially organized within the cell, and coordination between spatial and temporal regulatory modes can drive many interesting phenomena such as compartmentalized signaling [18, 19]. Both Ca^{2+} and cAMP are highly spatially compartmentalized and form signaling microdomains or nanodomains [20, 21]. While Ca^{2+} levels are locally controlled by channels, pumps, and intracellular buffering systems [4, 22], cAMP is thought to be regulated via controlled synthesis by adenylyl cyclases (ACs) and degradation by phosphodiesterases (PDEs) [23, 24]. Despite extensive studies on cAMP compartmentation, the mechanisms that spatially constrain this mobile second messenger still remain poorly understood [25–27].

Dysregulated circuits that give rise to too much or too little cAMP can be unhealthy; in fact, deregulated signaling events with resultant abnormal levels of cellular cAMP is a key pathophysiologic component in many human diseases (**Figure 1.1**; see **Table 2.1**). In the context of cancers, multiple studies across different cancers [breast [28], melanoma [29], pancreas [30], etc.] agree that high levels of cAMP are generally protective, whereas low cAMP levels fuel cancer progression [reviewed in [31]]. High cAMP inhibits several harmful phenotypes of tumor cells such as proliferation, invasion, stemness, and chemoresistance, while enhancing differentiation and apoptosis (**Figure 1.1**).
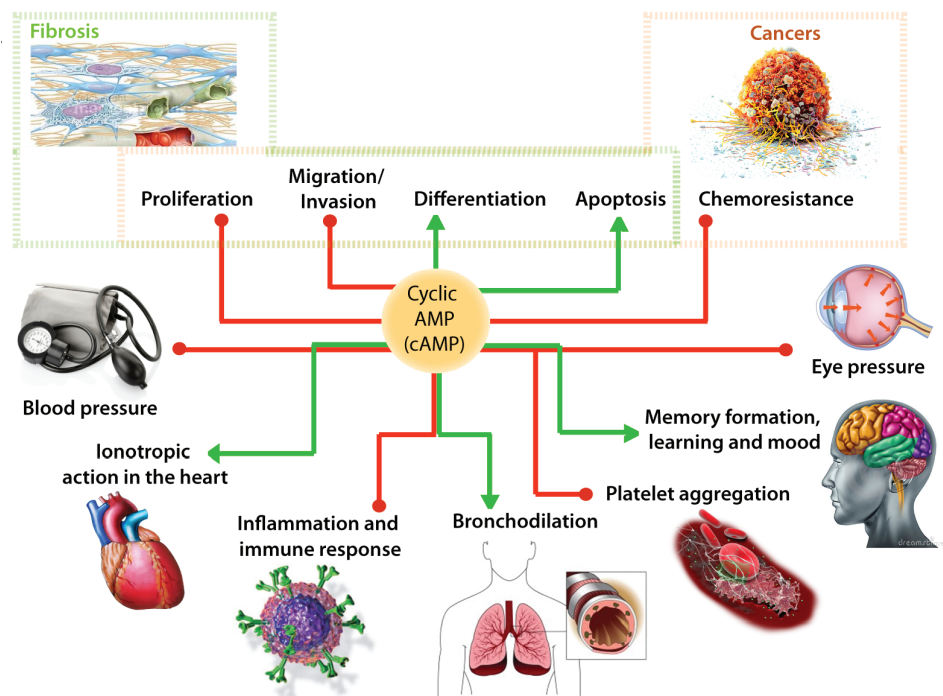
Figure 1.1: **An emerging paradigm for modulation of cellular cAMP.** (A) Schematic summarizing the role of cyclic AMP (cAMP) in diverse biological processes. In cancers (top right), cAMP is largely protective as it inhibits proliferation, invasion, chemoresistance, and promotes apoptosis and differentiation of tumor cells. Similarly, in the context of organ fibrosis, cAMP is a potent anti-fibrotic agent because it inhibits proliferation and migration and triggers apoptosis and return to quiescence for myofibroblasts, the major cell type implicated in fibrogenic disorders. Red lines indicate suppression and green lines indicate promotion.

Therapies that target the canonical GPCR/G-protein-cAMP signaling pathway have been successfully translated to the clinics, and they account for 40% of currently marketed drugs that

can treat a wide range of ailments [32], from hypertension to glaucoma. However, such strategies have largely failed to impact cancer care or outcome. Thus, how tumor cells avoid high levels of cAMP, despite the fact that there are is generally hyperactivation of receptors ("sources"), is puzzling. Efforts to elevate cAMP using PDE inhibitors, although perceived as successful at the bench (reviewed in Table 3 in [33]), showed controversial results in well-designed clinical trials [34], suggesting that inhibiting the "sinks" alone may not be enough. Consequently, despite a well-thought out therapeutic goal, i.e., elevate cAMP, a strategy to accomplish the same in chronic diseases like cancers has not emerged. Here we highlight the importance of an emergent field / paradigm in trimeric GTPase signaling and in the regulation of cellular cAMP; we discuss its importance in the tonic and robust suppression of cAMP, especially in the context of cancers.

1.1 Enter GEMs: An emerging paradigm in GPCR-independent G protein and cAMP signaling

Recent studies by the Ghosh lab and others have shown that heterotrimeric G proteins can be activated by integrins and growth factor receptor tyrosine kinases (RTKs) (reviewed in, [35]). Although these receptor classes are not typically coupled to heterotrimeric G proteins like the G protein-coupled receptors (GPCRs), both classes of receptors have been shown to modulate heterotrimeric G proteins and successfully transduce external stimuli into an intracellular cAMP signal [36, 37]. Where these receptors differ from GPCRs is that unlike GPCRs that rapidly perturb cAMP for a finite period of few hundred seconds, growth factor RTKs and Integrins signal over longer periods of time (~60 minutes) after an acute stimulus before reaching a steady state [38, 39]. Who or what may allow these receptors to couple to and modulate G proteins remained a puzzle for decades. One mechanism for such coupling that has emerged just within this past decade is non-receptor (i.e., cytosolic) modulators of G proteins that may contextually

and dynamically scaffold unlikely receptor classes to heterotrimeric G proteins. More specifically, studies focused on GIV (also known as Girdin/HkRP1/APE) the prototypical member of the family of proteins known as Guanine nucleotide Exchange Modulator (GEMs) have exposed the critical roles of a class of cytosolic scaffolds that use their modularity and motifs to trigger G protein signaling downstream of growth factor receptors [40–48] and integrins [49–52]. There have been four GEMs identified thus far, all implicated in diverse signaling paradigms: GIV was independently independently discovered by four groups [53–56] in 2005, Calnuc/Nucleobindin 1 and 2 (NUCB1 and NUCB2) in 2011 [57] and Daple in 2015 [58].

A series of studies from our group and others helped understand the unique features and different set of rules of GEM-dependent (and hence, GPCR-independent) G protein signaling [35, 59]. In brief, this signaling pathway has a distinctive temporal and spatial features and an unusual profile of receptor engagement: diverse classes of receptors, not just GPCRs can engage with GIV to trigger such activation. Such activation is spatially and temporally unrestricted, that is, can occur both at the plasma membrane (PM) and on internal membranes discontinuous with the PM, and can continue for prolonged periods of time. GEMs act within diverse signaling cascades and couple activation of these cascades to G-protein signaling via an evolutionarily conserved motif of ~30 amino acids that directly binds and modulates $G\alpha_i$ and $G\alpha_s$ proteins. It is via this short motif that GIV-GEM serves as a GEF for $G\alpha_i$ and as a GDI for $G\alpha_s$ in a temporally-spatially segregated manner that is controlled by two kinases [42]. Despite this apparent paradox of modulating $G\alpha_i$ and $G\alpha_s$, both forms of modulation lead to suppression of cellular cAMP [35]. Thus, unlike the canonical G protein/cAMP signaling paradigm, which is rigid (finite, is triggered exclusively by GPCRs and transduced via either Gi or Gs at a time, primarily at the PM), the temporal and spatial features of non-canonical G protein/cAMP signaling via GIV-family of cytosolic GEMs are unusually complex and relaxed. GIV uses this relaxed circuitry to integrate, reinforce and compartmentalize signals downstream of a diverse classes of receptors and G proteins in a way that enables it to orchestrate cellular phenotypes in a sustained

manner. While the molecular mechanisms that govern the unique spatiotemporal aspects of non-canonical G protein activation by GIV and the relevance of this new paradigm in health and disease has been reviewed elsewhere [59], the structural basis for GEM-dependent G protein activation has just begun to emerge. A recently published study [60] used the combined synergy of x-ray crystallography, molecular dynamics simulations, and other biophysical and biochemical approaches to reveal that despite differences in how GPCRs and GEMs bind G-proteins, they converge into allosteric mechanisms that cause a similar disruption of key nucleotide contacts in the hydrophobic core of the nucleotide-binding domain. Despite these insights, the impact of the unusual complex and relaxed spatiotemporal aspects of GEM-dependent G protein activation on cAMP production was difficult to deduce intuitively, and hence, required investigations from a systems level.

Chapter **1**, in part, is as it may appear in WIREs Syst Biol Med, Getz, M , Ghosh, P, Rangamani, P, Regulating cellular cyclic AMP: "Sources", "Sinks", and now, "Tunable Valves". The dissertation author was the primary author of this material.

Chapter 2

A predictive computational model reveals that GIV/Girdin serves as a tunable valve for EGFR-stimulated Cyclic AMP Signals

Michael Getz[1], Lee Swanson[2,3], Debashish Sahoo[4−6], Pradipta Ghosh[2,3,6*], Padmini Rangamani[7*]

[1] Chemical Engineering Graduate Program

[2] Department of Medicine

[3] Department of Cellular and Molecular Medicine

[4] Department of Computer Science and Engineering

[5] Department of Pediatrics

[6] Moores Comprehensive Cancer Center

[7] Department of Mechanical and Aerospace Engineering

University of California San Diego, La Jolla CA 92093

*To whom correspondence should be addressed;

E-mail: prghosh@ucsd.edu; prangamani@ucsd.edu.

Abstract

Cellular levels of the versatile second messenger, cyclic-(c)AMP are regulated by the antagonistic actions of the canonical G protein→adenylyl cyclase pathway that is initiated by G-protein-coupled receptors (GPCRs) and attenuated by phosphodiesterases (PDEs). Dysregulated cAMP signaling drives many diseases, *e.g.*, its low levels facilitate numerous sinister properties of cancer cells. Recently, an alternative paradigm for cAMP signaling has emerged in which growth factor-receptor tyrosine kinases (RTKs; *e.g.*, EGFR) access and modulate G proteins via a cytosolic guanine-nucleotide exchange modulator (GEM), GIV/Girdin; dysregulation of this pathway is frequently encountered in cancers. In this study, we present a network-based compartmental model for the paradigm of GEM-facilitated cross-talk between RTKs and G proteins and how that impacts cellular cAMP. Our model predicts that the cross-talk between GIV, $G\alpha_s$, and $G\alpha_i$ proteins dampens ligand-stimulated cAMP dynamics. This prediction was experimentally verified by measuring cAMP levels in cells under different conditions. We further predict that the direct proportionality of cAMP concentration as a function of receptor number and the inverse proportionality of cAMP concentration as a function of PDE concentration are both altered by GIV levels. Taken together, our model reveals that GIV acts as a tunable control-valve that regulates cAMP-flux after growth factor stimulation. For a given stimulus, when GIV levels are high cAMP levels are low and *vice versa*. In doing so, GIV modulates cAMP via mechanisms distinct from the two most-often targeted classes of cAMP modulators, GPCRs and PDEs.

Running title: A mathematical model for growth factor-stimulated cAMP signaling

Abbreviations used: **cAMP** – Cyclic adenosine monophosphate; **RTK** –Receptor Tyrosine Kinase; **EGFR** – Epidermal growth factor receptor; **GEM** – G protein exchange modulator; **GEF** – Guanine nucleotide exchange factor; **GDI** – Guanine nucleotide dissociation inhibitor; **SH2** – Src homology 2; **PM** – plasma membrane; **DAG** – Diacylglycerol; **EGF** – Epidermal growth

factor; **AUC** – Area under the curve; **AC** – Adenylyl cyclase; **PDE** – Phosphodiesterase; **AMP** – adenosine monophosptate; **ATP** – adenosine triphosphate; **CDK5** – cyclin dependent kinase 5; **PKC-θ** – Protein kinase C θ; **PLC-γ** – Phospholipase C γ; **Epac1** – Exchange factor directly activated by cAMP 1; **RIA** – Radioimmunoassay; **IBMX** – 3-isobutyl-1-methylxanthene.

Introduction

Cells constantly sense cues from their external environments and relay them to the interior; sensing and relaying signals from cell-surface receptors involves second messengers such as cyclic nucleotides [1, 2]. Of the various cyclic nucleotides, the first to be identified was cyclic adenosine 3,5-monophosphate (cAMP), a universal second messenger. cAMP relays signals triggered by hormones, ion channels, and neurotransmitters [3], and also binds and regulates other cAMP-binding proteins such as PKA and Epac1 [61].

Intracellular levels of cAMP are regulated by the antagonistic action of two classes of enzymes: adenylyl cyclases (ACs) and cyclic nucleotide phosphodiesterases (PDEs). ACs are membrane-bound enzymes that utilize ATP to generate cAMP. PDEs, on the other hand, are soluble enzymes that catalyze the degradation of the phosphodiester bond resulting in the conversion of cAMP to AMP. Overall, the level of cellular cAMP in physiology is finely balanced between synthesis by AC, degradation by PDEs, and regulatory feedback loops from PKA→PDE [3, 6–9] or others that act on ACs and PDEs [62–64]. Too much or too little cAMP is seen in many diseases. For example, high levels of cAMP have been shown to be generally protective in diverse cancers (*e.g.*, breast [28], melanoma [29], pancreas [30], *etc.*), whereas low cAMP levels fuel cancer progression [reviewed in [31]]. This is because cAMP inhibits several harmful phenotypes of tumor cells such as proliferation, invasion, stemness, and chemoresistance, while enhancing differentiation and apoptosis. Although drugs targeting the canonical GPCR/G-protein-cAMP signaling pathway have successfully translated to the clinic for tackling a wide range of ailments [32], from hypertension to glaucoma, such strategies have largely failed to impact cancer care or outcome. Thus, how tumor cells avoid high levels of cAMP appears to be incompletely understood, and therapeutic strategies to elevate cAMP remain unrealized.

Recently, the regulation of cAMP by non-canonical G protein signaling that is initiated by

growth factors [35, 65–67] has emerged as a new signaling paradigm. Growth factor signaling is a major form of signal transduction in eukaryotes, and dysregulated growth factor signaling (*e.g.*, copy number variations or activating mutations in RTKs, increased growth factor production/concentration) is often encountered in advanced tumors and is frequently targeted with varying degrees of success [68]. A body of work published by us and others have revealed that RTKs bind and activate trimeric G proteins via a family of proteins called Guanine-nucleotide Exchange Modulators (GEMs; [35]). GEMs act within diverse signaling cascades and couple activation of these cascades to G protein signaling via an evolutionarily conserved motif of ∼30 amino acids that directly binds and modulates $G\alpha_i$ and $G\alpha_s$ proteins. Most importantly, GIV-GEM serves as a GEF for $G\alpha_i$ and as a GDI for $G\alpha_s$ [42]. Despite this apparent paradox, both forms of modulation lead to suppression of cellular cyclic AMP [66]. By demonstrating how GIV, a prototypical member of a family of cytosolic guanine nucleotide exchange modulators (GEMs; [35, 42]), uses a SH2-like module [43] to directly bind cytoplasmic tails of ligand-activated RTKs such as EGFR [41], we provided a definitive structural basis for several decades of observations made by researchers that G-proteins can be coupled to and modulated by growth factors (reviewed in [69]). A series of studies that have followed since have revealed that growth factor-triggered non-canonical G protein→cAMP signaling through GIV has unique spatiotemporal properties and prolonged dynamics that are distinct from canonical GPCR-dependent signaling [reviewed in [65]]. In parallel, studies have also found that high levels of GIV expression fuels multiple ominous properties of cancer cells, *e.g.*, invasiveness, chemoresistance, stemness, survival, *etc.*, and is associated with poorer outcome in multiple cancers. Inhibition of GIV's G protein modulatory function has emerged as a plausible strategy to combat aggressive traits of cancers [70] (reviewed in [35, 67]). These findings provide us a unique opportunity to investigate, from a systems leve, how modulation of trimeric GTPase $G\alpha_i$ and $G\alpha_s$ by GIV downstream of growth factors regulates cAMP and what impact might such regulation have on the aggressiveness of cancers.

In this study, we develop a mathematical model of cAMP signaling that is triggered by ligand stimulation of EGFR, and to investigate how cAMP dynamics in cells is affected by the GIV-G$\alpha_{i/s}$ and PDE axes. Further, we also sought to connect the findings from the cell-based model to survival data from cancer afflicted patients by identifying the most consequential variables within this signaling pathway. In doing so, this model not only interrogates the crosstalk between two of the most widely studied eukaryotic signaling hubs [RTKs and G proteins], but also reveals surprising insights into the workings of GIV-GEM and provides a mechanistic and predictive framework for experimental design and clinical outcome.

Results and discussion

Phenomenological model reveals that GIV-associated timescales modulate cyclic AMP dynamics

The emerging paradigm of non-canonical modulation of Gα_i/Gα_s proteins by growth factor RTKs is comprised of several temporally and spatially separated components (**Figure 2.1A**). We first developed a phenomenological model to identify the network topology of RTK-G protein-cAMP signaling (**Figure 2.1B**). This network captures the key events of the steps shown in (**Figure 2.1A**). Briefly, receptor (R) stimulation is modeled using a time-dependent function S(t) to result in active receptor R*. R* then acts on GIV at two time scales – τ_1 for GIV-GEF activation and τ_2, for GIV-GDI activation. cAMP synthesis is directly proportional to the level of internalized, endosomal receptor R$_i^*$ with a time scale of τ_3. GIV-GDI inhibits the internalized receptor and GIV-GEF inhibits cAMP production. Even though none of the components in this model reflect actual biochemical species, the simplified model has the advantage of capturing the key timescales of the events leading up to cAMP production from RTKs. Varying these timescales alters the dynamics of GIV-GEF, GIV-GDI, and cAMP (**Figure 2.1C**, **D**, **A.1E**). Additionally, this

model has the advantage of being parametrized by a small number of variables and parameters (see SOM for details). Simulations from this model predict that GIV-GEF activation is rapid, whereas GIV-GDI activation is slow (**Figure 2.1C**). This temporal response is observed for a wide range of parameters with the internalization and degradation rates, k_4, k_5, as leading order contributors across most time points (**Figure A.1**). τ delays are shown to have lower contributions in cAMP response then the major rates, k_4, k_5 (**Figure A.1**). cAMP dynamics predicted from this simple model show a delayed increase in cAMP corresponding to the time scale of GIV-GDI in **Figure 2.1D**. Furthermore, changing the receptor density shows that the presence of GIV suppresses the cAMP production; the role played by GIV in modulating cAMP is stronger in higher RTK concentrations because of the competing effects of $G\alpha_s$ and $G\alpha_i$. This leads us to arrive at two conclusions: First, the network topology in the toy model, with GIV as the central regulator, is able to capture cAMP dynamics. Second, RTK copy number alone is an incomplete determinant of cAMP; RTK and GIV together determine cAMP concentrations.

Construction and experimental validation of a compartmental model for non-canonical G-protein signaling triggered by growth factors

Although the phenomenological model in (**Figure 2.1**) allowed us to identify key features of RTK-G protein-cAMP signaling, it does not contain enough information to compare simulation output against experimental measurements. Therefore, the topology model was expanded to a larger biochemical reaction network such that the modules reflected the timescales τ_1, τ_2, and τ_3 within a larger network model (**Figure 2.2A**). The model consists of four modules – **Module 1** focuses on the well-established dynamics of EGFR [71–73] (**Table A.4**); **Module 2** represents the dynamics of the formation of the EGFR·GIV·$G\alpha_i$ complex, representing τ_1 (**Table A.5**; within this complex GIV-GEM serves as a GEF for $G\alpha_i$); **Module 3** represents the dynamics of the formation of the $G\alpha_s$·GIV-GDI complex, representing τ_2 for GEF to GDI conversion (**Table A.6**;

14

within this complex GIV-GEM serves as a GDI for Gα_s); and **Module 4** represents the dynamics of cAMP formation and represents τ_3 for Gα_s activation by internalized receptors (**Table A.7, A.8**).

Within each module, the biochemical reaction network includes several known interactions curated from the literature along with kinetic parameters (see **Tables S2-S6** for references). However, to our knowledge, no mathematical models of GIV-GEM interactions within the RTK→G protein→cAMP pathway exist. Therefore, we had to estimate kinetic parameters for certain reactions in each module. Of the 76 kinetic parameters in the model, 57 parameters were from the literature while 19 were fit to experimental data. We fit the model to the experimentally measured dynamics of the EGFR·GIV·Gα_i complex (**Figure 2.2B**) and the Gα_s·GIV-GDI complex (**Figure 2.2C**). Because the actual concentration of this complex in cells is not known, and is likely to vary from cell to cell, we analyzed peak times and fold change of these complexes. The temporal dynamics of these normalized densities of both these complexes generated from simulations were in good agreement with experimental measurements, as determined by PLA and GST pulldown assays [42, 74] carried out in HeLa cells responding to EGF. We provide a detailed discussion of parameter estimation, goodness-of-fit, and uncertainty quantification in later sections. Our choice of experimental assays for validating the model and fitting parameters were carefully chosen into consideration the strengths and weaknesses of each assay (see Methods). We used this modular network to investigate the role played by GIV in regulating the dynamics of EGFR, EGFR·GIV·Gα_i complex, Gα_s·GIV-GDI complex, and cAMP.

Biological prediction: Compartmentalized modulation of Gα_i and Gα_s by GIV-GEM governs EGF-triggered cyclic AMP dynamics

Because EGF/EGFR triggers activation of Gα_i at the PM first, followed by activation of Gα_s on the endosomes later, production of cAMP must be a balance between the antagonistic

actions of these two G proteins on membrane-bound ACs (**Table A.7**). We assumed that the PM-pool of Gα_i inhibits the AC$\rightarrow$cAMP pathway at the PM. Similarly, because Gα_s is activated predominantly on endosomes and endosomal ACs [eACs] can be stimulated to synthesize cAMP locally [75], we assumed that the endosomal-pool of Gα_s likely stimulates the eAC$\rightarrow$cAMP pathway (**Table A.7**). To capture the dynamics of cAMP in our model network, we included such compartmentalized G protein-AC interactions.

Our model predicted that the early inhibition of cAMP is due to the Gα_i-mediated inhibition of AC (the green regime) (**Figure 2.2D**); cAMP production is increased later due to the activation of Gα_s on the endosome (the blue regime) (**Figure 2.2D**). These dynamics are consistent with previously published GIV-dependent cAMP dynamics, measured by FRET [42]. While activation of GIV-GEF occurs earlier [within 5 min] at the PM, conversion of GIV-GEF to GIV-GDI occurs later [15-30 min] when EGFR is already compartmentalized in endosomes (**Figure 2.1A**); such temporally separated compartmentalized modulation of two G$_\alpha$-proteins with opposing effects on AC ensures suppression of cAMP at both early and later times during EGF signaling [42]. Because GIV modulates both Gα_i and Gα_s in different compartments and at different time scales, the model predicts that increasing GIV concentration should dampen overall cAMP response to EGF, and that decreasing GIV concentration should do the opposite (**Figure 2.2D**, compare GIV = 0.01 μM with GIV = 10 μM). These predictions were validated experimentally by measuring cAMP in control (shControl) and GIV-depleted (shGIV; >95% depletion by band densitometry, see **Figure A.2E**) cells at various time points after EGF stimulation (**Figure 2.2E**) by a radioimmunoassay (RIA). We found that compared to control cells, cellular levels of cAMP were always higher, both at early and late time points after EGF stimulation. In fact, when superimposed, the model and experiment showed good agreement throughout 60 min (**Figure A.3, A.7, A.8**). As expected, sensitivity analyses confirmed that cAMP is sensitive to the initial concentrations of PDE and AC, and the reaction rates associated with AC, internalization, PKA, and PDE (**Tables A.14, A.17**).

To dissect what might be the relative contributions of the two G protein modulatory functions of GIV [GEF versus GDI] on cAMP production, we investigated cAMP dynamics in three conditions (**Figure 2.2D**) – 1) GEF-deficient but GDI-proficient (mimicked experimentally by the GIV-S1764D/S1689D mutant, GIV-DD [42], 2) both GEF- and GDI-deficient (mimicked experimentally by GIV-F1685A mutant, GIV-FA [42,76], and 3) GEF-proficient but GDI-deficient (an *in silico* mutant because there is no known mutant yet that can mimic this situation in experiments). In the first scenario, where GIV's GEF function is selectively lost, but GDI function is preserved, increase in cAMP concentration occurred early (**Figure 2.2D**, dashed cyan line) as observed previously in cells expressing the GIV-DD mutant [42]. In the second scenario, where both GEF and GDI functions were lost, increase in cAMP concentration occurred early and such elevation was sustained (**Figure 2.2D**, dashed dark green line), as observed previously in cells expressing the GIV-FA mutant [42]; this mirrored the profile observed in GIV-depleted cells (**Figure 2.2D**, solid green line). Finally, in the third scenario, selective blocking of GIV's GDI function using an *in silico* mutant resulted in an early decrease followed by a prolonged increase in cAMP concentration (**Figure 2.2D**, dot-dashed blue line).

While the dynamics of cAMP production provide insight into how different conditions lead to changes in concentration, the area under the curve [AUC] for cAMP concentration provides information critical for decision-making, buffers from time scale variations, and averages the effect of fluctuations in concentrations [77]. AUCs for cAMP at different time points were calculated to investigate how the cumulative cAMP signal varies under different GIV conditions (**Figure 2.2F**). For the control bars (in orange), we observe that at the 5 min time point, the AUC is negative. This represents the initial decrease in cAMP concentration. The AUC becomes positive and increases by 15 min, signifying a net accumulation of cAMP. The AUCs look similar in the GIV-FA mutant [defective in both GDI and GEF functions] as well as in the absence of GIV, i.e., it increases progressively through 60 min (**Figure 2.2F**, compare the light green and dark green bars). If GIV levels are increased (10 μM , red bars) the AUCs remain negative throughout,

showing the sustained nature of the dampening effect of GIV on cAMP. This dampening effect on cAMP is achieved primarily via activation of Gα_i in the short term [GEF regime] and via inhibition of Gα_s in the long term [GDI regime]. These findings are in keeping with the previously suspected role of GIV in reducing cellular cAMP, but the model reveals the relative contributions of GIV's GEF and GDI functions separated in time and space at a resolution that is experimentally unachievable.

Biological prediction: GIV dampens EGF/EGFR-triggered cyclic AMP production

Common wisdom from canonical signaling suggests that an increase in stimulus through receptor copy number leads to a proportional increase in cAMP concentration. Therefore, we would expect that an increase in EGFR density would lead to an increase in cAMP concentration. But the phenomenological model indicated that cAMP concentration depends on both the receptor copy number and GIV concentration, **Figure 2.1D**. We investigated how GIV concentration affects cAMP dynamics with varying EGF/EGFR numbers. When GIV concentrations were set to 0.01 μM in the model (to simulate cells that don't have GIV), increased input signals triggered increased output signals (**Figure 2.3A**, **A.10**); this effect was even more pronounced in the absence of PDE (**Figure 2.3E**). This proportional response was lost when GIV concentrations were set to high levels (GIV = 10 μM **Figure 2.3B**), *i.e.*, increased input signals failed to initiate proportional output signals; this effect was virtually unchanged and robustness was preserved despite the absence of PDE (**Figure 2.3F**). These effects are also evident by comparing the AUCs across the simulated conditions (**Figure 2.3C**, **G**).

To test these predictions, we measured cAMP by RIA in control and GIV-depleted HeLa cells as in **Figure 2.2E**, except in this instance we measured only at 60 min, but with varying doses of EGF [experimental equivalent of variable input in simulations]. To recapitulate simulations in the presence or absence of PDE, assays were carried out in parallel in the presence or absence of 3-

isobutyl-1-methylxanthine (IBMX), an inhibitor of PDE (**Figure 2.3D**, **H**). In the presence of GIV, cAMP production is robustly suppressed in response to increasing EGF ligand (**Figure 2.3G**). In the absence of GIV, cAMP production is sensitive to increased EGF, an effect that is further accentuated when PDEs are inhibited with IBMX (**Figure 2.3K**). Taken together, these results indicate that GIV primarily serves as a dampener of cellular cAMP that is triggered downstream of EGF. Unlike PDE, which reduces cellular cAMP by degrading it, GIV does so by fine-tuning its production by G proteins and membrane ACs. Thus, our model identified that GIV is a critical determinant of cAMP concentrations in response to EGFR signaling.

Model reveals that GIV-GEM may serve as a tunable valve for cAMP flux; high GIV implies low flux, whereas low GIV implies high flux

In order to quantify the extent of crosstalk between EGFR and GIV, we conducted simulations for a wider range of EGFR [36-1800 $molecules/\mu m^2$] and GIV concentrations [0.01-10 μM] and calculated the AUC for the cAMP dynamics (**Figure 2.4A**, **B**, **A.11**). In a low-EGFR state, varying GIV concentrations only resulted in cAMP changes within a narrow range; however, in a high-EGFR state varying GIV concentrations achieved a larger variance in cAMP (**Figure 2.4A**). To further dissect this space, we plotted the variations in AUC for EGFR and GIV variations (**Figure 2.4B**). The value of AUC corresponding to the control (GIV $1\mu M$ and EGFR 240 $molecules/\mu m^2$, **Table A.11**) is approximately 0.45 $\mu M \cdot min$ and is denoted by the yellow color and marked as a black solid line for different EGFR and GIV concentrations in the heat map; elevated cAMP level is denoted by green and reduced cAMP by red. We observed that increasing EGFR increased cAMP AUC in the setting of low GIV concentrations. But when GIV concentrations are high, cAMP AUC remained low regardless of increasing levels of EGFR, indicating that the impact of increasing GIV on cAMP AUC was higher than the impact of increasing EGFR. Therefore, GIV levels in conjunction with EGFR levels, can be thought of

as key determinants and high GIV in the setting of high EGFR may facilitate tonic suppression of cAMP levels regardless of pathway stimulation.

Another factor that plays an important role in regulating cAMP levels is PDE. We next conducted simulations for different GIV (0.01 to 1 μM) and PDE (0.04 to 2.5 μM) concentrations to identify how the crosstalk between these two variable components regulates cAMP levels. Within each category of PDE concentration [low vs high PDE states; (**Figure 2.4C**, **A.12**), cAMP levels are the highest when GIV levels are lowest, and *vice versa*. In the setting of low PDE activity, the impact of changing GIV was the highest, *i.e.*, the range of cAMP response was the widest. By contrast, in the setting of high PDE activity, the impact of changing GIV on the cAMP levels was minimal. These effects can be seen when comparing the AUCs for the low vs high PDE states, calculated over 1 hr (**Figure 2.4C**). While there is no significant change in the AUC with increasing GIV in a high-PDE state (red bars), increase in GIV leads to a decrease in cAMP in PDE state (green bars). That is, for a given GIV concentration, the effect of PDE is always stronger. Furthermore, a heat map of cAMP AUCs (**Figure 2.4D**) shows the interplay between PDE and GIV concentrations over a wide range. For low PDE concentration, increasing GIV decreases cAMP AUC, but the cAMP AUC is well above the yellow value (marked as control). However, increase in PDE concentration leads to a dramatic decline in cAMP AUC even when GIV levels are low; this condition is likely to result in futile cycling [high cAMP production due to low GIV and high cAMP clearance due to high PDE signaling]. Together, these findings indicate that the effect of GIV concentration on cAMP levels in cells is discernible only when PDE activity is low. Because high PDE state virtually abolishes all effects of GIV-dependent inhibition of cAMP production, we also conclude that in this GIV-PDE crosstalk, PDE is a dominant node and GIV is the subordinate node.

Our network model has helped us identify key design principles of the action of GIV-GEM within the EGF/EGFR signaling circuit by enabling construction of a map to identify

the relationship between the key components– input[EGFR]→valve[GIV] →output[cAMP]→ sink[PDE] (**Figure 2.4E**), validate the impact of such relationship with experimental assessment of cellular cAMP (**Figure 2.2**, **2.3**) and interpret the role of each component in the context of network architecture. That there is a complex, non-linear and non-intuitive crosstalk between EGFR, GIV, and PDE in regulating cAMP levels is evident from the fact that the isoplanes, which capture the same cAMP AUC are not flat but are bent surfaces in this space. It appears that variation of cellular concentration of functionally active GIV-GEM molecules serves as the most tunable component that regulates the flow of signal from EGF/EGFR [input] to cAMP [output] (**Figure 2.4E**). At low concentrations of GIV, such as those found in normal tissues, cAMP levels are sensitive to increased signal input via EGF/EGFR, i.e., higher input elicits higher output. Such sensitivity is virtually abolished and replaced by robustness at higher GIV concentrations found in a variety of cancers, i.e., higher input fails to elicit higher output and instead, cAMP levels stay at low and relatively constant. This 3-way interplay between EGFR, GIV and PDE is obvious also in experimental data derived from HeLa cells (**Figure 2.3D**, **H**) suggesting that GIV acts a tunable valve for the input-output relationships that govern RTK-G protein-cAMP signaling.

Clinical predictions from the model – from math to man

The signaling network model built using dynamic protein-protein interactions and enzymatic reactions during signal transduction predicts that GIV dampens cAMP signaling in response to EGF/EGFR stimulation over a 60-min time course [35, 65–67]. We chose to stick to 60 min because this is the time period when almost all the tyr-phosphorylated EGFR pool disappears, which coincides with the entry of EGFR into late endosomes, where ~60 % total EGFR remains while the remaining 40% is degraded in the endosomes [2]. In fact, modeling studies using a plethora of experimentally determined parameters [3] have concluded that transient responses exhibit pronounced maxima, reached within 15-30 sec of EGF stimulation and followed by a

decline to relatively low (quasi-steady-state) levels in all parameters tested at 60, 90 and 120 minutes; findings emphasized that ~60 min is the earliest time that is reflective of steady-state, whether it is immediate post-receptor event or gene change response or cellular phenotypes. We next asked if we could relate this prediction to patient clinical data for survival which reflect a steady-state that evolves over years, not just weeks or months. Numerous prior studies [28–31] have shown that low cAMP facilitates several ominous tumor cell traits, and hence, is permissive to cancer progression and worse outcome. Consistently, numerous studies have confirmed that high GIV levels (which our model predicts will lead to a tonic suppressed cAMP state regardless of the degree of stimuli) are generally associated with aggressive tumor cell traits and poorer clinical outcomes.

We begin by redefining the input and output for our system. The inputs for these analyses are EGFR mRNA, GIV mRNA, and PDE mRNA, which we use as a surrogate measure of copy number of proteins because others have shown that mRNA can indeed predict protein copy numbers per cell [78]and that mRNA abundance positively correlates with protein levels in healthy and cancer tissues [79]. The output is patient survival probability over time, an outcome which reflects tumor's aggressiveness, which we use as a surrogate measure of low or suppressed cAMP states. Then, the prediction from the signaling model can be recast as the following hypotheses – EGFR gene-expression levels or PDE gene-expression levels, which by themselves are yet to emerge as clinically useful prognosticators of survival, should become important determinants when analyzed within context of GIV. We formulate and test two hypotheses in the following sections.

Concurrent upregulation of both GIV and EGFR maximally reduces cAMP and carries poor prognosis in colorectal tumors

To determine the impact of crosstalk between EGFR and GIV on clinical outcome, we compared the mRNA expression levels to disease-free survival (DFS) in a data set of 466 patients with colorectal cancers (see Methods). Patients were stratified into negative (low) and positive (high) subgroups with regard to GIV (CCDC88A) and EGFR gene-expression levels with the use of the StepMiner algorithm, implemented within the Hegemon software (hierarchical exploration of gene-expression microarrays online; [80]) (**Figure 2.5A**). Kaplan-Meier analyses of DFS over time showed that among patients with high EGFR, expression of GIV at high levels carried a significantly poorer prognosis compared to those with low GIV (**Figure 2.5B**, **A.13**). Among patients with low EGFR, expression of GIV at high or low levels did not impact survival (**Figure 2.5C**, **A.13**). Among patients with low EGFR, expression of GIV at high or low levels did not impact survival (**Figure 2.5C**). That the impact of EGFR-GIV interplay on patient survival are significant in a rigorous Kaplan-Meier analysis of a sufficiently large cohort of patients, despite numerous independent variables indicates that the interplay between EGFR and the G protein modulator, GIV is an important determinant of cancer progression. More importantly, patients with tumors expressing high EGFR did as well as those expressing low EGFR provided the levels of GIV in those tumors was low. These findings reveal that 1) high levels of EGFR signaling does not, by itself, fuel aggressive traits or carry a poor prognosis, but does so when GIV levels are concurrently elevated; 2) in tumors with low GIV, the high EGFR signaling state may be critical for maintaining high cAMP levels and therefore, critical for dampening several aggressive tumor traits.

Concurrent downregulation of both GIV and PDE activity maximally increases cAMP and carries a good prognosis in colorectal tumors

Next, to determine the impact of crosstalk between various PDE isoforms and GIV on clinical outcome, we carried out using the StepMiner algorithm, implemented within the Hegemon software on the same set of 466 patients with colorectal cancers as before, except patients were now stratified into low and high subgroups with regard to GIV (CCDC88A) and PDE gene-expression (**Figure 2.5D**-**F**). Among the 11 known PDE isoforms, we evaluated those that have previously been linked to colon cancer progression [PDE5A (**Figure 2.5D**-**F**), 4A and 10A (**Figure A.13**)]. Kaplan-Meier analyses of DFS over time showed that although expression of GIV at high levels was associated with disease progression and poorer survival in both low and high PDE groups, the risk of progression was not statistically significant in the high-PDE state (**Figure 2.5E**) but highly significant in the low-PDE state (**Figure 2.5F**). Thus, the low GIV/low PDE signature carried a better prognosis compared to all other patients. Consistent with the fact that cAMP is a potent anti-tumor second messenger, these findings reveal that – 1) high levels of PDE signaling may not be a bad thing, especially when GIV levels are low; 2) in tumors with low PDE signaling, the low GIV signaling state may serve as a key synergy for driving up cAMP levels and therefore, critical for dampening several aggressive tumor traits.

Discussion

Systems biology aims to understand and control the properties of biological networks; experimental data collected using top-down approaches are used to construct *in silico* bottom-up models, with the ultimate goal of generating experimentally testable predictions. In this work, we used a systems biology approach to construct the first-ever compartmental network model of growth-factor triggered cAMP signaling, and identified two key features of non-canonical G

protein signaling via GIV-GEM.

First, we identified that compartmentalized RTK signaling at the PM and on the endosomes directly imparts a *delayed* and *prolonged* cAMP dynamics lasting over an hour, which is distinct from the canonical GPCR/G protein pathway; GPCRs initiate more rapid and finite cAMP dynamics in the order of msec to min (**Figure A.5**) [81]. In the case of GPCRs, the PM-based signals are believed to be the dominant component of the overall cAMP dynamics with signal attenuation during endocytosis (**Figure A.5**) [82]. By contrast, in the case of RTK-mediated cAMP dynamics via GIV-GEM, the post-endocytic (i.e., endosomal signaling) component constitutes a dominant component of the overall cAMP dynamics that are triggered by RTKs (**Figure A.5**). What may be the impact of these distinct temporal features on RTK signaling? It is noteworthy that RTK-triggered cAMP dynamics that are modulated by GIV-GEM spans 5 min to > 60 min, which coincides with other RTK signaling, trafficking events and transcriptional response, i.e., the major temporal domain of RTK activity, the so-called "window of activity" [83]. The 5 min to 1 h time scale encompasses the time of peak mRNA expression of many immediate-early genes (which peak at 20 min) and delayed-early genes (which peak between 40 min and 2 hours); these transcriptional targets not only generate feedback within the RTK-signaling cascade, but also set up crosstalk with other signaling pathways [83, 84]. In fact, GIV-GEM has indeed been found to modulate myriad downstream signaling pathways from the activity of small GTPases, kinases and phosphatases, to transcription factors [reviewed in [65]]; how GIV-GEM has such a widespread and broad impact had remained a mystery. It is possible that such broad impact could stem from GIV's ability to modulate the cellular levels of the versatile second messenger cAMP in a sustained manner throughout the window of RTK activity although other mechanisms might also be at play.

Second, our model identifies that GIV-GEM acts a tunable valve for cAMP by operating at the knot of a bow-tie architecture. Because layering of control of [information] flow is believed

to conform to an hourglass architecture [85], in which diverse functions and diverse components are intertwined via universal carriers, GIV's ability to control the universal carrier, cAMP, could explain why GIV has been found to be important for diverse cellular functions and impact diverse components [65].

Third, our work also provides valuable clues into the impact of increased robustness at high-GIV states in cancers. Robustness in signaling is an organizing principle in biology, not only for the maintenance of homeostasis but also in the development and progression of chronic debilitating diseases like cancers; it is widely accepted that tumor cells hijack such robustness to gain growth and survival advantage during the development of cancer [83, 86, 87]. Consistently, we found that GIV mRNA levels and DNA copy numbers are invariably higher across multiple cancers when compared to their respective normal tissue of origin (**Figure A.14, A.15**). Because GIV has been found to regulate several harmful properties of tumor cells across a variety of cancers (multiple studies, reviewed in [67]), it is possible that the high-GIV driven robustness maintains cAMP at low constant levels despite increasing input signals as a tumor evolves when targeted by biologicals or chemotherapy agents. Such a phenomenon could be a part of a higher order organizing principle in most aggressive cancers, and therefore, justify GIV as a potential target for network-based anti-cancer therapy.

Furthermore, the crosstalk between EGFR and GIV the we define here, and its impact on clinical outcome provide a plausible explanation for some long-standing conundrums in the field of oncology. Deregulated growth factor signaling (e.g., copy number variations or activating mutations in EGFR, increased growth factor production/concentration) is often encountered and targeted for therapy in advanced cancers [68]. Although activating EGFR mutations, copy number variations, and levels of EGFR protein expression seem to be closely related to each other [88], the prognostic impact of EGFR expression in cancers has been ambiguous [89]. In some cancers, high EGFR copy numbers are associated with poor outcome [90, 91]; in others, high EGFR

expression unexpectedly favors better overall and progression-free survival [92–94]. Thus, due to reasons that are unclear, not all tumors with high EGF/EGFR signaling have an aggressive clinical course. Dysregulated GIV expression, on the other hand, is consistently associated with poorer outcome across a variety of cancers [66]. Our findings that GIV levels in tumors with high EGFR are a key determinant of the levels of the anti-tumor second messenger cAMP, have provided a potential molecular basis for why elevated EGFR signaling in some tumors can be a beneficial in some, but a driver of metastatic progression in others. Because cAMP levels in tumor cells and GIV levels have been previously implicated in anti-apoptotic signaling [95] and the development of chemoresistance [96], it is possible that the GIV-EGFR crosstalk we define here also determines how well patients may respond to anti-EGFR therapies, and who may be at highest risk for developing drug resistance. Whether such is the case, remains to be evaluated. Similarly, in the context of PDE, it has been demonstrated that overexpression of PDE isoforms in various cancers leads to impaired cAMP and/or cGMP generation [24]. PDE inhibitors in tumour models *in vitro* and *in vivo* have been shown to induce apoptosis and cell cycle arrest in a broad spectrum of tumour cells [97]. Despite the vast amount of preclinical evidence, there have been no PDE inhibitors that have successfully translated to the cancer clinics. For example, based on the role of cAMP in apoptosis and drug resistance, our model predicts that those with low GIV/high EGFR [high cAMP state] are likely to respond well to anti-EGFR therapy inducing tumor cell apoptosis, whereas those with high GIV/high EGFR [low cAMP state] may be at highest risk for developing drug resistance. Similarly, our finding that low PDE levels in the setting of high GIV carries a poor prognosis predicts that the benefits of PDE inhibitors may be limited to patients who have low GIV expression in their tumors. Whether such predictions hold true, remains to be investigated.

Model Limitations

Although our model captures experimentally observed time courses and generates testable hypotheses, it has a few major limitations. From a model development standpoint, the compartmental well-mixed model we used does not account for the spatial location and geometries of the different compartments and cell shape, many of which can affect the dynamics of cell signaling [98, 99]. Furthermore, a major concern is the estimation of kinetic parameters for the different reactions. Of the 76 kinetic parameters in our model, a large majority (57) were from models published before. 19 parameters, all of which are related to GIV interactions with internalization, $G\alpha_s$, and $G\alpha_i$ were estimated from experimental data. The uncertainty in some of these parameters was quite large (**Figure A.6**). While sloppy parameter space is a problem common to many signaling networks [100], in this case, it is exacerbated by the fact that the model we have constructed is the first of its kind for this pathway. The issue with kinetic parameters also reflects the fact that the field of RTK-G protein regulation is relatively young and makes the case for more quantitative investigations of GIV-GEM modulated signaling. By themselves, these facts can lower the confidence in the exact temporal dynamics predicted by the model. However, our confidence in the model is bolstered by the timescales predicted by the phenomenological model and implications for patient survival data.

Additionally, our model focuses exclusively on cAMP as output signal and does not account for other EGF/EGFR-driven signaling pathways that are known to regulate cellular responses such as the Ras-Raf-MEK-ERK pathway. This pathway is known to modulate cAMP and be modulated by GIV via the ability of the latter to affect adaptor protein recruitment to the cytosolic tail of EGFR [41]. However, the vast parameter space associated with model building indicates that this pathway would require its own study. In addition, the dynamics of ERK1/2 activation on the endosomal structure would have to be explored due to GIV-GEM's interaction with endosomal maturation through $G\alpha_s$. The model expansion would lead to an even larger

parameter space, with less available data.

Moreover, our model focuses exclusively on EGFR and does not account for the diverse classes of receptors [multiple RTKs, GPCRs, integrins, etc.] that also use GIV to access and modulate G proteins. Model validations used HeLa cells not only because this is the most common model cell line that has been used exhaustively to study both GIV and EGFR biology by us and others, but also because it has a modest level of expression for both EGFR and GIV. Despite these restrictions, we can identify some fundamental features of growth factor-triggered cAMP signaling for the first time using systems biology, including the role of compartmentalization, cross-talk between EGFR and GIV, GIV-dependent robustness within the RTK-cAMP signaling axis, and cross-talk between PDE and GIV in controlling cAMP concentration. Although there exists many different signaling pathways downstream of EGFR. GIV-GEM is the only direct link between EGFR and G Proteins to date. Due to the high congruency between the model and validation this leads to two possibilities: either GIV-GEM interaction operates on a standalone basis, or there exist additional feedback loops where GIV-GEM acts as a leading order contributor (**Figure A.9**).

Conclusions

We conclude that GIV utilizes compartmental segregation to modulate the dynamics of RTK$\rightarrow$G protein$\rightarrow$cAMP signaling and confers robustness to these dynamics by functioning as a tunable control valve. Future systems efforts will build on this model to unravel further exciting features of GIV as a critical hub for signaling regulation at the knot of a bowtie [101] and elucidate the hidden complexity that arises from network architecture in non-canonical G protein signaling.

Methods

Modular construction of the reaction network

A biochemical network model was constructed to capture the main events in the signal transduction cascade from EGF to cAMP through GIV (**Figure 2.2A**). We constructed the compartmental computational model in a modular manner, where each module represents key events within the network. . The model was trained using key data sets published over the past decade on GIV-GEM, most notably, those that defined the spatio-temporal kinetics of EGFR·GIV, EGFR·GIV·Gα_i interactions [41, 47, 70], dynamics of phosphoregulation of GIV-GEM [74, 102], and most importantly, the dual modulation of G$\alpha_{i/s}$ by GIV-GEM that is brought about by temporally and spatially separated phosphorylation events [42]. Last, but not least, we also used published role of Gα_s in the feedback regulation of endocytic downregulation of EGF/EGFR signaling [40].

The model contains 76 kinetic parameters. 19 parameters were fit with varying confidence values(**Figure A.6**). Each kinetic parameter used in this model originated from peer-reviewed publications of computational models or from experimental measurement. The EGF/EGFR and trimeric GTPase related kinetic parameters were taken from work done by multiple independent groups, often cross-validated across groups engaged in studying each of these paradigms/pathways. For the GIV-related parameters that originate at the interface between the two pathways (EGFR and G proteins) we have used [42].

We note here that while there are many more biochemical components involved in signaling from EGF to cAMP, our choice of components was based on experimentally measured temporal dynamics of GIV-GEF and GIV-GDI functions. The modules are as follows.

Module 1 consists of EGFR activation through EGF and internalization dynamics leading

degradation due to the $G\alpha_s$·GIV-GDI complex. This module includes the phenomenon that endosomal maturation and EGFR degradation in lysosomes requires the presence of inactive $G\alpha_s$ [GDP-bound state] [40]. The presence of $G\alpha_s$ in the inactive state promotes maturation of endosomes, shuts down the mitogenic MAPK-ERK1/2 signals from endosomes and suppresses cell proliferation [40]. In the absence of $G\alpha_s$ or in cells expressing a constitutively active mutant $G\alpha_s$, EGFR stays longer in endosomes, MAPK - ERK1/2 signals are enhanced and cells proliferate [40] (**Figure A.5**).

Module 2 contains EGFR-mediated activation of p35 and downstream activation of $G\alpha_i$ though GIV-GEM; the fromer activated CDK5 which phosphorylates GIV at S1764 allowing the ability to activate $G\alpha_i$ [102]. This phosphoevent does not impact GIV's ability to inhibit $G\alpha_s$ [42] (**Figure A.2B**).

Module 3 contains EGFR-mediated activation of PLC-γ and downstream activation of PKC-θ; the latter phosphorylates GIV at S1689 and terminates its ability to activate $G\alpha_i$ [102]. This phosphoevent does not impact GIV's ability to inhibit $G\alpha_s$ [42]. Consequently, when it comes to G protein modulatory functions of GIV, phosphorylation by PKC-θ converts GIV-GEF into GIV-GDI (**Figure A.2D**).

Module 4 contains the dynamics of the AC and how it synthesizes cAMP, leading to downstream effectors and controllers (**Figure A.2C**) we currently only consider PDE feedback for cAMP reduction. Overall, the model contains 56 reactions. The complete set of reactions for each of the modules, their parameters and interactions, and the list of assumptions underlying network construction are provided as online supplementary materials (**Tables A.4 – A.8**, **Figure A.8**).

We assumed that the signaling components were present in large-enough quantities, and different concentrations of each component were computed to explore how varying expression levels in different tissues/cell types impact the signaling pathway. Such assumption allowed us

to generate a deterministic dynamical model. The model contains six different compartments: (i) PM, (ii) extracellular space, (iii) cytosol, (iv) endosomes, and (v) endosomal membranes. It was assumed that each compartment is well-mixed and fluxes were used to depict transport across the different compartments so that the dynamic changes in the concentrations of the different components can be tracked. Each interaction was modeled as a chemical reaction either using mass-action kinetics for binding-unbinding reactions, and Michaelis-Menten kinetics for enzyme-catalyzed reactions, as is standard for models such as this [103, 104].

The network of interactions was constructed using the Virtual Cell modeling platform and was later transferred to COPASI (version 4.24, build 197) (http://www.nrcam.uchc.edu, http://copasi.org/). We chose this platform because it is a user-friendly computational cell biology software, which allows us to generate the system of differential equations based on the input reactions and has been used successfully to model signaling networks of various sizes with a high degree of numerical accuracy [105–108]. The model was later exported into COPASI to leverage the inbuilt fitting techniques. Also, the Virtual Cell and COPASI platform has built-in capabilities to conduct dynamic sensitivity analysis, which is an important aspect of dynamic systems modeling. As we discuss in later sections, we use this capability to identify sources of system robustness and sloppiness.

Characteristics of the signaling cascade

In order to characterize the dynamics of the different protein activities, we use the area under the curve for the concentration versus time curve [77]. The area under the curve gives the total signal activated over the time of observation and for the ith species is given by AUC_i in Eq. **2.1**. This gives a measure of the total signal for different conditions.

$$AUC_i = \int_0^\infty X_i(t)dt \tag{2.1}$$

32

Comparison with experimental data

Raw data corresponding to **Figure 1C** and **D** of [42] was used for model fitting. The data was normalized such that the initial value was 1. Parameter fitting using COPASI [109] was used to then match the normalized experimental data against the model output, with corresponding expected initial values based on the experimental method. Goodness of fit between experimental values and model output was determined using a root mean squared error (RMSE).

Choice of assays for model validation

We chose to validate our temportal-spatial model for the dynamic assembly of the EGFR·GIV·Gα_i
and Gα_s·GIV-GDI complexes using previously published protein-protein interaction assays carried out in cells responding to EGF [42]. For EGFR·GIV·Gα_i complexes that are formed within 5 min after ligand stimulation at the plasma membrane, we modeled the GST pulldown assays carried out using GST-GIV-CT that is expressed in cells (and hence, phosphomodified in response to EGF stimulation) and endogenous Gα_i. The findings of these pulldown assays mirrored observations by FRET-based [47] and co-IP assays [41,43]. For Gα_s·GIV-GDI complexes that are formed later and on endosomes, we modeled the proximity-ligation assays (PLA) on endogenous GIV and Gα_s proteins, which provide a crude estimate of complexes on endomembranes.

Dynamic parametric sensitivity analysis

Since a continuing challenge in building computational models of signaling networks is the choice of kinetic parameters, we conducted a dynamic parametric sensitivity analysis. This sensitivity analysis of the model was performed with the goal of identifying the set of parameters and initial concentrations that the model response is most sensitive to. The log

sensitivity coefficient of the concentration of the ith species C_i, with respect to parameter k_j is given by [110, 111]

$$S_{i,j} = \frac{\partial \ln C_i}{\partial \ln k_j} \tag{2.2}$$

Since we are studying a dynamical system and not steady state behavior, we used COPASI to calculate the local log sensitivity at the 5, 15, 30, and 60 minute points (**Figure A.4**). The resulting values give information about the time dependence of parametric sensitivity coefficients for the system at those points. The variable of interest, C_i is said to be robust with respect to a parameter k_j if the log sensitivity is of the order 1 [110]. We refer the reader to [110, 111] for a complete introduction to dynamical sensitivity analysis. We conducted dynamic sensitivity analysis for all the kinetic parameters, initial concentrations of the different species, and compartment sizes in the model (**Figure A.4**). The variation (delta factor) used was 0.001 with a delta minimum of 1×10^{-12}; for a value X, $S \in [0.999X, 1.001X]$. Sensitive parameters or corresponding outputs of interest (cAMP, $G\alpha_s \cdot$GIV-GDI, EGFR$\cdot$GIV$\cdot G\alpha_i$) are reported in **Tables S12-S18**.

Measurement of cAMP

HeLa cells were serum starved (0.2 % FBS, 16 h) and incubated with isobutylmethylxanthine (IBMX, 200 μM, 20 min) followed by EGF. Stimulation was carried out either using fixed EGF concentrations followed by assessment of cAMP at various time points (as in **Figure 2.3B**) or using varying EGF concentrations followed by an assessment of cAMP at 60 min (as in **Figure 2.3F-J**). Reactions were terminated by aspiration of media and addition of 150 μl of ice-cold TCA 7.5% (w/v). cAMP content in TCA extracts was determined by radioimmunoassay (RIA) and normalized to protein [(determined using a dye binding protein assay (Bio-Rad)] [65, 112].

Data is expressed as fmol cAMP / μg total protein.

Stratification of colon cancer patients in distinct gene-expression subgroups and comparative analysis of their survival outcomes

The association between the levels of GIV (CCDC88A) and either EGFR or PDE mRNA expression and patient survival was tested in cohort of 466 patients where each tumor had been annotated with the disease- free survival (DFS) information of the corresponding patient. This cohort included gene expression data from four publicly available NCBI-GEO data-series (GSE14333, GSE17538, GSE31595, GSE37892) [113–116], and contained information on 466 unique primary colon carcinoma samples, collected from patients at various clinical stages (AJCC Stage I-IV/Duke's Stage A-D) by five independent institutions: 1) the H. Lee Moffit Cancer Center in Tampa, Florida, USA (n = 164); 2) the Vanderbilt Medical Center in Nashville, Tennessee, USA (n = 55); 3) the Royal Melbourne Hospital in Melbourne, Australia (n = 80); 4) the Institut PaoliCalmette in Marseille, France (n = 130); 5) the Roskilde Hospital in Copenhagen, Denmark (n = 37). To avoid redundancies (i.e. identical samples replicated two or more times across multiple NCBI-GEO datasets) all 466 samples contained in this subset were cross-checked to exclude the presence of duplicates. A complete list of all GSMIDs of the experiments contained within the NCBI-GEO discovery dataset has been published previously [80]. To investigate the relationship between the mRNA expression levels of selected genes (i.e. CCDCDDC, Wnt5a, EGFR and FZD7) and the clinical outcomes of the 466 colon cancer patients represented within the NCBI-GEO discovery dataset, we applied the Hegemon software tool [80]. The Hegemon software is an upgrade of the BooleanNet software [117], where individual gene-expression arrays, after having been plotted on a two-axis chart based on the expression levels of any two given genes, can be stratified using the StepMiner algorithm and automatically compared for survival outcomes using Kaplan-Meier curves and log-rank tests. Since all 466 samples contained

in the dataset had been analyzed using the Affymetrix HG-U133 Plus 2.0 platform (GPL570), the threshold gene-expression levels for GIV/CCDC88A, PDE and EGFR were calculated using the StepMiner algorithm based on the expression distribution of the 25,955 experiments performed on the Affymetrix HG-U133 Plus 2.0 platform. We stratified the patient population of the NCBI-GEO discovery dataset in different gene-expression subgroups, based on either the mRNA expression levels of GIV/CCDC88A alone (i.e. CCDC88A neg vs. pos), PDE alone (i.e., PDE neg vs. pos), EGFR alone (i.e. EGFR neg vs. pos), or a combination of GIV and either EGFR or PDE. Once grouped based on their gene-expression levels, patient subsets were compared for survival outcomes using both Kaplan-Meier survival curves and multivariate analysis based on the Cox proportional hazards method.

Acknowledgments

Competing Interests

The authors declare no competing interests.

Figure Legends

Figure 2.1: **An emerging paradigm for modulation of cellular cAMP by growth factors.** (**A**) A schematic showing the compartmental features of $G\alpha_i$ and $G\alpha_s$ modulation downstream of EGFR, based on previously published work [35, 40, 42]. (**B**) A circuit diagram of the phenomenological model for non-canonical G protein→cAMP axis that is initiated by EGFR through GIV-GEM's action on $G\alpha_i$ (inhibits AC) and $G\alpha_s$ (activates AC). Red lines indicate inhibition and black lines indicate activation. (**C**-**D**) Simulations for a set of 5000 random parameters for the network shown in **B**. (**C**) Dynamics of GIV-GEF and GIV-GDI activity from the model presented in (**B**). Lognormal standard deviations for GEF and GDI are shown in gray, with the black line showing the mean. (**D**) Dynamics of cAMP concentration from the model presented in (**D**). Lognormal standard deviations for GEF and GDI are shown for different receptor densities (R=0.1, 1, 10) in the presence (yellow line) and absence of (green line) GIV. Sensitivities of the model across all simulation time are shown in **Figure A.1** for both GIV(**A**) and no GIV cases (**B**)

Figure 2.2: **Dynamics of growth factor triggered cAMP signaling via GIV.** (**A**) A reaction network model showing the different signaling nodes and connections from EGFR to the cAMP→PKA signaling axis. Solid lines indicate a binding interaction; interrupted lines indicate enzymatic reaction. The color key (right, boxed) denotes the different cellular compartments. (**B**) Simulations of dynamics of the formation of the EGFR·GIV·$G\alpha_i$ complex, shown as the normalized membrane density, based on network module in (**A**). Experimental data was obtained from Figure 1D and S1 of [42] . (**C**) Dynamics of the formation of the $G\alpha_s$·GIV-GDI complex, a prerequisite event for inhibition of $G\alpha_s$ by GIV, were simulated based on the network diagram shown in (**A**). The membrane density of this complex was normalized to its initial value. Experimental data were obtained from Figure 1C of [42]. (**D**) Simulations of cAMP dynamics in response to EGF stimulation showing a dip in cAMP during the early phase 0-5 min phase (green region) and a delayed increase at approximately 10-60 min phase (blue region). These dynamics are dependent on GIV concentration; yellow line (control GIV in the model), red (high GIV), and green (low GIV). Three other conditions are also shown: 1) GIV in the absence of its GEF effect on $G\alpha_i$ (the GIV-DD mutant), 2) in the absence of both its GEF and GDI effects (GIV-FA mutant), and in the absence of its GDI effect (in the presence of an *in silico* GDI-deficient mutant). (**E**) control or GIV-depleted (shGIV) HeLA cells were serum starved (0.2% FBD, 16h) prior to stimulation with 50nM EGF for the indicated time points. Bar graphs compare the cAMP levels in shC vs shGIV cells at each time point; data are shown as mean $\pm$ S.D. for three independent experiments. ns= not significant; **p=0.01,****p=0.0001. (**F**) The area under the curve (AUC) for cAMP dynamics was calculated for different time points after EGF stimulation. The magnified image shows the AUC at 5 min. The model 95% confidence intervals and their related effects on the system dynamics can be found in **Figure A.6**

(A)

(B)

(C)

(D)

(E) cAMP response during EGF timecourse

(F)
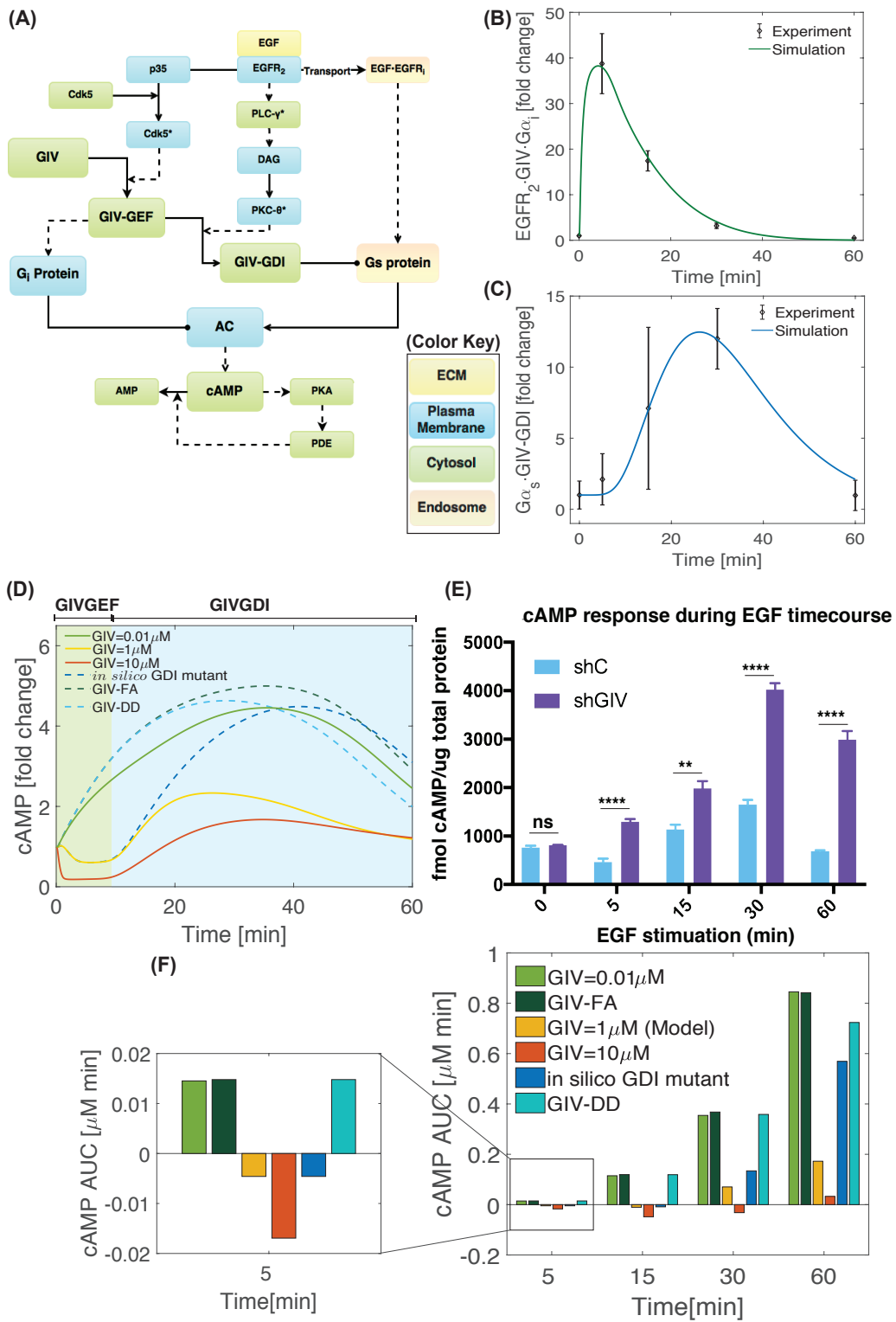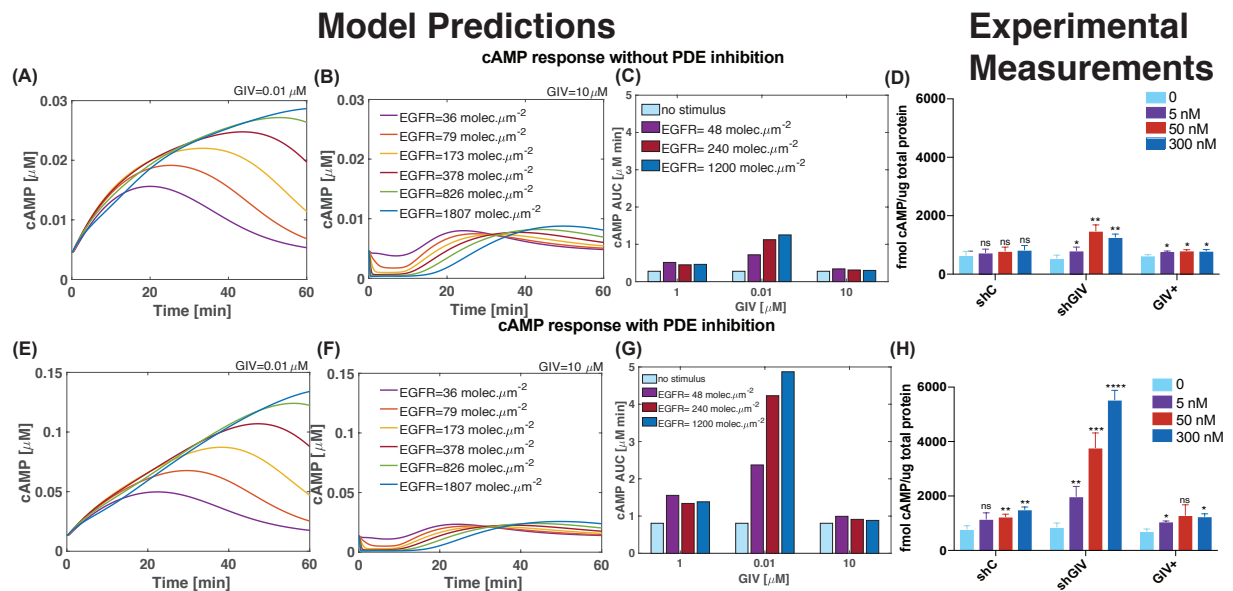
Figure 2.3: **Effect of varying EGF/EGFR on growth factor triggered cAMP signaling.** (**A**-**B**) Simulations comparing the impact of variable input signals [via EGF/EGFR] on cAMP dynamics in low GIV (**A**) and high GIV (**B**) states. (**C**) AUCs calculated from **A** and **B** are displayed. (**D**) Control (shC) or GIV-depleted (shGIV) HeLa cells or GIV-depleted cells rescued with shRNA-resistant GIV-WT (GIV+) were stimulated with EGF and assessed for cAMP levels at 60 min for three different concentrations of EGF. Bar graphs compare the cAMP levels in response to varying EGF concentrations. Error bars indicate mean $\pm$ S.D. of three independent experiments. ns= not significant; *p=0.05; **p=0.01; ***p=0.001. (**E**-**F**) Same as (**A**-**B**) with reduced concentration of PDE to mimic inhibition of cAMP in low GIV (**E**) and high GIV (**F**) states. (**G**) AUC calculations for (**E**) and (**F**). (**H**) Same as in **G**, with one additional step of pre-treatment of cells with 200 μM IBMX (20 min) prior to EGF stimulation. Error bars indicate mean $\pm$ S.D. of three independent experiments. *p=0.05; **p=0.01; ***p=0.001; ****p=0.0001.

Figure 2.4: **The impact of expression levels of EGFR, GIV, and PDE on cAMP dynamics.**
(**A**-**B**) AUCs for simulations comparing the impact of variable GIV expression on cAMP
dynamics in low EGFR (red) and high EGFR (green) states. (**B**) A heat map shows the area
under the curve for cAMP concentration over 1 h for different concentrations of GIV [X-axis]
and EGFR receptor [Y-axis]. The black line, over the yellow region, corresponds to the control
condition in the simulation. (**C**-**D**) AUCs for simulations comparing the impact of variable GIV
expression on cAMP dynamics in high PDE (red) and low PDE (green) states. (**D**) A heat map
shows the area under the curve for cAMP concentration over 1 h for different concentrations
of GIV [X-axis] and activity levels of PDE [Y-axis]. The black line, over the yellow region,
corresponds to the control condition in the simulation. (**E**) A 4-D map showing the relationships
between EGFR (input signal), GIV (control valve), and PDE (degradation sink) on cAMP
dynamics (output signal). The different planes on this map correspond to the same value of
cAMP AUC (see color key on right). The control value is shown in yellow (0.45 $\mu M.min$).
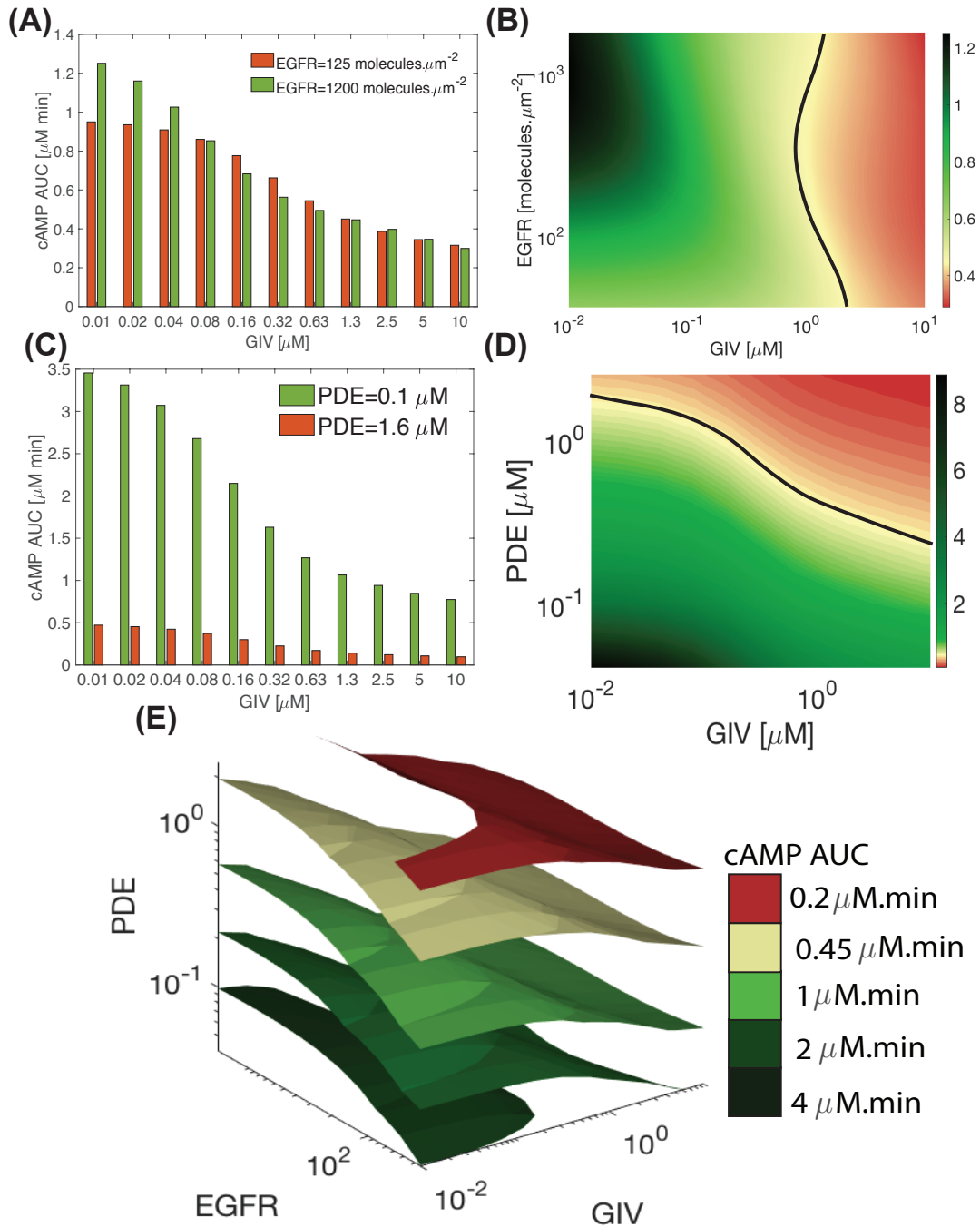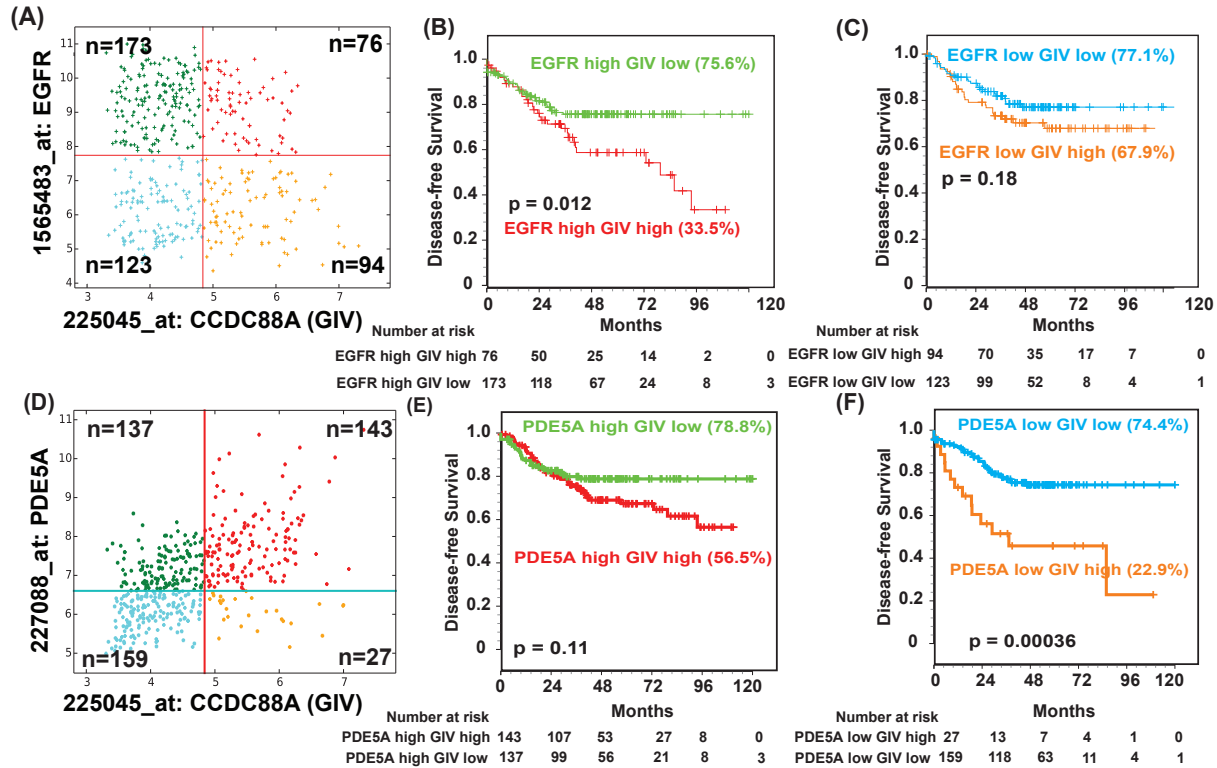
Figure 2.5: **The impact of levels of expression of EGFR, GIV, and PDE on cAMP dynamics; clinical outcome [disease-free survival] in patients with colorectal cancers.** (**A**-**C**) Hegemon software was used to graph individual arrays according to the expression levels of EGFR and GIV (CCDC88A) in a data set containing 466 patients with colon cancer (see Methods); (**A**). Survival analysis using Kaplan-Meier curves showed that among patients with high EGFR, concurrent expression of GIV at high levels carried significantly worse prognosis than those with low GIV (**B**). Survival analysis among patients with low EGFR showed that levels of expression of GIV did not have a significant impact on DFS (**C**). (**D**-**F**) Hegemon software was used to graph individual arrays according to the expression levels of PDE5A and GIV (CCDC88A) in a data set containing 466 patients with colon cancer (see Methods; **D**). Survival analysis using Kaplan-Meier curves showed that among patients with high PDE5A, high vs low GIV expression did not carry any statistically significant difference in DFS (**E**). Survival analysis among patients with low PDE5A showed that patients whose tumors had high levels of expression of GIV had a significantly shorter DFS than those with tumors expressing low levels of GIV (**F**).

Supplementary materials

Supplementary text and materials can be found at MBoC [118], included in appendix **A**.

Chapter **2**, in full, is a reprint of the material as it appears in M. Getz, L. Swanson, D. Sahoo, P. Ghosh, and P. Rangamani. A predictive computational model reveals that GIV/Girdin serves as a tunable valve for EGFR-stimulated Cyclic AMP Signals. Molecular Biology of the Cell, pages mbc.E18–10–0630, 2019. The dissertation author was the primary investigator and author of this paper.

2.1 As a tunable valve between the "sources" and "sinks", GEMs enable tonic modulation of cAMP, impart robustness

With the ultimate goal of generating experimentally testable predictions, recently we used a systems biology approach to understand the design principles of the GEM-dependent biological network with a focus on cAMP signaling [118]. We constructed the first-ever compartmental network model of growth-factor triggered cAMP signaling, and identified two key features of non-canonical G protein signaling via GIV-GEM. We focused the study on the epidermal growth factor (EGF) and its receptor (EGFR) because this pathway had the most experimental evidence to use towards building mathematical models and well-validated tools/readouts/approaches to validate/test model-inspired predictions. This endeavor resulted in three major findings.

First, the model implicated compartmentalized RTK signaling at the PM (where GIV serves as a GEF that triggers activation of $G\alpha_i$) and on the endosomes (where GIV serves as a GDI that inhibits activation of $G\alpha_s$) as a key contributor to the delayed and prolonged cAMP dynamics that is observed over an hour. Consequently, RTK-GIV-triggered cAMP dynamics spans 5 to ¿60 min, which coincides with other RTK-triggered mitogenic signaling pathways, trafficking events, and transcriptional response; This is the major temporal domain of RTK activity, the so-called "window of activity" [119]. Second, the model predicted and experimentally validated that GIV-GEM may serve as a tunable "valve" for cAMP regulation in cells. When all the known compartmental and reaction kinetics were accounted for, the model indicated that GIV levels (which vary in pathologic states; see **Table 2.1**), in conjunction with EGFR levels, can be thought of as key determinants, and high GIV in the setting of high EGFR may facilitate tonic suppression of cAMP levels regardless of pathway stimulation. In a low-EGFR state, varying GIV concentrations resulted in cAMP changes only within a narrow range; however, in a high-EGFR state, varying GIV concentrations achieved a larger variance in cAMP. In a low-GIV state,

varying EGFR concentrations resulted in cAMP changes; however, in high-GIV states, cAMP concentrations remained low regardless of increasing levels of EGFR. GIV levels, in conjunction with EGFR ("source") levels, emerged as key determinants, and high-GIV state regardless of the levels of activation of EGFR resulted in tonic suppression of cAMP levels, reminiscent of the actions of "valves" in any conduit [**Figure 2.6**]. The "valve" appears to be "closed" at high-GIV states, despite high levels of "sources", and hence, when "sources" and "valve" were compared head to head, the "valve" emerged as the dominant determinant of cellular levels of cAMP.

Third, the model also compared head to head the relative strengths of "valves" and "sinks". We found that the effect of GIV concentration on cAMP levels in cells is discernible only when PDE activity is low; a high-PDE state overshadowed all effects of changing levels of GIV and virtually abolished GIV-dependent changes in cAMP levels. When PDE activities are high, cAMP levels do not go up even in low-GIV states, likely because increased production is balanced by increased degradation. Why would a cell waste energy (ATP) in such a 'futile cycle'? This situation is reminiscent of the maintenance of steady-state cGMP levels in the sub-μM range in thalamic neurons by concomitant guanylyl cyclase and PDE2 activities [120] and cAMP levels in pyramidal cortical neurons by concomitant AC and PDE4 activities [121]. Prior studies have suggested that such tonic cAMP production and PKA activity enable signal integration and crosstalk with other cascades [122]; unlike an on/off system gated exclusively by $G\alpha_s$proteins, tonic activity allows both up- and downregulation by activation of $G\alpha_i$or inhibition of $G\alpha_s$(via GIV-GEM) and by PDEs. Our findings suggest that such up/down tunability is best achieved by changing the cellular concentrations of GIV. Because these predictions were also experimentally validated, PDEs ("sinks") were determined as a dominant node and GIV ("valve") as the subordinate node. Overall, these findings cemented the importance and relevance of GIV-GEM as a tunable "valve" for cellular cAMP within a new network module where there can be many "sources" (EGFR, and other receptors that also engage GIV-GEM) and "sinks" (diverse subtypes of PDEs). The impact of tuning the "valve" up or down (by changing levels

of GIV-GEM) was most pronounced in the setting of high "sources" (i.e., ligand activation of multiple receptors) and low "sinks" (PDE activity). While cAMP levels were flexible and responsive to ligand stimuli when GIV levels were maximally tuned down and the "valve" was open, robust suppression of cAMP was seen when GIV levels were maximally tuned up and the "valve" was closed [see **Figure 2.6**].

Because the flow of information in layers within signal transduction circuits in general [85, 101, 123], and more specifically for RTKs like EGFR [119, 124] is believed to conform to bow-tie microarchitecture, and cAMP is considered as one of the universal carrier molecules at the knot of such bowties which determines robustness [101], we conclude that GIV-GEM operates at the knot of the bow-tie as a tunable valve for controlling robustness within the circuit [**Figure 2.7**]. Because layering of control of information flow is believed to conform to an hourglass architecture [85], in which diverse functions and diverse components are intertwined via universal carriers, GIV's ability to control the universal carrier, cAMP could explain why GIV has been found to be important for diverse cellular functions and impact diverse components [65]. In an hourglass architecture, the lower and higher layers tend to see frequent evolutionary changes, while the carriers at the waist of the hourglass appears to be constant/invariant and sometimes, virtually 'ossified'. Of relevance to our model, the importance of cAMP appears to be indeed ossified from unicellular organism to human alike, and GEMs like GIV are expressed ubiquitously in all tissues from fish to man and GIV-like GEMs have so far been identified as early as in C. elegans [125].

2.1.1 Implications of the new network for cAMP signaling in disease pathogenesis

There are several implications of the newly built network model, which we summarize below.

First, our work provides valuable clues into the impact of increased robustness at high-GIV states in cancers. Robustness in signaling is an organizing principle in biology, not only for the maintenance of homeostasis but also in the development and progression of chronic debilitating diseases like cancers; it is widely accepted that tumor cells hijack such robustness to gain growth and survival advantage during the development of cancer [86, 87, 119]. Consistently, GIV mRNA levels and DNA copy numbers are invariably higher across multiple cancers when compared to their respective normal tissue of origin [summarized in [118]. Because GIV has been found to regulate several sinister properties of tumor cells across a variety of cancers (multiple studies, reviewed in [67], it is possible that the high-GIV driven robustness maintains cAMP at low constant levels despite increasing input signals as a tumor evolves when targeted by biologics or chemotherapy agents. Such a phenomenon could be a part of a higher order organizing principle in most aggressive cancers, and therefore, justify GIV as a potential target for network-based anti-cancer therapy.

Second, the findings from network modeling impacts biomarker development. Multiple biomarker studies in bona fide EGFR-driven cancers (lung cancer, colon cancer, and GBMs) that are currently treated with anti-EGFR agents have tried to harness the ability to measure EGFR protein or mRNA as predictive or prognostic biomarkers to tell us which patients will do better or worse. However, none have panned out. Our model predicted that changing levels of EGFR may be overshadowed in high-GIV states that can robustly suppress cellular cAMP. This prediction from our model, and the decades-old body of experiments showing that the impact of such tonic cAMP suppressive state on tumors is expected to be an increase in aggressive traits (**Table 2.1**) prompted us to hypothesize that levels of expression of EGFR may provide meaningful information about tumor aggressiveness only if it is evaluated in tumors with low GIV. Our findings on patients validated these predictions using one of the most important readouts of cancer aggressiveness, i.e., patient survival– i.e., high vs low EGFR levels correlated with poor vs good outcomes only when tumors had low GIV. By contrast, EGFR levels were irrelevant when

tumors had high GIV. Moreover, consistent with the mathematical model which showed that high-GIV/high-EGFR states were accompanied by a robust inhibition of cAMP despite high levels of stimuli, Kaplan–Meier curves for a high GIV/high EGFR signature carried the worst prognosis compared to all other patients combined. Thus, high levels of EGFR signaling does not, by itself, fuel aggressive traits or carry a poor prognosis, but does so when GIV levels are concurrently elevated. In addition for tumors with low GIV, the high EGFR signaling state may be beneficial for maintaining high cAMP levels and therefore, critical for dampening several aggressive tumor traits (**Table 2.1**). Because cAMP levels in tumor cells and GIV levels have been previously implicated in anti-apoptotic signaling [95] and the development of chemoresistance [96], it is possible that the GIV-EGFR crosstalk we modeled recently also determines how well patients may respond to anti-EGFR therapies and who may be at highest risk for developing drug resistance. Whether such is the case, remains to be evaluated.

Third, the network model may also guide the development of anti-cancer therapeutics. For example, in the context of PDEs, it has been demonstrated that overexpression of PDE isoforms in various cancers leads to impaired cAMP and/or cGMP generation [24]. PDE inhibitors in tumour models in vitro and in vivo have been shown to induce apoptosis and cell cycle arrest in a broad spectrum of tumour cells [97]. Despite the vast amount of preclinical evidence, there have been conflicting reports on its efficacy in the clinic [34]. Our finding that low PDE levels in the setting of high GIV carries a poor prognosis predicts that the benefits of PDE inhibitors may be limited to patients who have low GIV expression in their tumors. Similarly, in the context of anti-EGFR therapies, researchers have come to realize that anti-EGFR therapeutics may unpredictably lead to two flavors of outcome that are attributed to kinase-independent functions of EGFR [reviewed in [126]] on the one hand, they may achieve the desirable therapeutic benefits, but on the other hand, their use may trigger the acquisition of resistance during treatment or may cause more harm in tumors that are innately resistant. Our model predicts that those with low GIV/high EGFR [high cAMP state] are likely to respond well to anti-EGFR therapy inducing tumor cell apoptosis,

whereas those with high GIV/high EGFR [low cAMP state] may be at highest risk for developing drug resistance. Whether such predictions hold true, and whether these insights may impact patient outcomes remains to be seen.

Fourth, the network model helps extrapolate findings to other disease states beyond cancers that are fueled by aberrant cAMP signaling, where GIV levels are also concomitantly altered. Because our network model revealed how the 'tunability' of the "valve" impacts tonic levels of cellular cAMP over long time spans reaching steady-state kinetics, and valve-like GEMs are indeed found to be persistently dysregulated (either up- or downregulated) in diverse chronic disease states beyond cancers (cataloged in **Table 2.1**), it is possible that GIV levels may need to be maintained only within a narrow range in the healthy state [middle; **Figure 2.7**]. Because GIV is expressed at very high levels in the brain and reproductive organs (testes and ovary) and only in low levels in epithelial cells [54, 55], it is likely that the optimal physiologic range of expression varies between cell types. What is clear is that in each disease state, the level of GIV expression and its predicted impact on cellular cAMP (based on our model) is consistent with the observed impact of cAMP in disease pathogenesis [see **Table 2.1**]. It is noteworthy that each of these disease states have multiple different classes of receptors ("sources") and, in some cases also PDEs ("sinks") implicated in pathogenesis, further supporting the previously drawn conclusion that GIV-GEM may be operating as a tunable valve es at the knot of the bow-tie shaped network, controlling robustness within the circuit; persistent "open" or "closed"-states of the valve may contribute to disease pathogenesis perhaps via its ability to control cellular concentrations of second messengers such as cAMP [**Figure 2.7**].

2.1.2   Conclusions and Perspective

Cellular levels of cAMP impacts a wide range of signals in diverse pathways, and a cell's ability to maintain these levels within a physiologic range is critical for health. Too much or

too little cAMP is often encountered in disease states. Although diverse "sources" (receptors) and "sinks" within the cAMP network may be contributing to these diseases, it is possible that a tunable "valve" such as GEMs that is stuck persistently in either "open" or "closed" state may be a common (i.e., an invariant) contributor or driver in the disease network. Because GIV and GEMs like GIV have been implicated in multiple disease states, GEMs constitute a hitherto untapped class of targets that could be exploited for reinstating physiologic cAMP signaling in multiple diseases.

Chapter **2.1**, in part, is as it may appear in WIREs Syst Biol Med Getz, M , Ghosh, P, Rangamani, P, Regulating cellular cyclic AMP: "Sources", "Sinks", and now, "Tunable Valves". The dissertation author was the primary author of this material.

Table 2.1: GIV, cAMP levels and disease states

Disease state	Tissue	Levels of GIV-GEM/GEM activity, and implicated in disease	Derangement of cAMP (predicted)	Derangement of cAMP pathway (experimentally confirmed and implicated in disease pathogenesis)
Cancers [EMT, invasion and metastasis, stemness]	Tumor cells and stroma	Elevated levels of mRNA and protein; GEM function ON [multiple studies, summarized in [67]]	Suppressed than normal	Suppressed (pharmacologic elevation inhibits motility, invasion) [127–132]
Cancers (emergence of resistance)	Tumor cells	Elevated levels of mRNA and protein; GEM function ON [133–135]	Suppressed than normal	Suppressed (pharmacologic elevation overcomes resistance, increase apoptosis) [95, 136]
Nephrotic syndrome	Podocytes	GIV is elevated and activation of its GEF function is required for podocyte recovery [137]		Nephritic glomeruli generated less cyclic AMP than normal glomeruli (11 and 26 pmol) [138]. Attenuated generation of cyclic AMP in response to ligands is connected to the augmented accumulation of fibronectin in nephritic glomeruli [139]
Liver fibrosis	Hepatic stellate cells, Kupffer cells	Elevated levels of mRNA and protein; GEM function ON [112]	Suppressed than normal	Augmentation of forskolin-induced increase in intracellular cyclic AMP level (inhibitory effect on HSC activation [140]). Quiescent HSCs have high levels of cAMP-PKA-phospho-CREB signaling, which decreases upon HSC activation; activation of PKA restores phospho-CREB levels and inhibits proliferation of activated HSCs [141, 142].
Type II DM, Insulin resistance	Muscle (skeletal)	Decreased levels of GIV [70, 143]	Elevated than normal	High levels of cAMP induces insulin resistance [144–149]; [150]. Insulin triggers PDE activity for cAMP degradation. [151]. PDE3B is activated by Akt downstream of insulin [152]. Levels of PDE3B are reduced in DM, and restored by TZDs [153].
Alzheimer's disease	Neurons	Decreased levels of GIV protein [154]	Increased (predicted)	Increased [155]
Autism	Cultured peripheral blood lymphocytes	Gain of copy number for GIV [156].	Suppressed cAMP (predicted)	Low cyclic AMP confirmed in programmed neuronal stem cells. Compensatory high cAMP in CSF and peripheral blood. Addition of cAMP restored defective signaling within the cAMP pathway.
Acute myocardial infarction and other vascular endothelial injury Cardiac and smooth muscle cells	Elevated levels of mRNA and protein [157–159]	Suppressed cAMP (predicted)	Suppressed in acute MI in humans: Reviewed in [160]. Suppression of cAMP after vessel injury is required for neointima repair	
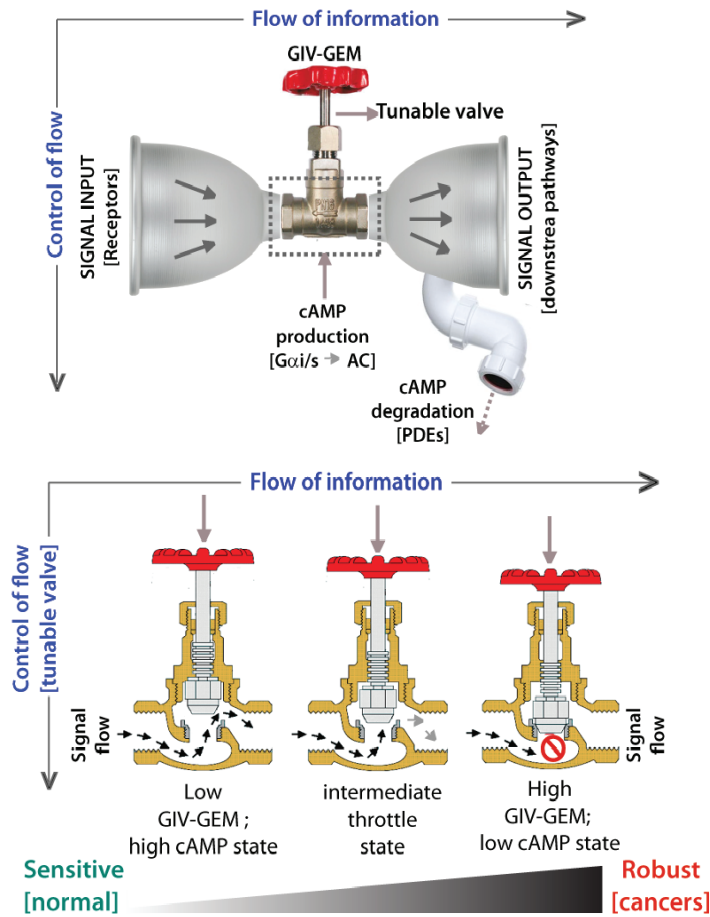
Figure 2.6: **Schematic summarizing the unique impacts of GIV-GEM on the EGFR→cAMP pathway, as revealed by systems biology.** Top: Within the 'bow-tie' microarchitecture of layered signal flow in any circuit, incoming signals from RTKs like EGFR [signal input; left] are integrated by core proteins like GIV [center] that activate second messengers like cAMP, which subsequently impacts multiple target proteins such as kinases, phosphatases, and transcription factors [output signals; right]. Prior systems biology work had concluded that cellular concentrations of cAMP is a key determinant of robustness at the core of information (signal) flow [85, 101, 123]. While cAMP production is tuned up or down by variable levels of GIV and its compartmentalized action on Gai/Gas and ACs within the RTK-cAMP pathway, cAMP degradation by PDEs serves as a dominant sink [drain pipe]. Bottom: Within the hourglass microarchitecture for vertical flow of 'control', up/down-regulation of GIV-GEM in cells serves as a tunable control valve, allowing cells to control cAMP production in cells responding to growth factors. When GIV-GEM expression is low [as seen in the normal epithelium], increasing input signals can trigger some of the highest levels of cellular cAMP, thereby conferring sensitivity (left). Increasing GIV-GEM expression throttles the cAMP response [middle], such that, when GIV-GEM is expressed highly [as seen across all cancers, cAMP levels remain low, regardless of the amount of input signals, thereby conferring robustness [right]].
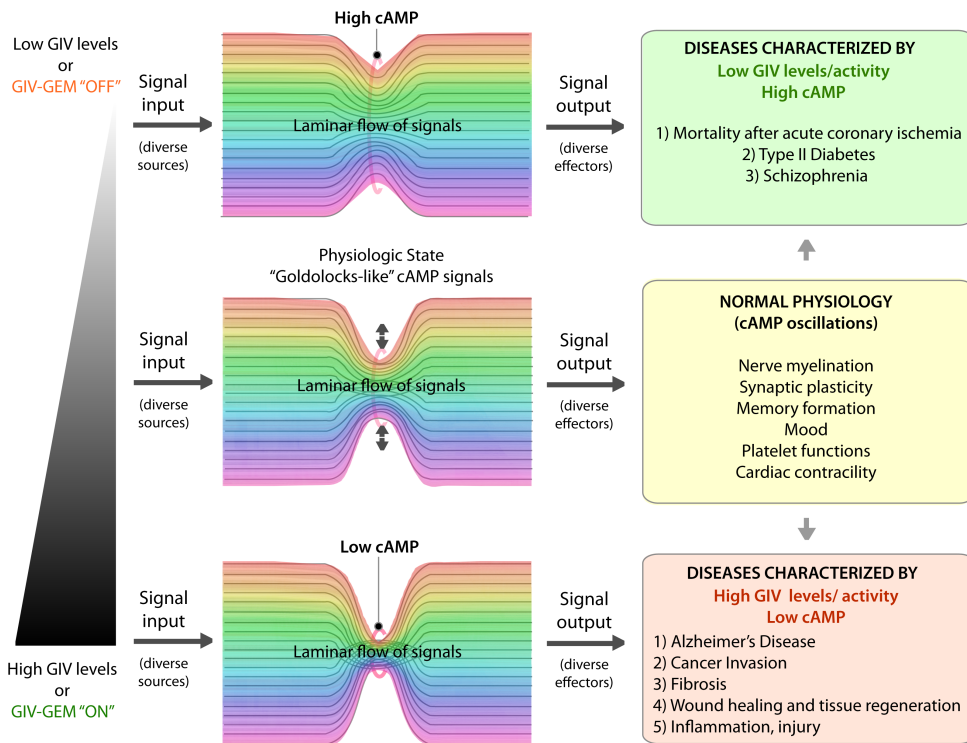
Figure 2.7: **Schematic summarizing the diverse pathologic states that feature either too little or too much GIV.** Because of its ability to serve as a tunable valve for cellular cAMP concentrations, too high or too low levels of expression of GIV may robustly regulate the tonic levels of cAMP in cells. Low GIV-states are associated with high cAMP (top), high GIV-states are associated with low cAMP (bottom). Text boxes on the right list pathophysiologic conditions associated with deregulated GIV and cAMP states (see also **Table 2.1**).

Chapter 3

Spatially compartmentalized phase regulation of a Ca^{2+}-cAMP-PKA oscillatory circuit

B. Tenner[1,2]**, M. Getz**[3]**, B. Ross**[2]**, D. Ohadi**[4]**, C. Bohrer**[1]**, E. Greenwald**[2]**, S. Mehta**[2]**, J. Xiao**[1]**, P. Rangamani**[3,4,*]**, J. Zhang**[1,2,*]

Signaling networks are spatiotemporally organized in order to sense diverse inputs, process information, and carry out specific cellular tasks. In pancreatic β cells, Ca^{2+}, cyclic adenosine monophosphate (cAMP), and Protein Kinase A (PKA) exist in an oscillatory circuit characterized by a high degree of feedback, which allows for specific signaling controls based on the oscillation frequencies. Here, we describe a novel mode of regulation within this circuit involving a spatial dependence of the relative phase between cAMP, PKA, and Ca^{2+}. We show that nanodomain clustering of Ca^{2+}-sensitive adenylyl cyclases drives oscillations of local cAMP levels to be precisely in-phase with Ca^{2+} oscillations, whereas Ca^{2+}-sensitive phosphodiesterases maintains out-of-phase oscillations outside of the nanodomain, representing a striking example and novel mechanism of cAMP compartmentation. Disruption of this precise in-phase relationship perturbs Ca^{2+} oscillations, suggesting that the relative phase within an oscillatory circuit can encode

specific functional information. This example of a signaling nanodomain utilized for localized tuning of an oscillatory circuit has broad implications for the spatiotemporal regulation of signaling networks.

3.1 INTRODUCTION

Cyclic adenosine monophosphate (cAMP) and Ca^{2+} act as essential second messengers in almost every cell type and regulate many functional pathways within a cell, such as hormonal signal transduction, metabolism, and secretion [3, 4]. In some cell types, including neurons, cardiomyocytes, and pancreatic β cells, these messengers' concentrations oscillate intracellularly [10, 11], and the oscillations encode critical signaling information (e.g. signal strength, duration, and target diversity) into parameters such as frequency and amplitude [12, 13]. This is perhaps best exemplified in the β cell where oscillations of Ca^{2+} drive pulsatile insulin secretion [17] as well as oscillations in cAMP levels [15, 16]. Furthermore, Ca^{2+}, cAMP, and the downstream cAMP-dependent kinase Protein Kinase A (PKA) constitute a highly-coordinated oscillatory circuit responsible for integrating metabolic and signaling information [14]. In addition to temporal control, biochemical pathways are also spatially organized within the cell [18, 19]. Both Ca^{2+} and cAMP are highly spatially compartmentalized and form signaling microdomains or nanodomains [20, 21]. While Ca^{2+} levels are locally controlled by channels, pumps, and intracellular buffering systems [4, 22], cAMP is thought to be regulated via controlled synthesis by adenylyl cyclases (ACs) and degradation by phosphodiesterases (PDEs) [23, 24]. Despite extensive studies on cAMP compartmentation, the mechanisms that spatially constrain this mobile second messenger remain poorly understood [25–27]. Furthermore, it is not clear how spatial regulation of a second messenger influences its dynamic behaviors in the context of coordinated oscillations.

In this study, we investigated the spatiotemporal organization of the Ca^{2+}-cAMP-PKA oscillatory circuit in pancreatic β cells and discovered that the relative, oscillatory phase between cAMP/PKA and Ca^{2+} is spatially regulated within signaling nanodomains. By combining live-cell dynamic imaging, super-resolution microscopy, and computational modeling, we further found that fine-scale, compartment-specific perturbations of this precise phase dynamic impacts

Ca^{2+} oscillations in the β cells. These findings suggest that the relative phase in oscillatory signaling circuits, like the amplitudes and frequencies of biochemical signals, represents yet another mode of informational encoding and processing, which is subjected to spatiotemporal regulation within the cell.

3.2   RESULTS

3.2.1   The relative phase of β cell cAMP and Ca^{2+} oscillations is compartmentalized

In order to study the spatiotemporal relationship between key players of the Ca^{2+}-cAMP-PKA circuit, we chose to focus our attention on an important class of molecular scaffolds, A-Kinase Anchoring Proteins (AKAPs), which are responsible for recruiting PKA to specific substrates at distinct subcellular locations. In several excitable cell types, the plasma membrane (PM) localized scaffold protein AKAP79 (AKAP150 rodent ortholog) has been shown to organize a macromolecular complex with binding partners that include PKA, the voltage-gated Ca^{2+} channel $Ca_V 1.2$, Protein Kinase C (PKC), the Ca^{2+}/calmodulin-dependent protein phosphatase calcineurin, Ca^{2+}-sensitive ACs, AMPA receptors, and many others [161]. Due to the extensive and multivalent nature of AKAP79/150 and a report describing the functional impairment of glucose-stimulated insulin secretion (GSIS) in pancreatic β cells upon its knock-out [162], we hypothesized that the AKAP79/150 scaffold might play an important role in the spatiotemporal regulation of the Ca^{2+}-cAMP-PKA oscillatory circuit. Specifically, we were interested in testing if AKAP79/150 is able to create a spatially-distinct compartment in which recruitment of signaling effectors can locally fine-tune and reshape signaling dynamics within the circuit [163, 164]. In order to test this hypothesis, we monitored intracellular cAMP and Ca^{2+} using the FRET-based cAMP biosensor (Ci/Ce)Epac2-camps [165] and the red Ca^{2+} indicator RCaMP [166] in MIN6 β cells. By fusing (Ci/Ce)Epac2-camps to the full-length AKAP79 scaffold and transiently

transfecting the targeted sensor, we measured cAMP concentration changes in the immediate vicinity of AKAP79/150 (**Fig. 3.1a**). As a control, we also targeted the cAMP probe to the general plasma membrane by adding a lipid modification domain [167]. These targeted biosensors allowed us to compare the dynamics within the AKAP79/150-specific compartment versus the general plasma membrane compartment (**Fig. 3.1a**).

Although both targeted sensors were effectively trafficked to and uniformly distributed along the plasma membrane (**Supplementary Fig. 3.7a,b**), we observed notable differences in their respective cAMP signals relative to Ca^{2+} oscillations after triggering the circuit (**Fig. 3.1b**) with tetraethylammonium chloride (TEA, 20mM), a potent K^+ channel blocker. cAMP oscillations measured within the AKAP79/150 compartment were in-phase with oscillating Ca^{2+} such that each transient spike in intracellular Ca^{2+} was closely associated with a transient increase in cAMP (**Fig. 3.1c**) (n=60). This was in sharp contrast to cAMP oscillations measured within the general plasma membrane compartment where each local Ca^{2+} peak corresponded to a local trough in cAMP (n=24), followed by a slow reversal of both signals to a pre-stimulated baseline (**Fig. 3.1d**). While this out-of-phase cAMP-Ca^{2+} oscillations were consistent with those observed in the cytoplasm of β cells, in phase cAMP-Ca^{2+} oscillations had not be observed under these conditions [14, 168]. To quantify the cAMP-Ca^{2+} phase relationship, we measured the lag time by calculating the cross-correlation between the two normalized, oscillatory signals and finding the absolute value of the shortest delay yielding the maximum correlation (see appendix **B** for details) (**Fig. 3.1e**). In-phase cAMP oscillations corresponded to short lag times (typically ¡20 sec) while out-of-phase oscillations mostly possessed longer lag times. Within the AKAP79/150 compartment, cAMP lagged behind Ca^{2+} by an average of only 13±3sec; however, cAMP within the general plasma membrane compartment oscillated with a lag time of 47±4sec, relative to Ca^{2+} (**Fig. 3.1f**). This stark difference in the cAMP-Ca^{2+} phase relationship suggests that the relative phase of this oscillatory circuit is compartmentalized and hints at differential regulation of the circuit between the AKAP79/150 compartment and the general plasma membrane compartment.

3.2.2 Oscillatory phase is regulated by balanced activities of Ca^{2+}-sensitive ACs and PDEs

Given that in-phase cAMP oscillations were only observed within the AKAP79/150 compartment (**Fig. 3.1c**) and out-of-phase cAMP oscillations were observed in the general plasma membrane compartment (**Fig. 3.1d**) and cytoplasm [14], we hypothesized that Ca^{2+} oscillations are coupled to cAMP oscillations by a ubiquitous mechanism throughout the cell, while additional mechanisms specifically regulate the phase relationship within the AKAP79/150 compartment. We first sought to identify the component that is responsible for coupling cAMP dynamics to Ca^{2+} dynamics globally. Since TEA induces continuous Ca^{2+} oscillations, we determined the temporal relationship between Ca^{2+} and cAMP at the general plasma membrane more precisely by measuring the impulse response of the circuit following a transient membrane depolarization. After the addition of KCl (15mM) followed by a subsequent washout to elicit a transient influx of Ca^{2+} [169], we observed a synchronous cAMP decrease (n=20) followed by a return to baseline (**Fig. 3.2a**). This data suggests that increasing cytosolic Ca^{2+} was coupled to a decrease in cAMP at the plasma membrane via Ca^{2+}-sensitive AC or PDE activities. Given that Ca^{2+}-inhibited ACs (AC5, AC6) have low specific activity both in the presence and absence of physiological Ca^{2+}, as well as a lower distribution in the pancreas [170], we instead focused on probing the roles of PDEs. The Ca^{2+}-dependent PDE1 family in MIN6 cells, specifically PDE1C, has been implicated in modulating GSIS [171]. Indeed, acute addition of 8MM-IBMX (100 μM), a relatively selective PDE1 inhibitor, effectively uncoupled cAMP dynamics from Ca^{2+} oscillations (**Fig. 3.2b, Supplementary Fig. 3.8a**) (n=18), indicating that Ca^{2+}-triggered activation of PDE1 mediates the transient cAMP decreases. We also observed that the overall increase in cAMP led to an increase in the Ca^{2+} oscillation frequency, consistent with the previously identified role of cAMP/PKA in regulating the Ca^{2+} oscillations [14]. We tested the roles of two additional families of abundant PDEs in pancreatic β cells, PDE3 and PDE4, by acute pharmacologic inhibition. While treating cells with either milrinone (PDE3 inhibitor, 10μM,

n=12) or rolipram (PDE4 inhibitor, $1\mu M$, n=15) slightly increased cAMP levels, neither inhibitor had an effect on cAMP-Ca^{2+} coupling or relative phase (**Supplementary Fig. 3.8b,c**). These data suggest that PDE1 is the key component that couples Ca^{2+} and cAMP oscillations within this signaling circuit.

How is the phase relationship between Ca^{2+} and cAMP regulated within distinct signaling compartments? In order to gain a more quantitative understanding of the regulation of the cAMP-Ca^{2+} phase relationship, we created a simplified mathematical model involving Ca^{2+}, cAMP, and Ca^{2+}-driven PDE and AC activity components [172] (**Fig. 3.2c**, see appendix **B** for details). This simple circuit represents the key aspects of the oscillatory cAMP-Ca^{2+} circuit and is applicable to different signaling compartments. Opposed to the Ca^{2+}-stimulated PDE1 [173] is the Ca^{2+}-stimulated AC8 [174, 175], an abundant Ca^{2+}-sensitive transmembrane AC isoform in β cells that has been shown to mediate sustained insulin secretion and associate with the AKAP79/150 scaffold [169, 176, 177]. By computationally manipulating the activity of each arm, we found that cAMP can oscillate either out-of-phase or in-phase when a simulated Ca^{2+} pulse train is used as an input (**Fig. 3.2c**). In particular, when the relative activity of PDE1 is greater than the activity of AC8, Ca^{2+}-driven cAMP degradation dominates, resulting in an out-of-phase cAMP-Ca^{2+} relationship. On the other hand, if the relative activity of AC8 is greater than that of PDE1, Ca^{2+}-stimulated cAMP production is favored and an in-phase relationship is observed, consistent with previous modeling studies [178, 179].

Thus, our simplified model indicates that the phase relationship can be tuned by altering the relative strength between Ca^{2+}-sensitive ACs and PDEs (**Fig. 3.2c**). This model provided a blueprint for understanding the interplay between the Ca^{2+}-stimulated AC/PDE balance and the cAMP-Ca^{2+} phase relationship within the AKAP79/150 compartment. Based on the findings from our model, we predicted that decreasing the relative contribution of AC8 will shift the cAMP-Ca^{2+} phase relationship from in-phase to out-of-phase, as the relative contribution from

Ca^{2+}-triggered PDE1 increases. To test this prediction, we knocked-down endogenous AC8 in the MIN6 cells [180] and observed that most cells exhibited an out-of-phase cAMP oscillation within the AKAP79/150 compartment (avg. lag time 37 ± 9sec, n=11) (**Fig. 3.2d**), indicating an AC8-specific role in mediating the cAMP-Ca^{2+} phase signature.

Conversely, increasing the relative contribution of AC8, for example by increasing the concentration of AC8, should shift the cAMP-Ca^{2+} phase relationship from out-of-phase to in-phase. To test this prediction, we overexpressed full-length AC8 and examined the effect in the general plasma membrane compartment. Interestingly, we found that AC8 overexpression reversed the out-of-phase cAMP-Ca^{2+} phase relationship in a titratable manner where the percentage of in-phase oscillating cells correlated with increasing amounts of the cotransfected AC8 (avg. lag time 23 ± 2 sec, n=56) (**Fig. 3.2e, Supplementary Fig. 3.9a-c**). This demonstrates that higher levels of AC8 are sufficient to reverse the cAMP phase at the plasma membrane. In summary, these phase manipulation experiments suggest that the cAMP-Ca^{2+} phase relationship is representative of a sensitive, compartmentalized balance between the Ca^{2+}-stimulated activities of PDE1 and AC8.

3.2.3 Membrane-localized AKAP150:AC8 nanoclusters regulate cAMP-Ca2+ oscillatory phase

The close spatial juxtaposition between the AKAP79/150 and general plasma membrane compartments presents a significant challenge for cAMP compartmentation where cAMP oscillations are distinctly regulated within these adjacent signaling domains. Indeed, how cAMP, a rapidly diffusing small molecule, is spatially compartmentalized in cells is not yet clearly understood, especially given the low catalytic efficiency of a single cAMP-producing AC and degrading PDE [25,181]. Given that AKAP79/150 exists in nanoclusters at the plasma membrane in multiple cell types [182,183] and associates with AC8 in β cells [176], we hypothesized that

AC8 could form nanoclusters on the plasma membrane of MIN6 cells and compartmentalize cAMP dynamics. To test this hypothesis, we examined the spatial organization of AC8 and AKAP150 at the membrane using Stochastic Optical Reconstruction Microscopy (STORM). We found the AKAP150 molecules were organized in clusters with a mean radius of 127 ± 9nm and an average nearest-neighbor spacing of 313 ± 20nm between cluster centers (n=20) (**Fig. 3.3a**), consistent with many recent reports demonstrating AKAP79/150's tendency to cluster/multimerize in other cell types [182–185]. Thus, the AKAP79/150 compartment-specific cAMP phase is likely representative of the balanced cAMP generation and degradation within these AKAP clusters.

Due to the known interaction between AKAP79/150 and AC8 [176], next we probed the spatial organization of AC8 using STORM. We found AC8 also distributes non-uniformly at the plasma membrane and clusters with a mean radius of 88 ± 8nm and an average nearest-neighbor spacing of 292 ± 16nm between cluster centers (n=16) (**Fig. 3.3b**). With the evidence of the nanoscale organization of AKAP150 and AC8 on the plasma membrane, we further hypothesized that the increased spatial density of Ca^{2+}-driven cAMP sources within the AKAP150 clusters, in conjunction with dispersed PDE1 in the cytosol [24, 186], is important in compartmentalizing cAMP production and mediating the in-phase cAMP signal at the AKAP79/150 scaffold. To test this idea, we sought to build a mathematical framework to describe the spatial compartmentalization of the in- and out-of-phase cAMP-Ca^{2+} oscillations. Briefly, we used the AKAP79/150:AC8 cluster pattern measurements from the STORM imaging to set model parameters in a hexagonal prism domain (200nm edge, 600nm depth) with one AKAP79/150:AC8 cluster centered in the domain for simulation (**Fig. 3.4a**, see appendix **B** for model development details). We extended a previous well-mixed β cell model [14] to include the Ca^{2+}-sensitive PDE1 and a 3D spatial component with cAMP diffusion ($D_{cAMP} = 60$ μm^2/s, [187]). By localizing AC8 within the AKAP79/150:AC8 cluster on the plasma membrane face and leaving PDE1 well-mixed throughout the volume, we could simulate Ca^{2+}-driven cAMP oscillations that were in-phase within the immediate vicinity of a cluster, but sharply transitioned out-of-phase outside the cluster.

Specifically, during a Ca^{2+} influx event, Ca^{2+}-triggered cAMP production dominated at the center of the AKAP79/150 cluster while Ca^{2+}-triggered cAMP degradation was favored outside the cluster at the PM and in the center of the unit volume (**Fig. 3.4a**). Not surprisingly, the regime that recapitulates this phase relationship is sensitive to the spatially-restricted AC8/PDE1 balance and the diffusivity of cAMP. Assuming that AC8 clustering is driven by AKAP150:AC8 interactions, weakening this interaction would then reduce the AC8 cluster stabilization and lead to a redistribution of AC8 away from the nanoclusters and a decrease in the local concentration of AC8 within the clusters (**Fig. 3.4c**). Without the high local concentration of AC8 driving a net positive cAMP production within an AKAP79/150 cluster, the spatial domain at the PM where cAMP oscillates in-phase with Ca^{2+} is predicted to shrink while the out-of-phase regime expands and can reverse the phase at the cluster center (**Fig. 3.4d**).

To test this prediction, we overexpressed the amino terminus of AC8 (AC^{81-106}) required for interaction with AKAP79/150 [176] in order to compete with the binding of endogenous AC8 with the endogenous AKAP150 scaffold. The disruption of the AKAP150:AC8 interaction was validated by using proximity ligation assay (PLA) as an in situ assay for visualizing the interaction between AKAP150 and AC8. Compared to non-transfected cells, cells expressing the AC^{81-106} peptide had a 39±4% reduction in the number of PLA signals, indicating a decrease in AKAP150:AC8 interaction (**Supplementary Fig. 3.10a,b**). Furthermore, STORM imaging showed that overexpression of the AC^{81-106} peptide led to a decrease in the percentage of AC8 single molecule localizations within AC8 nanoclusters (n=9) (**Fig. 3.5a**), consistent with the predicted redistribution of AC8 molecules (**Fig. 3.4b**). To test the functional impact of loss of AC8 molecules from the nanoclusters, we measured AKAP79/150-localized cAMP in the presence of AC^{81-106} and observed a significant increase in the average lag time (43±6sec, n=33) (**Fig. 3.5c**). This is due to a higher proportion of cells exhibiting out-of-phase cAMP oscillations, indicating that the AKAP79/150:AC8 competitor peptide was sufficient in reversing the phase relationship in the AKAP79/150 compartment. Interestingly, we also observed many

cells displaying irregular Ca^{2+} oscillations as indicated by a disruption in the periodic timing of individual cells' Ca^{2+} peaks (**Fig. 3.5c**). This nanoscale perturbation establishes the regulatory role of the AKAP79/150:AC8 interaction in mediating the compartmentalized cAMP-Ca^{2+} phase relationship.

3.2.4 AKAP79/150-mediated phase relationship modulates oscillatory Ca2+

Next we more systematically examined the impact of perturbing the precisely regulated phase relationship within the AKPA79/150 compartment. Due to the modulatory role of PKA in the Ca^{2+}-cAMP-PKA oscillatory circuit and the interaction between PKA and AKAP79/150, we wondered how the in-phase cAMP oscillations with respect to Ca^{2+} are translated into PKA activities and if spatial compartmentalization of the phase relationship is also maintained at the PKA activity level. Therefore, we extended our 3D model to include AKAP79/150-associated PKA (see appendix **B** for model details). According to this extended model, PKA activity oscillations exhibit distinct phase relationships with respect to Ca^{2+} within and out of the AKAP79/150 compartment (**Supplementary Fig. 3.11a**). To test this prediction, we fused our FRET-based biosensor for PKA activity (AKAR4) [188] to either full-length AKAP79 or the PM-targeting motif and expressed the sensors in MIN6 cells. Upon TEA stimulation, PKA activity was observed to oscillate with a lag time of time 25±6sec (n=15) within the AKAP79/150 compartment but with a lag time of 55±8sec (n=12) (**Supplementary Fig. 3.11b-d**) at the general plasma membrane, indicating that the compartmentalized phase relationship is preserved from cAMP to PKA.

Spatiotemporal organization of PKA signaling and its phosphorylation targets via AKAPs have been implicated in regulating several important pathways. For example, PKA has been shown to phosphorylate $Ca_V1.2$ in an AKAP79/150-dependent manner and this modification can influence the open probability of the channel [189], suggesting a mechanistic link between local

cAMP/PKA activity and global oscillatory Ca^{2+}. Thus, we sought to study the functional role of the spatially-compartmentalized cAMP-Ca^{2+} phase relationship in regulating intracellular Ca^{2+} dynamics. We measured Ca^{2+} oscillations by RCaMP either in the presence of the EGFP-tagged AKAP79/150:AC8 disruptor peptide, AC^{81-106}, or EGFP alone as a control. Population-wide differences in Ca^{2+} dynamics, such as strength and timing, were observed in AC^{81-106}-transfected cells and visualized in heat maps depicting the normalized Ca^{2+} signal per cell versus time (**Fig. 3.6a**). Interestingly, we found that the expression of the disruptor peptide was correlated with a significant decrease in the peak ratio between the second Ca^{2+} peak and the first Ca^{2+} peak (control avg. -1.6%, n=270; AC^{81-108} avg. -10.8%, n=562), post TEA addition, indicative of less sustained oscillations (**Fig. 3.6b,c**). In addition to intracellular Ca^{2+} concentration, the precise timing of internal oscillatory events is critical for modulating the β cell's functions, such as glucose homeostasis and pulsatile insulin secretion [190]. In the presence of the disruptor peptide, cells also exhibited a longer elapsed time between oscillatory Ca^{2+} peaks (control avg. 3.9±0.1min, n=270; AC^{81-108} avg. 4.6±0.1min, n=562), suggesting that the timing of the signaling circuit was disturbed (**Fig. 3.6b,c**). In addition to the precise timing, the regularity of cytoplasmic Ca^{2+} in β cells is crucial in mediating pulsatile insulin secretion from the pancreas [191, 192]. By stratifying the disruptor peptide-expressing cell population into "low", "medium," and "high" expressers, and performing a blinded classification of responding cells based on the regularity of the Ca^{2+} oscillation (see appendix **B** for details), we found a positive correlation between the percentage of cells exhibiting irregular oscillations and the expression level of the disruptor peptide (42% for low-expressing vs. 68% for high-expressing AC^{81-106} disruptor) (**Fig. 3.6d**). Taken together, these data signifies that the compartmentalized cAMP-Ca^{2+} phase relationship regulates the oscillatory Ca^{2+} signal and plays an important role in determining the pace, regularity and sustainability of the Ca^{2+} oscillations.

3.3 DISCUSSION

Biological oscillations represent a rich way of encoding information. Here we show the phase in an oscillatory signaling circuit, like the amplitude and frequency, represents a novel mode of informational encoding which itself can be spatiotemporally regulated. In the case of the Ca^{2+}-cAMP-PKA circuit, the oscillatory cAMP/PKA phase relative to a widespread Ca^{2+} signal is distinctly regulated within two adjacent plasma membrane compartments through intracellular organization of scaffolds and signaling effectors. Localized perturbation of this spatial phase signature disrupts global Ca^{2+} oscillations and thus has far-reaching consequences on the functional landscape of the β cell.

Compartmentalization of cAMP/PKA signaling is instrumental in processing a diverse set of inputs and mediating specific cellular functions; however, the mechanistic details of compartmentalization are still largely unresolved [26]. Given the measured kinetic rates of most ACs and PDEs, coupled with apparent fast diffusion of the small cAMP molecule, the generation of local cAMP gradients around single enzymes is unmaintainable [181]. Context-dependent discrepancies in some of the kinetics (i.e. differences of in vitro versus in vivo measurements) or slower cAMP diffusion due to buffering have been proposed as potential mechanisms for cAMP compartmentalization [187]. Here we propose that the nanoscale organization of key cAMP effectors and regulators as a novel mechanism for cAMP compartmentation. Despite the slow rates measured for individual ACs, we computationally and experimentally describe conditions in which the generation of compartmentalized cAMP can emerge from the clustering of many AC8 enzymes at the membrane and bulk distribution of PDE1 in the cytoplasm. Alternations to this nanoscale organization lead to dysregulated Ca^{2+} oscillations, demonstrating the functional importance in maintaining this organization. This system also serves as a general demonstration of how a cell can translate a global signal (Ca^{2+}) into a compartmentalized signal (cAMP/PKA activity) by local activation and global inhibition, a strategy that is likely utilized in many other

68

cellular contexts.

Multiple mechanisms could contribute to the consequences of reversing the compartmentalized cAMP phase at AKAP79/150 in β cells. AKAPs can recruit PKA to regulate channel activities [182, 193, 194], such as in the regulation of voltage-mediated Ca2+ entry via PKA-dependent phosphorylation of $Ca_V 1.2$ [189] or the modulation of store-operated Ca^{2+} entry by both PKA-dependent STIM1 and Orai1 phosphorylation [195, 196]. Additional levels of regulatory feedback within the Ca^{2+}-cAMP-PKA oscillatory circuit have also been identified, such as a negative feedback loop involving PKA phosphorylation of AC8, thereby fine-tuning the circuit dynamics [197]. Localized cAMP/PKA signaling at the AKAP79/150 scaffold might also play a role in directly regulating downstream insulin secretion due to close interactions between AKAP79/150 and the insulin secretory granules via $Ca_V 1.2$ [198]. Several important processes and components of the secretory machinery have been identified as targets of PKA signaling here, such as PKA-dependent mobilization of granules [199] and modulation of the synaptosomal protein SNAP25 [200]. In addition to PKA-dependent secretory control, cAMP has recently been implicated to play a role in fusion pore formation via a cAMP-regulated guanine exchange factor Epac [201]. Compartmentalized cAMP/PKA signaling at the AKAP79/150 macromolecular complex is likely involved in the regulation of many β cell processes and more work will be needed to further establish the link between the oscillatory circuit and the mechanisms involved in decoding the information embedded in the local phase relationship.

The Ca^{2+}-cAMP-PKA oscillatory circuit in pancreatic β cells integrates many important regulators of cellular function, and the precise coordination of each is required for proper signaling control. Here we have uncovered a spatiotemporal organization of the circuit where the oscillatory phase between cAMP/PKA and Ca^{2+} depend on the spatial proximity of the AKAP79/150 scaffold protein. The construction principles of this signaling nanodomain, including the spatial distributions of sinks and sources, likely represent a generalized strategy for the generation of

many other compartmentalized signals and provide a unique modality in which cells embed, process, and produce signaling information.

3.4   Materials and Methods

3.4.1   Gene Construction

For AKAP79-(Ci/Ce)Epac2-camps, AKAP79 (from Dr. John D. Scott) was PCR amplified to have HindIII/BamHI digestion sites and (Ci/Ce)Epac2-camps (from Dr. D. Cooper) was PCR amplified to have BamHI/EcoRI digestions sites. Both fragments were inserted into pcDNA3 (Invitrogen) backbone for mammalian expression (cAMP sensor is C terminal to AKAP79). For AKAP79-AKAR4, a similar approach was taken where AKAR4 was dropped between BamHI/EcoRI. For AC8 (from Dr. D. Cooper), AC^{81-108}, and PDE1C (cDNA from Dr. Yan Chen), Gibson Assembly was used to insert the genes into the pcDNA3 mammalian expression vector. The shAC8 construct for AC8 knockdown was previously verified and a gift from Dr. Jochen Lang. RCaMP was a gift from Dr. Loren Looger.

3.4.2   Cell Culture

MIN6 cells (a mouse insulinoma β cell line) were plated onto sterilized glass coverslips in 35-mm dishes and grown to 50–90% confluency in DMEM (10% FBS, 4.5g/L glucose) at 37°C with 5% CO2. Cells were transfected using Lipofectamine 2000 (Invitrogen) and grown 20–48 h before imaging.

3.4.3   Imaging

Cells were washed twice with Hanks' balanced salt solution buffer and maintained in the dark at room temperature. Cells were imaged on a Zeiss Axiovert 200M microscope with a cooled charge-coupled device camera (MicroMAX BFT512, Roper Scientific, Trenton, NJ) controlled by METAFLUOR 6.2 software (Universal Imaging, Downingtown, PA). Dual cyan/yellow emission ratio imaging used a 420DF20 excitation filter, a 450DRLP dichroic mirror, and two emission filters [475DF40 for CFP and 535DF25 for YFP]. RFP fluorescence was imaged using a xxx

excitation filter, a xxx dichroic mirror, and a 653DF95 emission filter. GFP fluorescence was imaged using a 480DF30 excitation filter, a 505DRLP dichroic mirror, and a 535DF45 emission filter. These filters were alternated by a filter-changer Lambda 10–2(Sutter Instruments, Novato, CA). Exposure time was 50–500 ms, and images were taken every 10–30 s. Fluorescence images were background-corrected by subtracting the fluorescence intensity of background with no cells from the emission intensities of cells expressing fluorescent reporters. The ratio of yellow/cyan emission, RFP intensity, and GFP intensity were then calculated at different time points. The values of all time courses were normalized by dividing each by the average basal value before drug addition. Custom Java code, MATLAB scripts, and CellProfiler (Broad Institute) pipelines were written to segment cells, select ROIs, and analyze traces.

For confocal imaging, images were collected with a C2 plus on a Nikon Ti2 inverted microscope equipped with a Plan Apo lambda 60x oil immersion objective NA 1.4. YFP fluorescence fluorescence was excited with the 488nm line from a LU-N4 laser. Images were acquired with a DUVB detector collecting emission from 495nm to 600nm with a virtual spectral GaAsP detector controlled by NIS Elements software. The pinhole was set at 30μm. Frame size was 1024 x 1024pix.

3.4.4   Super-resolution Imaging (STORM)

For fixed-cell stochastic optical reconstruction microscopy (STORM) imaging, cells were fixed with 4% paraformaldehyde (PFA) and 0.2% glutaraldehyde (GA) for 20 min and then washed with 100 mM glycine in Hanks' balanced salt solution (HBSS) to quench the free PFA. Cells were permeabilized and blocked in a permeabilization solution with 0.1% Triton X-100, 0.2% bovine serum albumin, 5% goat serum, and 0.01% sodium azide in HBSS. The cells were then incubated overnight at 4°C with an anti-AC8 antibody (Abcam, ab196686) at a 1:2000 dilution or an anti-AKAP150 (Millipore Sigma 07-210) antibody at a 1:500 dilution,

followed by 1 to 2 hours with goat anti-rabbit Alexa 647–conjugated antibody (ThermoFisher Scientific, A21245) at 1:1000 dilution. The cells were then post-fixed again in 4% PFA and 0.2% GA, quenched with 100 mM glycine in HBSS, and washed with HBSS to prepare for imaging. Immediately before imaging, the medium was changed to STORM-compatible buffer (50 mM tris-HCl (pH 8.0), 10 mM NaCl, and 10% glucose) with glucose oxidase (560 μg/ml), catalase (170 μg/ml), and mercapto-ethylamide (7.7 mg/ml). STORM images were obtained using a Nikon Ti total internal reflection fluorescence (TIRF) microscope with N-STORM, an Andor IXON3 Ultra DU897 EMCCD, and a 100× oil immersion TIRF objective. Photoactivation was driven by a Coherent 405-nm laser, while excitation was driven with a Coherent 647-nm laser. All image analysis and image reconstruction were performed using both Nikon Elements analysis software and custom-written MATLAB scripts. Blinking correction was performed by implementing the pairwise Distance Distribution Correction (DDC) algorithm [202]. Cluster property measurements were performed using Ripley-K analysis and custom mean-shift code for segmentation.

3.4.5   Proximity Ligation Assay

Antibodies for AC8 and AKAP150, mentioned in STORM section, were buffer exchanged into DPBS and conjugated with MINUS or PLUS oligos, following the Sigma DuoLink in situ Probemaker kits. PLA experiments were performed using the Duolink®in situ red kit for proximity ligation assays according to the provided protocol. The only protocol modification was to extend the amplification time by 50 min. Briefly, cells were fixed and permeabilized as in the STORM experiments before incubation with PLUS and MINUS oligo-conjugated primary antibodies for 30 min at 37°C each with washes after each step. Ligation of the nucleotides and amplification of the strand occurred sequentially by incubating cells with first ligase then polymerase and detection solution. PLA experiments with AKAP95 antibodies from different species were used as positive controls in HEK293T cells, and experiments with just one oligo-

73

labeled primary antibody or the other were our negative control. Images were acquired on a Nikon Ti Eclipse epifluorescence scope with z-control and maximum intensity projections were created. A cross section of the nucleus (3.6-5 μm) was also acquired and the number of dots per cell was counted using the nucleus as reference.

3.4.6 Computational Modeling

3.4.7 Well-mixed system

Assumptions

- Signaling components are present in large enough quantities that concentration changes are smooth and move in a deterministic fashion.

- Well-mixed kinetic rate constants contain conversion factors between compartments, i.e membrane to cytosol.

- Binding interactions occur rapidly enough such that any kinetic parameter, k, remains constant on surfaces [203].

- A-kinase-anchoring protein (AKAP) does not alter the activity of the catalytic subunits of Protein kinase A (PKA) instead it only affects localization.

- Ca^{2+} independent activity of Adenylyl cyclase (AC) is of the same strength as inactive Ca^{2+} dependent Adenylyl cyclase (AC8) and stays at a constant value.

Model Development

We constructed a biochemical network to represent interactions between Ca^{2+} and cAMP in β-cells, **Figure 3.1B**, [14, 204] after a depolarization event. The computational model considered the dynamics of calcium, potassium, leaky, and calcium-sensitive potassium channels

74

(**Table B.1**). Importantly, we included feedback of PKA with KATP channels and the inclusion of Ca^{2+}-sensitive ACs and PDEs. The model contains **92** parameters with **11** free parameters. The values of the parameters are constrained through both previously peer-reviewed publication results [14, 173, 174, 205, 206] and with new experimental results using obtained FRET measurements. To constrain source and sink activation rates, previously published literature of AC and PDE stimulus-response curves (of related isoforms) was utilized [173, 174]. COPASI was used to calculate initial guesses for kinetic activation parameters. FRET measurements took precedence over binding curves, especially for the spatial model (section **3.4.9**) where further fitting routines were performed to refine the model. Model variations were performed to attain both semi-physiological concentrations (within the ranges of the sensor) and phase (period and relation) information. Predictions are made on qualitative behavior as opposed to quantitative as proper parameter fitting would require much more data than available for this system.

Values and reaction sets used in the well-mixed model can be found in **Tables B.1, B.2, B.3, and B.5**. The network of interactions was constructed using COPASI (version 4.23, build 184)
(http://www.nrcam.uchc.edu, http://copasi.org/). The model was built in COPASI to leverage the inbuilt fitting techniques for initial parameter guesses pre-FRET.

Well-mixed computational results

The network shown in **Figure 3.1B** has been shown to exhibit oscillations through cAMP variation due to the action of PKA on IP3 receptors and KATP Plasma membrane channels. This network has been studied in many labs previous work [14, 171, 190, 204, 207] and has been explored to show:

- The system can be moved in and out of phase through tuning of AC [204].

- The oscillation rate can be tuned through PKA feedback to KATP channels [14].

- Both Ca^{2+} sensitive PDE and AC is necessary for oscillations to occur [14].

Our model results agree with the above findings.

Variations in the connection strength of sources and sinks also introduced another finding–changing the component's (source or sink) variability in the regime of Ca^{2+} spiking (0.1-1.2μM) a switch in phase can also be observed, **Figure B.2**. Compared to well-mixed results, **Figure B.2a**, by decreasing the activation rate of Ca_2AC from 56 to 0.6 s^{-1}, a switch in phase can occur, **Figure B.2c**. Yet, we notice how increasing PDE activity does not switch the phase **Figure B.2b**, only after subsequently decreasing PDE and CaM association does cause the phase change **Figure B.2d**. This is due to both changes being required for the activity variation of PDE to out perform that of AC. These findings lead to more questions about how source and sink activities relate in a variable Ca^{2+} regime.

Well-mixed reaction tables

See appendix **B** for model tables.

3.4.8   Minimal model to explore Ca^{2+}-cAMP phase behavior

Based on the well-mixed model, we propose a minimal circuit to understand the phase behavior of Ca^{2+}-cAMP. Consider the following system in **Figure 3.2c**, where Ca^{2+} is the stimulus which uses a pulse train to set influx times, AC is an activator, PDE1C is an inhibitor, and cAMP is the response element.

Assumptions

The system is in a state such that the change in cAMP allows for further Ca^{2+} influx in a semi predictable manner, as represented by the pulse train. Therefore this system is deemed to be stable if there exists a Ca^{2+} value that gives a stable solution for cAMP. All constants must be positive to remain physically relevant. We assume that there exists a constant independent source and sink within the system. The Ca^{2+} dependent and independent sources are localized homogeneously on the membrane, with both sinks located uniformly in the cytosol. For simplicity, we assume that the activation function for both *AC* and *PDE1C* are linear functions of Ca^{2+} of the form $aS + b$.

Governing Equations

We define a stimulus (S, Ca^{2+}) and a response element (R, cAMP). The well-mixed rate of change function for cAMP is then given by,

$$\frac{dR}{dt} = v_1\left(a_1 S + b_1\right) - v_2\left(a_2 S + b_2\right)R + v_{ip} - v_{id}R$$

Here, v_1 denotes the velocity of cAMP production by AC, v_2 the rate of degradation by PDE, and v_{ip} and v_{id} the rates of independent production and degradation respectively.

Analytical solutions for the minimal model

To analyze if the system lies in an in- or out-of-phase state we find the direction of the system change after initialization to S_0 [*i.e.* the basal stimulus (initial concentration of Ca^{2+})]. First we must solve for R_0 (initial concentration of cAMP) by setting $\frac{dR}{dt} = 0$, we find:

$$R_0 = \frac{v_1\left(a_1 S_0 + b_1\right) + v_{ip}}{v_2\left(a_2 S_0 + b_2\right) + v_{id}}$$

We start the system at equilibrium and prescribe a discontinuous pulse of S from S_0 to S_h, akin to VGCC opening allowing Ca flux. Therefore solving for the sign of R, we sobtain

$$
\frac{dR}{dt}\Big|_{t=0} = v_1\left(a_1 S_h + b_1\right) + v_{ip} - \left(v_2\left(a_2 S_h + b_2\right) + v_{id}\right)\frac{v_1\left(a_1 S_0 + b_1\right) + v_{ip}}{v_2\left(a_2 S_0 + b_2\right) + v_{id}}
$$

$$
\frac{dR}{dt}\Big|_{t=0} = \frac{\left(v_1 a_1\left(v_2 b_2 + v_{id}\right) - v_2 a_2\left(v_1 b_1 + v_{ip}\right)\right)\left(S_h - S_0\right)}{v_2\left(a_2 S_0 + b_2\right) + v_{id}}
$$

Since we consider the sign we can then characterize the solution by

$$
\frac{v_1 a_1\left(v_2 b_2 + v_{id}\right)}{v_2 a_2\left(v_1 b_1 + v_{ip}\right)} > 1 \qquad \text{in phase (low } \tau\text{)}
$$

$$
\frac{v_1 a_1\left(v_2 b_2 + v_{id}\right)}{v_2 a_2\left(v_1 b_1 + v_{ip}\right)} = 1 \qquad \text{transition (flat line)}
$$

$$
\frac{v_1 a_1\left(v_2 b_2 + v_{id}\right)}{v_2 a_2\left(v_1 b_1 + v_{ip}\right)} < 1 \qquad \text{out of phase (high } \tau\text{)}
$$

This model was then computationally run to confirm the results with arbitrary parameters (**Figure 3.2c**). The system was ran with all parameters at 1 except v_1 and v_2 at values of 4 and 2, respectively and vice-versa.

Numerical implementation of the minimal model

We performed numerical simulations in MATLAB R2018b and checked against analytic solutions provided in the previous section. Minimal model solutions are found in **Figure 3.2c**.

3.4.9   Simulations of the full spatial systems

For computational simplification, simulations were performed with a Gaussian profile on the top boundary, the size of the domain and Gaussian profile were informed by STORM images, **Figure 3.3**. The system is a hexagonal prism with outer radius of $0.4\mu m$ and depth $0.6\mu m$ with periodic boundary conditions in the x and y planes, see **Figure 3.4a**. The top plane is assumed to be the membrane and the bottom is a no flux condition. For the membrane plane, a Gaussian

profile was normalized such that the average value is $4 \times 10^{-10} \frac{mol}{m^2}$. The Ca^{2+} sensitive AC initial conditions (Gaussian profile) is fixed for all simulation time by setting the diffusion constant to ≈ 0.

Assumptions

- Membrane patterns are pre-existing and not effected by a single signaling event such that no diffusion occurs.

- Clustering events were approximated by a Gaussian profile in the center of the hexagonal prism.

Model development

Although our system does show the ability to oscillate in and out of phase in a well-behaved manner, this will not produce our desired form if a homogenous boundary is present. Previous studies have looked at spatial gradients in the context of cAMP and PKA and found out that a localization must occur for the system to form one [208]. Therefore, when moving to a 3D spatial map, we must consider how two solution regimes can be recovered. Experimental data suggest that AKAP dimerizes and may form oligomers [161, 209], which is important for the function of these cells [210]. This could allow spatial instabilities like those seen in [211] used to describe post synaptic domains. The final Gaussian profile on the top boundary had the size of the domain and Gaussian profile informed by STORM images of AC clustering (**Figure 3.3**). Statistics of the images show that, on average, 90% of the AC in storm sits within 54 nm of the cluster center. The system was determined to be 0.35x0.35x0.6 μm hexagonal prism with a Gaussian standard deviation of 25 nm.

Kinetic parameters were used the same as the well-mixed model, except for a few cases in which tuning through surface/volume relationships were needed. Post fitting was performed

to further refine the relationship of PDE and AC through use of obtained FRET measurements (see section **3.4.10**). Due to the large computational expense of the model PDE interactions were reduced to two steps (**Table B.8**).

Numerical Simulation

The well-mixed network was imported into COMSOL Multiphysics®5.4 (Build:295), to solve the spatial model with in-homogeneous boundary conditions.

PKA spatial response mirrors cAMP

PKA with full diffusion values ($\approx 10 \mu m^2$s) did not follow cAMP dynamics and only elicited one global response. We asked if this was due to AKAP patterning at the surface, which should mirror the AC profile at the surface. Adding this interaction into the model did not allow any sizable spatial gradient to develop. Recent work has suggested the PKA catalytic subunit in the presence of non-excess cAMP is effectively activated but its diffusion is restricted [212]. By varying the diffusion constant, we found PKA activity could follow cAMP dynamics in the nanocluster and PM compartments in our computational model for restricted diffusivities (**Supplementary Fig. 3.11a**). We experimentally tested this prediction using the AKAP79-fused and PM-targeted PKA activity sensors and found that indeed PKA activity did follow the cAMP-Ca^{2+} phase relationship within the two compartments (**Supplementary Fig. 3.11b-d**). This suggests that anchored PKA holoenzyme action is much more restricted than originally anticipated.

3.4.10   Comparisons to experimental data

Raw FRET data (**Figure 3.1**) was used for model refinement. The data was compared for oscillation time and phase, with expected cAMP concentration falling in the sensors sensitive

range of $\approx$0.1-10μM. Voltage gated channel sensitivities were not tuned, and only connection strengths between CaM to ACs and PDEs, which are largely less constrained in comparison, were varied. Values modified from the well-mixed model values can be found in **Tables B.6, B.7, B.8**.

Model validation and predictions

The model was validated on predictions to concentration perturbations (AC, PDE, ect.) and disruption of patterning (AC binding disruption) and their changes to the phase of the signal. The system, once moved to the spatial model, was allowed free parameters along the four component axis for connection and strength of ACs and PDEs. This includes the flux differential between basal and activated ACs and PDEs.

Spatial reaction tables

See appendix **B** for model tables.

Chapter **3**, in full, has been submitted for publication as it may appear in ELife, Brian Tenner, Michael Getz, Brian Ross, Donya Ohadi, Christopher H. Bohrer, Eric Greenwald, Sohum Mehta, Jie Xiao, Padmini Rangamani, Jin Zhang, Spatially compartmentalized phase regulation in the Ca 2+ -cAMP-PKA oscillatory circuit. The dissertation author was the second author of this material.
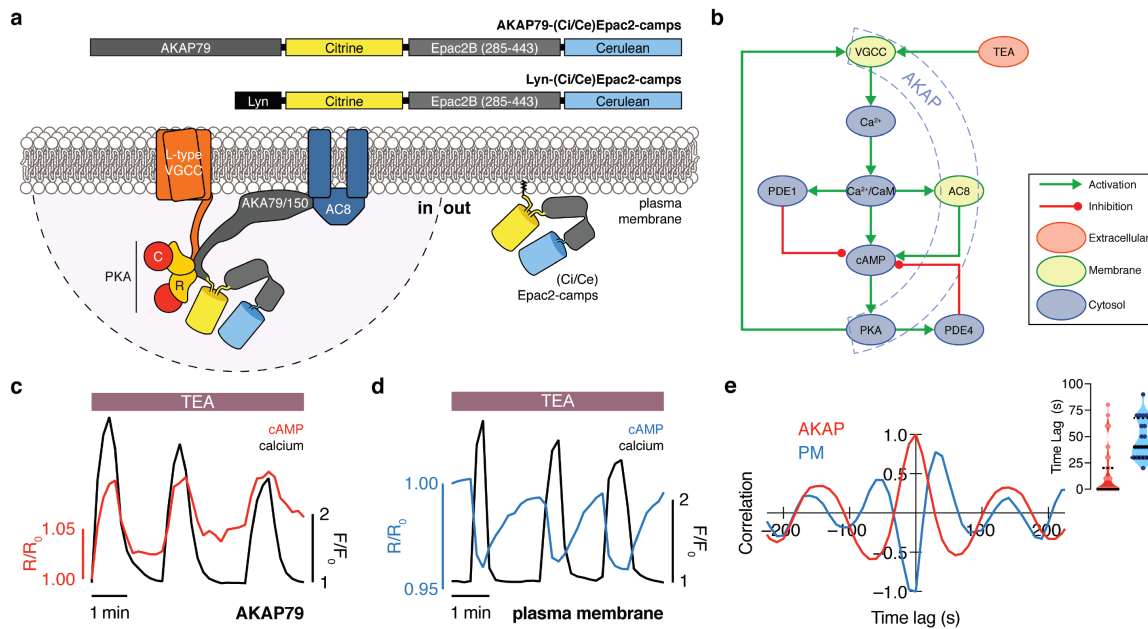
Figure 3.1: **The phase of oscillating cAMP is shifted between the AKAP79/150 compartment and the general plasma membrane compartment, relative to Ca^{2+}.** (A) Depiction of the AKAP79 compartment and plasma membrane compartment, including the targeted cAMP biosensor (Ci/Ce)Epac2-camps to measure the compartment-specific cAMP signaling. Schematics of the lyn-(Ci/Ce)Epac2-camps and AKAP79-(Ci/Ce)Epac2-camps sensors. (B) Network diagram describing the key players in the Ca^{2+}-cAMP-PKA oscillatory circuit in the β cell. (C) Representative single cell trace of an in-phase oscillating β cell with AKAP79-(Ci/Ce)Epac2-camps and RCaMP, whole-cell fluorescence measured. Red trace is cAMP (cyan direct channel divided by CY-FRET channel) and black trace is Ca^{2+} (RFP). (D) Representative single cell trace of an out-of-phase oscillating β cell with lyn-(Ci/Ce)Epac2-camps and RCaMP, whole-cell fluorescence measured. Blue trace is cAMP (cyan direct channel divided by CY-FRET channel) and black trace is Ca^{2+} (RFP). (E) Cross-correlation between the oscillatory Ca^{2+} and cAMP signals from the representative in-phase AKAP79 (red) and out-of-phase plasma membrane (PM, blue) β cells from C, D. Time lag (sec) between the cAMP and Ca^{2+} signals for the two compartments (AKAP79/150, red, is 13sec ± 3sec and PM, blue, is 47sec ± 4sec) (p¡0.05).
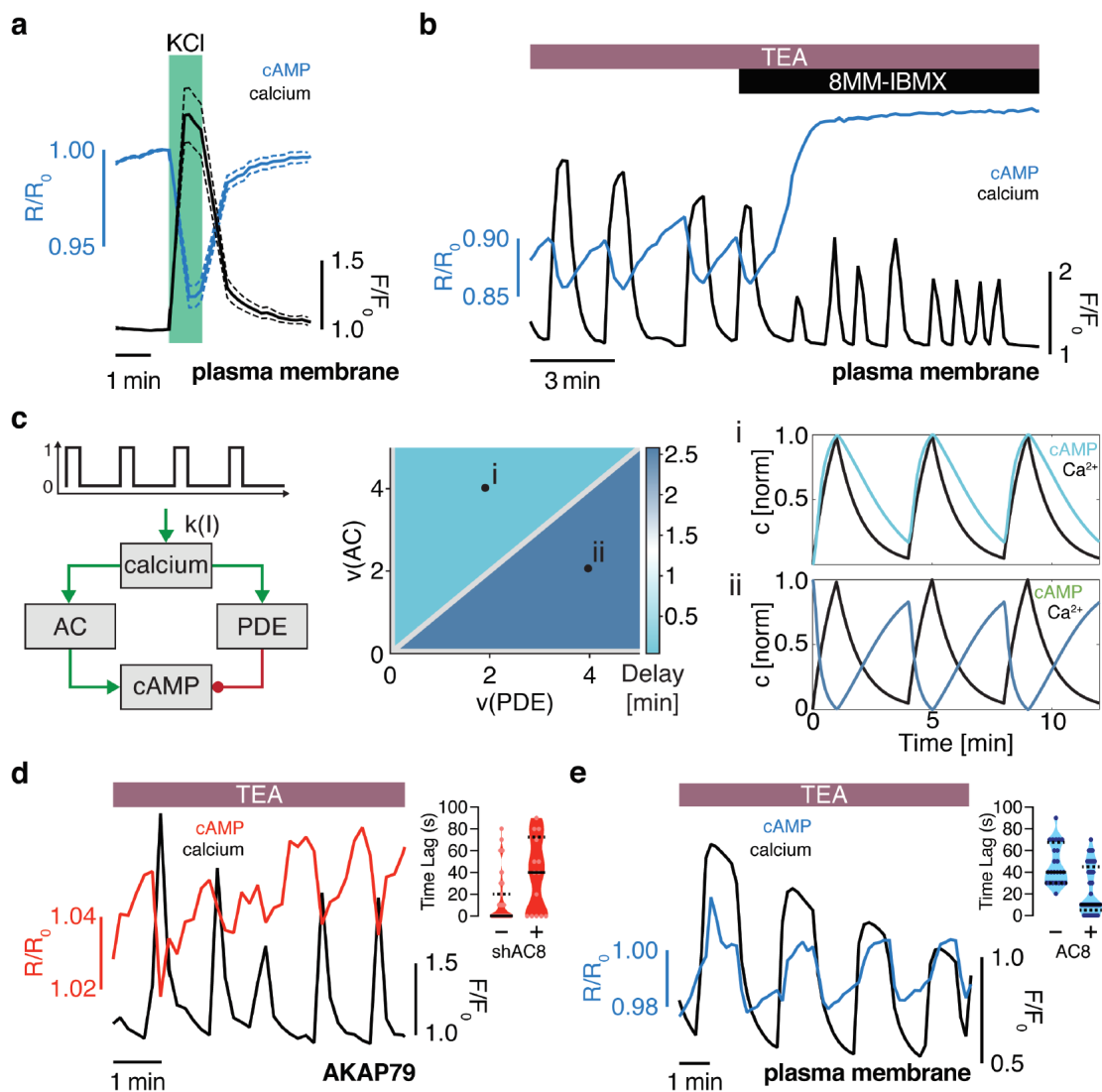
Figure 3.2: **The oscillation phase is regulated by a balance between Ca^{2+}-sensitive AC and PDE activity.** (A) Impulse response of plasma membrane cAMP (blue) to a spike in Ca^{2+} entry (black), triggered by KCl-mediated membrane depolarization (wash in/out). The transient decrease in PM-cAMP is coupled to the transient increase in intracellular Ca^{2+}. (B) Acute inhibition of Ca^{2+}-sensitive PDE1 decouples the out-of-phase PM-cAMP oscillations from Ca^{2+} oscillations, as observed in this representative cell trace (Ca^{2+} - black, PM-cAMP – blue). (C) The oscillatory phase of cAMP can be manipulated by tuning the relative activity of Ca^{2+}-sensitive PDE and AC, as demonstrated by a simple toy model. (D) Knocking down AC8 is correlated with an increase in the time lag for oscillatory cAMP at the AKAP79/150 microdomain (37sec), indicating more cells exhibiting out-of-phase cAMP oscillaitons (representative cell trace, Ca^{2+} - black, AKAP79/150-cAMP – red). (E) Co-expressing AC8 is sufficient to reverse the phase of cAMP at the PM (23s) to in-phase (representative cell trace, Ca^{2+} - back, PM cAMP – blue).

83

Figure 3.3: **AKAP150 and AC8 both form nanoclusters at the surface of MIN6 β cells.** (A) Representative super-resolution STORM image of the AKAP150 scaffold (scale 5*μ*m, inset 500nm). Ripley-K analysis measures the average radii of the nanoclusters and indicates that AKAP150 forms clusters of 127nm. The nearest-neighbor distance distribution describes the distance between nanoclusters (average distance for AKAP150 is 313nm). (B) Representative super-resolution STORM image of Ca^{2+}-sensitive AC8 (scale 5*μ*m, inset 500nm) depicts AC8 nanoclusters of average radius 88nm and average nearest-neighbor distance 292nm.
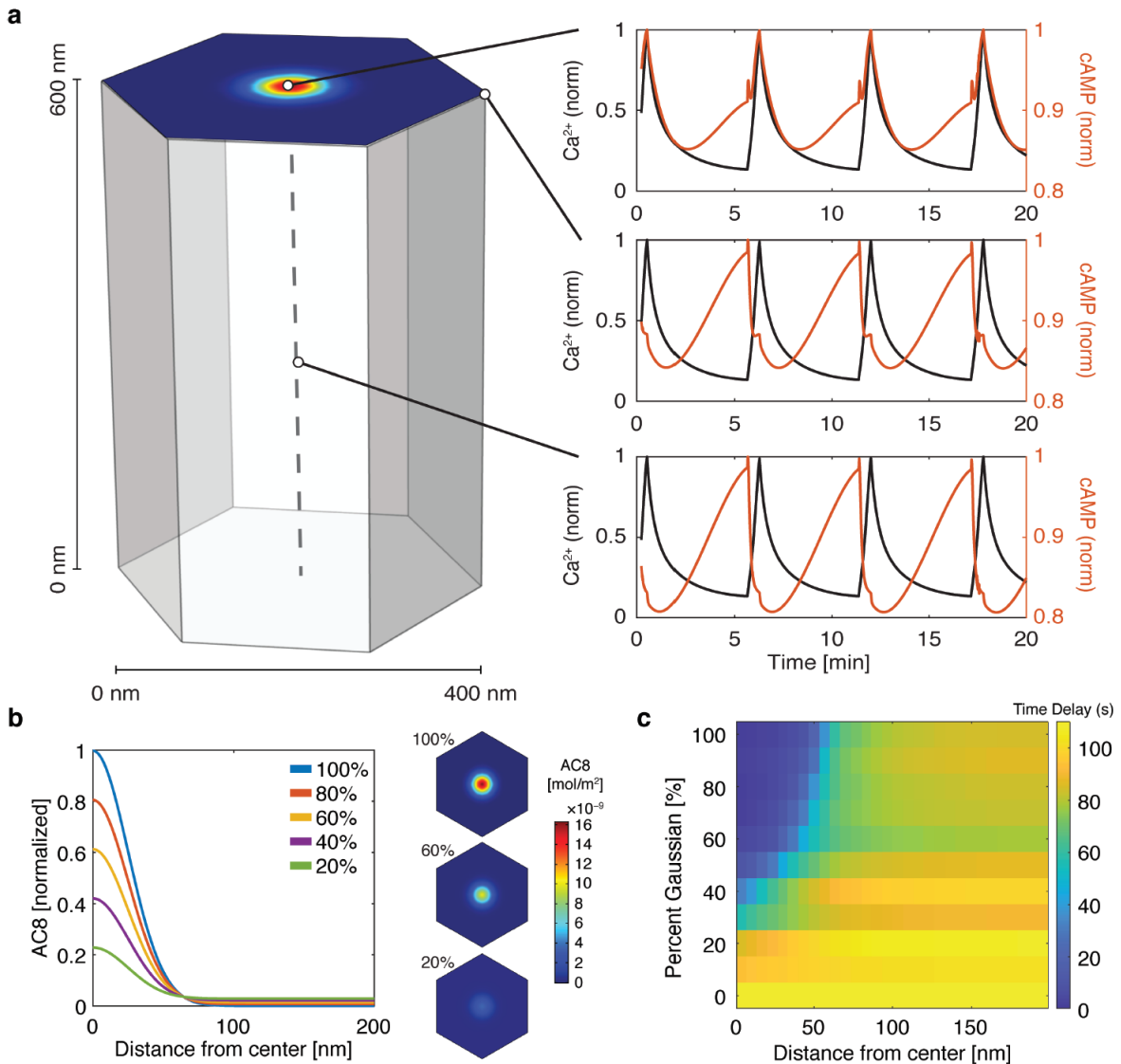
Figure 3.4: **cAMP-Ca^{2+} phase relationship can be described by a 3D reaction-diffusion model involving clusters of AKAP79/150 and AC8.** (A) 3D reaction-diffusion model with a single AKAP79/150:AC8 co-cluster positioned at the PM in the β cell in a hexagonal prism volume. cAMP oscillates in-phase immediately within the AKAP79/150:AC8 nanocluster due to the high effective concentration of AC8, but out-of-phase at the PM or cytosol due to the presence of PDE1 (cAMP – red, Ca^{2+} - blue). (B) Disruption of AKAP79/150:AC8 interaction can redistribute AC8 from within the cluster to the PM, shown by the half-Gaussian cross-sections and representative AC8 concentration heatmaps at the PM. (C) Heatmap depicting the time lag (s) for AC8 distribution (% Gaussian) and spatial distance (nm) from cluster center along PM.
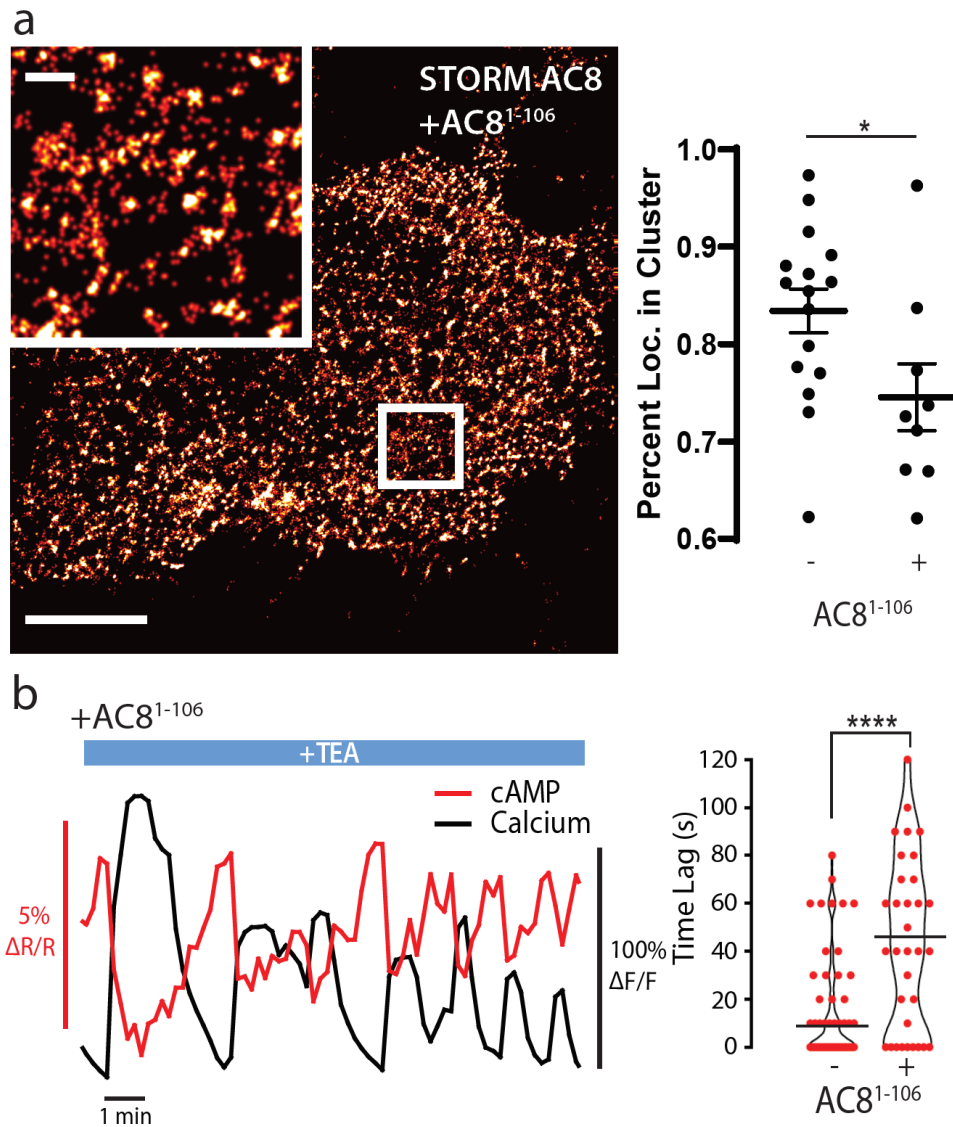
Figure 3.5: **Disruption of the AKAP79/150:AC8 interaction is associated with a redistribution of AC8 at the PM and a phase shift of cAMP at the AKAP79/150 nanodomain.** (A) Over-expression of the N-terminus of AC8 that is necessary and sufficient for mediating the AKAP79/150:AC8 interaction redistributes AC8 from within nanoclusters to the general PM, as seen in the STORM image (scale 5μm, inset 500nm) and measured by the percent of localizations that fall into nanoclusters. (B) AKAP150 nanoclustering is unaffected by the AC8 N-terminal fragment. (C) Disruption of the AKAP79/150:AC8 interaction lengthens the time lag between the cAMP (red) and Ca^{2+} (black) signals at the AKAP79/150 compartment (avg. time lag in absence of disruptor is 13sec $\pm$ 3sec, and presence of disruptor 43sec $\pm$ 6sec, p¡0.05) due to more cells displaying out-of-phase cAMP oscillations.
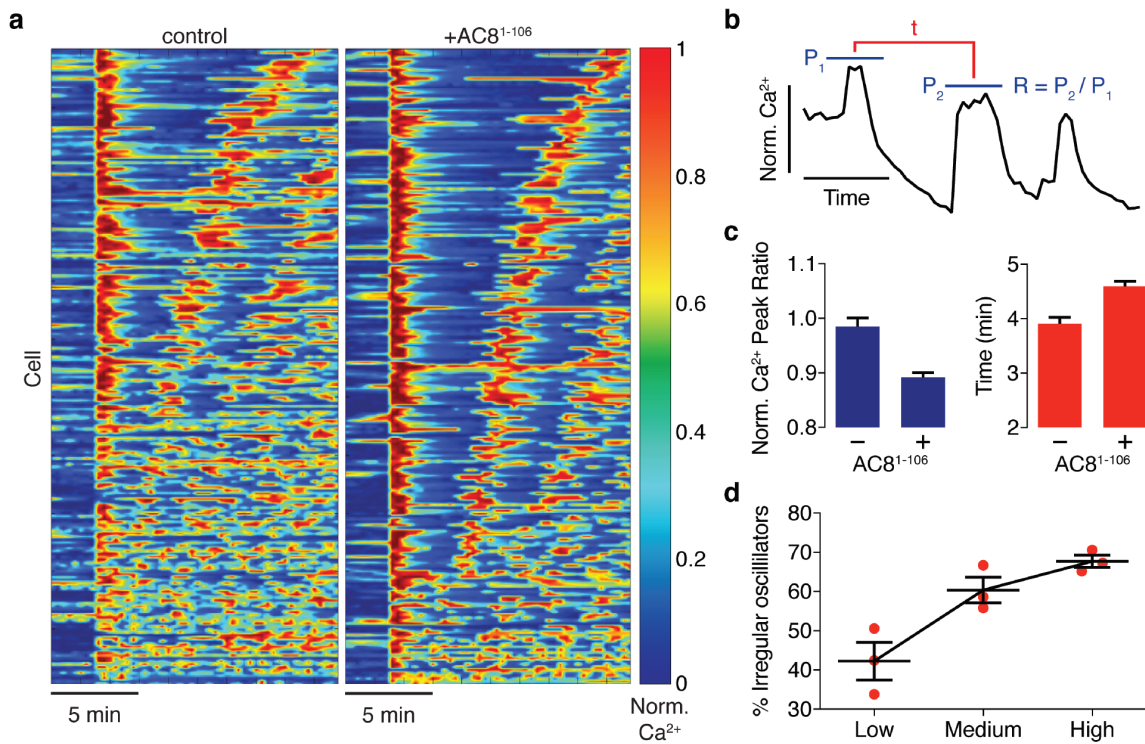
Figure 3.6: **Ca^{2+} oscillatory dynamics are affected by expression of the disruptor peptide in β cells.** (A) Heatmap depicting Ca^{2+} oscillations for 220 randomly selected cells with EGFP alone co-expressed (control) or EGFP-tagged AC$^{81-106}$ (AKAP79/150:AC8 disruptor), ordered by a mixed parameter describing the time lag between the first two Ca^{2+} peaks and the avg. timelag between all Ca^{2+} peaks. (B) Schematic describing two Ca^{2+} oscillatory parameters, the ratio between the first two Ca^{2+} peaks and the interpeak timing. (C) The peak ratio is decreased in the presence of the AKAP79/150:AC8 disruptor, indicating less of a sustained Ca^{2+} oscillatory response. Over-expression of the disruptor also lengthens the timing between peaks. (D) Expression level of the disruptor is correlated with an increase in the percentage of cells eliciting irregular oscillations.
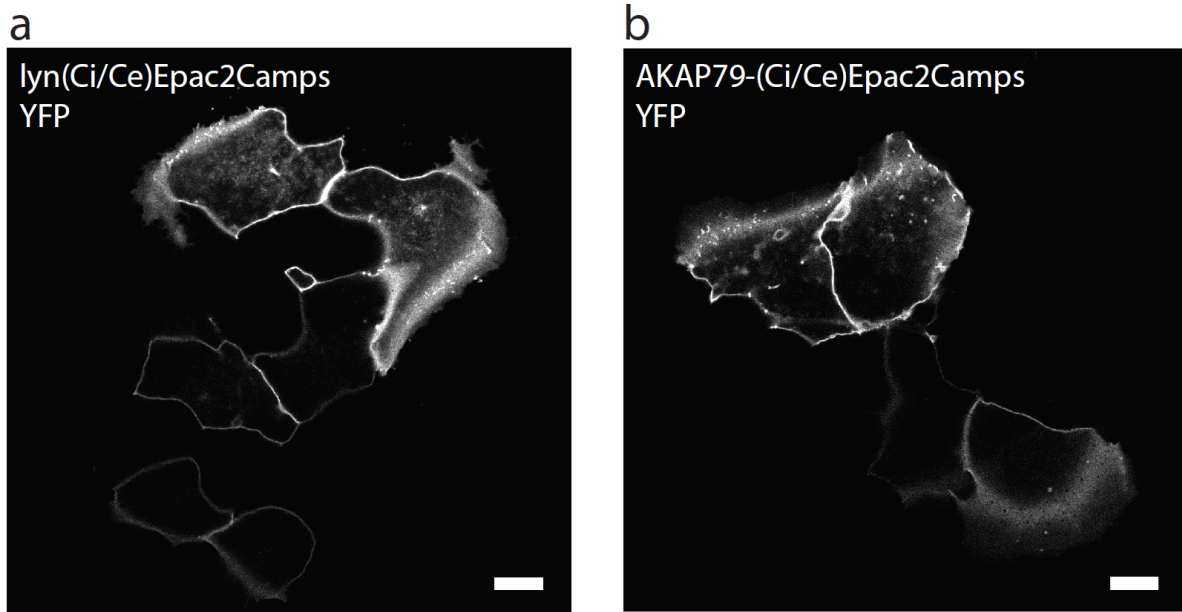
Figure 3.7: **Supplementary; The AKAP79/150 and PM targeted sensors are localized at the plasma membrane.** (A) Confocal image of lyn(Ci/Ce)Epac2camps showing efficient localization of the probe at the PM in MIN6 cells (YFP channel, scale 5μm). (B) Confocal image of AKAP79-(Ci/Ce)Epac2camps also depicting localization of the scaffold-fused biosensor at the PM in MIN6 cells (YFP channel, scale 5μm).
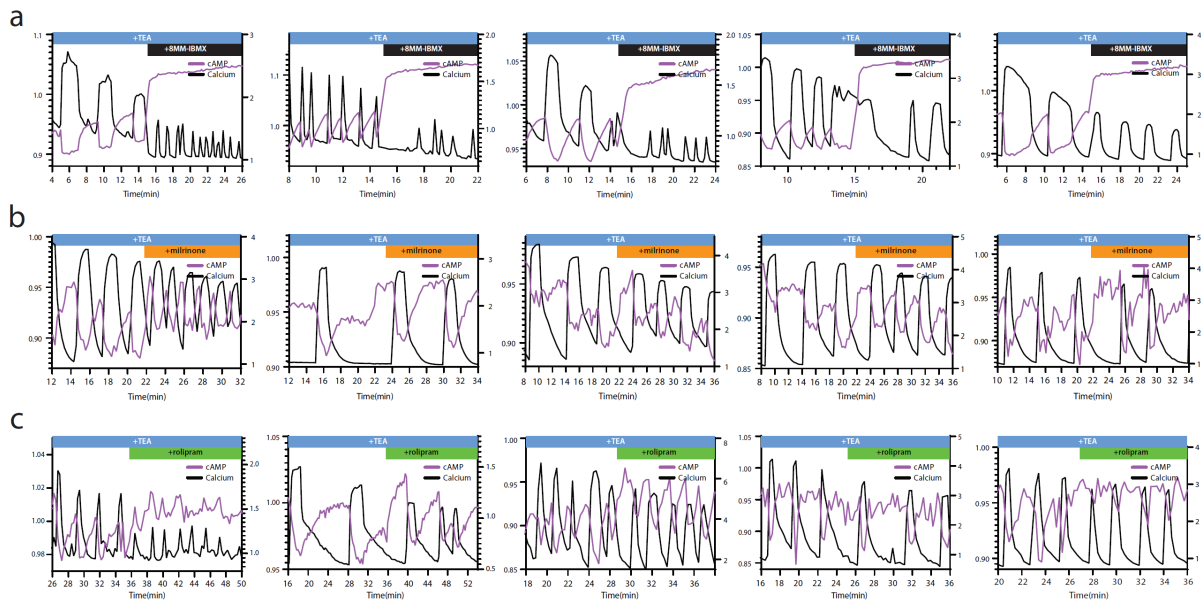
Figure 3.8: **Supplementary; The Ca^{2+}-dependent cAMP response is dependent on PDE1, but not PDE3 or PDE4.** (A) Representative single cell traces depicting the decoupling of oscillating cAMP at the PM (measured by lyn-(Ci/Ce)Epac2camps, purple trace) from oscillating Ca^{2+} (black trace) upon inhibition of PDE1C with 8MM-IBMX. (B) Representative single cell traces showing that the phase of cAMP at the PM (purple trace) relative to Ca^{2+} (black trace) is not affected by inhibition of the abundant PDE3 (milrinone). (C) Representative single cell traces showing that the phase of cAMP at the PM (purple trace) relative to Ca^{2+} (black trace) is also not affected by inhibition of PDE4 (rolipram).
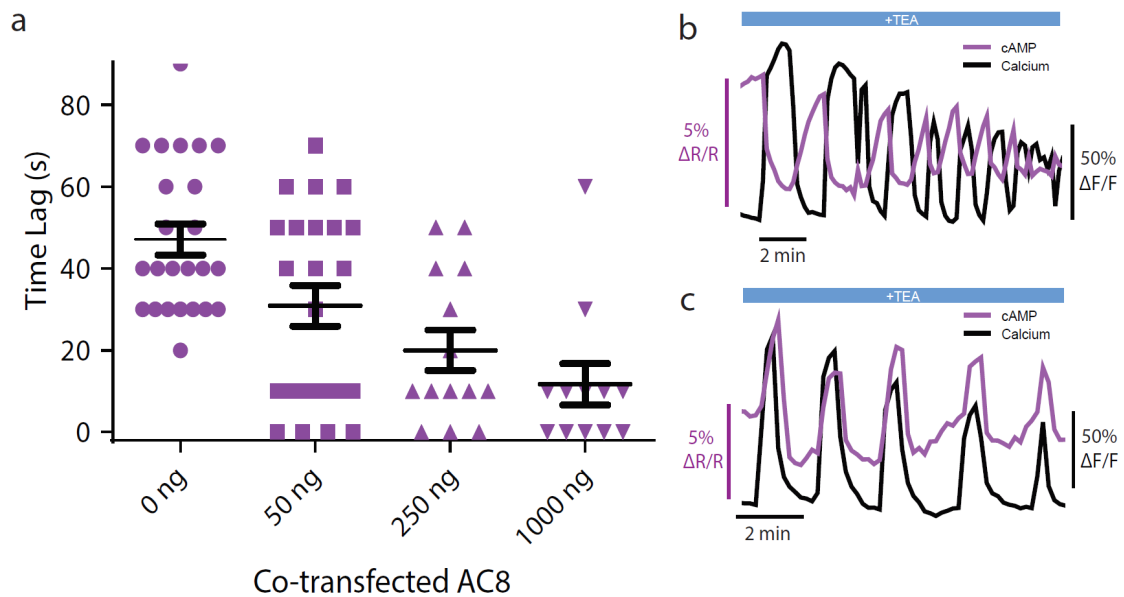
Figure 3.9: **Supplementary; The cAMP-Ca^{2+} phase relationship at the PM can be tuned by expression of the Ca^{2+}-dependent AC8.** (A) Plot depicting a dose-dependence between the time lag of cAMP at the PM and the amount of AC8 co-transfected. (B) Representative single cell trace of an oscillating β cell with 0ng of an AC8 expression vector co-transfected, illustrating an out-of-phase cAMP-Ca^{2+} phase relationship. Purple trace is cAMP at PM and black trace is Ca^{2+}. (C) Representative single cell trace of an oscillating β cell with 1μg of an AC8 expression vector co-transfected, illustrating an in-phase cAMP-Ca^{2+} phase relationship. Purple trace is cAMP at PM and black trace is Ca^{2+}.

a

b
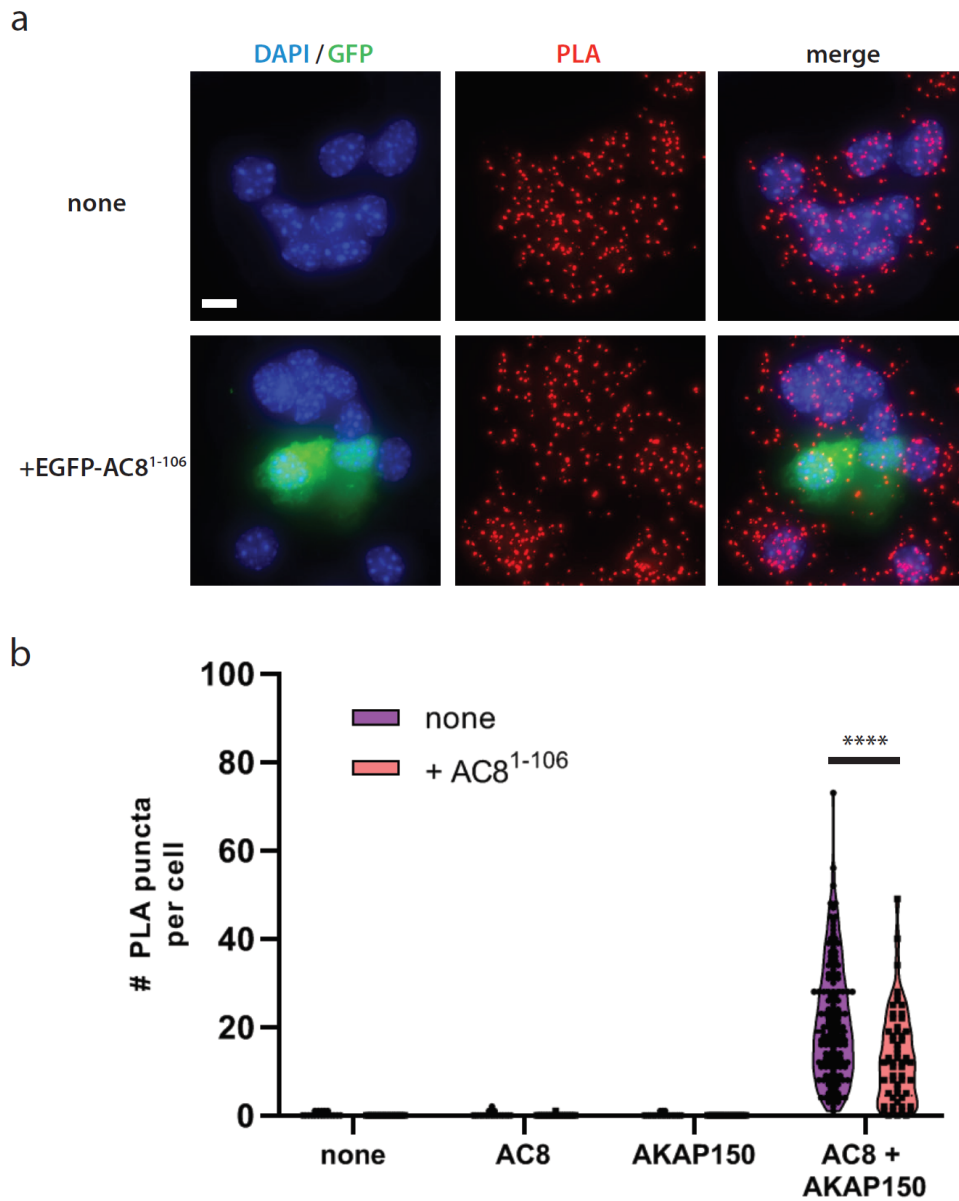
Figure 3.10: **Supplementary; Expression of the N-terminus of AC8 is sufficient to perturb the interaction between endogenous AKAP150 and AC8 in MIN6.** (A) Widefield maximum intensity projections of a Proximity Ligation Assay to depict the extent of interactions between AC8 and AKAP150 in MIN6 β cells (scale $10\mu m$). Expression of EGFP-tagged AC^{81-106} results in less PLA puncta per cell. (B) # of PLA signals per AC^{81-106}-expressing cell is significantly decreased compared to non-transfected control ($p<0.05$).
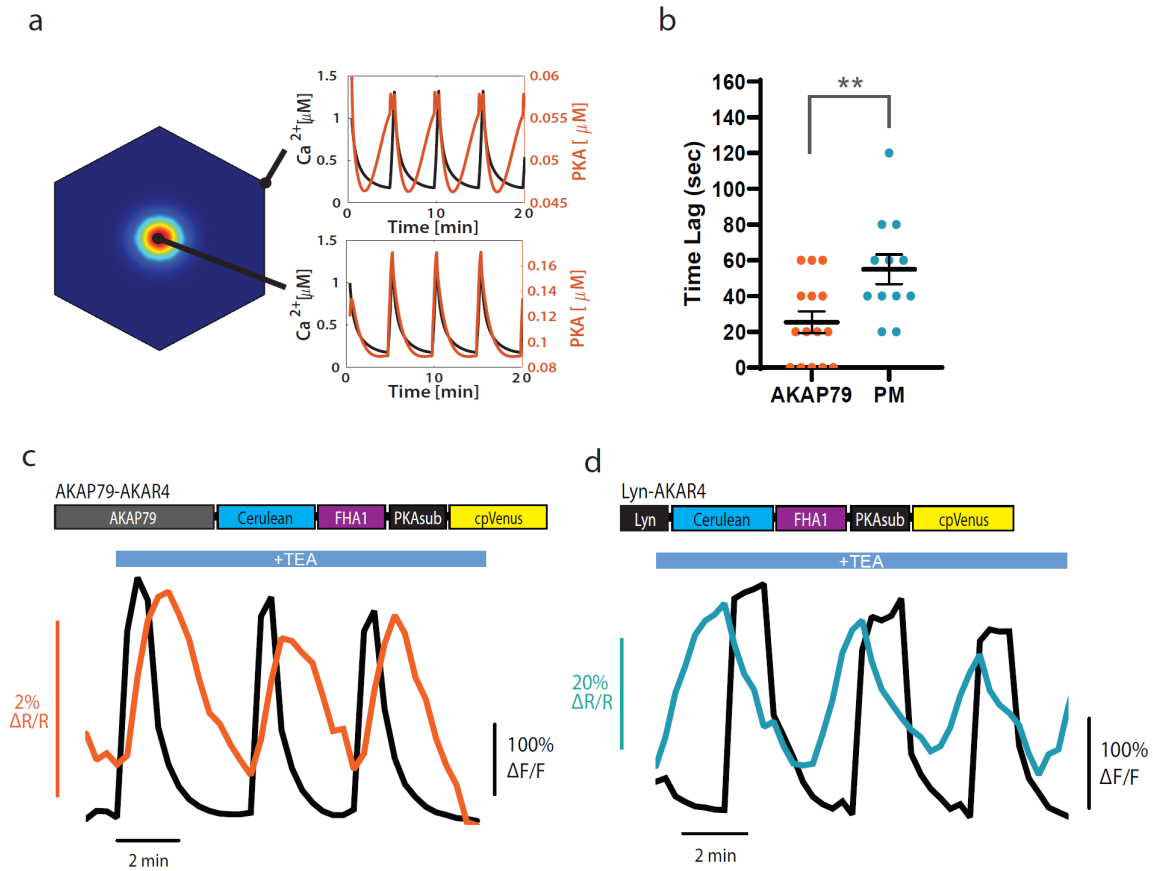
Figure 3.11: **Supplementary; Oscillating PKA activity phase is also spatially compartmen-talized at the PM.** (A) By extending our 3D model, PKA activity is predicted to oscillate near the center of the AKAP79/150:AC8 cluster with a short time delay and a longer delay outside of the cluster, relative to Ca^{2+}. (B) Experimentally-measured time lag between PKA activity oscillations and Ca^{2+} for AKAP79 (orange) and the general PM (teal) compartments. (C) Representative single cell trace showing in-phase PKA activity within the AKAP79 compartment. Orange trace is PKA activity at AKAP79 (CY-FRET channel divided by cyan donor channel) and black trace is Ca^{2+} (RFP). (D) Representative single cell trace showing out-of-phase PKA activity within the general PM compartment. Teal trace is PKA activity at PM (CY-FRET channel divided by cyan donor channel) and black trace is Ca^{2+} (RFP).

Chapter 4

cAMP spatiotemporal interactions and outcomes are deeply coupled with fine-tuned machinary.

Many process of cells have increasingly been studied in terms of spatial heterogeneity though such processes as phase transitions. Localization of catalysts can then play a crucial role in controlling spatial and temporal signals. What function does this interaction elicit, and how is this process controlled; more importantly, how is this misregulated?

Chapter **2** we discussed a novel protein interaction allowing for a 'tunable valve' function on cAMP output. We conclude that GIV utilizes compartmental segregation to modulate the dynamics of RTK→G protein→cAMP signaling and confers robustness to these dynamics by functioning as a tunable control valve. Future systems efforts will build on this model to unravel further exciting features of GIV as a critical hub for signaling regulation at the knot of a bowtie [101] and elucidate the hidden complexity that arises from network architecture in non-canonical G protein signaling.

Chapter **3** we discussed the many biological systems which show complex spatial response

upon a stimulus impulse, or depolarization event, where losing this interaction causes the network to misbehave. Ca^{2+}-cAMP pancreatic insulin release, arrhythmia, and brain voltage models all rely on proper depolization for function. We disscused how the Ca^{2+}-cAMP Beta Cell system and how membrane heterogeneity effects and controls the elicited response.

We can consider the well mixed dynamic results to answer how can we control the phase; as previously shown in chapter **3**, under certain assumptions a 4 component model system is built and analyzed to describe the phase relationship to input parameters. In order to form a spatial gradient within the reaction network's topology a heterogeneous boundary condition must exist, we discuss how heterogeneous conditions exist; and postulate at a turing pattern generated through set interaction rules of receptors and scaffolds.

We can therefore build a set of models to test for the existence of Turing patterns. Simular to other plasma membrane Turing patterns, Haselwandter *et al.* [211, 213] has shown a crucial interaction that must exist is self assembly into homo-trimers. For our set of rules this is satisfied through $Ca_V\beta$ [214], patterning events are likely centered around $Ca_V\beta$ and AKAP interactions as hinted at in AC^{81-106} (AKAP79/150:AC8 disruptor) expressed experiments (**Supplementary Figure 3.10**). Methods to determine existence of a Turing pattern can be found in Sections **C** and **D** in which patterning events can be observed for multiple cytosol/plasma membrane coupled systems. These findings hint at an intricate interaction between the boundary and volume. With large heterogeneous variations, solutions with phase shifts become more common. This emphasizes the strength of the patterning events at the PM, instabilities must exist that sufficiently drive a concentration gradient to obtain our desired solution type. It therefore becomes obvious that expansions to further elucidate these interactions are needed in both the PM and volume space.

Therefore it can be concluded that the control of sources and sinks in the persepective of cAMP can be a viable condition for disease states to arise. Understanding these conditions

continue to be a stuggle within the medical and computational communities. Continued studies on these network motifs and others continue to be viable sources for identifying novel targets for treatment.

Appendix A

Supplemental Materials for A predictive computational model reveals that GIV/Girdin serves as a tunable valve for EGFR-stimulated Cyclic AMP Signals

A.1 Supplementary Movie Legends

Supplementary Movie 1: Activation of $G\alpha_s$ in response to EGF, as determined by nanobody Nb37-GFP in control HeLa cells [shControl]. The movie shows EGF-dependent activation of $G\alpha_s$ as detected by live-cell imaging using the $G\alpha_s$ conformational biosensor nanobody Nb37-GFP that binds and helps detect the nucleotide-free intermediate during $G\alpha_s$ activation [82]. In control HeLa cells responding to EGF little or no $G\alpha_s$ activity was seen. Quantification of these findings have been published in [42] (Magnification, 63 x).

Supplementary Movie 2: Activation of $G\alpha_s$ in response to EGF, as determined by nanobody NB37-GFP in GIV-depleted HeLa cells (shGIV). The movie show EGF-dependent activation of $G\alpha_s$ as detected by live-cell imaging using the $G\alpha_s$ conformational biosensor nanobody Nb37-GFP that binds and helps detect the nucleotide-free intermediate during $G\alpha_s$ activation [82]. Compared with controls (Movie S1), in GIV-depleted cells a significant increase in $G\alpha_s$ activity was seen on vesicular structures that are likely to be endosomes. Quantification of these findings have been published in [42] (Magnification, 63x).

A.2 Introduction to modeling chemical reactions

A.2.1 Mass-action kinetics

We generated an ordinary differential equation (ODE) for every species using mass-action kinetics for each binding reaction. The law of mass action states that the rate of a chemical reaction is proportional to the product of the concentration of the reactants raised to the power of their stoichiometric coefficient. For example, consider the one-reaction system:

$$X + Y \rightleftharpoons 2Z, \tag{A.1}$$

where the forward and backward rates are k_1 and k_2. The differential equations describing the dynamics of species X, Y, and Z under mass-action kinetics are:

$$\frac{d[X]}{dt} = k_2[Z]^2 - k_1[X][Y] \tag{A.2}$$
$$\frac{d[Y]}{dt} = k_2[Z]^2 - k_1[X][Y]$$
$$\frac{d[Z]}{dt} = k_1[X][Y] - k_2[Z]^2.$$

Mass action kinetics rely on the assumption that the rate constant, k, is constant over time. However, within a restricted space such as a membrane, the rate constant may change over time due to restricted diffusion and mass action kinetics may not be accurate [203]. We assumed that most binding interactions occur rapidly enough such that k remains constant.

A.2.2   Michaelis-Menten kinetics

We used Michaelis-Menten kinetics to model enzyme-catalyzed reactions. When a reaction is catalyzed by an enzyme with kinetic properties k_{cat} and K_M,

$$S \xrightarrow{\text{E}} P,$$
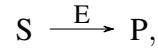
then the reaction rate is given by

$$\frac{d[S]}{dt} = -\frac{k_{cat}[E][S]}{K_M + [S]} = \frac{d[P]}{dt}. \tag{A.3}$$

For Michaelis-Menten kinetics to apply, the concentrations of the reactants and products must be in large enough quantities, and one of the following conditions must apply:

1. The concentration of substrate is very much larger than the concentration of products: [S]≫[P].

2. The energy released in the reaction is very large: $\Delta G \ll 0$.

A.2.3   Transport between compartments

Flux between different cellular compartments was modeled as a reaction rate that captures the rate of species transport per unit time. For the transport of species A between compartments c and d, we used rate equations of the form

$$\frac{dA_c}{dt} = -k_1[A_c] + k_2[A_d], \tag{A.4}$$

where k_1 and k_2 are the transport in and out of compartment c respectively. When utilizing flux for compartmental transport it is important to note the interaction is only valid when the

compartments are large and the corresponding surface area conversion factors are accounted for. Reactions that used fluxes to model different cellular components as follows: phosphorylated EGF-EGFR$_2$ internalization [R4], EGFR internalization [R8], Gα_i transport to an endosome [R19], Gα_i-GDP transport to PM [R21], AC internalization [R32], and Gα_s internalization [R37].

A.3 Model development for growth-factor based cAMP signaling

A.3.1 Phenomenological model

We defined a simple, phenomenological model for the system based on information from legacy literature, **Figure 2.1A**, simple fluxes were chosen to capture the biochemical interactions with a minimal number of components. The phenomenological model aims to identify the 'minimal' network module that can capture the interactions of EGFR, GIV, and G proteins to modulate cAMP flux, independent of parameter values. We define these interactions as follows:

Table A.1: Description of the simplified interactions of the phenomenological model.

Reaction	Explanation
$k_2[\text{EGFR(t)}][\text{EGF(t)}]S(t)$	S(t)=1 for $0 < t < 30$ and 0 otherwise; binding interaction with ligand
$k_5[\text{EGFR}_{2i}^*(t)](1 + sc[\text{GDI}(t)])$	degradation scaling with GDI concentration from basal by sc
$k_6[\text{EGFR}_2^*(t - \delta_2)][\text{GIV}(t)]$	activation delay of GEF - approximation of Cdk5 chain
$k_7[\text{EGFR}_2^*(t - \delta_3)][\text{GEF}(t)]$	activation delay of GDI - approximation of PKC chain
$k_{base}(1 - k_{ACI}[\text{EGFR}_2^*(t)][\text{GEF}(t)])$	inhibition of AC - decreases basal rate as a function of EGFR and GEF
$k_{AC}[\text{EGFR}_{2i}^*(t - \delta_1)]$	activation of AC - assumed as a function delayed on internal EGFR concentration

EGF is presented as a stimulus from 0 to 30 minutes with constant value on 1 and 0 at all other times. This mirrors stimulus used in experimental conditions. EGFR and cAMP concentrations are initialized at 1. GIV concentration is set by mass conservation $GIV = 1 - [GEF] - [GDI]$. All other initial conditions are set to 0. The phenomenological model was then modeling by the following ODEs.

$$\frac{d[\text{EGFR}]}{dt} = -k_2[\text{EGFR(t)}][\text{EGF(t)}]S(t) + k_{r2}[\text{EGF-EGFR}(t)]$$

$$\frac{d[\text{EGF-EGFR}]}{dt} = k_2[\text{EGFR}(t)][\text{EGF}(t)]S(t) - k_{r2}[\text{EGF-EGFR}(t)]...$$
$$-2k_3[\text{EGF-EGFR}(t)]^2 + 2k_{r3}[\text{EGFR}_2^*(t)]$$

$$\frac{d[\text{EGFR}_2^*]}{dt} = 2k_3[\text{EGF-EGFR}(t)]^2 - 2k_{r3}[\text{EGFR}_2^*(t)] - k_4[\text{EGFR}_2^*(t)] + k_{r4}[\text{EGFR}_{2i}^*(t)]$$

$$\frac{d[\text{EGFR}_{2i}^*]}{dt} = k_4[\text{EGFR}_2^*(t)] - k_{r4}[\text{EGFR}_{2i}^*(t)] - k_5[\text{EGFR}_{2i}^*(t)](1 + sc[\text{GDI}(t)])$$

$$\frac{d[\text{GEF}]}{dt} = k_6[\text{EGFR}_2^*(t - \delta_2)][\text{GIV}(t)] - k_{r6}[\text{GEF}(t)]...$$
$$-k_7[\text{EGFR}_2^*(t - \delta_3)][\text{GEF}(t)] + k_{r7}[\text{GDI}(t)]$$

$$\frac{d[\text{GDI}]}{dt} = k_7[\text{EGFR}_2^*(t - \delta_3)][\text{GEF}(t)] - k_{r7}[\text{GDI}(t)]$$

$$\frac{d[\text{cAMP}]}{dt} = (k_{base} + k_{AC}[\text{EGFR}_{2i}^*(t - \delta_1)])(1 - k_{ACI}[\text{EGFR}_2^*(t)][\text{GEF}(t)]) - k_{deg}[\text{cAMP}(t)]$$

This model has 3 time delays, 15 kinetic parameters, and 7 variables. To constrain the model, a large range of possible parameters were simulated, as shown in **Table A.2**. Parameter values are chosen though uniformly distributed values across x$\in [a, b]$ were the parameter is defined as 10^x. k_{base} was set to be equal to k_{deg} such that the steady state of cAMP is 1. The value of k_{base} is assumed as it only encodes the basal degradation and production rates (which

control max and min peak values). Simulations were conducted for 5000 runs and log-normal distributions were calculated and reported (**Figure 2.1**). A secondary variation was also performed with all parameters fixed except time delays, τ. The values for the variation are chosen from uniformly distributed values across $x \in [a, b]$. 5000 runs for each simulation were conducted and normal distributions were calculated and reported (**Figure A.1**).

Table A.2: Values used to simulate the phenomenological model for a primary kinetic variation and a secondary time delay variation.

Parameter	primary range	secondary range	units
τ_1	0.5	[0.1, 8.1]	min
τ_2	5	[0.1, 8.1]	min
τ_3	3	[0.1, 8.1]	min
$k_{base} = k_{deg}$	0.25	0.25	$\sharp s^{-1}, s^{-1}$
k_2	$[10^0, 10^2]$	10^1	$s^{-1}\sharp^{-1}$
k_{r2}	$[10^{-1}, 10^1]$	$10^{0.5}$	s^{-1}
k_3	$[10^0, 10^2]$	10^1	$s^{-1}\sharp^{-1}$
k_{r3}	$[10^{-1}, 10^1]$	$10^{0.5}$	s^{-1}
k_4	$[10^{-3}, 10^{-1}]$	10^{-1}	s^{-1}
k_{r4}	$[10^{-4}, 10^{-2}]$	10^{-2}	s^{-1}
k_5	$[10^{-3}, 10^{-1}]$	10^{-2}	s^{-1}
k_6	$[10^{-1}, 10^0]$	10^0	$s^{-1}\sharp^{-1}$
k_{r6}	$[10^{-2}, 10^{-1}]$	$10^{-1.5}$	s^{-1}
k_7	$[10^{-1}, 10^0]$	$10^{-0.5}$	$s^{-1}\sharp^{-1}$
k_{r7}	$[10^{-3}, 10^{-2}]$	$10^{-2.5}$	s^{-1}
k_{AC}	$[10^0, 10^1]$	10^1	s^{-1}
k_{ACI}	$[10^{-1}, 10^0]$	10^1	$\sharp^{-2}$
sc	$[10^0, 10^2]$	10^1	s^{-1}

A.3.2 Sensitivity analysis of the phenomenological model

To determine the relative sensitivities of each parameter across the simulation time, variance-based sensitivity analysis was performed [215–217]. The analysis describes the sensitivities of the phenomenological model with respect to the uncertainty in kinetic parameters k. Given the model form, the first order effect of the factor X_i on the variance is $V_{X_i}(E_{X_{\sim i}(Y|X_i)})$, where $X_{\sim i}$ is the matrix of all factors but X_i. When compared against the total variance, S_i is retrieved, where $S_i = \frac{V_{X_i}(E_{X_{\sim i}(Y|X_i)})}{V(Y)}$. The total index S_{Ti} does the same but considers all higher order effects of X_i through calculation of $E_{X_{\sim i}}(V_{X_i}(Y|X_i))$. To find these values, a hypercube composed of two independent sampling matrices A and B of size Nx$2k$ is created (where k is the number of uncertain parameters and N is the number of random samples). A third matrix is then sampled, A_B^i, defined as the matrix A with the ith column sampled from matrix B. We then define $V_{X_i}(E_{X_{\sim i}(Y|X_i)}) = \frac{1}{N}\sum_{j=1}^{N} f(B)_j(f(A_B^i)_j - f(A)_j)$ and $E_{X_{\sim i}}(V_{X_i}(Y|X_i)) = \frac{1}{2N}\sum_{j=1}^{N}(f(A)_j - f(A_B^i)_j)^2$. The solution in **Figure A.1** used N=20000 and i=14 (excluding time delays and the basal cAMP rates) and results are shown for the sensitivities across the complete simulation time (excluding small variance values, which are unreliable and insignificant).

A.3.3 Compartment sizes

We conducted simulations using the following compartments for a computational HeLa cell: cytoplasm, plasma membrane, endosome, endosomal membrane, and a nucleoplasm. We assumed that the cell was spherical shaped and used a cytosolic volume of 2000 μm^3 [218]. We assumed the endosomes to be fixed in size during the time course of signaling, with a diameter of 87 nm [71], slightly smaller than the size of a large endosome (100nm). Villasenor *et al.* [219] reported that about 50 endosomes are created after 30 min of $10\frac{ng}{mL}$ EGF stimulation in HeLa

cells. Using this value, we calculated the total endosomal volume to be $0.138\ \mu m^3$ and surface area of $5\ \mu m^2$ using $V = n\frac{4}{3}\pi r^3$ and membrane area by $A = n4\pi r^2$, where n is the final number of endosomes. The different compartment sizes are shown in **Table A.3**.

Table A.3: Sizes of different compartments used within the model

Compartment	size	Notes and References
EC	$5000\ \mu m^3$	-
PM	$1256\ \mu m^2$	[218]
Cytosol	$2000\ \mu m^3$	[218]
Endosome	$0.138\ \mu m^3$	[219], Est.
Endosomal membrane	$5\ \mu m^2$	[219], Est.
Nucleosol	$200\ \mu m^3$	Assumed 10% of Cytosol

A.3.4 Model Kinetics

We conducted simulations for 60 min based on the time course of RTK$\rightarrow$cAMP signaling [42]. We did not account for the regeneration of ATP and PIP$_2$, and assumed that these values are constant and high. We did not include mitogen-activated protein kinase (MAPK) or calcium pathways in this model. This model has 76 kinetic parameters of which 19 are fit and the remainder are taken from the literature. Of the 19 kinetic parameters that were fit, 7 of them affect cAMP dynamics but only 4 change the dynamics of cAMP.

A.3.5 Module 1: EGF Receptor Module

The receptor module captures the key events of

1. Ligand binding and dimerization.

2. Receptor activation and internalization.

3. Receptor endosomal recycling.

4. Receptor $G\alpha_s$-GDP dependent degradation.

This module is based on Shoerberl *et al.* [71] for EGFR activation, internalization, and recycling. Binding of EGFR to scaffolding proteins was not included in this model. $G\alpha_s \cdot$GIV-GDI dependent degradation of EGFR was modeled based on [40]. Although the exact mechanism of $G\alpha_s$-GDP based degradation is unknown, we used a constitutive model to capture the effect of degradation of EGFR by $G\alpha_s$ using a $G\alpha_s$-GDP independent basal rate and a $G\alpha_s$-GDP dependent catalytic rate. In this Module there are 10 reactions, 14 kinetic parameters. Of these, 3 were fit to experimental data (**Figures 2.2**, **A.3**)

Kinetic parameters

The kinetic binding parameters were chosen based on the values given in Schoeberl *et al.* [71], Berkers *et al.* [72], and French *et al.* [73]. The rate of EGF binding to EGFR at the plasma membrane was set through values reported in Berkers *et al.* [72]. The binding rate of endosomal EGF to EGFR was set by the relative ratio of pH=6 and pH=7.4 as shown in French *et al.* [73]. Degradation of EGFR was set through the global parameters k_b, basal degradation, and k_c, $G\alpha_s$-GDP-dependent degradation. The internalization and degradation rates were modified to fit experimental data for receptor internalization as shown in [219, 220] and for experimental data shown in **Figure 2.1E-F**, **A.3**.

A.3.6 Module 2: Transactivation of $G\alpha_i$ by EGFR via GIV-GEF interactions

The GIV-GEF module captures the key events of

1. Activation of GIV through CDK5.

2. GIV·EGFR binding and amplification of receptor signaling events.

3. Formation of EGFR·GIV·Gα_i complex and activation of Gα_i.

The activating step for GIV-GEF is CDK5-mediated phosphorylation of S1674 on GIV [42]. GIV-GEF is then later turned "off" by PKC-θ, which is activated downstream of PLC-γ. Once activated, GIV-GEF binds to EGFR and Gα_i-GDP to assemble the EGFR·GIV·Gα_i complex [41]. Previously published pathways, kinetics and dynamics of CDK5 activation were used to build the model [221–223] (see 'Kinetic parameters' section below). We did not track the dynamics of $\beta\gamma$ in this model. In this Module there are 7 reactions, 14 kinetic parameters. Of these, 4 were fit to experimental data (**Figures 2.2**, **A.3**).

Kinetic parameters

Kinetic parameters were determined through a combination values from the literature and experimental data fitting. Activation of p35 by the receptor (**Table A.5** reaction 12), was determined using rates from Bhalla *et al.* [103] and by fitting simulations to new (cAMP time-course) and previously published experimental data (GIV-GEM IB), **Figure 2.1E-F**, **A.2E-F**, **A.3** , [42]. The rate of p35 degradation was determined based on the known half-life of 20 to 30 min [224] then refit to the GIV-GEF curve, **Figure A.3**. Maximum binding of CDK5 to p35 (**Table A.5** reaction 13), was set to 80% based on published experimental data [221]. Binding of CDK5 to active p35 was assumed to be very rapid. The rate of GIV-GEF activation by CDK5 (**Table A.5** reaction 14), was fit to immunoblotting data [42] (**Figure 2.1E-F**, **A.2E-F**, **A.3**). EGFR$_2$·GIV and EGFR·GIV·Gα_i formation rates were determined by fitting of experimental data using COPASI [225] and using the experimentally determined dissociation constant (K_d) of EGFR·GIV·Gα_i formation [41, 70].

A.3.7 Module 3: Transinhibition of Gα_s by EGFR via GIV-GDI

The GIV-GDI module captures the key events of

1. PLC-γ activation and PIP$_2$ hydrolysis.

2. Enhanced PLC-γ activation through EGFR$_2$·GIV.

3. DAG dependent PKC-θ activity.

4. Termination of GIV-GEF [for Gα_i], and its conversion to GIV-GDI through PKC-θ and reduction of GEF activity.

The action of PKC-θ on GIV was based on prior work [42], which showed that targeted phosphorylation on site S1689 terminates GIV's GEF function, only allowing GDI function to be active. For the purposes of our model, it was assumed that the PLC-γ→PKC-θ axis acts after CDK5, as shown previously [42]. In doing so, the PLC-γ→PKC-θ axis phosphorylates GIV-GEF that is activated by CDK5, but not inactive GIV [42].

In the model, activation of PKC-θ was achieved through the action of PLC-γ. PLC-γ activation was modeled to be a function of both EGFR and EGFR$_2$·GIV; the latter assumption was made based on prior work [41], which showed that GIV enhances EGF triggered PLC-γ signaling. Once active, PLC-γ hydrolyzes PIP$_2$, creating IP$_3$ and DAG [226]; DAG then binds and activates PKC-θ, inducing the localization of the latter to the PM. PKC-θ then phosphorylates GIV-GEF in both the unbound and the receptor bound form. Gα_s·GIV-GDI complex formation and function was based on [40, 42] where it was shown to only act of the GDP form of Gα_s. In this Module there are 11 reactions, 16 kinetic parameters. Of these, 6 were fit to experimental data (**Figures 2.2**, **A.3**).

Kinetic parameters

The initial choice of kinetic parameters were based on the previously published rates for activation of PLC-γ, PIP$_2$, and IP$_3$ degradation [103]. These parameters were then refined by fitting the dynamics of the Gα_s·GIV-GDI complex to immunobloting data [42] (**Figure 2.1E**-**F**, **A.2E**-**F**, **A.3**); the rate of GDI activation through PKC-θ and the rate of formation of the Gα_s·GIV-GDI complex were determined by fitting simulations to immunoblot data (**Figure 2.1E**-**F**, **A.2E**-**F**, **A.3**).

A.3.8   Module 4: Reactions for the production and degradation of cAMP

The cAMP module captures the key events of

1. Inhibition of basal activity of the PM-pool of AC by Gα_i.

2. Activation of endosome-pool of AC by Gα_s.

3. Internalization of AC, Gα_s, Gα_i.

4. Production of cAMP, activation of PKA, and PDE.

In the model, we assumed that AC activation through EGFR occurs only on the endosome [37,222], because we assumed that EGFR is only able to activate G$_s$ proteins on the endosome. Binding of internalized Gα_s-GTP to AC activates and allows increased catalytic activity of AC [227]. The binding of Gα_i to AC was modeled to reflect the inhibition of all AC activity [228]. AC inhibition was allowed to occur on both membranes.

cAMP production by AC was modeled with Michaelis-Menten kinetics [227]. Because cellular ATP is in the millimolar range [229], a large excess compared to the concentrations of the signaling molecules, the concentration of ATP was assumed to be constant. Once four

cAMP molecules bind to the four distinct binding sites on PKA, the quadruple occupancy leads to activation of the catalytic subunit, PKAc, which separates from regulatory subunit [230]. In our model, PKA activation was modeled using a Hill equation [231]. We assumed that PKAc had the same steady state concentration in the nucleosol as the cytosol. PDE activation through PKAc and enzymatic function was based on [227]; cAMP is degraded by PDE. We did not consider any AKAPs or AKIPs because they fall outside the scope of the current model; it possible that their inclusion may impact response strength and timescales. In this Module there are 23 reactions, 14 kinetic parameters. Of these, 3 were fit to experimental data (**Figures 2.2**, **2.3**, and **A.3** were fit to **Figure A.8**).

Kinetic parameters

Previously published activation kinetics of the AC→cAMP→PKA cascade [227] were modified to be closer to observed experimental values [232, 233]. Alousi *et al.* [232] estimated a ratio of Gα_s to AC of greater than 33.3, while Post [233] reported a value of 78.3 in isolated adult rat ventricular myocytes. We therefore chose a ratio of 50 to set our initial values. The binding rates of Gα_s-GTP and Gα_i-GTP to AC were based on values in [227]. Rates of inactivation of Gα_s and Gα_i bound to AC were determined by the GTP hydrolysis activity of AC [234]. Internalization rates of Gα_s and AC were defined as the same parameter, k_{int}, determined through fitting to immunoblot data [42] (**Figure 2.1E**-**F**, **A.2E**-**F**, **A.3**). The kinetic rates governing PKA activity were determined by using steady state dose-response curves to fit a Hill equation (**Figure A.8**) [231], dissociation of cAMP from the regulatory subunits [235], and reformation of the PKA holoenzyme.

A.3.9   Role of additional interactions from CDK5 and PKC-θ to PDE

Previous studies have shown that both CDK5 [236] and PKC-θ [237] influence PDE activation. We modeled interactions of CDK5 and PKC-θ to activation of PDE, leading to further suppression of the cAMP signal; the additional interactions are shown in **Table A.9**. The addition of these interactions did not alter the time course of cAMP production but reduced the amount of cAMP produced **Figure A.9**.

Kinetic parameters

We tested the role of additional PDE activation pathways through CDK5 and PKC-θ [236, 237]; We assumed these interactions would double the maximum PDE concentration based on previously published data [236, 237] that has shown that suppressing the affects of CDK5 and PKC-θ on PDE reduced PDE activity by 1.25 to 1.5-fold.

A.4   Parameter estimation, model access, and additional results

The simulations for the phenomenological network, shown in **Figure 2.1**, were carried out in MATLAB using dde23. The MATLAB files used to generate results can be found in supplementary files under the name GETZ_2019_cAMP.m (**Figure 2.1**) and GETZ_2019_cAMP_timedelay.m (**Figure A.1E**). Code for the variance based sensitivity is GETZ_2019_cAMP_sens.m (**Figure A.1**).

The simulations for the full network, shown in **Figure 2.2**, were carried out in COPASI. The COPASI files used to generate results can be found in supplementary files under the name GETZ_2019_cAMP_full.m (**Figure 2.2**), GETZ_2019_cAMP_full_PM_EM.m (**Figure A.5**), and GETZ_2019_cAMP_full_feedback.m (**Figure A.9**). COPASI (http://copasi.org/) is supported by

National Institutes of Health, NIH (USA) (Grant GM080219 NIGMS), BBSRC (UK) (Grant BB/J019259/1), and BMBF Federal Ministry of Education (Germany). Previous versions of the full model were build in the Virtual Cell [VCell]. The Virtual Cell is supported by NIH Grant Number P41 GM103313 from the National Institute for General Medical Sciences. A detailed protocol/user guide on how to develop models in Virtual Cell has been published elsewhere [106, 238].

A.4.1 Parameter estimation with COPASI

Parameter estimation was originally carried out using COPASI [225] built into the VCell program [106]. Parameter estimation was then expanded into the COPASI environment. Fitting was conducted simultaneously on GIV-GEF(IB), GIV-GDI(IB), cAMP(RIA), EGFR·GIV·Gα_i (IB), and Gα_s·GIV-GDI (PLA) data with respective initial values (IB carries a higher initial GIV concentration due to experimental over expression). The particular estimation method used was evolutionary programming (EP) for 300 generations with a 25 population size using 1 random number generator. This was performed for two runs before results were reported. Evolutionary programming functions as follows: once presented with a optimization problem, i.e. minimizing error between the absolute values of experimental data and simulation data (E=$|y_1 - y_2|$), the algorithm develops a set of potential solutions by varying parameters chosen by the user. At the next "generation" each individual solution produces two "offspring" one of the same solution and one with slight random parameter variations. Therefore, at the end of this generation there are double the number of potential solutions. These are then reduced to the original number of solutions by comparing the error against the other solutions, keeping only the lowest errors and deleting all other solutions. For more information on this method see [239].

A.4.2 EGFR dynamics at the plasma membrane and the endosomal membrane

Module 1 of the reaction network models the dynamics of EGFR at the PM and the endosome (**Figure A.2A**, **Table A.4**). At the PM, EGFR is activated by ligand binding, receptor dimerization, and cross-phosphorylation; activated EGFR is internalized to the early endosome through endocytosis, from where it can be either recycled or degraded [71]. Active PM EGFR also forms a complex with GIV-GEM, and via GIV with $G\alpha_i$, leading to the activation of $G\alpha_i$ [42]. On the other hand, while it remains unclear when and where EGF/EGFR activates $G\alpha_s$, it is known that a pool of GIV that is on endosomes containing internalized EGFR binds and inactivates $G\alpha_s$ on the endosomal membrane. Once inactivated, $G\alpha_s$-GDP enhances the degradation rate of internalized, endosomal EGFR, thereby limiting the pool of receptors available for recycling to the PM and serves to attenuate growth factor signaling [40].

Simulations from the model show that EGFR dynamics is governed by multiple time-scales when ligand stimulation triggers the redistribution of receptors from the PM to different pools (**Figure A.5A**). The PM-pool of active receptors increases rapidly upon ligand stimulation (**Figure A.5A**, red line) and subsequently recruits GIV, forming GIV-GEF·EGFR complexes (**Figure A.5A**, purple line). The endosomal pool of active receptors increases at a slower time scale (**Figure A.5A**, yellow line) than the PM-pool of active receptors. Recycling of the endosomal pool of receptors to the PM leads to a small second burst in the PM pool of receptors around 10 min (**Figure A.5A**, yellow line). These findings are in agreement with Schoeberl et al. [71], indicating that our model accurately captures the EGFR dynamics. The total number of active receptors decreases over time because of $G\alpha_s$-GDP-dependent receptor degradation (**Figure A.5A**, blue line). The pool of receptors in the GIV-GEF·EGFR complex subsequently interact with $G\alpha_i$ at the PM to form the EGFR·GIV·$G\alpha_i$ complex. The effect of kinetic parameters of EGFR dynamics is shown in **Figure A.7A**-**C**and we find that the balance of PM-pool versus

internalized pool of EGFR is closely regulated by both the internalization rate and the $G\alpha_s$-GDP dependent receptor degradation rate [40].

A.4.3 Dynamics of $G\alpha_i$ signaling: activation kinetics are shaped by both upstream EGFR dynamics and downstream PLC-$\gamma\rightarrow$ DAG $\rightarrow$PKC-θ signaling events

We next asked how EGFR dynamics affect the dynamics of $G\alpha_i$ signaling at the PM. Activation of EGFR at the PM triggers a series of downstream events, including the activation of CDK5 at the PM by its cofactor, p35 [240]. CDK5 phosphorylates GIV at Ser(S)1675 and enhances GIV's ability to bind $G\alpha_i$, *i.e.*, CDK5 turns inactive GIV to into active GIV-GEF [74]. This allows GIV to couple $G\alpha_i$ to EGFR by assembling ternary EGFR·GIV·$G\alpha_i$ complexes at the PM [47] and activate $G\alpha_i$ in the vicinity of ligand-activated EGFR (**Module 2** in the model, **Figure A.2A**, **Table A.4**, **A.5**). EGFR also triggers the activation of the PLC-γ-DAG-PKC-θ pathway [241]; PKC-θ phosphorylates GIV at S1689 and terminates GIV GEF activity towards $G\alpha_i$ [102]. Such sequential phosphorylation has another function – it converts GIV that is a GEF for $G\alpha_i$(GIV-GEF) into GIV that now serves as a GDI for $G\alpha_s$(GIV-GDI); GIV-GDI binds and inhibits GDP exchange on $G\alpha_s$ [42].

We asked, how do the CDK5 and the PLC-γ pathways regulate dynamics of the EGFR·GIV·$G\alpha_i$ complex formation, which is the key precursor event essential for transactivation of $G\alpha_i$ by EGF/EGFR [43, 47].

Sensitivity analyses showed that despite the substantial number of model parameters (Tables **A.12** and **A.15**), the formation of the EGFR·GIV·$G\alpha_i$ complex is sensitive only to a few kinetic parameters and initial conditions over time (**Tables A.12** and **A.15**, **Figure A.7**). For example, a ten-fold variation of the forward rate for the binding of GIV-GEF to the activated

receptor (k_f in reaction 15, **Table A.5**) affected the peak values of the complex formation but not the temporal features of the EGFR·GIV·Gα_i complex formation (**Figure A.7D**). Similarly, the activation of the GIV-GEF function by CDK5 (reaction 14, **Table A.5**) affected the density of the complex but not the temporal dynamics (**Figure A.7E**).

The dynamics of the EGFR·GIV·Gα_i complexes, however, were sensitive to the initial concentrations of Gα_i (expected), GIV (expected), Cdk5 (expected), PIP$_2$ (unexpected) and PLC-γ (unexpected) (**Table A.12**). The sensitivity of EGFR·GIV·Gα_i complex formation to PIP$_2$ and PLC-γ likely stems from network cross-talk, because the PLC-γ→DAG→PKC-θ pathway terminates GIV-GEF, triggering the dissociation of GIV and Gα_i, which triggers the disassembly of the EGFR·GIV·Gα_i complexes (**Figures A.2A, A.2B**). Changes in PLC-γ impacted both the density and temporal dynamics of the EGFR·GIV·Gα_i complexes. As expected, when the PLC-γ→DAG→PKC-θ pathway is inhibited, the lifetime of GIV-GEF is prolonged and *vice versa*. This effect is evident when comparing the normalized densities against experiments (**Figure A.7F**).

We conclude that early activation of GIV-GEF, and the observed dynamics of the assembly of EGFR·GIV·Gα_i complexes are not only dependent on the upstream kinetics of EGFR activation, but also on the downstream conversion of GIV-GEF to GIV-GDI, mediated by the PLC-γ→DAG→PKC-θ pathway. Findings also indicate that the connections within the network effectively capture the dynamics of transactivation of Gα_i by EGFR via GIV-GEF.

A.4.4 Dynamics of Gα_s activation is most compatible with delayed activation triggered by internalized EGFR and inactivation by GIV-GEM on endosomes

Although GIV-GDI inhibits the activity of Gα_s-GTP [42], the exact mechanism of Gα_s activation by EGFR is currently unknown. Prior studies have shown that Gα_s is located on early, sorting and recycling endosomes [242] and that upon EGF stimulation, its activation/inactivation on endosomes regulates endosome maturation and EGFR degradation [243]; in cells without Gα_s, or in those expressing a constitutively active mutant Gα_s, internalized EGFR stays longer in endosomes, thereby, prolonging signaling from that compartment [40]. We asked when and where Gα_s is activated. Because compartmentalized EGFR signaling (PM versus endosomes) occurs on different time scales (**Figure A.2A**), and Gα_i and Gα_s have different timescales of activation [5 min and 15 min respectively] [42], we reasoned that computationally predicted dynamics of all three possible scenarios of compartmentalized Gα_s activation *i.e.* [1) exclusively at the PM 2) exclusively at the endosomes; and 3) both at the PM and then on the endosomes (**Figure A.5B**), can provide insights into which option might be in accordance with the actual observed time scales for the same.

In the first scenario, where ligand-activated EGFR triggers Gα_s activation exclusively at the PM, activation is predicted to be rapid with peak concentration at 35 sec, similar to the case of β2-adrenergic receptors peak activity at 15 sec [244] (also see **Figure A.5C**); this kinetic pattern mimics the dynamics of rapid EGFR activation at the PM. In the second scenario, where ligand-activated EGFR triggers Gα_s activation exclusively on endosomal membranes, the time of peak activity is around 15 min (**Figure A.5C**, red line), in accordance with the time scales of Gα_s activation and cAMP production [42]. Finally, if we consider a scenario where ligand-activated EGFR triggers Gα_s activation both at the PM and on endosomes, we observe a first peak of rapid activation at around 35 sec, followed by a second burst at around 15 min. In all three

scenarios, activation of Gα_s [concentration of Gα_s-GTP] was higher in the absence of GIV's GDI activity (i.e., when the concentration of GIV is set to zero; **Figure A.5C**). Based on the dynamics of EGFR at the PM [rapid, almost instantaneous] and on the endosome [approximately 10 min] (**Figure A.5A**) and similar timescales for Gα_s activation observed from the different modes of Gα_s activation (**Figure A.2E**), we predict that Gα_s is likely activated on endosomes.

To validate model predictions, we used a Gα_s conformational biosensor, nanobody Nb37-GFP that binds and helps detect the nucleotide-free intermediate during Gα_s activation [42]. Prior studies have extensively validated this tool and demonstrated its ability to detect Gα_s activation in real time, both at the PM (seen as a burst of signal in the cell periphery) and within early and recycling endoscomes (seen as dynamic punctate vesicles inside cells [82, 245–247]. In control cells, no significant Gα_s activity was detected, neither at the PM, nor on endosomes, neither before, nor after ligand stimulation, indicating that Gα_s is either not activated after EGF stimulation or that its activity is efficiently suppressed by some modulator, presumably GIV, for sustained periods of time. In GIV-depleted cells [80-85% depletion of endogenous GIV by shRNA sequence targeting the 3' UTR [42] **Figure A.2F**], Gα_s activity was easily detected roughly 15 min after ligand stimulation and exclusively on vesicular structures, likely to be endosomes (**Figure A.2F**); no such signal was noted at the PM, which is where canonical activation of Gα_s by GPCR is initiated [42]. These results obtained in live cells using conformation sensitive antibodies reveal a much delayed and compartmentalized pattern of non-canonical cyclical activation/inactivation of G$\alpha_s$downstream of EGF; findings are also consistent with our *in vitro* enzymology assays published previously [42] in that GIV's GDI function normally inhibits Gα_s activity (hence not much fluorescence in control cells, but increased signals in GIV-depleted cells). As for what activates Gα_s downstream of EGF/EGFR, few studies have shown that EGFR binds Gα_s [37, 248] through its juxtamembrane region [249], and that this interaction triggers phosphoactivation of Gα_s [248]. Such transactivation of Gα_s by EGFR in cardiomyocytes is accompanied by augmented AC activation, elevation of cAMP, increased heart rate and contractility [248, 250].

Our model neither proves nor disproves this model for direct transactivation of Gα_s by EGFR, but reveals that activation of Gα_s is delayed and pinpoints endosomes as the site of such activation.

Finally, we evaluated the dynamics of formation of the Gα_s·GIV-GDI complex [**Module 2**; **Figure 2.1F**], the precursor event that is essential for transinhibition of Gα_s by EGF/EGFR [42]. Our model for the dynamics of assembly of Gα_s·GIV-GDI complexes (**Table A.4**, **A.6**, **A.7**) included the kinetics of receptor internalization, Gα_s activation by internalized receptors, conversion of GIV-GEF to GIV-GDI by the PLC-$\gamma$$\rightarrow$DAG$\rightarrow$PKC-$\theta$ pathway, and the Gα_s-GDP-dependent degradation of endosomal EGFR (**Figure A.2A**). Simulations from this model showed a good qualitative agreement between normalized Gα_s·GIV-GDI complex formation between model and cell-based experiments [42].

The role of kinetic parameters and initial conditions affecting the formation of the Gα_s·GIV-GDI complex were explored in detail (**Figure A.7**) and we found that the dynamics of Gα_s·GIV-GDI complex formation is more sensitive to internalization and degradation of EGFR than to any other kinetic parameters. However, our model was unable to capture the precipitous reduction in the normalized concentrations of Gα_s·GIV-GDI complexes at 60 min. We speculate that the discrepancy between model and experiment may stem from the fact that the model is fine-tuned to compute the Gα_s·GIV-GDI complexes that are located exclusively on the endosomes, whereas the experiment assessed Gα_s·GIV-GDI complexes in whole cells (not restricted to the endosomes) by proximity ligand assays (PLA) on endogenous proteins or by GST pulldown assays using cell lysates as source of Gα_s. Experimentally, it is not yet possible to assess specifically the number of cytosolic versus endosomal vs other membrane-localized Gα_s·GIV-GDI complex numbers in living cells responding to EGF. Because Gα_s on endosomes escapes redistribution after ligand stimulation, it has a prolonged half-life to enable sustained signaling from that location [251]. It is possible that the endosomal pool of GIV-GDI has a similarly prolonged half-life, which could explain the unexpectedly high number of complexes

117

predicted at 60 min.

Alternatively, the discrepancy may simply reflect an incompleteness in network modeling. For example, one plausible group of unknown proteins that are missing in our model are down-stream phosphatases that presumably act on GIV-GDI on endosomes, and are responsible for the decline in the number of $G\alpha_s \cdot GIV\text{-}GDI$ complexes at later time points.

Tables

Table A.4: Reactions for **Module 1**, outlining EGFR activation, internalization, and degradation. In this table there are 10 reactions, 14 kinetic parameters. Of these, 3 were fit to experimental data (**Figures 2.2**, **A.3**).

#	Reaction	Reaction flux	Kinetic Parameters	Ref.
1	EGF+EGFR $\leftrightarrow$ EGF·EGFR	k_f[EGF][EGFR] $-$ k_r[EGF-EGFR]	k_f=3 $s^{-1} \cdot \mu M^{-1}$, k_r=0.014 s^{-1}	[71–73]
2	2 EGF·EGFR $\leftrightarrow$ EGF·EGFR$_2$	k_f[EGF·EGFR]$^2 -$ k_r[EGF·EGFR$_2$]	k_f=0.01 $\frac{\mu m^2}{s.molecule}$, k_r=0.1 s^{-1}	[71]
3	EGF·EGFR$_2$ $\leftrightarrow$ EGF·EGFR*$_2$	k_f[EGF·EGFR$_2$] $-k_r$[EGF·EGFR*$_2$]	k_f=1 s^{-1}, k_r=0.01 s^{-1}	[71]
4	EGF·EGFR*$_2$ $\leftrightarrow$ EGF·EGFR*$_{2i}$	k_f[EGF·EGFR$_2$]	k_f=0.002 s^{-1}	[71, 219, 220]
5	EGF$_i$+EGFR$_i$ $\rightarrow$ EGF·EGFR$_i$	k_f[EGF$_i$][EGFR$_i$] $-k_r$[EGF·EGFR$_{2i}$]	k_f=0.14 $s^{-1} \cdot \mu M^{-1}$, k_r=0.0195 s^{-1}	[71–73]
6	2 EGF·EGFR$_i$ $\rightarrow$ EGF·EGFR$_{2i}$	k_f[EGF·EGFR$_i$]$^2 -$ k_r[EGF·EGFR$_i$]	**k_f=1x10$^{-20}\frac{\mu m^2}{s.molecule}$**, k_r=0.1 s^{-1}	[71]
7	EGF·EGFR$_{2i}$ $\rightarrow$ EGF·EGFR*$_{2i}$	k_f[EGF·EGFR$_{2i}$] $-k_r$[EGF·EGFR*$_{2i}$]	k_f=1 s^{-1}, k_r=0.01 s^{-1}	[71]
8	EGFR$_i$ $\rightarrow$ EGFR	k_f[EGFR$_i$] $- k_r$[EGFR]	k_f=0.005 s^{-1}, k_r=5x10^{-5} s^{-1}	[71]
9	EGF·EGFR*$_{2i}$ $\rightarrow$	$(k_{base} + k_c$[G$_s$-GDP$_i$ +Gα_s·GIV-GDI])$*$[EGF·EGFR$_{2i}$]	**k_{base}=1.1x10^{-8} s^{-1}**, **k_c=2.2x10$^{-7}\frac{\mu m^2}{s.molecule}$**	[40, 71, 219] [1]
10	EGF$_i$ $\rightarrow$ EGF$_{deg}$	$(k_{base} + k_c$[G$_s$-GDP$_i$ +Gα_s·GIV-GDI])$*$[EGF$_i$]	**k_{base}=1.1x10^{-8} s^{-1}**, **k_c=2.2x10$^{-7}\frac{\mu m^2}{s.molecule}$**	[71]

---

[1]This reaction occurs on all EGFR species on the endosome.

Table A.5: Reactions for **Module 2**, outlining protein-protein interactions leading to the transactivation of $G\alpha_i$ by EGFR via GIV-GEF. In this table there are 7 reactions, 14 kinetic parameters. Of these, 5 were fit to experimental data (**Figures 2.2**, **A.3**).

#	Reaction	Reaction flux	Kinetic Parameters	Ref.
11	p35 $\rightarrow$ p35*	$\frac{k_{cat}[\text{EGF-EGFR}_2][p35]}{K_M+[p35]} - k_r[\text{p35*}]$	K_M=957$\frac{molecule}{\mu m^2}$, k_{cat}=0.1 s^{-1}, k_r=0.001 s^{-1}	[98, 224]
12	p35*+CDK5 $\rightarrow$ CDK5*	$k_f[\text{p35*}][\text{cdk5}] - k_r[\text{cdk5*}]$	k_f=45 $\mu M^{-1}\cdot s^{-1}$, k_r=10 s^{-1}	[221, 222]
13	GIV $\rightarrow$ GIV-GEF	$\frac{k_{cat}[\text{CDK5*}][\text{GIV}]}{K_M+[GIV]} -k_r[\text{GIV-GEF}]$	K_M=6 μM, **k_{cat}=0.6** s^{-1}, **k_r=0.006** s^{-1}	Est.[1], [221]
14	GIV-GEF + EGF·EGFR*$_2$ $\leftrightarrow$ EGFR$_2$·GIV	$k_f[\text{GIV-GEF}][\text{EGF·EGFR*}_2]$ $k_r[\text{EGFR}_2\cdot\text{GIV}]$	**k_f=0.0015** $\mu M^{-1}\cdot s^{-1}$ **k_r=1.1x10^{-7}** s^{-1}	[41]
15	$G\alpha_i$-GDP + EGFR$_2$·GIV $\leftrightarrow$ EGFR$_2$·GIV·$G\alpha_i$	$k_f[\text{EGFR}_2\cdot\text{GIV}][G\alpha_i\text{-GDP}] - k_r[\text{EGFR}_2\cdot\text{GIV}\cdot G\alpha_i]$	k_f=5 $\frac{\mu m^2}{s.molecule}$, k_r=1150 s^{-1}, (K_d=0.24 μM)	[70]
16	EGFR$_2$·GIV·$G\alpha_i$ $\rightarrow$ $G\alpha_i$-GTP +EGFR$_2$·GIV	$k_f[\text{EGFR}_2\cdot\text{GIV}\cdot G\alpha_i]$	**k_f=14.5** s^{-1}	[103]
17	$G\alpha_i$-GTP $\rightarrow$ $G\alpha_i$-GDP	$k_f[G\alpha_i\text{-GTP}]$	k_f=0.139 s^{-1}	[234]

---

[1]Using experimental CDK5 activities [221], an initial guess was used for the rate, and then refined through fitting simulations to experimental data.

[2]Internalization rates were found by fitting simulations to experimental data.

Table A.6: Reactions for **Module 3**, outlining protein-protein interactions leading to the transibhibition of Gα_s by EGFR via GIV-GDI activation. In this table there are 11 reactions, 16 kinetic parameters. Of these, 5 were fit to experimental data (**Figures 2.2**, **A.3**).

#	Reaction	Reaction flux	Kinetic Parameters	Ref.
18	PLC-γ* → PLC-γ	k_f[PLC-γ*]	k_f=3.8x10^{-4} s^{-1}	[98][1]
19	PLC-γ → PLC-γ*	$\frac{k_{cat}[\text{EGFR}_2 \cdot \text{GIV}][\text{PLC-γ}]}{K_M+[\text{PLC-γ}]}$	k_{cat}=0.1 s^{-1}, K_M=1 μM	[41, 98].[2]
20	PIP2 → IP3+DAG	$\frac{k_{cat}[\text{PLC-γ*}][\text{PIP2}]}{K_M+[PIP2]}$	k_{cat}=14 $\frac{molecule}{\mu m^2 \cdot \mu M.s}$, K_M=5000 $\frac{molecule}{\mu m^2}$	[103]
21	IP3 → Inositol	k_f[IP3]	k_f=2.5 s^{-1}	[103]
22	PKC-θ+DAG → PKC-θ*	k_f[PKC-θ][DAG] $-k_r$[PKC-θ*]	k_f=0.1 $\mu M^{-1} \cdot s^{-1}$, k_r=1x10^{-5} s^{-1}	[252, 253]
23	DAG → DAG$_{deg}$	k_f[DAG]	**k_f=6.7 x 10^{-4} s^{-1}**	[253]
24	PKC-θ* → PKC-θ + DAG$_{deg}$	k_f[PKC-θ*]	k_f=0.028 s^{-1}	[253] Est.[3]
25	EGFR$_2$·GIV→ GIV-GDI + EGF-EGFR*$_2$	$\frac{k_{cat}[\text{PKC-θ}][\text{EGFR}_2 \cdot \text{GIV}]}{K_M+\text{EGFR}_2 \cdot \text{GIV}}$	**k_{cat}=2.5 s^{-1},** **K_M=35 $\frac{molecule}{\mu m^2}$**	[103]
26	GIV-GEF → GIV-GDI	$\frac{k_{cat}[\text{PKC-θ}][\text{GIV-GEF}]}{K_M+[GIV-GEF]}$	**k_{cat}=1 s^{-1}**, K_M=6 μM	[103]
27	GIV-GDI → GIV	k_f[GIV-GDI]	**k_f=0.0011 s^{-1}**	Est.[1]
28	GIV$_{89p}$ → GIV	k_f[GIV$_{89p}$]	k_f=0.01 s^{-1}	Est.

---

[1]Degradation rate set to assumed 30 min half life, assumed no activation through EGFR

[2]assumed to be a generic rate of 0.1 s^{-1} and 1μM

[3]Degradation rate of DAG assumed 10x faster when bound to PKC-θ, values were fit using a 10x faster rate as a starting point.

Table A.7: Reactions for **Module 4**, outlining reactions for the activation and inhibition of cAMP. In these tables there are 23 reactions, 14 kinetic parameters. Of these, 6 were fit to experimental data (**Figures 2.2**, **A.3**), and 3 were fit to **Figure A.8**.

#	Reaction	Reaction flux	Kinetic Parameters	Ref.
29	AC$\leftrightarrow$ AC$_i$	k_f[AC] -k_r[AC$_i$]	k_{fint}=4.6x10^{-5} s^{-1} k_{rint}=8.8x10^{-5} s^{-1}	Est.[1]
30	AC+Gα_i-GTP $\rightarrow$ AC$_{inactive}$	k_f[AC][Gα_i-GTP]	k_f=0.523 $\frac{\mu m^2}{s.molecule}$	[227, 228]
31	AC$_{inactive}$ $\rightarrow$ AC+Gαi-GDP	k_f[AC$_{inactive}$]	k_f=0.1667 s^{-1}	[234][2]
32	Gα_s-GDP-$\beta\gamma$ $\rightarrow$ Gα_s-GDP-$\beta\gamma_i$	k_f[Gα_s-GDP-$\beta\gamma$] -k_r[Gα_s-GDP-$\beta\gamma_i$]	**k$_{fint}$=4.6x10^{-5} s^{-1}** **k$_{rint}$=8.8x10^{-5} s^{-1}**	[98] Est.[1]
33	Gα_s-GDP-$\beta\gamma_i$ $\rightarrow$ Gα_s-GTP$_i$+$\beta\gamma_i$	$\frac{k_{cat}[\text{EGF-EGFR*}_{2i}][\text{G}\alpha\text{s-GDP-}\beta\gamma_i]}{K_M+[\text{G}\alpha\text{s-GDP-}\beta\gamma_i]}$	**k$_{cat}$=0.4 s^{-1},** K_M=3000 $\frac{molecule}{\mu m^2}$	[98] Est.[3]
34	Gα_s-GDP$_i$ +GIV-GDI $\leftrightarrow$ Gα_s-GDP-GDI	k_f[Gα_s-GDP][GIV-GDI] $-$ k_r[Gα_s-GDP-GDI]	**k$_f$=2.9 $\mu M^{-1} \cdot s^{-1}$,** **k$_r$=0.0015 s^{-1}**	[254] Est.[1]
35	Gα_s-GDP$_i$ +GIV $\leftrightarrow$ Gα_s-GDP-GDI	k_f[Gα_s-GDP][GIV-GDI] $-$ k_r[Gα_s-GDP-GDI]	k_f=2.9*0.05 $\mu M^{-1} \cdot s^{-1}$, k_r=0.0015 s^{-1}	[254] [1]
36	Gαs-GTP$_i$ $\rightarrow$ Gαs-GDP$_i$	k_f[Gαs-GTP$_i$]	k_f=0.139 s^{-1}	[227]
37	$\rightarrow$ I, Gα_s-GDP-GDI$\rightarrow$	k_f[Gα_s-GDP-GDI+Gα_s-GDP$_i$],**k$_I$=4.3x10^7 s^{-1}** [I][Gα_s-GDP-GDI]		Est[4]
38	Gαs-GDP$_i$ + $\beta\gamma_i$ $\rightarrow$ Gαs-GDP-$\beta\gamma_i$	k_f[Gαs-GDP][$\beta\gamma$]	k_f=0.00148 $\frac{\mu m^2}{s.molecule}$	[227]
39	AC$_i$ + Gαs-GTP $\rightarrow$ AC*	k_f[Gαs-GTP][AC]	k_f=0.0021 $\frac{\mu m^2}{s.molecule}$	[227]

---

[1]Rate found through immunoblot data fitting; unphosphorylated state set to GDI binding rates(#34) with ratio of activities.

[2]set at the same rate of Gα_s GAP activity.

[3]set with immunoblot data fitting around values used in [98], after converting units to surface density.

[4]Assumed an integral degradation of the Gα_s·GIV-GDI complex to recover the 60 minute experimental time point, The exact action is unknown.

#	Reaction	Reaction flux	Kinetic Parameters	Ref.
40	AC* $\to$ AC$_i$ + Gαs-GDP	$k_f[\text{AC*}]$	k_f=0.1667 s^{-1}	[234]
41	ATP $\to$ cAMP	$\frac{k_{cat}([\text{AC}]+\kappa[\text{AC}_i])[\text{ATP}]}{K_M+[\text{ATP}]}$	k_{cat}=0.12 s^{-1}, K_M=1030 μM, κ=0.004	[227][1]
42	ATP $\to$ cAMP	$\frac{k_{cat}[\text{AC*}][\text{ATP}]}{K_M+[\text{ATP}]}$	k_{cat}=13 s^{-1}, K_M=315 μM	[227, 232]
43	cAMP $\to$ AMP	$\frac{k_{cat}[\text{PDE}][\text{cAMP}]}{K_M+[\text{cAMP}]}$	k_{cat}=2 s^{-1}, K_M=1.51 μM	[227]
44	4cAMP + R$_2$C$_2$ $\to$ 2PKA + R$_2$	$\frac{k_{cat}[\text{R}_2\text{C}_2][\text{cAMP}]^{1.75}}{K_M^{1.75}+[\text{cAMP}]^{1.75}}$	**k$_{cat}$=0.05** s^{-1}, **K$_M$=0.54** μM	[231, 255]
45	R$_2$ $\to$ R$_2$u + 2cAMP	$k_f[\text{R}_2]$	k_f=0.0167 s^{-1}	[235]
46	R$_2$u $\to$ R$_2$uu + 2cAMP	$k_f[\text{R}_2\text{u}]$	k_f=2.78 x 10^{-4} s^{-1}	[235]
47	R$_2$uu + 2PKA $\to$ R$_2$C$_2$	$k_f[\text{R}_2\text{uu}][\text{PKA}]^2$	**k$_f$=10** $\mu M^{-2} \cdot s^{-1}$	Est.[2]
48	PDE $\to$ PDE*	$\frac{k_{cat}[\text{PKA}][\text{PDE}]}{K_M+[\text{PDE}]}$	k_{cat}=5 s^{-1}, K_M=0.5μM	[227]
49	PKA $\leftrightarrow$ PKA$_{inact}$	$k_f[\text{PKA}]-k_r[\text{PKA}_{inact}]$	k_f=1x10^{-4} s^{-1}, k_r=1 s^{-1}	[103]
50	cAMP $\to$ AMP	$\frac{k_{cat}[\text{PDE*}][\text{cAMP}]}{K_M+[\text{cAMP}]}$	K_M=1.26 μM, k_{cat}=5 s^{-1}	[227]
51	PDE* $\to$ PDE	$\frac{k_{cat}[\text{PP-PDE}][\text{PDE*}]}{K_M+[\text{PDE*}]}$	K_M=8 μM, k_{cat}=5 s^{-1}	[227]

---

[1]κ is the conversion factor from PM to EM

[2]Rate was determined through fitting steady state responses to a Hill function, see **Figure A.8**

[3]Rates were set to preserve the expected longer timescale events

Table A.9: Reactions for the additional interactions modeling the effect of PKA and CDK5 phosphorylation of PDE.

#	Reaction	Reaction flux	Kinetic Parameters	Reference
52	PDE → PDE*	$\frac{k_{cat}[\text{PKC}\theta*][\text{PDE}]}{K_M+[\text{PDE}]}$	K_M=0.89 μM, k_{cat}=15 s^{-1}	[237]
53	PDE → PDE*	$\frac{k_{cat}[\text{CDK}*][\text{PDE}]}{K_M+[\text{PDE}]}$	K_M=0.5 μM, k_{cat}=1 s^{-1}	[236]

Table A.10: Reactions for rapid production of cAMP at the PM (blue line in **Figure A.5**) using the dynamics shown in [81].

#	Reaction	Reaction flux	Kinetic Parameters	Ref.
54	Gα_s-GDP-$\beta\gamma_i$ → Gα_s-GTP + $\beta\gamma$	$\frac{k_{cat}[\text{EGF-EGFR}*_2+\text{EGFR}_2\cdot\text{GIV}][\text{G}\alpha_s\text{-GDP-}\beta\gamma_i]}{K_M+[\text{G}\alpha_s\text{-GDP-}\beta\gamma_i]}$	K_M=3000 $\frac{molecule}{\mu m^2}$, k_{cat}=0.4 s^{-1}	Est.[1]
55	AC+Gα_s-GTP→ AC*	$k_f[\text{AC}][\text{G}\alpha_s\text{-GTP}]$	k_f=0.525 $\frac{\mu m^2}{s.molecule}$	[227]
56	AC*→ AC+Gα_s-GDP	$k_f[\text{AC}*]$	k_f=0.1667 s^{-1}	[227]
57	Gα_s-GTP→ Gα_s-GDP	$k_f[\text{G}\alpha_s\text{-GTP}]$	k_f=0.139 s^{-1}	[227]
58	Gα_s-GDP+$\beta\gamma$ → Gα_s-GDP-$\beta\gamma_i$	$k_f[\text{G}\alpha_s\text{-GDP}][\beta\gamma]$	k_f=0.125 $\frac{\mu m^2}{molecules.s}$	[227]
59	Gα_s-GDP+GIV-GDI → Gα_s·GDI	$k_f[\text{G}\alpha_s\text{-GDP}][\text{GIV-GDI}]-k_r[\text{G}\alpha_s\cdot\text{GDI}]$	k_f=2.9 $\mu M^{-1}\cdot s^{-1}$, k_r=0.0015 s^{-1}	[227]
60	ATP → cAMP	$\frac{k_{cat}[\text{AC}*][\text{ATP}]}{K_M+[\text{ATP}]}$	K_M=315 μM, k_{cat}=13 s^{-1}	[227]

---

[1]rates were set the same on PM as on Endosomal Membrane

Table A.11: Initial conditions for components (components not listed have zero initial conditions)

Species	Initial concentration	Compartment	Notes and References
EGFR	240 molecule.μm^{-2}	PM	[218, 256]
EGF	0.05 μM	EC	Experiment stimulation
PLC-γ	0.1 μM	Cytosol	Assumed
PKC-θ	0.1 μM	Cytosol	Assumed
ATP	5000 μM	Cytosol	[227]
cAMP	0.0045 μM	Cytosol	basal SS[1]
PKA	0.0066 μM	Cytosol	basal SS[1]
PDE	0.345 μM	Cytosol	basal SS[1]
R2C2	0.0967 μM	Cytosol	basal SS[1]
AMP	1000 μM	Cytosol	[227]
PDEp	0.055 μM	Cytosol	basal SS[1]
PPPDE	0.2 μM	Cytosol	Assumed
GIV	0.831 μM	Cytosol	Set such that GIV$_{total}$ = 1 μM
GIV-GEF	0.05 μM	Cytosol	Assumed; immunoblot values
GIV$_{89p}$	0.1 μM	Cytosol	Assumed; GDI initial form
Gs-GDI$_b$	786 molecule.μm^{-2}	Edosomal membrane	Assumed
CDK5	0.05 μM	Cytosol	Assumed; [221]
R2	6x10^{-5} μM	Cytosol	basal SS[1]
R2u	0.004 μM	Cytosol	basal SS[1]
R2uu	0.0025 μM	Cytosol	basal SS[1]
p35	957 molecule.μm^{-2}	PM	Set such that p35$_{total}$ = 1 μM
Gα$_i$-GDP	48 molecule.μm^{-2}	PM	Set to exp. immunoblot value.
AC	30 molecule.μm^{-2}	PM	Average of [227] and [232]
PIP2	9570 molecule.μm^{-2}	PM	Assumed
EGFR·GIV·Gα$_i$	0.01 molecule.μm^{-2}	PM	experimental immunoblot value
Gα$_s$-GDP-βγ	1500 molecule.μm^{-2}	PM	Calculated from AC to Gα$_s$ ratio [233]
Gα$_s$·GIV-GDI	75 molecule.μm^{-2}	Endosomal membrane	experimental immunoblot value

---

[1] All basal steady sates are set by running basal AC stimulation until a stable response was received.

Table A.12: Local sensitivity analysis of EGFR·GIV·Gα_i complex with respect to initial conditions. The colors indicate the sensitivity to the respective parameter; red indicates that the EGFR·GIV·Gα_i complex is sensitive to changes in the initial concentration of the corresponding parameter (i.e. sensitivity index greater than 1) and blue indicates that the EGFR·GIV·Gα_i complex is partially sensitive to changes in the initial concentration of the corresponding parameter (i.e. sensitivity index greater than 0.5) over the time course of signaling. Sensitivity is shown at 5, 15, 30, and 60 min intervals.

Initial Parameter	5 min	15 min	30 min	60 min
G$_{\alpha i}$-GDP				7.3312
PLC-γ		0.78	0.89	1.15

Table A.13: Local sensitivity analysis of Gα_s·GIV-GDI complex with respect to initial conditions. The colors indicate the sensitivity to the respective parameter; red indicates that cAMP is sensitive to changes in the initial concentration of the corresponding parameter (i.e. sensitivity index greater than 1) and blue indicates that Gα_s·GIV-GDIis partially sensitive to changes in the initial concentration of the corresponding parameter (i.e. sensitivity index greater than 0.5) over the time course of signaling. Sensitivity is shown at 5, 15, 30, and 60 min intervals.

Initial Parameter	5 min	15 min	30 min	60 min
Cdk5	1.18	0.7		
GIV	1.15	0.76		
PLC-γ	0.89			
PKC	0.66			

Table A.14: Local sensitivity analysis of cAMP with respect to initial conditions. The colors indicate the sensitivity to the respective parameter; red indicates that cAMP is sensitive to changes in the initial concentration of the corresponding parameter (i.e. sensitivity index greater than 1) and blue indicates that cAMP is partially sensitive to changes in the initial concentration of the corresponding parameter (i.e. sensitivity index greater than 0.5) over the time course of signaling. Sensitivity is shown at 5, 15, 30, and 60 min intervals.

Initial Parameter	5 min	15 min	30 min	60 min
AC	329	376	512	1980
PDE	0.78	0.74	0.6	0.54

Table A.15: Local sensitivity analysis of EGFR·GIV·Gα$_i$ complex with respect to the model kinetic parameters. The colors indicate the sensitivity to the respective parameter; red indicates that the EGFR·GIV·Gα$_i$ complex is sensitive to changes in the value of the corresponding parameter (i.e. sensitivity index greater than 1) and blue indicates that the EGFR·GIV·Gα$_i$ complex is partially sensitive to changes in the value of the corresponding parameter (i.e. sensitivity index greater than 0.5) over the time course of signaling. Sensitivity is shown at 5, 15, 30, and 60 min intervals. The index in the square brackets refer to the reaction number.

Parameter[reaction]	5 min	15 min	30 min	60 min
k_f[R31]	0.7			
k_f[R16]	0.6			
k_f[R24]		0.84	1	0.87
k_{cat}[R25]		0.76	0.64	1.03
k_{cat}[R19]		0.72	0.77	1.29
k_m[R19]		0.66	0.71	0.82
k_f[R4]		0.63	2.44	7.44
k_m[R20]				7.88
k_m[R25]				4.33
k_r[R11]				0.96
k_r[R1]				0.61
k_r[R12]				0.54
k_r[R3]				0.53
k_r[R13]				0.53

Table A.16: Local sensitivity analysis of Gα$_s$·GIV-GDI complex with respect to the model kinetic parameters. The colors indicate the sensitivity to the respective parameter; red indicates that the Gα$_s$·GIV-GDI complex is sensitive to changes in the value of the corresponding parameter (i.e. sensitivity index greater than 1) and blue indicates that the Gα$_s$·GIV-GDI complex is partially sensitive to changes in the value of the corresponding parameter (i.e. sensitivity index greater than 0.5) over the time course of signaling. Sensitivity is shown at 5, 15, 30, and 60 min intervals. The index in the square brackets refer to the reaction number.

Parameter[reaction]	5 min	15 min	30 min	60 min
k_I[R37]				1.08
k_f[R4]				0.7
k_{cat}[R13]	1.23	0.71		
k_m[R13]	1.09	0.63		
k_f[R35]	0.95	0.58		
k_f[R38]	0.92	0.58		
k_{cat}[R26]	0.84	0.52		
k_r[R13]		0.51		
k_f[R14]	1.02			
k_f[R36]	0.9			
k_{cat}[R19]	0.87			
k_m[R26]	0.8			
k_m[R19]	0.79			
k_f[R24]	0.65			
k_f[R13]	0.6			
k_f[R24]	0.59			

Table A.17: Local sensitivity analysis of cAMP with respect to the model kinetic parameters. The colors indicate the sensitivity to the respective parameter; red indicates that the cAMP production is sensitive to changes in the value of the corresponding parameter (i.e. sensitivity index greater than 1) and blue indicates that cAMP production is partially sensitive to changes in the value of the corresponding parameter (i.e. sensitivity index greater than 0.5) over the time course of signaling. Sensitivity is shown at 5, 15, 30, and 60 min intervals. The index in the square brackets refer to the reaction number.

Parameter[reaction]	5 min	15 min	30 min	60 min
k_{fint}	1.04	0.64		
k_{cat}[R41]	0.88	0.57	0.5	
k_f[R30]	0.78	0.64		
k_f[R16]	0.71	0.6		
k_f[R14]	0.67			
k_{cat}[R43]	0.67	0.57		
k_m[R43]	0.67	0.64		
k_m[R25]		0.53		
h[R44]			0.93	1.27
k_f[R4]				0.69

Table A.18: Local sensitivity analysis of components with respect to the model compartment sizes. The colors indicate the sensitivity to the respective parameter; red indicates that the cAMP production is sensitive to changes in the value of the corresponding parameter (i.e. sensitivity index greater than 1) and blue indicates that cAMP production is partially sensitive to changes in the value of the corresponding parameter (i.e. sensitivity index greater than 0.5) over the time course of signaling. Sensitivity is shown at 5, 15, 30, and 60 min intervals. The index in the square brackets refer to the reaction number.

Component[Compartment]	5 min	15 min	30 min	60 min
cAMP[PM]		0.71		
$G\alpha_s$·GIV-GDI[PM]	2.44	1.54	0.7	
$G\alpha_s$·GIV-GDI[Cyto]	1.25	0.85		

A.5   Supplementary Figures
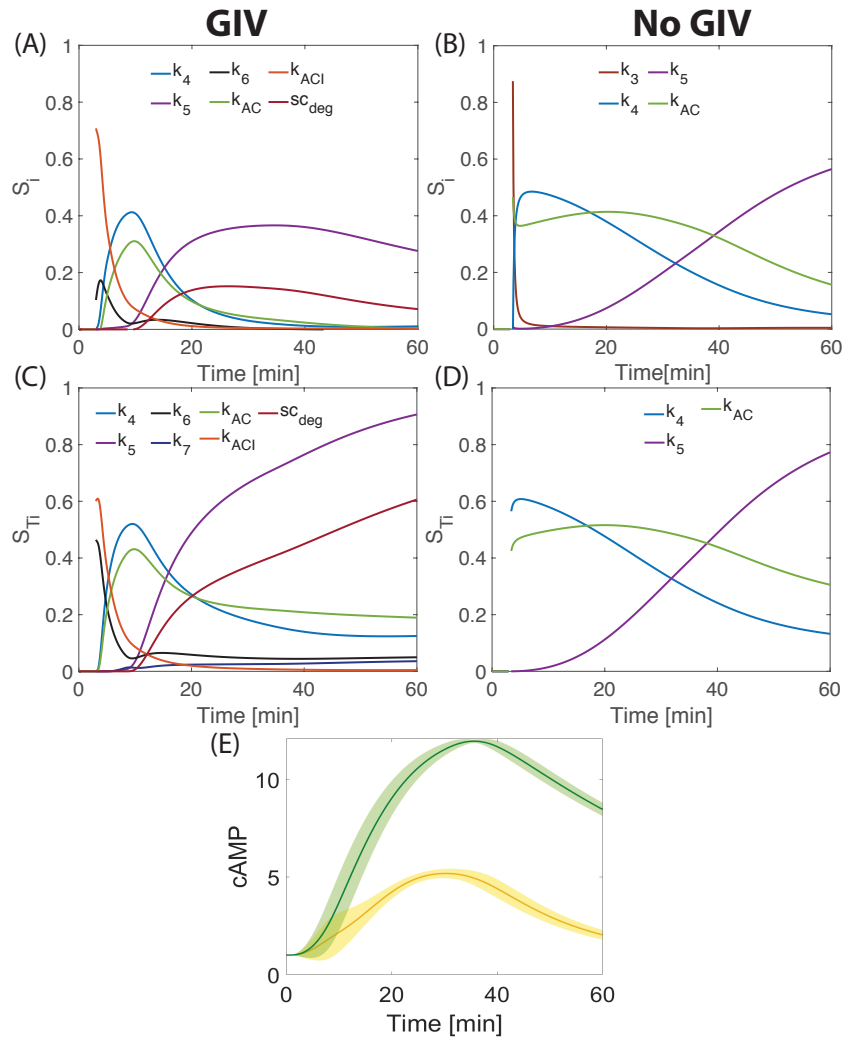
Figure A.1: **(Supplementary to Figure 2.1):** **(A-B)** Sensitivities of the phenomenological model across time through the variance based sensitivity analysis. Reported sensitivities are shown for both the GIV (**A**) and no GIV (**B**) cases. In both the GIV and no GIV cases the highest order sensitivities are shown to always include the degradation and internalization. But, the presence of GIV lowers the AC contribution in the late time scales. (**C-D**) Total sensitivities of each parameters show the same trend with even higher contributions for both internalization and degradation. Thus, it can be determined that the internalization and degradation rates are key parameters that the system is sensitive to, especially at later times. (**E**) Variations of the τ delays were performed and the normal distributions of the cAMP profile are reported for the no GIV (green) and GIV (yellow) conditions.
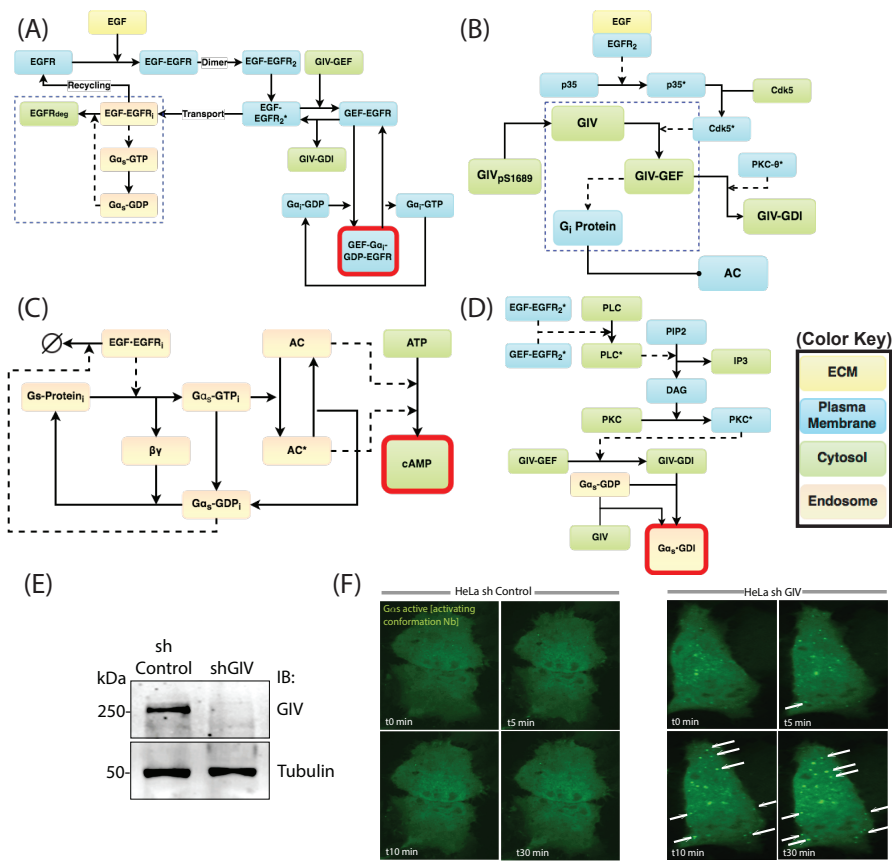
Figure A.2: (**Supplementary to Figure 2.2**): (**A**) Network module showing the interactions of Gα_s and Gα_i with GIV at the PM and the endosome membrane. (**B**) A reaction network model showing the different signaling nodes and connections from EGFR to the AC signaling axis. Solid lines indicate a binding interaction; interrupted lines indicate enzymatic reaction. (**C**) Network showing receptor interactions with feedback from Gα_s-GDP whose presence on endosomes accelerates receptor degradation due to rapid endosomal maturation [40].(**D**) Network module showing the activation of GIV-GDI and binding of Gα_s with GIV at the the endosome membrane. For all networks, the color key (right, boxed) denotes the different compartments in which the components reside.(**E**) Equal aliquots of lysates of Hela cells used in (**E**) were analyzed for GIV depletion by immunoblotting(IB). Band densitometry confirmed > 95% depletion of GIV. (**F**) Freeze-frame images from live cell movies showing the dynamics of G$\alpha_s$activation in response to EGF, as determined by a biosensor that binds and helps detect the nucleotide-free intermediate during Gα_s activation [42]. Control (shControl) and GIV-depleted (shGIV) Hela cells expressing GFP-tagged anti-Gα_s·GTP conformational biosensor, nanobody Nb37-GFP were serum starved overnight and stimulated with 50 nM EGF and analyzed by live cell imaging using a Leica scanning disk microscope for 20 min. Freeze frames from representative cells are shown. In the presence of GIV (shControl) little or no Gα_s activity was seen after EGF stimulation; however, in GIV-depleted cells, Gα_s activity was seen on vesicular structures, likely to be endosomes (arrowheads; see Supplementary Movies 1-2). Bright puncta = active Gα_s on endocytic vesicles and/or endosomes. Bar = 10 μm.
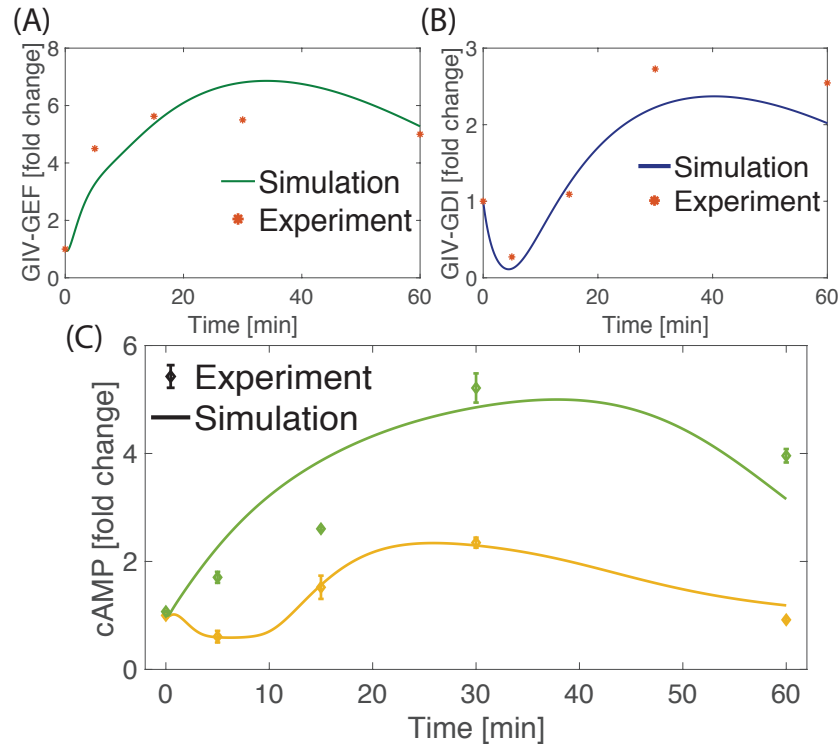
Figure A.3: (**Supplementary to Figure 2.2**): **Parameter estimation and validation of the cAMP, and cytosolic GEF and GDI concentrations concentration.** (**A-B**) Comparison of simulation and experimental data for GIV-GEF and GIV-GDI. The concentration of GIV-GEF and GIV-GDI was normalized to its peak value and compared against experimental data (*). Experimental data were obtained from Figures 1D and S1 of [42], in which protein-protein interaction assays were performed using lysates of cells responding to EGF. (**C**) Comparison of cAMP time course from simulations and experiments. Simulations of dynamics of the production of cAMP based on the network modules was performed. The concentration of cAMP was normalized to its initial value and compared experimental data in which control or GIV-depleted (shGIV) HeLA cells were serum starved (0.2% FBD, 16h) prior to stimulation with 50nM EGF for the indicated time points. cAMP produced in response to EGF was measured by radioimmunoassay (RIA) as detailed in the main text 'Materials and method' section. Error bars indicated mean S.D of three independent experiments. ns= not significant; **p=0.01,****p=0.0001. cAMP was normalized against the initial value to ensure the pre-stimulation steady state concentrations of cAMP are satisfied.
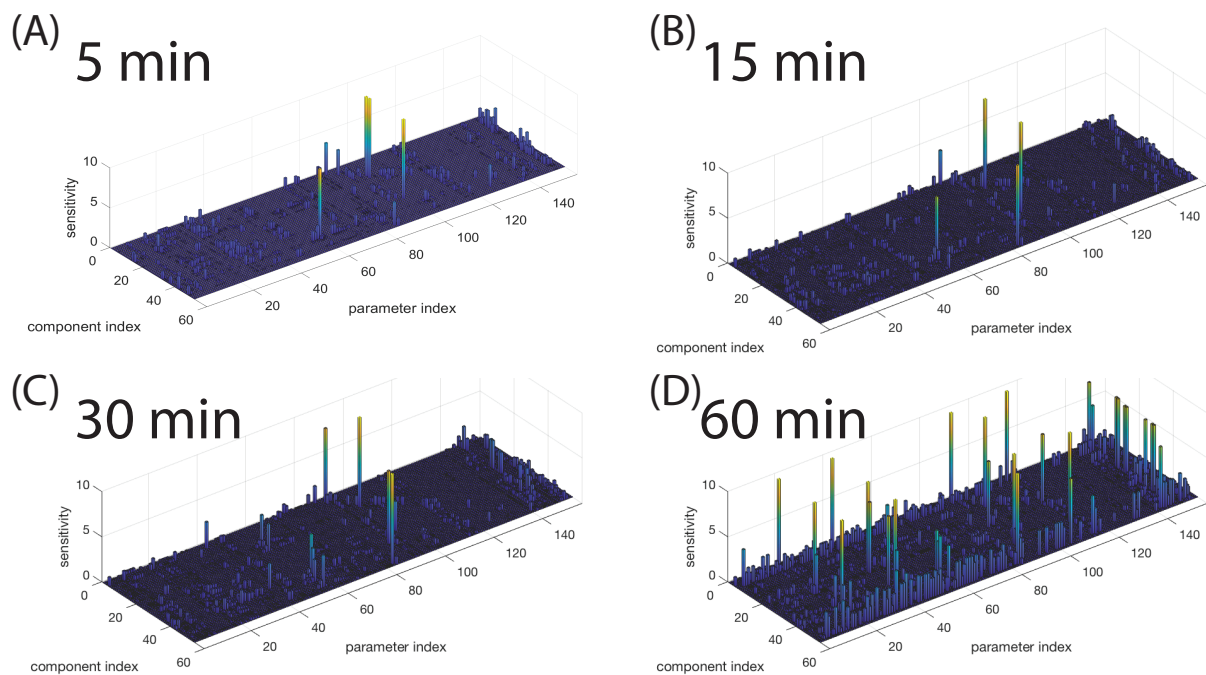
Figure A.4: **(Supplementary to Figure 2.2): Sensitivities of all components in the model.** Parameter sensitives taken at 5(**A**), 15(**B**), 30(**C**), and 60 min(**D**), (see supplementary file indexnumbers.csv) for index numbers. See **Tables A.12**, **A.15**, **A.13**, **A.16**, **A.14**, **A.17**, **A.18** for the sensitivities of the fitting components against sensitive parameters.
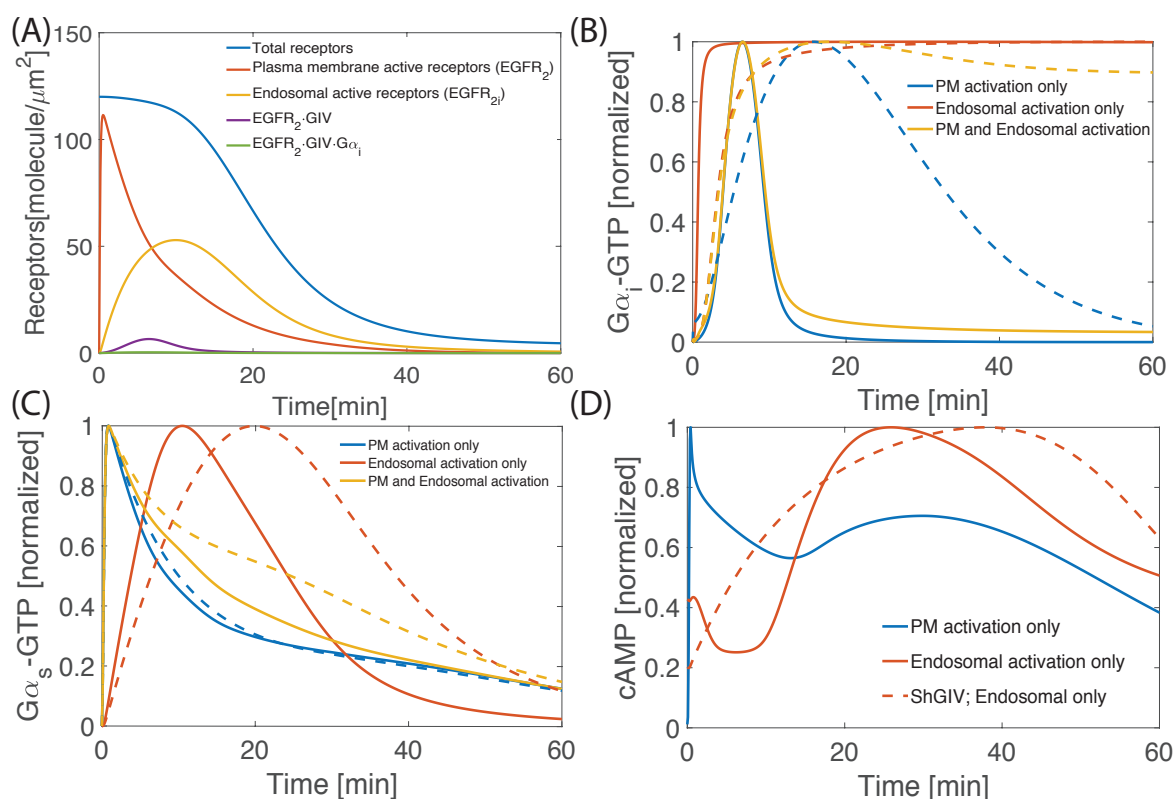
Figure A.5: (**Supplementary to Figure 2.2**): (**A**) Graphs display the dynamics of different pools of EGFR over 1 hour as determined by simulations. EGFR dimer dynamics at the PM (red line), at the endosome (yellow line), bound to GIV-GEF (purple line), and in the EGFR·GIV·Gα_i complex (green line) are shown. The total number of dimerized receptors (blue line) decreases over time due to receptor degradation. (**B**) Simulations conducted for the module shown in **A** shows that Gα_i-GTP dynamics at the PM are unaffected by the compartment in which Gα_s-GTP is activated. (**C**) Simulations conducted for the module shown in **A** comparing the dynamics of Gα_s activation in response to growth factor stimulation in 3 compartmental settings [see color key] and in the presence [solid lines] or absence [interrupted] of GIV. Activation of Gα_s at the PM alone is predicted to have a rapid activation and inactivation kinetics, while Gα_s activation on the endosome membranes is predicted to confer prolonged dynamics over longer time scales. In all cases, the presence/absence of GIV only impacts the prolonged phase, predicting higher Gα_s activation without GIV. (**D**) Simulations of cAMP dynamics that is initiated by the canonical GPCR-stimulated pathway (β2-adrenergic receptor stimulating Gα_s; blue line) and the non-canonical RTK-stimulated pathway that is modulated by GIV-GEM (red lines; solid = with GIV; interrupted = without GIV). In both cases, cAMP values (y axis) were normalized to the max value during a 60 min simulation. Canonical signaling is finite with a predominant PM phase, the non-canonical pathway features prolonged time scales due to a predominant endosomal phase. The interrupted line at approximately 5 min indicates the time period when ligand activated EGFR is typically rapidly endocytosed, marking a watershed between end of PM and beginning of endosomal phase of signaling.

134

Figure A.6 (Supplementary to Figure 2.2):

Parameter	Value	95% confidence
G_s k_{cat}	0.4	[0, 2.58]
$k_{r,int}$	6.67e-5	[0, 3.69e-4]
K_M EGFR-GEF to GDI	2e-15	[0, 1.36e-11]
K_{cat} EGFR-GEF to GDI	2.5	[0, 8.39]
DAG deact	0.028	[0, 0.098]
GEFGDIkcat	1	[0, 3.38]
GDI funct	2.91	[2.33, 3.5]
integral k_f	4.3e7	[0, 1e8]
k_r GIVGDI	0.0003	[0, 0.0038]
k interalization	4.58e-5	[2.92e-5, 6.24e-5]
DegGDI	0.001	[9e-4, 0.0012]
Giact	14.5	[13.7,15.2]
GEFEGFR.k1	0.00145	[0.0011, 0.0018]
GEFEGFR.k2	1e-7	[0, 9.3e-6]
DegGEF	0.0065	[0.0022, 0.011]
GEFactkcat	0.6	[0.31, 0.89]
kbase	1e-8	[0, 3.2e-7]
kc	1.3e11	[1.59e11, 1.05e11]
v11.k1	4e-5	[0, 8.59e-3]

Figure A.6: (**Supplementary to Figure 2.2**): Confidence intervals (95%CI) were calculated for the fit parameters for both high(solid line) and low (dashed line) bounds. When performing single variable variations, the confidence with respect to cAMP can be classified into 3 classes: (**A**) sensitive with qualitative change in cAMP dynamics, (**B**) sensitive without qualitative change in cAMP dynamics, and (**C**) insensitive. Of the 19 fit, 7 are sensitive, but only 4 change the form of the solution. Of those 4, internalization rate can be treated as a phenomenological constant used to fix time courses (among other steps). This leaves us with three other parameters, that are GIV related, and poorly constrained. These can be explained by the relatively new pathway we are working on and these parameters can be refined as more data is made available.

Figure A.7: (**Supplementary to Figure 2.2**): Simulations are shown for the dynamics of the PM (red line) and endosomal (yellow line) pools of EGFR computed over 1 h based on network Module 1. Parameter variations were conducted for values one order of magnitude above and below the control value for (**A**) basal degradation rate (reaction 9 in **Table A.4**), and (**B**) rate of Gα_s-GDP dependent catalytic degradation of EGFR (reaction 9 in **Table A.4**), (**C**) receptor internalization rate (reaction 4 in **Table A.4**). The solid line shows the value used in the control model, the dot dashed lines represent a ten-fold increase the value of the parameter from the control value and the dashed lines represent a ten-fold decrease in the value of the kinetic parameter from the control value. Variation of the basal degradation rate of EGFR doesn't affect either the PM or endosomal receptors(**A**; see also **Figure A.6**). Variation of the Gα_s-GDP-dependent catalytic degradation rate of EGFR affects the endosomal receptor pool proportionally, with no discernible effect on the PM receptor pool (**B**; see also **Figure A.6**). On the other hand, variation in the rate of internalization of EGFR affects both the PM and endosome pool of receptors. An increase in the rate of internalization of EGFR leads to a rapid decrease in the PM receptor pool with a corresponding rapid increase in the endosome pool of receptors (**C**). (**D**) the effect of the binding rate constant of GIV-GEF to ligand-bound, dimerized EGFR (reaction 14 in **Table A.5**) on the dynamics of the formation of the EGFR·GIV·Gα_i complex. (**E**) the effect of CDK5-mediated phosphorylation of GIV to GIV-GEF on the formation of the EGFR·GIV·Gα_i complex (k$_{cat}$ reaction 13 in **Table A.5**).(**F**) Simulations display the effect of PKC-θ-mediated phosphorylation at S1689 for GIV-GEF·EGFR, resulting in conversion of GIV-GEF to GIV-GDI (reaction 25 in **Table A.6**; see also **Figure A.6**). Changing this k$_{cat}$ changes the dynamics of the EGFR·GIV·Gα_i complex formation such that a decrease in this rate constant leads to a prolonged lifetime of the complex. (**G**) Variation of the binding rate of GIV-GDI binding rate to G$_{\alpha s}$-GDP (reaction 34 in **Table A.7**) affects both the density of the bound Gα_s·GIV-GDI molecules and the temporal dynamics. (**H**) Varying the internalization rate of dimerized EGFR, from the PM to the endosomal compartment (reaction 4 in **Table A.4**) dramatically changes the dynamics of the Gα_s·GIV-GDI complex formation. Faster internalization rates of EGFR lowered the density of the complex and the complexes were assembled earlier than observed in experiments (**H**). Reducing the rate of EGFR internalization, on the other hand, also lowered the density of Gα_s·GIV-GDI complexes, and they were assembled later. Variations of the internalization of receptors greatly effected cAMP and PKA production within simulations (**J,K**; blue line) leading to a high (high internalization) or long and low (low internalization) response. (**I**) The dynamics of the Gα_s·GIV-GDI complex formation are affected by the catalytic degradation rate of internalized dimerized EGFR, which is enabled by Gα_s-GDP [40] (reaction 9 in **Table A.4**). The effect of changing this parameter was proportional on both the membrane density of the Gα_s·GIV-GDI complex and affected the peak time and dynamics of the complex formation. Because the degradation of internalized EGFR requires endosomal maturation that is enhanced by Gα_s-GDP [40], increasing the rate of Gα_s-GDP dependent endosome maturation and EGFR degradation decreased the Gα_s-GDI density and increased the rate of the Gα_s·GIV-GDI complex formation, whereas decreasing the rate of the Gα_s- GDP-mediated EGFR degradation increased the density of the complex formation and slowed down the process. Variations of the catalytic degradation of receptors greatly effected cAMP and PKA production within simulations (**J,K**; green line) leading to a low (high degradation) or high and sustained (low degradation) response. Variation of the Gα_s·GIV-GDI interpolation function (reaction 37 in **Table A.7**) affects both the density and timescales of cAMP(**L**) and Gα_s·GIV-GDI(**M**) with a high rate leading to an ShGIV type response due to low Gα_s·GIV-GDI densities (**M**)
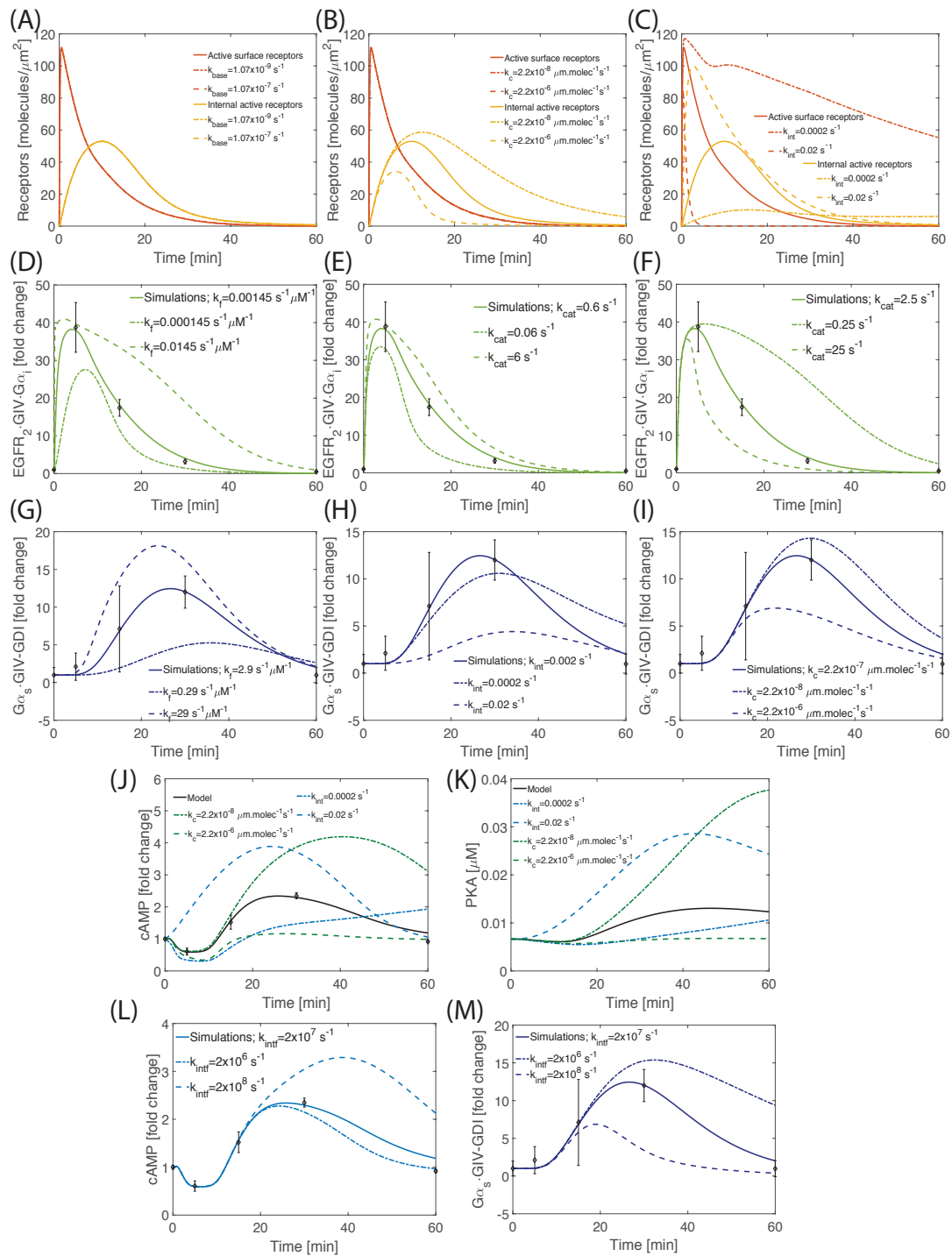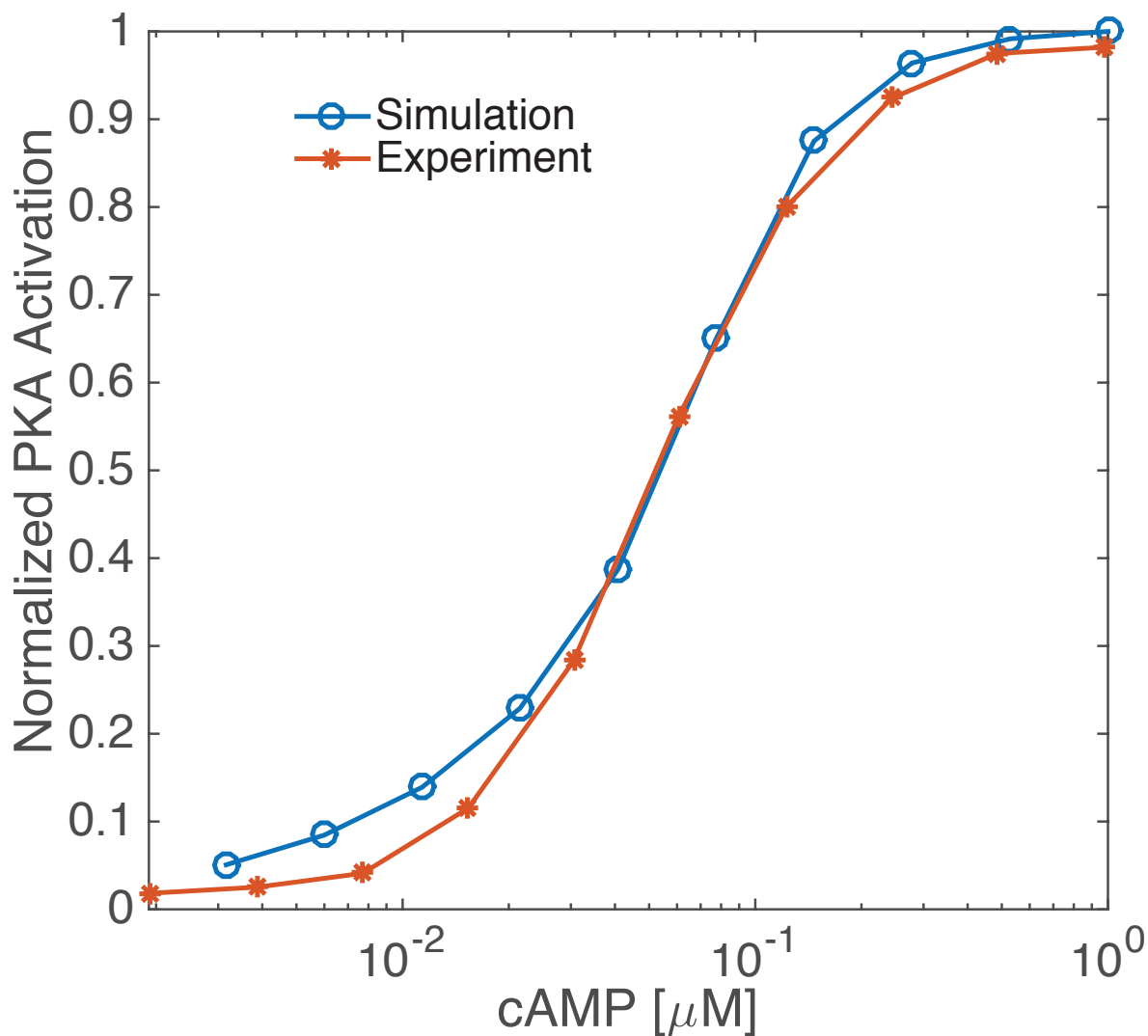
Figure A.8: (**Supplementary to Figure 2.2**): **Parameter estimation and validation of cAMP-PKA interactions.** Dose response curve for PKA activation as a function of cAMP concentration was calculated from simulations and compared against previously published experiments. The red starred line shows the normalized PKA activation from [231] and the blue line shows the model PKA activation as a function of cAMP concentration. Experimental data from Bruystens *et al.* [231] was fit to a Hill function to obtain a Hill coefficient of n=1.73 and an EC_{50}=54 nM. These values were used in our model (**Module 4, Reactions 47-50**) to obtain a good qualitative agreement between simulations and experimental data for cAMP-mediated activation of PKA.
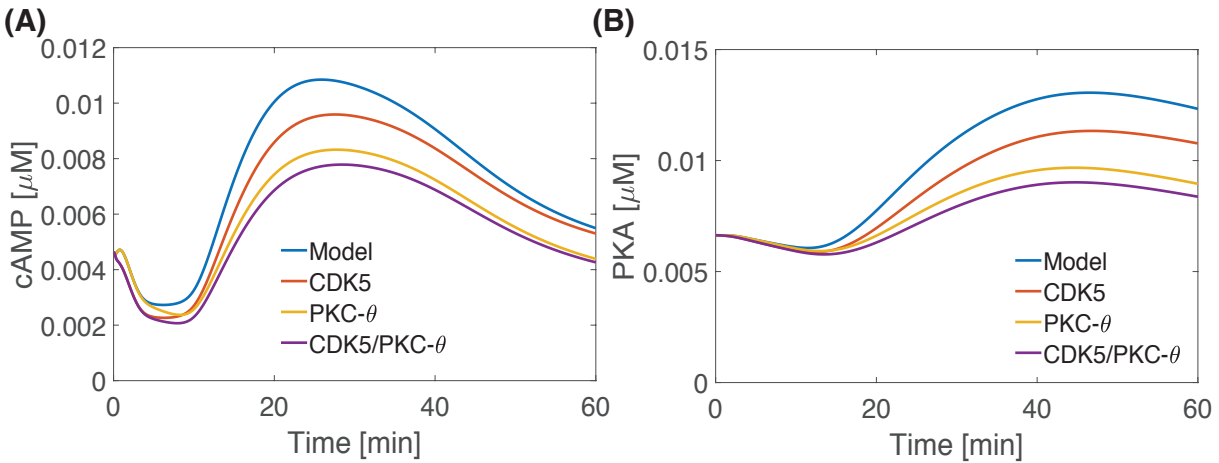
Figure A.9: (**Supplementary to Figure 2.2**): **Effect of PKC-θ and CDK5 phosphorylation on PDE phosphorylation**. Simulations of the impact of phosphorylation of PDE by PKC-θ and CDK5 (reactions are shown in **Table A.9**) on (**A**)cAMP and (**B**) PKC-θ are shown. The control values of cAMP and PKC-θ without accounting for either of the two feedforward interactions are shown in blue. Inclusion of the feedforward loops. i.e., phosphorylation of PDE by either CDK5 alone (red) or PKC-θ alone (yellow), or both (purple) are also displayed. When both CDK5 and PKC-θ feedback loops are taken into account (purple), PDE activity appears to be enhanced because cellular cAMP dynamics are significantly dampened.
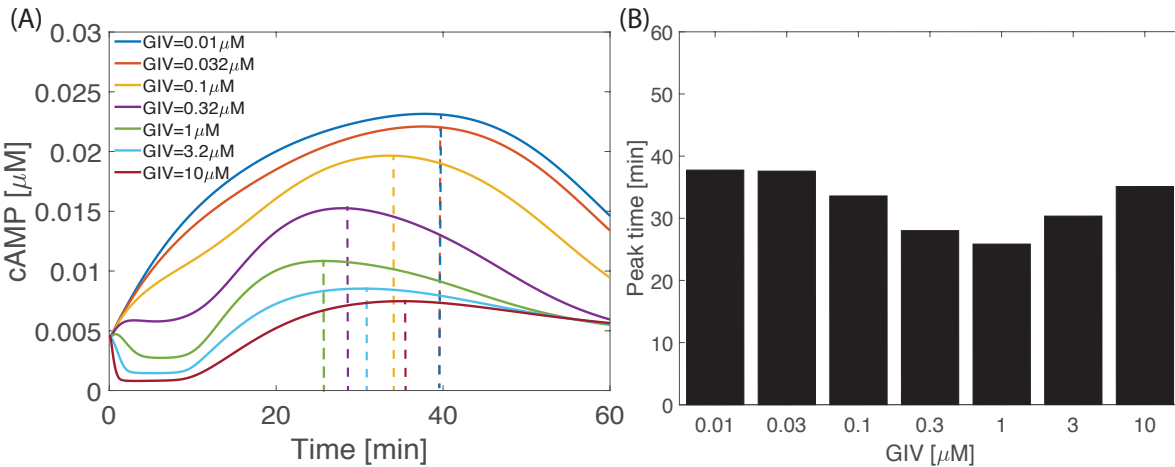
Figure A.10: (**Supplementary to Figure 2.3**): **Concentration of GIV proteins in cells affects peak cAMP time.** Simulations were performed by varying the concentration of GIV with values ranging from 0.05 to 10 μM, the peak times for cAMP were then extracted (**A**). These times were then plotted on a bar graph (**B**). cAMP peak times were found to shorten and then lengthen with increasing GIV concentrations in a non-linear manner. The initial, low GIV, peak time decrease is due to the action of $G\alpha_s \cdot$GIV-GDI shortening the timescale of $G\alpha_s$ activation. While the later, high GIV, increase is due to the cAMP the action of $G\alpha_i$ inhibition becoming more prevalent over the $G\alpha_s$ generation of cAMP.
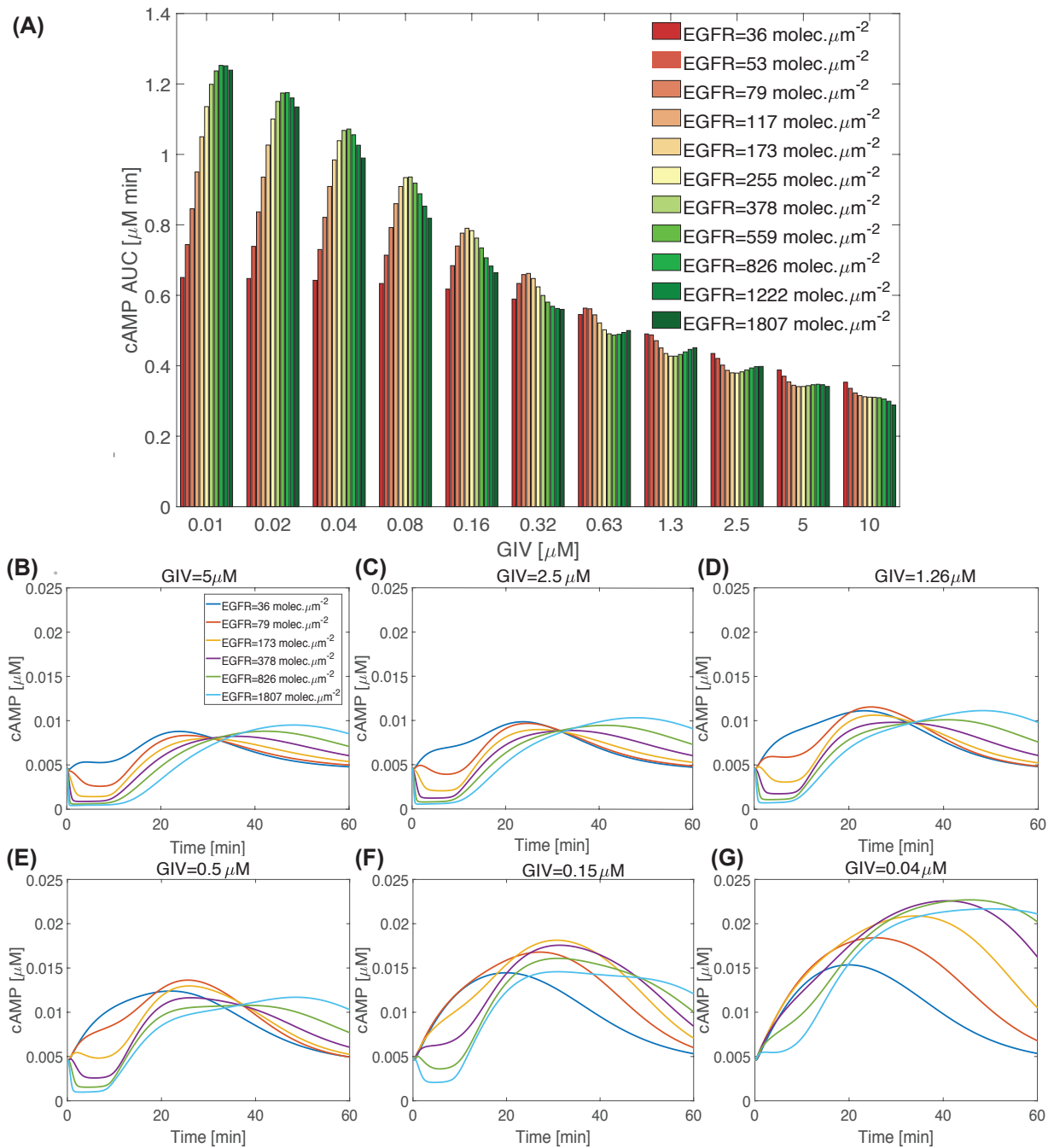
Figure A.11: (**Supplementary to Figure 2.4**): **Impact of varying EGFR and GIV concentrations on cellular levels of cAMP** (**A**) cAMP AUC, computed at 1 h is shown for different values of GIV and EGFR. Time-course of cAMP for various EGFR concentrations at (**B**) GIV=5 μM, (**C**) GIV=2.5 μM, (**D**) GIV=1.26 μM, (**E**) GIV=0.5 μM, (**F**) GIV=0.15 μM, (**G**) GIV=0.04 μM are shown.
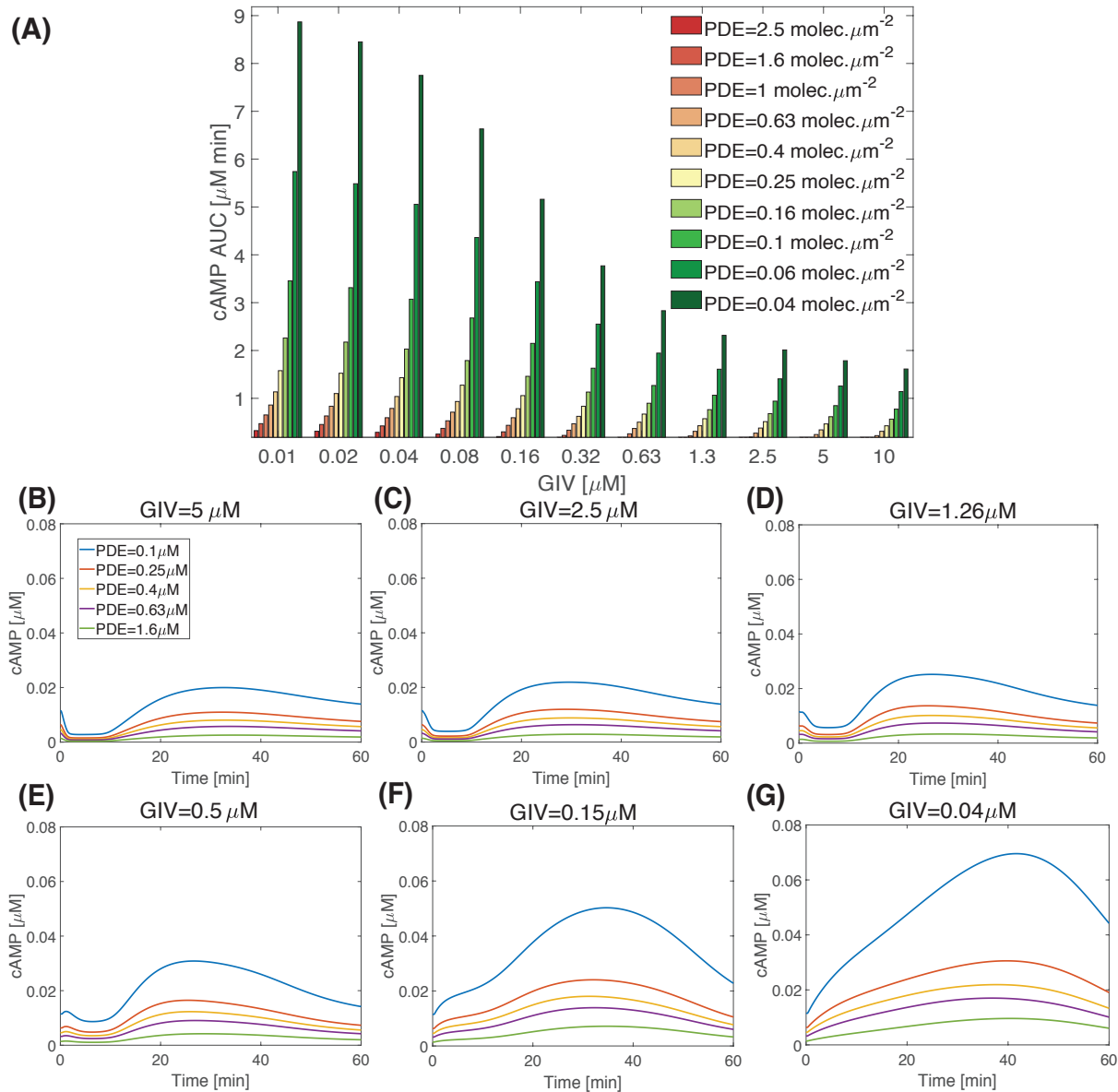
Figure A.12: (**Supplementary to Figure 2.4**): **Impact of varying PDE and GIV concentrations on cellular levels of cAMP**. (**A**) cAMP AUC, computed at 1 h is shown for different values of GIV and PDE. Time-course of cAMP for various PDE concentrations at (**B**) GIV=5 μM, (**C**) GIV=2.5 μM, (**D**) GIV=1.26 μM, (**E**) GIV=0.5 μM, (**F**) GIV=0.15 μM, (**G**) GIV=0.04 μM are shown.
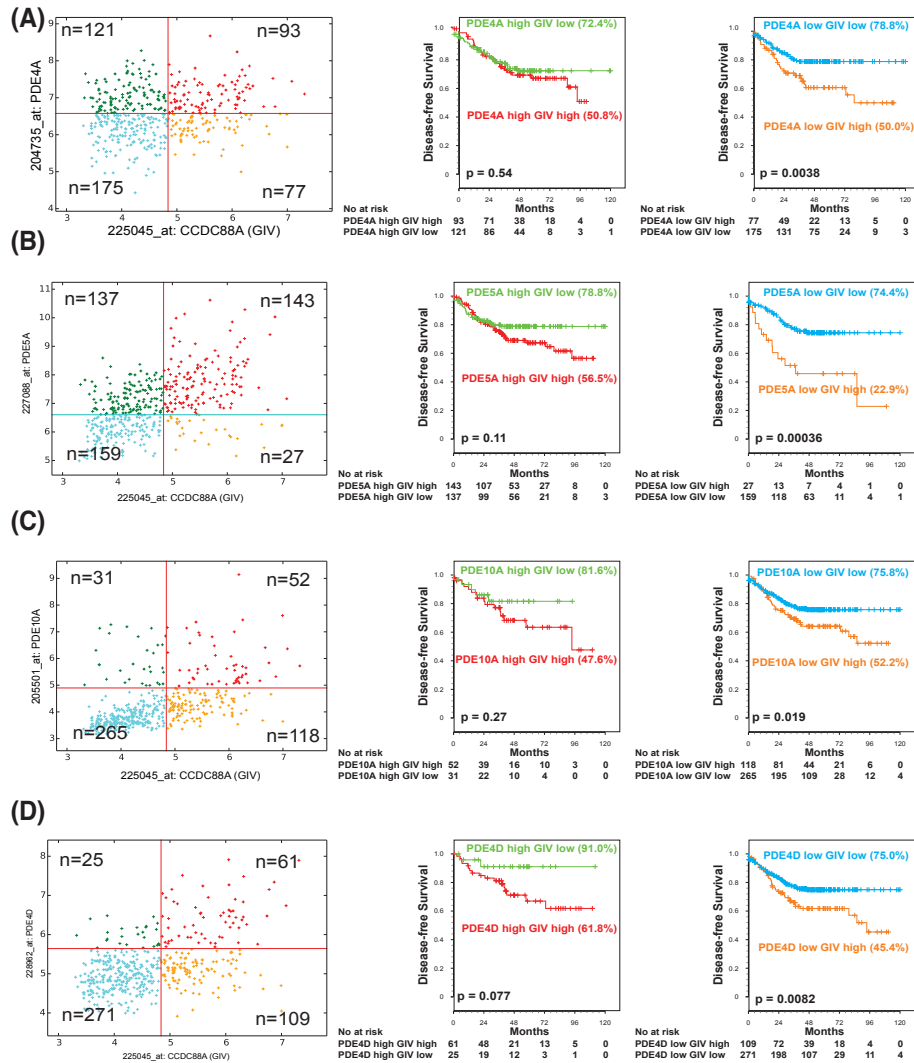
Figure A.13: (**Supplementary to Figure 2.5**): **The impact of levels of expression of GIV and PDE on cAMP dynamics; comparison of model predictions and clinical outcome [disease-free survival] in patients with colorectal cancers**. (**A**-**D**) GIV expression status in colon cancers has an impact on disease-free survival (DFS) only when the level of expression of various PDE isoforms are low. Hegemon software was used to analyze individual arrays according to the expression levels of GIV (CCDC88A) and either PDE4A (**A**), or 5A (**B**), 10A (**C**), 4D (**D**) in a data set containing 466 patients with colon cancer (Left panels, **A**-**D**; see Methods; **E**). Survival analysis using Kaplan-Meier curves showed that among patients with high PDEs [middle panels, **A**-**D**], high vs low GIV expression did not carry any statistically significant difference in DFS (all p values > 0.05). Survival analysis among patients with low PDEs [right panels, **A**-**D**] showed that patients whose tumors had high levels of expression of GIV had a significantly shorter DFS than those with tumors expressing low levels of GIV (all p values < 0.05). See also **Figure 2.5** for patient survival curves for PDE5A isoform and GIV on DFS.

142
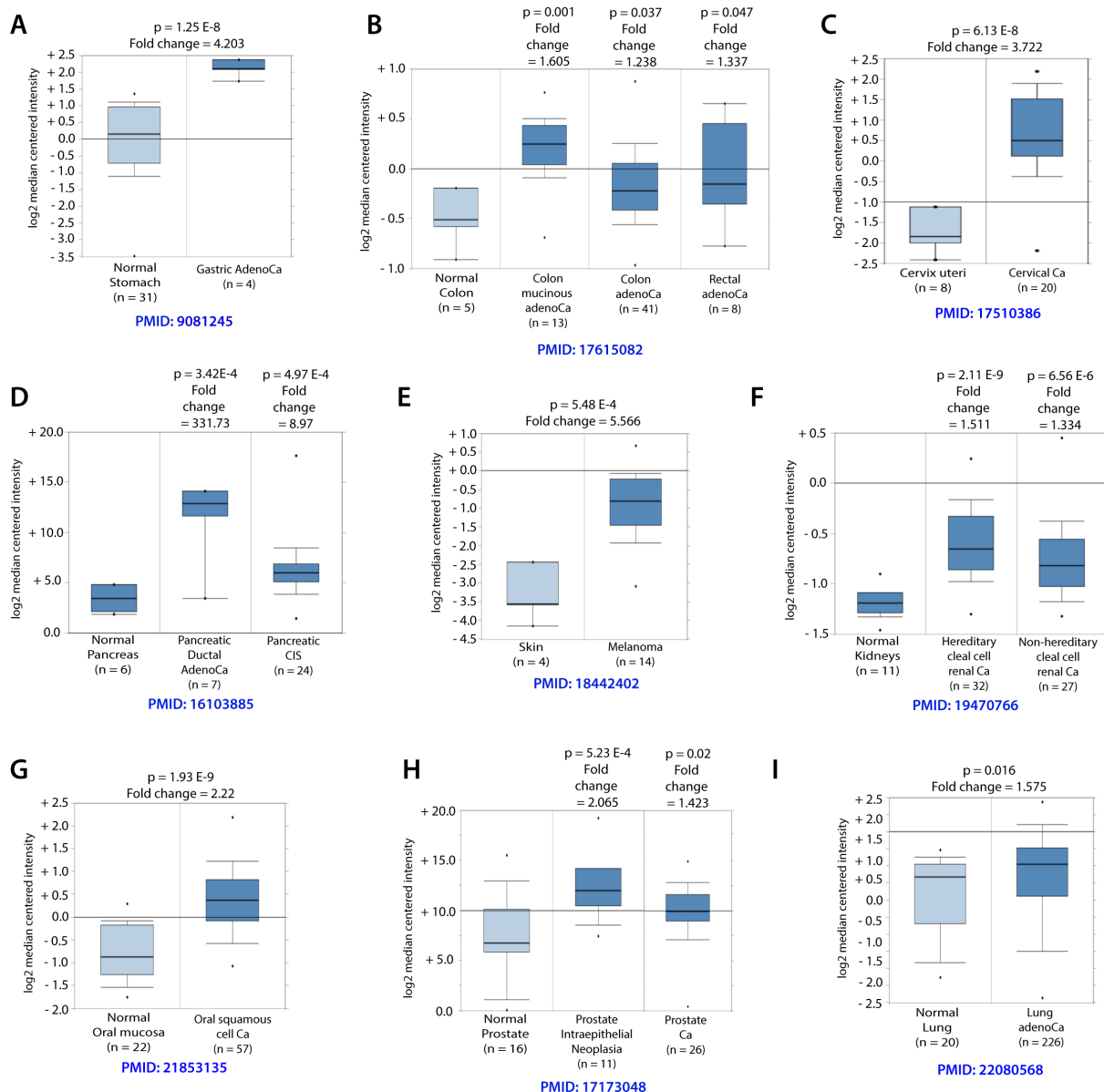
Figure A.14: **(Supplementary to Figure 2.5): GIV mRNA expression is elevated in various cancers.** Expression levels of GIV [CCDC88a] mRNA in normal vs. cancers was analyzed in publicly available RNA Seq datasets using Oncomine.org. PMIDs listed under each box plot refers to the original manuscript associated with the dataset.
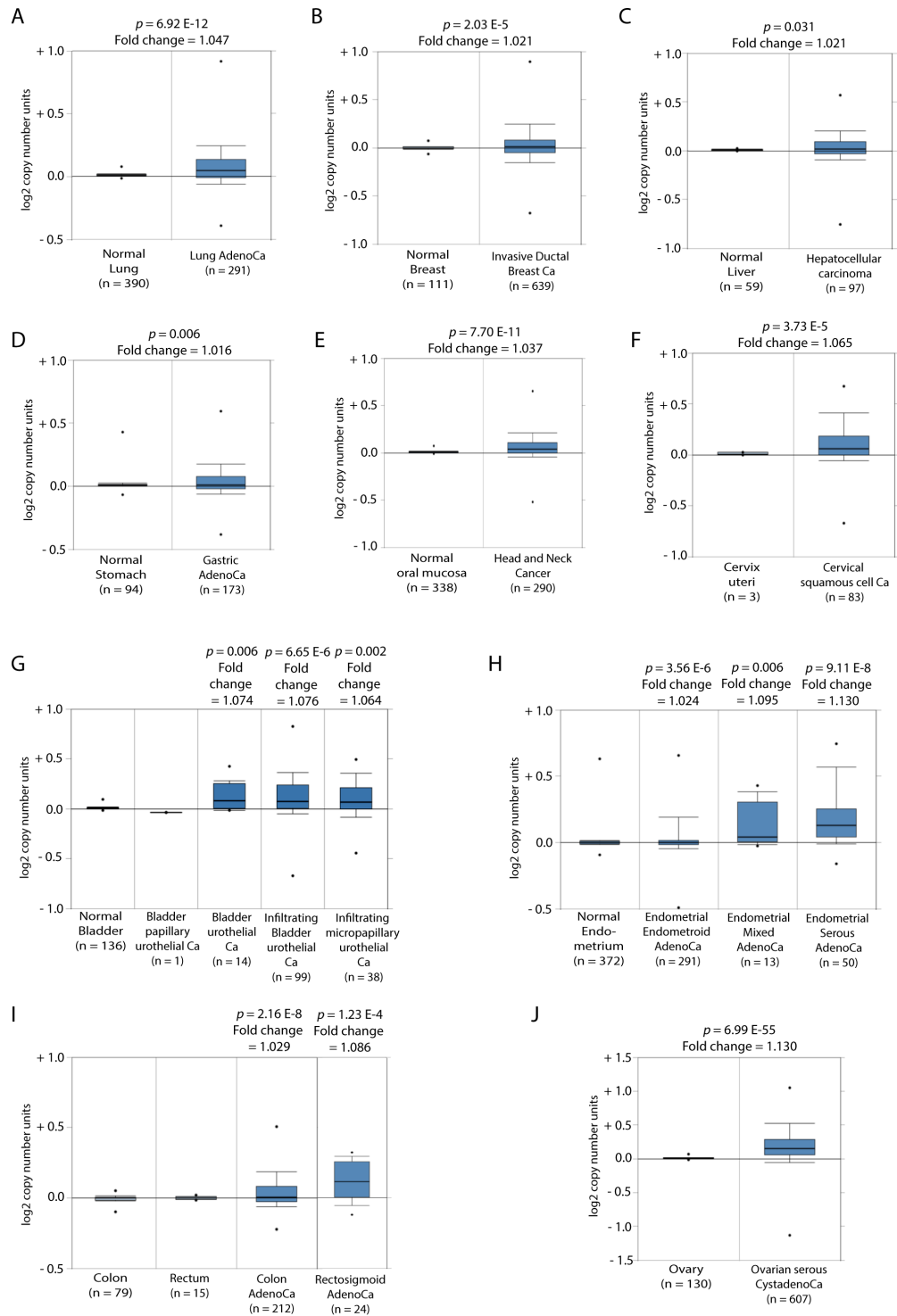
Figure A.15: **(Supplementary to Figure 2.5) Copy numbers of GIV-gene is elevated in various cancers.** Copy numbers of GIV gene is elevated in various cancers. TCGA datasets were analyzed for copy number variations (CNV) in GIV gene [CCDC88a] in normal vs. cancers using Oncomine.org.

Appendix **A**, in full, is a reprint of the supplemental material as it appears in M. Getz, L. Swanson, D. Sahoo, P. Ghosh, and P. Rangamani. A predictive computational model reveals that GIV/Girdin serves as a tunable valve for EGFR-stimulated Cyclic AMP Signals. Molecular Biology of the Cell, pages mbc.E18–10–0630, 2019. The dissertation author was the primary investigator and author of this paper.

Appendix B

Supplementary information for Spatially compartmentalized phase regulation in the Ca^{2+}-cAMP-PKA oscillatory circuit

B. Tenner[1,2]**, M. Getz**[3]**, B. Ross**[2]**, D. Ohadi**[4]**, C. Bohrer**[1]**, E. Greenwald**[2]**, S. Mehta**[2]**, J. Xiao**[1]**, P. Rangamani**[3,4,]*****, J. Zhang**[1,2,]*****

[1]Department of Biophysics and Biophysical Chemistry, The Johns Hopkins University School of Medicine, Baltimore, MD 21505, USA.

[2]Department of Pharmacology, University of California, San Diego, La Jolla, CA 92093, USA.

[3]Chemical Engineering Graduate Program, University of California, San Diego, La Jolla, CA 92093, USA.

[4]Department of Mechanical and Aerospace Engineering, University of California, San Diego, La Jolla, CA 92093, USA.

*Correspondence to: jzhang32@ucsd.edu; padmini.rangamani@eng.ucsd.edu

B.1   cAMP Analysis and Quantification

AKAP79-(Ci/Ce)Epac2-camps transfected cells displayed cAMP oscillations that were either in-phase or out-of-phase with their respective Ca^{2+} signal. This was in sharp contrast to responsive lyn-(Ci/Ce)Epac2-camps transfected cells where all cells yielded only out-of-phase oscillations. We found a strong correlation between the AKAP79-fused sensor expression level and the observed cAMP-Ca^{2+} phase relationship, with cells having lower levels of sensor present displaying predominantly in-phase cAMP oscillations and cells with higher levels of the AKAP79/150-fused biosensor exhibiting out-of-phase oscillations (**Accessory Fig. B.1a-c**). Overexpression of the AKAP79 scaffold likely changed the stoichiometry of the signaling complexes and resulted in unsuccessful targeting of the biosensor to functional AKAP79/150 domains, and so in this manuscript we considered only TEA-responsive cells below an AKAP79 expression threshold determined by the YFP acceptor fluorescence (**Accessory Fig. B.1a-c**).

B.2   Time Lag Calculation

Due to the heterogeneity of cellular Ca^{2+} and cAMP/PKA activity oscillatory responses in each cell (i.e. variations in frequency, amplitude, and regularity), we sought an applicable metric to describe the phase relationship. Here we measure the lag time (sec) between the Ca^{2+} signal trace and the cAMP/PKA activity signal trace. Specifically, we high-pass filtered both the Ca^{2+} and cAMP/PKA activity traces (approx.. 20 min) to subtract out slowly varying baseline changes, normalized the traces so that the maximum intensity/FRET ratio was set to 1, and then computed the cross-correlation to measure the signal overlap for different lag times. To calculate the lag time, we identified peaks in the cross-correlation passing a peak prominence cutoff and found the absolute value of the shortest lag time corresponding to a peak maximum. For in-phase oscillations, the lag time was typically small ($\tau \leq 20$ sec) due to the two signal traces oscillating in synchrony. However, out-of-phase oscillations typically corresponded to longer lag times ($\tau ¿$

20 sec) due to the anti-phasic relationship seen in the peak timing and peak shape. Analysis was performed with custom scripts in MATLAB and Java, and pipelines in CellProfiler.

B.3 Quantification of Nanodomain Perturbation Effects on Global Ca^{2+}

In order to measure the effects of AKAP79/150:AC8 disruption on Ca^{2+} dynamics, we transiently transfected and expressed AC^{81-106} in MIN6 and measured Ca^{2+} with RCaMP. For quantification of the interpeak timing and peak ratio, we first selected cells that responded to the TEA treatment, identified Ca^{2+} peaks passing a peak prominence cutoff, and finally calculated the avg. time between peak maxima and RFP intensity ratio between the second and first Ca^{2+} peak maxima. To find the percentage of cells with regular vs. irregular Ca^{2+} oscillations, we randomized all Ca^{2+} traces from the experimental and control samples and performed a blinded classification to sort the single cell traces as regular, irregular, or nonresponsive. Analysis was performed with custom scripts in MATLAB and Java, and pipelines in CellProfiler.

B.4 Well-mixed system

B.4.1 Well-mixed reaction tables

Table B.1: Voltage Gated Channel Reactions

#	Species	Expression	Parameters	Ref.
1	Membrane Voltage	$\frac{dV}{dt} = \frac{-I_{Ca} - I_K - I_L - I_{KCa}}{C_m}$	C_m=5.3 pF	[14]
2	Ca^{2+} current	$I_{Ca} = g_{Ca} m_\infty (V - E_{Ca})$	g_{Ca}=600 pS, E_{Ca}=100 mV	[14]
3	Fraction of open VGCC (at steady state)	$m_\infty = \frac{1}{2} \left(1 + tanh \left(\frac{V - v_1}{v_2} \right) \right)$	v_1=-20 mV, v_2=24 mV	[14]
4	K$^+$ current	$I_K = g_K w (V - E_K)$	g_K=240 pS, E_{Ca}=-75 mV	[14]
5	Fraction of open K$^+$ channels (at steady state)	$\frac{dw}{dt} = \frac{\phi(w_\infty - w)}{\tau}$	ϕ=35 $\frac{1}{s}$	[14]
6	Time constant for K$^+$ channel open probability	$\tau = \frac{1}{cosh\left(\frac{V - v_3}{2v_4}\right)}$	v_3=-16 mV, v_4=11.2 mV	[14]
7	leak current	$I_L = g_L (V - E_L)$	g_L=150 pS, E_L=-75 mV	[257]
8	Ca^{2+} gated K$^+$ current	$I_{KCa} = g_{KCa} \frac{Ca}{Ca + K_{KCa}} (V - E_K)$	g_{KCa}=2000 pS, E_{Ca}=-75 mV, K_{KCa}=5 μM	[14]

Table B.2: Ca Flux and Reactions

#	Reaction	Reaction flux	Kinetic Parameters	Ref.
9	$\to$ Ca	$j_{\text{Ca}_V}(1 + k_{\text{PKA}_V}[\text{PKA}]) + j_{\text{Ca}_I}$	k_{PKAV}=3000$s^{-1} \cdot \mu M^{-1}$	[14]
10	j_{Ca_V}	$f_i(-\alpha I_{Ca} - v_{LPM}[\text{Ca}])$	f_i=1x10^{-5} α=0.0045 $\mu M \cdot$fA$^{-1} \cdot$s^{-1} v_{LPM}=75^{-1}	[14]
11	j_{Ca_I}	$\frac{Ck_{IP3R}[\text{PKA}]A[\text{Ca}]}{1+A[\text{Ca}]+[B][\text{Ca}]^2}([\text{Ca}_{stores}]-[\text{Ca}])-\frac{V_s[\text{Ca}]^2}{K_s^2+[\text{Ca}]^2}$	K_s=10μM, Ca$_{stores}$=1.56μM, V$_s$=0.1$\mu M \cdot s^{-1}$, k$_{IP3R}$=0.05, A=0.2869μM^{-1}, B=2.869μM^{-2}, C=0.2133	[14]
12	2Ca + CaM $\leftrightarrow$ Ca^{2}CaM	$k_f[\text{Ca}][\text{CaM}] - k_r[\text{Ca}^2\text{CaM}]$	k_f=3.6 $s^{-1} \cdot \mu M^{-1}$, k_r=8 s^{-1}	[206]
13	Ca + Ca^{2}CaM $\leftrightarrow$ Ca^{3}CaM	$k_f[\text{Ca}][\text{Ca}^2\text{CaM}] - k_r[\text{Ca}^3\text{CaM}]$	k_f=11 $s^{-1} \cdot \mu M^{-1}$, k_r=195 s^{-1}	[206]
14	Ca + Ca^{3}CaM $\leftrightarrow$ Ca^{4}CaM	$k_f[\text{Ca}][\text{Ca}^3\text{CaM}] - k_r[\text{Ca}^4\text{CaM}]$	k_f=59 $s^{-1} \cdot \mu M^{-1}$, k_r=500 s^{-1}	[206]
15	AC + Ca^{2}CaM $\leftrightarrow$ CaM·AC	$k_f[\text{AC}][\text{Ca}^2\text{CaM}] - k_r[\text{CaM·AC}]$	k_f=1.7 $s^{-1} \cdot \mu M^{-1}$, k_r=10 s^{-1}	[174, 175]
16	CaM·AC + 2Ca $\leftrightarrow$ AC*	$K_{cat}\frac{[\text{Ca}][\text{CaM·AC}]}{\text{Ca}+K_m} - k_r[\text{AC*}]$	K_{cat}=59.5 s^{-1}, K_m=0.1 μM, k_r=10 s^{-1}	[174, 175]
17	PDE + Ca^{2}CaM $\leftrightarrow$ CaM·PDE	$k_f[\text{PDE}][\text{Ca}^2\text{CaM}] - k_r[\text{CaM·PDE}]$	k_f=435 $s^{-1} \cdot \mu M^{-1}$, k_r=1 s^{-1}	[173]
18	CaM·PDE + 2Ca $\leftrightarrow$ PDE*	$K_{cat}\frac{[\text{Ca}][\text{CaM·PDE}]}{\text{Ca}+K_m} - k_r[\text{PDE*}]$	K_{cat}=1.81 s^{-1}, K_m=0.18 μM, k_r=1 s^{-1}	[173]
19	PDE + Ca^{4}CaM $\leftrightarrow$ PDE*	$k_f[\text{PDE}][\text{Ca}^4\text{CaM}] - k_r[\text{PDE*}]$	k_f=435 $s^{-1} \cdot \mu M^{-1}$, k_r=1 s^{-1}	[173]

Table B.3: cAMP Reactions

#	Reaction	Reaction flux	Kinetic Parameters	Ref.
20	$\rightarrow$ cAMP	$k_{base}([\text{CaM·AC}]+[\text{AC}]+[\text{AC}_{ind}])+k_{act}[\text{AC*}]$	k_{base}=0.1 s^{-1}, k_{act}=0.785 s^{-1}	[14, 204]
21	cAMP$\rightarrow$	$k_{base}[\text{cAMP}]\frac{[\text{CaM·PDE}]+[\text{PDE}]}{[\text{cAMP}]+K_m}+k_{act}\frac{[\text{cAMP}][\text{PDE*}]}{[\text{cAMP}]+K_m}$	k_{base}=0.2 s^{-1}, K_m= 0.6 μM k_{act}=2.5 s^{-1}	[14, 204]
22	cAMP$\rightarrow$	$V_{ind}\frac{[\text{cAMP}]}{[\text{cAMP}]+K_m}$	V_{ind}=2.5 $\mu M \cdot s^{-1}$, K_m= 1.4 μM	[14, 204]
23	cAMP + R2 $\rightarrow$ R2$_b$	$k_f[\text{cAMP}][\text{R2}]-k_r[\text{R2}_b]$	k_f=1 $s^{-1}\cdot \mu M^{-1}$, k_r=0.00033 s^{-1}	[205]
24	cAMP + R2$_b$ $\rightarrow$ R2$_{ba}$	$k_f[\text{cAMP}][\text{R2}_b]-k_r[\text{R2}_{ba}]$	k_f=1 $s^{-1}\cdot \mu M^{-1}$, k_r=0.00105 s^{-1}	[205]
25	cAMP + R2$_b$ $\rightarrow$ R2$_{bb}$	$k_f[\text{cAMP}][\text{R2}_b]-k_r[\text{R2}_{bb}]$	k_f=1 $s^{-1}\cdot \mu M^{-1}$, k_r=0.00132 s^{-1}	[205]
26	cAMP + R2$_{ba}$ $\rightarrow$ R2$_{bba}$	$k_f[\text{cAMP}][\text{R2}_{ba}]-k_r[\text{R2}_{bba}]$	k_f=1 $s^{-1}\cdot \mu M^{-1}$, k_r=0.0013 s^{-1}	[205]
27	cAMP + R2$_{bb}$ $\rightarrow$ R2$_{bba}$	$k_f[\text{cAMP}][\text{R2}_{bb}]-k_r[\text{R2}_{bba}]$	k_f=1 $s^{-1}\cdot \mu M^{-1}$, k_r=0.00103 s^{-1}	[205]
28	cAMP + R2$_{bba}$ $\rightarrow$ R2$_{bbaa}$	$k_f[\text{cAMP}][\text{R2}_{bba}]-k_r[\text{R2}_{bbaa}]$	k_f=1 $s^{-1}\cdot \mu M^{-1}$, k_r=0.0114 s^{-1}	[205]
29	PKA + R2 $\rightarrow$ R2C	$k_f[\text{PKA}][\text{R2}]-k_r[\text{R2C}]$	k_f=1 $s^{-1}\cdot \mu M^{-1}$, k_r=1.26E-7 s^{-1}	[205]
30	PKA + R2$_b$ $\rightarrow$ R2$_b$C	$k_f[\text{PKA}][\text{R2}_b]-k_r[\text{R2}_bC]$	k_f=1 $s^{-1}\cdot \mu M^{-1}$, k_r=2.52E-7 s^{-1}	[205]

Table B.4: cAMP Reactions (cont.)

#	Reaction	Reaction flux	Kinetic Parameters	Ref.
31	PKA + R2$_{ba}$ → R2$_{ba}$C	k_f[PKA][R2$_{ba}$] − k_r[R2$_{ba}$C]	k_f=1 $s^{-1} \cdot \mu M^{-1}$, k_r=3.4E-6 s^{-1}	[205]
32	PKA + R2$_{bba}$ → R2$_{bba}$C	k_f[PKA][R2$_{bba}$] − k_r[R2$_{bba}$C]	k_f=1 $s^{-1} \cdot \mu M^{-1}$, k_r=0.000936 s^{-1}	[205]
33	PKA + R2$_{bbaa}$ → R2$_{bbaa}$C	k_f[PKA][R2$_{bbaa}$] − k_r[R2$_{bbaa}$C]	k_f=1 $s^{-1} \cdot \mu M^{-1}$, k_r=0.645 s^{-1}	[205]
34	cAMP + R2C → R2$_b$C	k_f[cAMP][R2C] − k_r[R2$_b$C]	k_f=1 $s^{-1} \cdot \mu M^{-1}$, k_r=0.000659s^{-1}	[205]
35	cAMP + R2$_b$C → R2$_{ba}$C	k_f[cAMP][R2$_b$C] − k_r[R2$_{ba}$C]	k_f=1 $s^{-1} \cdot \mu M^{-1}$, k_r=0.0142s^{-1}	[205]
36	cAMP + R2$_{ba}$C → R2$_{bba}$C	k_f[cAMP][R2$_{ba}$C] − k_r[R2$_{bba}$C]	k_f=1 $s^{-1} \cdot \mu M^{-1}$, k_r=0.358s^{-1}	[205]
37	cAMP + R2$_{bba}$C → R2$_{bbaa}$C	k_f[cAMP][R2$_{bba}$C] − k_r[R2$_{bbaa}$C]	k_f=1 $s^{-1} \cdot \mu M^{-1}$, k_r=7.84s^{-1}	[205]
38	PKA + R2$_b$C → R2$_b$C$_2$C	k_f[PKA][R2$_b$C] − k_r[R2$_b$C$_2$]	k_f=1 $s^{-1} \cdot \mu M^{-1}$, k_r=0.00324 s^{-1}	[205]
39	PKA + R2C → R2C$_2$	k_f[PKA][R2C] − k_r[R2C$_2$]	k_f=1 $s^{-1} \cdot \mu M^{-1}$, k_r=2.81E-6 s^{-1}	[205]
40	PKA + R2$_{ba}$C → R2$_{ba}$C$_2$	k_f[PKA][R2$_{ba}$C] − k_r[R2$_{ba}$C$_2$]	k_f=1 $s^{-1} \cdot \mu M^{-1}$, k_r=0.666 s^{-1}	[205]
41	cAMP + R2C$_2$ → R2$_b$C$_2$	k_f[cAMP][R2C$_2$] − k_r[R2$_b$C$_2$]	k_f=1 $s^{-1} \cdot \mu M^{-1}$, k_r=0.762s^{-1}	[205]
42	cAMP + R2$_b$C$_2$ → R2$_{ba}$C$_2$	k_f[cAMP][R2$_b$C$_2$] − k_r[R2$_{ba}$C$_2$]	k_f=1 $s^{-1} \cdot \mu M^{-1}$, k_r=2.91s^{-1}	[205]

Table B.5: Initial Conditions

#	Species	Initial Value	Reference
IC1	AC8	1 μM	
IC2	AC$_{ind}$	1 μM	
IC3	Ca^{2+}	1 μM	
IC4	CaM	10 μM	
IC5	cAMP	0.1 μM	
IC6	PDE1	1 μM	
IC7	PDE4	0.4 μM	
IC8	R2C2	0.4 μM	
IC9	V	-60 mV	

B.5 Simulations of the full spatial systems

B.5.1 Reaction tables of modified well-mixed parameters for the spatial model

Table B.6: Ca Flux and Reactions modified from **Table B.1**

#	Reaction	Reaction flux	Kinetic Parameters	Ref.
S1	$\rightarrow$ Ca	$j_{Ca_V}(1+k_{PKA_V}[PKA])+j_{Ca_I}$	$k_{PKAV}=100\mu M^{-1}$	FRET constraint
S2	j_{Ca_V}	$f_i(-\alpha I_{Ca}-v_{LPM}[Ca])$	$f_i=1\mathrm{x}10^{-6}$, $\alpha=4.15\mathrm{x}10^5\ mol\cdot m^{-2}\cdot A^{-1}\cdot s^{-1}$, $v_{LPM}=7.5\mathrm{x}10^{-4}\ m\cdot s^{-1}$	[14]
S3	j_{Ca_I}	$\frac{Ck_{IP3R}[PKA]A[Ca]}{1+A[Ca]+[B][Ca]^2}([Ca_{stores}]-[Ca])-\frac{V_s[Ca]^2}{K_s^2+[Ca]^2}$	$K_s=10\mu M$, $Ca_{stores}=1.56\mu M$, $V_s=0.1\mu M\cdot s^{-1}$, $k_{IP3R}=0.05\mu M^{-1}s^{-1}$, $A=0.2869\mu M^{-1}$, $B=2.869\mu M^{-2}$, $C=0.2133$	[14]
S4	AC + Ca^{2}CaM $\leftrightarrow$ CaM·AC	$k_f[AC][Ca^2CaM]-k_r[CaM\cdot AC]$	$k_f=10.8\ s^{-1}\cdot\mu M^{-1}$, $k_r=10\ s^{-1}$	FRET constraint
S5	CaM·AC + 2Ca $\leftrightarrow$ AC*	$K_{cat}\frac{[Ca][CaM\cdot AC]}{Ca+K_m}-k_r[AC^*]$	$K_{cat}=90\ s^{-1}$, $K_m=1\ \mu M$, $k_r=10\ s^{-1}$	FRET constraint
S6	PDE + Ca^{2}CaM $\leftrightarrow$ CaM·PDE	$k_f[PDE][Ca^2CaM]-k_r[CaM\cdot PDE]$	$k_f=0.25\ s^{-1}\cdot\mu M^{-1}$, $k_r=1\ s^{-1}$	FRET constraint
S7	CaM·PDE + 2Ca $\leftrightarrow$ PDE*	$K_{cat}\frac{[Ca][CaM\cdot PDE]}{Ca+K_m}-k_r[PDE^*]$	$K_{cat}=60\ s^{-1}$, $K_m=1\ \mu M$, $k_r=1\ s^{-1}$	FRET constraint
S8	PDE + Ca^{4}CaM $\leftrightarrow$ PDE*	$k_f[PDE][Ca^4CaM]-k_r[PDE^*]$	$k_f=0.25\ s^{-1}\cdot\mu M^{-1}$, $k_r=1\ s^{-1}$	FRET constraint

Table B.7: cAMP Reactions modified from **Table B.3**

#	Reaction	Reaction flux	Kinetic Parameters	Ref.
S9	$\rightarrow$ cAMP	$k_{base}([CaM{\cdot}AC]+[AC]+[AC_{ind}])+k_{act}[AC^*]$	k_{base}=0.2 s^{-1}, k_{act}=23.55 s^{-1}, AC_{ind}=3x10^{-8} $mol{\cdot}m^{-2}$	FRET constraint
S10	cAMP$\rightarrow$	$k_{base}[cAMP]\frac{[CaM{\cdot}PDE]+[PDE]}{[cAMP]+K_m}+$ $k_{act}\frac{[cAMP][PDE^*]}{[cAMP]+K_m}$	k_{base}=0.6 s^{-1}, K_m= 0.6 μM k_{act}=720 s^{-1}	FRET constraint
S11	cAMP$\rightarrow$	$V_{ind}\frac{[cAMP]}{[cAMP]+K_m}$	V_{ind}=0.25 $\mu M{\cdot}s^{-1}$, K_m= 1.4 μM	FRET constraint
S12	2cAMP + R2C2 $\rightarrow$ R2C + PKA	$k_f[cAMP]^2[R2C2]-$ $k_r[R2C][PKA]$	k_f=20 $min^{-1}{\cdot}\mu M^{-2}$, k_r=12 $min^{-1}{\cdot}\mu M^{-1}$	
S13	2cAMP + R2C $\rightarrow$ R2 + PKA	$k_f[cAMP]^2[R2C]-$ $k_r[R2][PKA]$	k_f=20 $min^{-1}{\cdot}\mu M^{-2}$, k_r=12 $min^{-1}{\cdot}\mu M^{-1}$	

Table B.8: Added AKAP interactions for the spatial model

#	Reaction	Reaction flux	Kinetic Parameters	Ref.
S14	AKAP + R2 $\rightarrow$ AKAP-R2	$k_f[R2][AKAP\text{-}R2C2]-$ $k_r[AKAP\text{-}R2]$	k_f=1 $s^{-1}{\cdot}\mu M^{-1}$ k_f=0.1 s^{-1}	Est.
S15	AKAP + R2C $\rightarrow$ AKAP-R2C	$k_f[R2C][AKAP\text{-}R2C2]-$ $k_r[AKAP\text{-}R2C]$	k_f=1 $s^{-1}{\cdot}\mu M^{-1}$ k_f=0.1 s^{-1}	Est.
S16	AKAP + R2C2 $\rightarrow$ AKAP-R2C2	$k_f[R2C2][AKAP\text{-}R2C2]-$ $k_r[AKAP\text{-}R2C2]$	k_f=1 $s^{-1}{\cdot}\mu M^{-1}$ k_f=0.1 s^{-1}	Est.
S17	2cAMP + AKAP-R2C2 $\rightarrow$ AKAP-R2C + PKA	$k_f[cAMP]^2[AKAP\text{-}R2C2]-$ $k_r[AKAP\text{-}R2C][PKA]$	k_f=20 $min^{-1}{\cdot}\mu M^{-2}$, k_r=12 $min^{-1}{\cdot}\mu M^{-1}$	
S18	2cAMP + AKAP-R2C $\rightarrow$ AKAP-R2 + PKA	$k_f[cAMP]^2[AKAP\text{-}R2C]-$ $k_r[AKAP\text{-}R2][PKA]$	k_f=20 $min^{-1}{\cdot}\mu M^{-2}$, k_r=12 $min^{-1}{\cdot}\mu M^{-1}$	

Table B.9: ICs and diffusion

#	Species	Initial value	Diffusion	Ref.
SIC1	Ca^{2+}	$0.001 \mu M$	$100 \frac{\mu m^2}{s}$	[258], Est. from steady state
SIC2	CaM	$2.9 \, \mu M$	$10 \frac{\mu m^2}{s}$	Est. from steady state[1]
SIC3	Ca_2CaM	$0.1 \, \mu M$	$10 \frac{\mu m^2}{s}$	Est. from steady state[1]
SIC4	Ca_3CaM	$4x10^{-3} \, \mu M$	$10 \frac{\mu m^2}{s}$	Est. from steady state[1]
SIC5	Ca_4CaM	$1x10^{-2} \, \mu M$	$10 \frac{\mu m^2}{s}$	Est. from steady state[1]
SIC6	R_2	$0.04 \, \mu M$	$10 \frac{\mu m^2}{s}$	Est. from steady state[1]
SIC7	R_2C_2	$0.2 \, \mu M$	$10 \frac{\mu m^2}{s}$	Est. from steady state[1]
SIC8	PKA	$0.05 \, \mu M$	$0.01 \frac{\mu m^2}{s}$	Est. from steady state, diffusion fitted
SIC9	PDE1	$0.9 \, \mu M$	$10 \frac{\mu m^2}{s}$	Est. from steady state[1]
SIC10	$PDE1_{act}$	$1x10^{-3} \, \mu M$	$10 \frac{\mu m^2}{s}$	Est. from steady state[1]
SIC11	CaMPDE1	$1x10^{-3} \, \mu M$	$10 \frac{\mu m^2}{s}$	Est. from steady state[1]
SIC12	AC	$4x10^{-10} \frac{mol}{m^2}$	0	Est.
SIC13	CaMAC	$0 \frac{mol}{m^2}$	0	Est.
SIC14	AC_{act}	$0 \frac{mol}{m^2}$	0	Est.
SIC15	AC_{ind}	$4x10^{-10} \frac{mol}{m^2}$	$1 \frac{\mu m^2}{s}$	Est.[2]
SIC16	V	-60 mV	$1 \frac{\mu m^2}{s}$	[14, 207][2]
SIC17	cAMP	$4x10^{-6} \, \mu M$	$60 \frac{\mu m^2}{s}$	[187], Est. from steady state

[1]For all cytosolic species without well constrained diffusions we defined them as $10 \frac{\mu m^2}{s}$
[2]For all membrane species without well constrained diffusions we defined them as $1 \frac{\mu m^2}{s}$
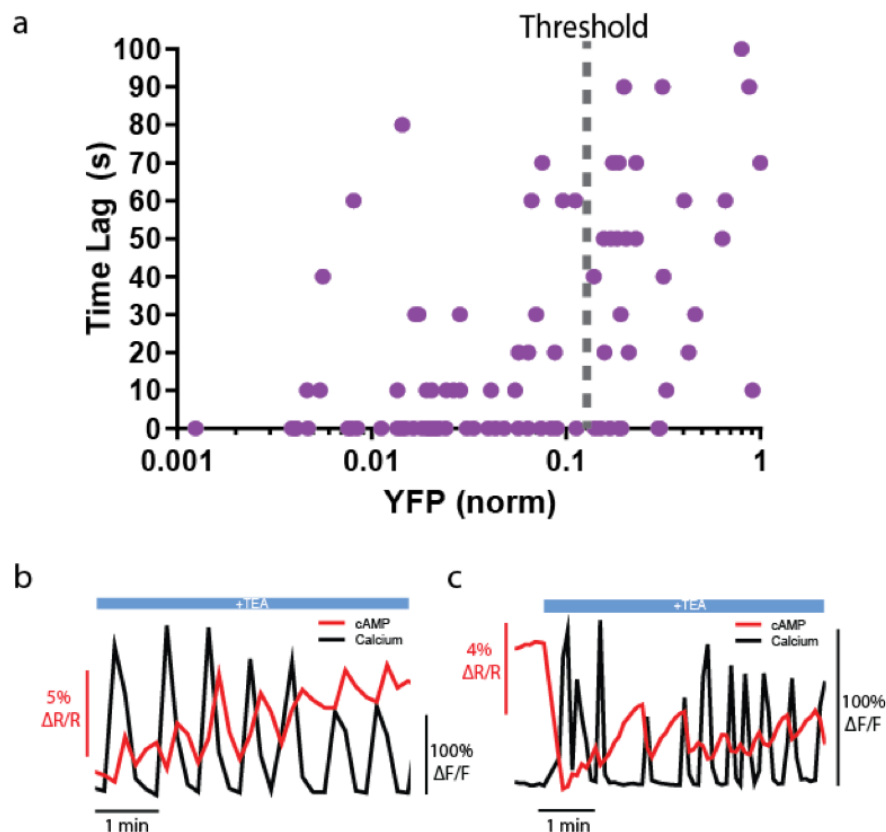
Figure B.1: **Phase of cAMP correlates with expression level of the AKAP79-(Ci/Ce)Epac2-camps.** (A) Scatter plot of the time lag (sec) and the YFP donor channel intensity (normalized to non-saturating maximum) for each cell expressing AKAP79-(Ci/Ce)Epac2camps. Cells with higher expression of the probe correlated with a longer time lag, therefore a YFP intensity threshold was designated for analysis purposes. (B) Representative single cell trace of an oscillating β cell with a YFP donor intensity below the threshold, depicting in-phase cAMP oscillations relative to Ca^{2+}. Red trace is cAMP (cyan direct channel divided by CY-FRET channel) and black trace is Ca^{2+} (RFP). (C) Representative single cell trace of an oscillating β cell with a YFP donor intensity above the threshold, depicting out-of-phase cAMP oscillations relative to Ca^{2+}. Red trace is cAMP (cyan direct channel divided by CY-FRET channel) and black trace is Ca^{2+} (RFP).
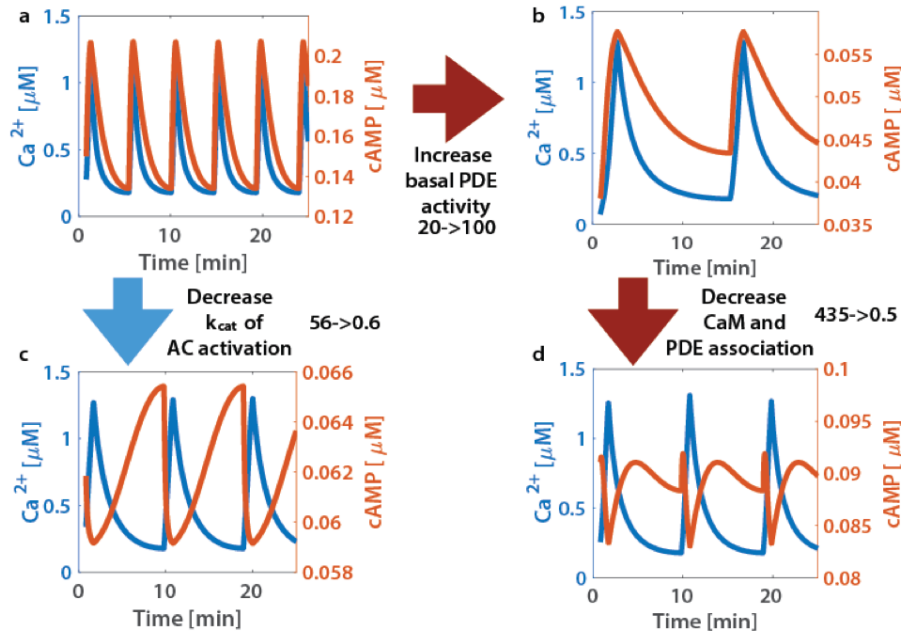
Figure B.2: **Phase is driven by activity variability within the Ca^{2+} oscillatory regime.** System phase can be switched by tuning the association of CaM to sources (ACs) and sinks (PDEs). (**a**) At base system conditions, the system acts in an in-phase manner. (**c**) Decreasing the rate of Ca^{2+} association to the AC-CaM complex causes the phase to switch to out-of-phase. (**b**) increasing basal PDE activity does not allow a phase switch, only after decreasing PDE and CaM association rates will the system allow a phase switch (**c**). A phase switch is controlled by the variability in the activity of source or sink. If the sink dominates, then the system is out of phase. If the source dominates, the system is in phase.

158

Appendix C

Stability analysis in spatial modeling of cell signaling

Michael C. Getz[1]**, Jasmine A. Nirody**[2]**, and Padmini Rangamani**[3][1]

[1] Chemical Engineering Graduate Program, University of California San Diego, La Jolla, CA, USA.

[2] Biophysics Graduate Program, University of California, Berkeley, CA, USA.

[3] Department of Mechanical and Aerospace Engineering, University of California San Diego, La Jolla, CA, USA.

Advances in high-resolution microscopy and other techniques have emphasized the spatio-temporal nature of information transfer through signal transduction pathways. The compartmentalization of signaling molecules and the existence of microdomains are now widely acknowledged as key features in biochemical signaling. To complement experimental observations of spatio-temporal dynamics, mathematical modeling has emerged as a powerful tool. Using modeling, one can not only recapitulate experimentally observed dynamics of signaling molecules, but also gain an understanding of the underlying mechanisms in order to generate experimentally testable predictions. Reaction–diffusion systems are commonly used to this end; however, the

analysis of coupled nonlinear systems of partial differential equations, generated by considering large reaction networks is often challenging. Here, we aim to provide an introductory tutorial for the application of reaction–diffusion models to the spatio-temporal dynamics of signaling pathways. In particular, we outline the steps for stability analysis of such models, with a focus on biochemical signal transduction.

C.1 Introduction

Biochemical signal transduction is critical for information transfer from the extracellular environment to the intracellular structures. The spatio-temporal activation profile of signaling proteins affects the gene expression patterns and can result in different functional responses within the cell. Furthermore, specificity of signaling is determined by the spatial and temporal dynamics of the downstream components [259]. The localization of the signaling components to the various subcellular locations including internal membranes and membrane microdomains has a strong impact on cellular function [259].

Spatial segregation of enzymes can lead to intracellular concentration gradients of signalling molecules [259, 260]. Using a mathematical model for a membrane bound activator and a cytoplasmic inactivator, it was shown that cell size and shape control signaling pathways; the resulting intracellular gradients can be used to define regions where specific enzyme reactions may proceed and other regions where the reactions may not proceed [260]. This work highlighted the role of spatial segregation of the activator and deactivator. When the activator and inactivator are both present in the same cellular compartment, there will be no gradient of the activated state of the signaling component. This is particularly relevant to events such as phosphorylation (spatial separation of kinase and phosphatase) and GTPase activation (spatial separation of guanine nucleotide exchange factor (GEFs) and GTPase activating protein (GAPs)) and in general for the role of spatial compartmentalization and shape in the generation of signaling gradients [98].

In addition to dynamics governed by the different compartments of the system, the nature of the temporal dynamics can also affect the signaling dynamics. Signaling cascades exhibit a large variety of dynamical features such as multistability [261–263] and oscillations [172, 264, 265], which are often parameter dependent. Coupling these dynamical behaviors with their spatial counterparts can then give rise to very interesting spatial patterns depending on the balance

between reaction and diffusion. However, the analysis of partial differential equations, particularly studying the dependence of the system response on parameters is non-trivial. The stability analysis of partial differential equations is a complex topic that is contained in many mathematics textbooks [266–269], but not often presented in a manner accessible to a systems biologist. Therefore, we provide here a tutorial that introduces the stability analysis of reaction-diffusion equations.

This tutorial begins with a broad overview of spatio-temporal dynamics of pattern formation at multiple scales in biology (Figure **C.1**A) and lays out a general modeling framework. Then using three specific examples, we demonstrate how to conduct the stability analysis. We envision that this tutorial will enable the reader to carry out preliminary analyses of parameter space for reaction-diffusion equations and set the stage for more detailed analysis.

C.2 Pattern formation and reaction-diffusion equations at different scales

C.2.1 Turing patterns: reaction diffusion models at the organism scale

The history of pattern formation in reaction-diffusion systems can be traced back to Alan Turing [270]. In 1952, Turing showed that under specific conditions, the solution of reaction-diffusion equations can result in the formation of stable patterns [270]. The primary feature of such a model system is a short-range activation and a long-range inhibition [271]. The resulting competition between the different diffusion rates can then lead to formation of stable patterns. Although the reactions in the original model were between two sets of hypothetical molecules randomly diffusing and reacting, the analysis is a central feature of studying reaction-diffusion equations. Subsequently, Murray and others expanded this idea to propose that the formation of animal coat patterns could be explained by Turing patterns (Figure **C.1**A). Of course, these patterns are at the length scale of an organism, significantly larger than the length scale of single
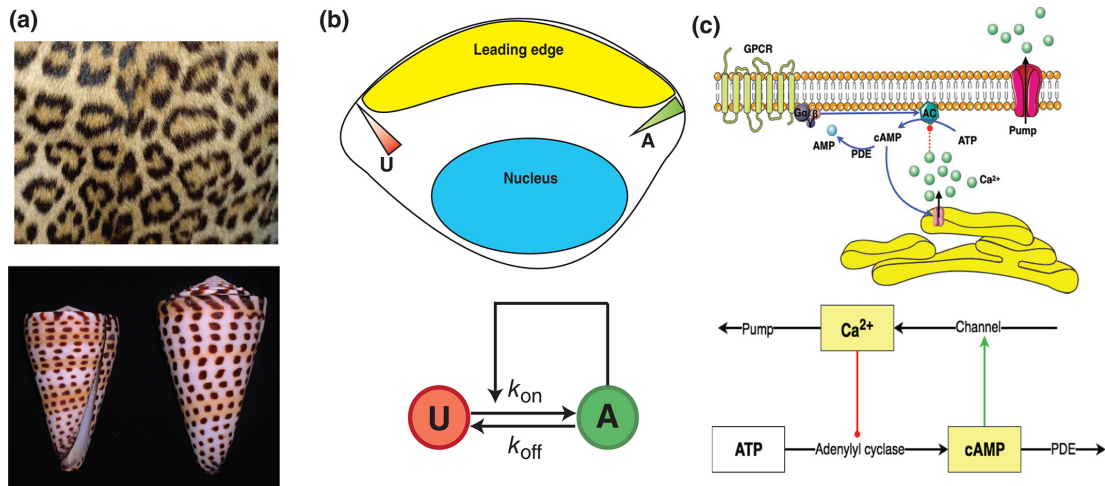
Figure C.1: Examples of spatio-temporal patterns at different biological length scales. (a) Organism length scale patterning is seen in leopard spots (top) and conus sea shells (bottom) (Source: Wikimedia commons, open access images). (b) Cellular length scale patterning during cellular polarization with Rho/Rac during chemotaxis. (c) Second messenger signaling and cross talk between cAMP and Ca^{2+} is an example of a spatio-temporal signaling response of small molecules within cells.

cell signaling, and even though no particular morphogen has been identified with coat patterns, the phenomenological framework using the Turing model to explain the stripes and spots of animals helps us understand the balance between diffusion and chemical reaction rates and how these manifest themselves as "diffusion-driven instabilities" [263].

More recently, Turing patterns have been applied to the analysis of fish stripe patterns [272] and sea shell patterns [273]. Kondo and colleagues showed that during sexual conversion in two species of *Genicanthus*, which share almost all of their morphological properties, the directional stripe patterns arise transiently in random positions and computational analysis using Turing patterns can be very powerful in analyzing the evolution of these patterns. Additionally, Meinhardt *et al.* [273] had previously shown pigment patterns in *mollusc* shells can be explained through Turing patterns (Figure **C.1**A). We reproduce the analysis of the classical Turing model in Section **C.5.1**.

C.2.2   Pattern formation in development: reaction diffusion models at the tissue scale

Pattern formation is a critical part of embryonic development and maturation determining cell sorting and cell fate. During vertebrate limb development, chondrogenesis, a process involving precartilage condensation occurs periodically along the anterior-posterior axis of the distal tip region. Since this region has no pre-existing periodic pattern, a Turing-like model was suggested to be a potential underlying mechanism [274]. Subsequently, transforming growth factor β (TGF-β) was hypothesized to be the molecule responsible for the observed cell sorting during development [275]. Miura *et al.* also showed that the behavior of TGFβ2 exemplifies a system capable of satisfying the Turing pattern requirement of short-range activation, through TGFβ2 mRNA promotion, and long-range inhibition criteria, through a lateral inhibitory mechanism [275], which is as yet unknown. Studies on this mechanism constitute ongoing research [276].

Another dramatic example of pattern formation within tissues can be seen in in the Drosophila eye, which is formed from 800 ommatidia structures [277]. Each ommatidia has 20 distinct cells and the cells in the ommatidia and the ommatidia themselves arrange in a very precise repeating pattern resembling a crystalline structure [278]. The formation of this complex structure is driven by a cell-to-cell signaling cascade and drives the observed specification of cell order in the tissue. The signaling interaction that drives this cellular patterning is thought to be the Notch-Delta cascade for lateral inhibition. Which as *Physical biology of the cell* describes as "a process in which one cell assumes a particular fate and then communicates that fate to neighboring cells preventing them from doing the same thing, allowing for a separate fate" [278]. Notch-Delta signaling leads to a spatially inhomogeneous assembly of cells during development and "salt and pepper patterns" [277, 278].

C.2.3 Patterns within cells: intracellular signaling

The idea of Turing pattern formation can be easily extended to intracellular signaling, since the cascade of biochemical reactions often display non linear chemical kinetics [278]. An excellent example of this is the activation of the small Rho GTPases, Rho and Rac for cell polarization through spatial amplification (Figure **C.1**B). It has been shown that the system of three Rho GTPases involved in cell polarization Cdc42, Rac, and Rho, can be reduced to a pair of active and inactive proteins in a phenomenological model (Figure **C.1**B) [279]. Mori *et al.* [262] used the simplified model to identify the wave-pinning behavior of Rho and Rac during cell polarization, which we will discuss as an example in this tutorial (Section **C.5.2**).

Intracellular signaling-related patterns are also observed in bacteria; polarization may also be caused by transient signals such as the dynamics of the Min proteins in *E. coli* [280]. The main polarization arises from the binding of Min D and Min E, which delocalizes the previously membrane associated MinD into the cytosol. This interaction results in a wave of high MinE concentration traveling from the cell center to a pole, where it dissipates. MinD reassembles on the membrane at the other pole and attracts a fresh pool of MinE, causing the wave-like disassembly of MinD again. This model explains the pole-to-pole oscillation of MinC/D and how this impacts the assembly of the bacterial cytoskeletal protein FtsZ in the center of the cell prior to cell division.

Second messenger molecules such as Ca^{2+} and cAMP are central to many signaling pathways, including G-protein coupled receptor signaling and growth factor signaling [281, 282]. Both these second messengers are known to exhibit oscillatory dynamics, a feature critical to their function in cells [264]. Additionally, the formation of cAMP microdomains and Ca^{2+} sparks and waves are examples of small molecules effecting distinct spatio-temporal patterns to regulate signaling and downstream effects at specific locations in cells. Not only do these two small molecules regulate a multitude of processes, they also interact (Figure **C.1**C) to

couple their dynamic behavior and generate signaling crosstalk downstream of receptors [172]. A phenomenological model for second messenger signaling is explored in Section **C.5.3**.

C.3   Spatio-temporal modeling of signaling: the need for analysis

Mathematical models have proven to be extremely useful in elucidating the properties of biological signaling networks [39, 283, 284]. While well-mixed models of signaling can be described using ordinary differential equations (ODEs) to quantify the dynamics of various signaling components, in order to consider the spatial aspects of signaling, we need to consider reaction-diffusion models that can be described using partial differential equations (PDEs) [99, 227, 285].

Signaling models often result in systems of coupled non linear partial differential equations, with multiple parameters. Non linear models often exhibit a rich behavior as parameters are varied, making analysis of these systems challenging. One way to analyze these systems of PDEs is to conduct simulations across a range of parameters. There have been an increasing number of tools to computationally model signaling that use finite-element, finite-volume and finite-difference methods [286]. The finite-element solution method (FEM) reduces the PDE form to an intergral differential equation for an approximate solution aiming to minimize error with a fast solution. Finite difference (FD) uses the surrounding spatial coordinates to convert the PDE into a system of linear algebraic equations in an explicit (uses the current timestep), or implicit (uses the next time step, found through analytic methods) fashion. Finite volume method is similar to FEM and FD except that this method uses the volume integral of the governing equation. Commercial examples for a finite difference solver include MATLAB's 1D finite difference solver *pdepe*. Commercial examples of a finite element solver is COMSOL's PDE solver. Since, many other tools have been developed to help with modeling signaling networks such as VCell [287]

and MCell [288–290].

Despite the tools available to numerically solve PDEs, it is important to understand some basic features about the stability behavior of these equations for a variety of reasons. One, simple analysis methods help us identify the parameter space that we want the system to operate in. Two, understanding how the structure of the equations govern their steady state behavior can inform the development of new models. And three, experimental design for both *in vitro* and *in vivo* systems can be informed by the analysis of key components (see the Rho/Rac example in Section **C.5.2**).

One of the ongoing challenges facing the systems biology community is that the methods of analysis are often found in mathematics textbooks and the material may or may not be accessible to a researcher wishing to conduct such an analysis. This tutorial aims to provide an example based approach on how to conduct stability analysis for PDEs, with the examples geared towards cell signaling. This material is not intended to replace the mathematical biology textbooks but to present a gentle introduction to a complex topic and lowering the barrier to cross-disciplinary study. All Mathematica and MATLAB files used are provided as supplementary material.

C.4 General model framework: how to conduct analysis

C.4.1 Reaction-diffusion equations

We consider chemical reactions occurring along a one-dimensional segment ($0 \leq x \leq L$), which serves as an approximation of a transection of the cell. Here, we provide a general example with two species U and A. We denote the concentrations of these species as u and a respectively,

both in units of molecules/length. The partial differential equations are:

$$\frac{\partial a}{\partial t} = D_a \frac{\partial^2 a}{\partial x^2} + f(a,u)$$

$$\frac{\partial u}{\partial t} = D_u \frac{\partial^2 u}{\partial x^2} + g(a,u). \tag{C.1}$$

The choice of functions $f(a,u)$ and $g(a,u)$ are dependent on the type of the reactions being modeled, $f(a,u)$ and $g(a,u)$ often contain parameters that represent the reaction rate constants. We will first outline the general analysis method to understand the steady state behavior and then apply it to three specific systems to demonstrate its usefulness. We note that this material can be found in textbooks that discuss analysis of PDEs [263, 267, 268] and is succinctly reproduced here for completeness.

C.4.2   Stability analysis for the well-mixed system

The first step is to find *steady state* solutions (a^*, u^*) of the purely kinetic system (in the case of homogeneous spatial conditions, i.e. "well-mixed"), we solve for $(f(a,u), g(a,u)) = (0,0)$. Additionally, in some systems, if A and U are conserved, we impose that the initial amount of A(A_0) and U(U_0) satisfies $P = U_0 + A_0 = U(t) + A(t)$, where P is a constant denoting the total amount of species. Depending on the form of $f(a,u)$ and $g(a,u)$, multiple steady states may exist.

Note that these *homogenous equilibria* also serve as steady states for the spatially extended system. We wish to analyze their stability throughout the parameter space. We must therefore linearize the functions $f(a,u)$ and $g(a,u)$ to discern their behavior. After linearizing around $a(t)$ and $u(t)$ by a taylor series expansion where Δa and Δu are small, the function returns as,

$$\frac{\partial \Delta a}{\partial t} = f(a(t), u(t))_a * (\Delta a) + f(a(t), u(t))_u * (\Delta u) + O(|a|^2) + O(|u|^2)$$

where $f(a(t), u(t))$ is the function value at time t and $f(a,u)_a$, $f(a,u)_u$ denote the partial derivatives of $f(a,u)$ with respect to a and u. The linearized expression can then be shown in the form of a Jacobian, $[\frac{\partial \Delta a}{\partial t} \ \frac{\partial \Delta u}{\partial t}]^T = J|_{(a^*,u^*)}[\Delta a \ \Delta u]^T$. The Jacobian matrix for the purely kinetic system is therefore,

$$
J|_{(a^*,u^*)} = \begin{pmatrix} f(a^*,u^*)_a & f(a^*,u^*)_u \\ g(a^*,u^*)_a & g(a^*,u^*)_u \end{pmatrix}.
\tag{C.2}
$$

Note this method of analysis only holds int the local area around the *homogenous equilibria* and fails if the point is too far or second order effects are not negligible.

Next, for the well mixed system, we look at the eigenvalues, denoted as λ, of the *Jacobian matrix* to analyze the linear stability of these states under small perturbations from equilibrium [267]. An equilibrium point is said to be stable if the eigenvalues of the $J|_{(a^*,u^*)}$ all have real parts less than or equal to zero and unstable if any one eigenvalue has a real part greater than zero. For certain choices of reaction parameters, both two stable and one unstable steady states exist; this is called the *bistable regime*. Within this region, either of the two steady states may be reached for the same set of kinetic parameters, depending on the initial conditions of the system (*i.e.*, the 'starting' concentrations). Bistability is a common feature in biochemical reaction networks, particularly those containing positive feedback loops [291]. Through bistability, positive feedback loops may allow for a sustained cellular response to a transient external stimulus [291], a central feature in cell polarization. For example, in bistable systems such as MAP kinase, there are two stable steady states and one unstable steady state and a sustained response upon stimulation is exibited [281, 292].

C.4.3 Stability analysis for the spatial model

What happens when we consider a spatially heterogeneous system? In order to obtain the spatially heterogeneous solutions, we linearize Equations (**C.1**) about the steady state to obtain,

$$
\frac{\partial}{\partial t}
\begin{bmatrix} \Delta a \\ \Delta u \end{bmatrix}
=
\begin{bmatrix} D_a & 0 \\ 0 & D_u \end{bmatrix}
\frac{\partial^2}{\partial x^2}
\begin{bmatrix} \Delta a \\ \Delta u \end{bmatrix}
+ J
\begin{bmatrix} \Delta a \\ \Delta u \end{bmatrix}.
\tag{C.3}
$$

Here, J is the Jacobian for the (spatially homogeneous) reaction equations. In order to analyze the stability of this system with respect to perturbations, we must first note that now these perturbations depend both on time and space. A convenient form for such perturbations is $\frac{\partial}{\partial t}[\Delta a \; \Delta u] = [\Delta a \; \Delta u] e^{-\lambda t} e^{ikx}$, where the term e^{ikx} is a common way of representing a spatial wave, where k is the wavenumber of the Fourier mode (we refer the interested reader to [268]). Substituting this into the linearized Equation (**C.3**) leads to the Jacobian of the spatially extended system

$$
J^* =
\begin{pmatrix}
f(a,u)_a - D_a k^2 & f(a,u)_u \\
g(a,u)_a & g(a,u)_u - D_u k^2
\end{pmatrix}.
\tag{C.4}
$$

The eigenvalues of this matrix allow us to study the stability properties of the system: nonnegative eigenvalues correspond to a loss of stability of the system. Since the eigenvalue expressions contain the unknown parameter k, we consider a *one parameter family of solutions*, one for each wavenumber. Note that the eigenvalues for the well-mixed system are achieved when $k = 0$. Primarily, we are interested in the emergence of heterogeneous patterns that occur via perturbations within a finite range of critical wavenumbers $0 \leq k_c \leq k_{\max}$ [263, 268] .

The value of these critical wavenumbers becomes important when we are faced with a finite domain size. Since cells are of finite size, we want to investigate how the length of the domain affects the system response. This is because the spatial pattern that emerges from an instability corresponding to a wavenumber k has wavelength $\omega = \frac{2\pi}{k}$; accordingly, for

finite systems, only values of k above a certain threshold will generate any meaningful spatial patterns [263, 268] .

These equations can also be normalized through diffusion [263] to receive:

$$J^* = \begin{pmatrix} \gamma f(a,u)_a - k^2 & \gamma f(a,u)_u \\ \gamma g(a,u)_a & \gamma g(a,u)_u - Dk^2 \end{pmatrix}.$$
(C.5)

where γ is the "scale factor" ($\gamma = \frac{S}{D_a}$) correcting for the size of the domain (S) and $D = \frac{D_u}{D_a}$ thus allowing easier relation of diffusive ratios to stability profiles. The normalized 2 component case is expanded and applied in Section **C.5.1**.

C.5 Examples of spatio-temporal dynamics

In this section, we demonstrate the above analytical protocol using three examples, each representing a distinct origin of spatial patterning. First, we discuss Turing's "diffusion-driven instability" using morphogenesis as a classical example. Second, we consider a situation in which spatial patterns arise even though the criteria for Turing instabilities are not met, via the "pinning" of a traveling wave. To illustrate this phenomena, we turn to a simple model of eukaryotic cell polarization. And finally, we demonstrate using a four-component example, how oscillations in second messenger signaling can be analyzed to identify the governing length and time scales of the system.

C.5.1 Patterns in organisms: "how the leopard got its spots"

Morphogenesis, the process by which an embryo gains its structure during development, is one of the most studied problems in biology. In particular, Turing's model of pattern formation, originally applied to the development of animal coat patterns [270], proved useful for describing this phenomenon. Murray [263] used and analyzed the following system of non linear reactions,

which has since become the classical example of the Turing instability. In this system, $f(a,u)$ and $g(a,u)$ are described as follows:

$$f(a,u) \quad = b-a-\frac{\rho au}{1+a+Ka^2} \tag{C.6}$$

$$g(a,u) \quad = \alpha(c-u)-\frac{\rho au}{1+a+Ka^2},$$

where b, α, ρ, K, and c are positive parameters. Since, modified and more complex networks for Turing pattern generation have developed [293–295].

Well-mixed model

We first begin with the analysis of the well-mixed model before considering the full reaction-diffusion system. This system has two homogeneous steady states, which are obtained by solving $f(a,u)=0$ and $g(a,u)=0$. The solutions to $f(a,u)=0$ and $g(a,u)=0$, which are the nullclines are shown in Figure **C.2**(A). The intersection of the two nullclines gives the three fixed points for a and u. We denote them (a_1^*,u_1^*), (a_2^*,u_2^*), and (a_3^*,u_3^*). These solutions depend on the different parameters present in $f(a,u)$ and $g(a,u)$. An analytic solution can also be found by rearranging the equations to obtain a cubic equation and finding its roots. All non-imaginary positive solutions are admissible but we do not explicitly write out the cubic expression for the sake of brevity.

Next, we construct the Jacobian of this system to obtain

$$J = \begin{pmatrix} \frac{\rho u(Ka^2-1)}{(1+a+Ka^2)^2} - 1 & \frac{-a\rho}{1+a+Ka^2} \\ \frac{\rho u(Ka^2-1)}{(1+a+Ka^2)^2} & -\alpha - \frac{a\rho}{1+a+Ka^2} \end{pmatrix}. \tag{C.7}$$

We then evaluate the eigenvalues of this Jacobian matrix for the different steady states. Under certain parameter choices, we receive three solutions (remembering to ignore any imaginary solutions to the cubic equation) we now evaluate the stability of these points. For these sets, (a_1^*,u_1^*) and (a_3^*,u_3^*) return negative eigenvalues for the Jacobian meaning they are stable. However

for (a_2^*, u_2^*) the eigenvalues of the Jacobian has positive real parts, indicating that (a_2^*, u_2^*) is unstable and in the presence of any perturbations at (a_2^*, u_2^*) the system will head to the solutions (a_1^*, u_1^*) or (a_3^*, u_3^*). The solution space depends on the model parameters. In Figure **C.2** B and C, we show how the solution space for a^* depends on the parameters b and c respectively.

Spatial patterns

The criteria for an equilibrium point to undergo a diffusion-driven instability are as follows.

- First, the equilibrium point must be stable for the purely kinetic system and the loss of stability in the steady state must be purely spatially dependent, so we can consider (a_1^*, u_1^*) or (a_3^*, u_3^*) but not (a_2^*, u_2^*). In other words they must satisfy the conditions:

$$f_a + g_u < 0 \tag{C.8}$$

$$f_a g_u - f_u g_a > 0 \tag{C.9}$$

to make the eigenvalues of the Jacobian positive and therefore stable for the kinetic system.

- Second, the Jacobian of the spatially extended system must satisfy the following to undergo a spatial instability:

$$\text{tr}(J^*) = Df_a + g_u > 0, \tag{C.10}$$

$$\det(J^*) = (Df_a + g_u)^2 - 4D(f_a g_u - f_u g_a) > 0. \tag{C.11}$$

For the above system, the conditions for the Turing mechanism are met, and spatial patterning through a diffusion-driven instability can occur. Note that there are six parameters left in the system, including $D = D_u/D_a$, b, c, K, α, and ρ. In Figure **C.2**, we fix K, α, and ρ and study the effect of D on the phase space admitting Turing patterns over the ranges of parameters b and c.
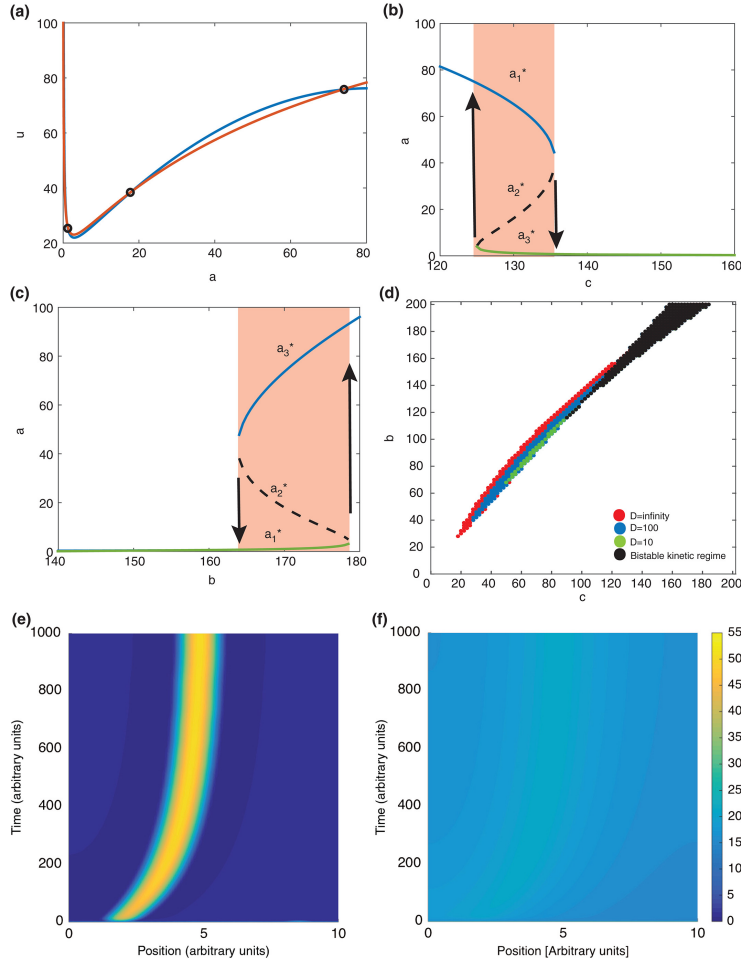
Figure C.2: Steady state behavior for the Turing model. For (a)-(d), The following parameters are fixed as follows: $\alpha = 1.5, \rho = 13, K = 0.125, b = 160, c = 140$. (a) The nullclines show the intersection of $f(a,u) = 0$ and $g(a,u) = 0$ and the three steady states at the chosen parameters. (b) Variations of the parameter c and (c) variations of the parameter b affect the steady states of a. The two stable steady states a_1^* and a_3^* are shown as solid blue and green lines, respectively; the unstable steady state a_2^* is shown as a dashed line. (d) Region of parameter space in the system (Eq. **C.7**) that allows for Turing patterns for the ratio of diffusion constants $D = D_a/D_u$: $D = 10^{-1}$ (green), $D = 10^{-2}$ (blue) and $D = 0$ (red). As the D increases, the region over which Turing patterns can be observed increases. (e-f) Simulations of Eq. **C.7** were conducted in MATLAB's 1D PDE solver *pdepe*. The parameters used were $\alpha = 1.5, \rho = 13, K = 0.125, c = 80, b = 100$, and $D_a = 0.1$. For a system size for L=10 a single stripe appears at the center. Concentrations of a (e) and u (f) are shown. Initial conditions were set as randomized along x around the values [a,u]=1.

When $D = 10$, the range of b and c over which Turing patterns are observed is small. However, as D increases, the range of b and c increases. Biologically, this means when U diffuses much faster

than A, the range of parameters *b* and *c* over which Turing patterns can be observed increases. For more details on linear instabilities via the Turing mechanism, we again refer the interested reader to [263]. A representative pattern is shown in Figure **C.4**, where MATLAB's 1-D PDE solver, *pdepe*, was used to generate solutions based on initial conditions randomized along the spatial dimension, *x*, around the values [a,u]=1.

Key takeaway points

Classical Turing systems consist of two components, usually an activator and an inhibitor. Since Turing's original paper on pattern formation via a reaction-diffusion mechanism, several models have been proposed that are applicable to a wide variety of biochemical problems [293–295].

Above, we have described and analyzed Thomas' model for substrate inhibition based on experiments in which an immobilized enzyme on a membrane reacts with diffusing substrate and co-substrate molecules [296]. This model, and several others proposed after it [297, 298] help us understand biologically plausible mechanisms of signaling. Some of the key points to note from studies of Turing patterns are noted below.

1. **Specific kinetics are required for Turing patterns.** Two component mechanisms, like the one described in Eq. **C.7**, can generate spatially heterogeneous patterns. Whether or not systems are capable of generating spatial patterns through a Turing mechanism depends on the reaction kinetics. In particular, we have outlined the conditions required in Eqs. **C.8**,**C.10**,**C.11**. In general, these systems crucially have an activation-inhibition form (Figure **C.1**A). Further details on such mechanisms can be found in [263].

2. **Diffusion can lead to instabilities under certain conditions.** Given that the kinetics fulfill the conditions outlined above, Turing instabilities can arise only if the ratio of

diffusion constants, $D = D_u/D_a \neq 1$. These spatial heterogeneities arise especially when the diffusion constant of the activator in the system is smaller than that or the inhibitor (called LALI, or "local activation, lateral inhibition" mechanisms). The concept of diffusion-driven instability was groundbreaking when it was first proposed because diffusion was long-considered to be a stabilizing presence.

C.5.2 Cell polarization

Polarization is fundamental to eukaryotic motility, morphogenesis, and division. Cell polarization is the process of reorganization of the cytoskeleton into distinct front and back regions in response to a stimulus. Recently, Mori *et al.* [262] presented the "wave pinning polarization" or WPP model, a minimal model of cell polarization, that demonstrated both bistability and spatial patterning. In this system, the kinetics of the two species are given by:

$$f(a,u) = u\left(k_0 + \frac{\gamma a^2}{K^2 + a^2}\right) - k_{off}a \qquad (C.12)$$

$$g(a,u) = -f(a,u) = -u\left(k_0 + \frac{\gamma a^2}{K^2 + a^2}\right) + k_{off}a.$$

After their initial proposal of the WPP model [262], the authors considered several important extensions [299–301]. However, a full characterization of the equilibrium behavior of the system as a function of the properties and amount of the GTPases has been rarely discussed. In one study, local perturbation analysis was utilized to discuss system behavior in terms of the GTPase properties [302]. In this section, we outline such a characterization for the basal rate of activation k_0 and the average amount of total protein p.

Well-mixed model

As before, we begin by analyzing the reaction-only ODE model before considering the full reaction-diffusion system. The WPP model has three steady states, which we denote (a_1^*, u_1^*),

(a_2^*, u_2^*), and (a_3^*, u_3^*). To assess the stability of each of these steady states, we look at the *Jacobian matrix* of the system:

$$J = \begin{pmatrix} \frac{2auK^2\gamma}{(a^2+K^2)^2} - k_{\text{off}} & k_0 + \frac{\gamma a^2}{K^2+a^2} \\ -\frac{2auK^2\gamma}{(a^2+K^2)^2} + k_{\text{off}} & -k_0 - \frac{\gamma a^2}{K^2+a^2} \end{pmatrix}.$$
(C.13)

Example equilibrium curves for $\gamma = 1, k_{\text{off}} = 1, K = 1$ are shown for various values of average total protein p in Figure **C.3**. For the WPP model, a_1^* and a_3^* are stable (shown as green and blue solid lines, respectively), while a_2^* is unstable (shown as a black dashed line). To illustrate this, consider the basal rate parameter k_0 as a function of an external stimulus S (*i.e.*, $k_0 = k_0^* S$). Now, we can look to the plots in Figure **C.3** as dose-response curves — the cell responds to external stimulus S by producing the activated protein A.

As S (and consequently k_0) is slowly increased, the concentration of A follows along the curve corresponding to a_1^* (green) until it crosses the bistable region, after which the equilibrium value is suddenly larger at a_3^* (blue). If the stimulus is removed, and the level of S decreases, the higher-valued equilibrium is maintained within the bistable region; this behavior, where the dose-response relationship is in the form of a loop rather than a curve, is called *hysteresis*. If the bistable regime is large enough, in particular if it extends to $k = 0$, an essentially irreversible response to transient stimuli may be elicited (as is seen for $p = 3$ in Figure **C.3**(D)).

Figure **C.4**(a) shows the bistability region for the WPP model as the total average protein concentration p and the basal activation rate k_0 are varied. From the sloping shape of the bistable region, we can see that for sufficiently high values of total protein (for the set of parameters in Figure **C.4**(a) (gray region), $p \geq 3$), an 'irreversible' response may be generated: both steady states are stable even when the stimulus is removed, at $k_0 = 0$.

1-D spatial model

Having characterized the bistable regime of the well-mixed model, we now turn our attention to the full reaction-diffusion system. The homogenous equilibria also serve as steady states for the spatially extended system and as before, we are interested in their stability throughout the parameter space.

Recall that for the spatially homogenous system, we turned to the Jacobian to analyze the linear stability of these states under small perturbations from equilibrium. The eigenvalues of J are

$$\lambda^{\pm} = \frac{1}{2}\left[(f_a - f_u - (D_A + D_U)k^2) \pm \sqrt{(f_a - f_u - (D_A + D_U)k^2)^2 - 4(D_A D_U k^4 + (D_A f_u - D_u f_a)k^2)}\right].$$

(C.14)

As the expressions for the eigenvalues now contain the additional unknown k, we are now interested in a *family of solutions*, one for each wavenumber. The eigenvalues for the nonspatial system are achieved when $k = 0$, and are given by $\lambda^- = f_a - f_u$ and $\lambda^+ = 0$; therefore any spatially homogeneous perturbation will relax back to the spatially uniform steady state. We are instead interested in the emergence of heterogeneous patterns that occur via perturbations within a finite range of critical wavenumbers $0 \leq k_c \leq k_{max}$.

The region of 'linear instability' is highlighted in orange in Figure **C.4** (b) for $k = 0.2$ μm^{-1}. This corresponds to a pattern of wavelength $\omega = \frac{2\pi}{k} \approx 30$ μm. This length scale is intermediate among the motile eukaryotic cells that use Rho GTPases to generate polarity. In this region, one or both of the steady states, (a_1^*, u_1^*) and (a_3^*, u_3^*), lose stability with respect to an inhomogeneous perturbation as shown above (see Figure **C.4** (b)).

We note that the region computed is for diffusion coefficients $D_U = 10\,\mu m^2 s^{-1}$ and $D_A = 0.1\,\mu m^2 s^{-1}$. A similar parameter topology (with slightly larger regions of instability) was found in a reduced one-species model where infinite cytoplasmic diffusion was assumed [303]. The

disparity in diffusion coefficients assumed in Figure **C.4** presupposes the compartmentalization of the two species: a protein diffuses far more slowly on the membrane than in the cytosol (here, we assume the ratio of diffusion coefficients to be ≈ 0.01 [304]). In the following sections, we will assess the importance of this presumption. In addition, the parameter space for the full model can admit a surrounding region where front-like solutions are observed. In this region, a stalled wave can appear when the system is subjected to a directed stimulus (e.g., a gradient), sufficiently 'noisy' initial conditions, or if the domain exhibits some intrinsic polarity at $t = 0$. The parameters chosen by Mori *et al.* fall within this region; their simulations demonstrate that this 'intrinsic polarity' may arise via 'sufficiently noisy' initial conditions, as seen in Figure **C.4** [262]. It is important to note that all patterns are similar and only differ due to different initial conditions (as in what side the wave pins on). [305]

To find solutions allowing this stalled wave solution we look for a solution containing a critical value of species u, u_c, which is in the bistable regime. u_c describes the point at which the 'wave front' speed switches sign, and therefore is the solution with no 'wave front'. The boundaries of this regime are calculated by solving for values where the forward rate of reaction, $u_c \left(k_0 + \frac{\gamma a^2}{K^2 + a^2} \right)$, equals the reverse rate, $k_{off}a$, across the high, a_+, and low, a_-, solution. This solution is called the Maxwell condition and admits the ranges of u in which a stalled wave is possible: [262]

$$I(b) = \int_{a_-}^{a_+} f(a, u) da = 0. \tag{C.15}$$

We then use the mass conservation condition to compute this region in (k_0, p) space. While this is not analytically feasible for the WPP model, numerically solving the integral provides an accurate characterization of this region. The method outlined here is not specific to the WPP model, or even to models of cell polarity. To make such a phase-space analysis more accessible to the biological community, we provide an easy-to use GUI to allow readers to analyze the stability properties of other systems of interest.

A representative wave pinning pattern generated using MATLAB's 1-D PDE solver, *pdepe*, is shown in Figure **C.4**. To induce a spatial gradient initial conditions were set as the basal solution of (a_1^*, u_1^*), then a_1^* was set as $2a_1^*R$ where R is a random number between 0 and 1. To obtain a spatially differing solution the random distribution of R must be heavy towards one side of the cell.

Key take-away points

The analysis above provides us significant insight into the behavior of the WPP model throughout the parameter space (Figure **C.4**). Using this, we can point out several notable properties of the model as they pertain to cell polarization. We note these below properties are predicted using analyses performed on a 1D spatial model. Extension of the model to three, or even two, dimensions may (and likely do) result in different behaviors [306].

1. **Importance of compartmentalization:** The Rho GTPase family is large and varied, and is present in eukaryotes spanning from *C. elegans* to humans. However, one common feature of these proteins is *compartmentalization*: the active form is bound to the membrane, while the inactive form diffuses in the cytoplasm [307]. This feature has been shown to be important for cell polarization [262, 299, 300]. We illustrate the necessity of membrane localization by considering how the phase space of the WPP model in Figure **C.4** changes if both species are contained in the cytoplasm.

   Qualitatively, the dependence of polarization on compartmentalization is relatively intuitive. As A and U constitute GTP- and GDP-bound versions of a single protein, their cytoplasmic diffusion rates are likely very similar. Given this, one would not expect the formation of any sort of regular pattern with no initial spatial structure.

   We show this quantitatively by defining the ratio of the diffusion rates $D = D_A/D_U$, and

considering the effect of this quantity on the regimes allowing spatially heterogeneous solutions. For one membrane-bound and one cytoplasmic species, we take this ratio to be ≈ 0.01 [304].

When $D = 1$, no spatially heterogeneous patterns can be generated, and this region disappears altogether. However, as D decreases, spatial patterns are supported for a finite range of wavenumbers (Figure **C.4**(b)) [299]. As the rate of diffusion of U increases, the maxima of $\lambda(k)$ move towards $k = 0$, eventually displacing the uniform steady state in the limit $D_U \to \infty$ [303]. This trend is not symmetric — as D increases from 1, there is no consequent extension of the multistable regime. This is similar to the formation of Turing patterns in local excitation, global inhibition models; for an overview of this brand of models with respect to cell polarization, we refer the reader to several excellent reviews [262, 300, 306].

2. **Benefit of being big:** In addition to the importance of different diffusion rates between active and inactive forms, we can use the fact that the range of critical wave numbers is bounded above to consider the existence of a corresponding *lower bound* on the length of the cell L.

   The value of the maximum critical wavenumber $k_{\max}$ for a feasible value of D is quite low (Figure **C.4**). This suggests that smaller cells are less sensitive to polarization, while larger cells are able to respond more robustly. Interestingly, this result has been observed experimentally: cells were found to become significantly more sensitized as they were flattened in a confined channel [260, 308, 309] .

3. **Spontaneous polarization:** Recall that k_0 can be written as a function of the concentration of some stimulus S: $k_0(S) = k_0^* S$. This formulation allows us to characterize parameter values which allow for *spontaneous polarization* in the absence of a directed external stimulus.

Certain, but not all, cells are able to spontaneously self-polarize. In the WPP model, we consider the regimes crossed in Figure **C.3**(d) by the line $k_0 = 0$. We see that polarization in the absence of a stimulus is possible if the value of p is sufficiently high. Given sufficient initial conditions, due to the slow diffusion of a, the value of p will increase only on one side of the cell to achieve sufficient p concentrations. This is consistent with experimental observations that the constitutive expression of Rho GTPases result in extension of randomly oriented lamellopodia and membrane ruffling [310] .

4. **Polarization strategies:** The parameter space topology for the WPP model contains two distinct regions that allow for non-homogenous equilibrium solutions. Because of the choice of parameters in Mori *et al.* [262], the system behavior in only one of these regions, corresponding to stalled-wave solutions (shaded in blue in Figure **C.3**) was explored.

   In general, Turing patterns form more easily (*i.e.*, in response to far smaller perturbations) than patterns formed by a wave-pinning mechanism. However, they occur on a far slower timescale [262, 300, 306]. The existence of a Turing-like instability regime in addition to a region which admits stalled-wave solutions presents cells with multiple strategies for polarization.

C.5.3   Second messenger signaling and oscillations

In this section, we demonstrate the stability analyses as applied to a phenomenological model of second messenger signaling. Small molecules such as cAMP and Ca^{2+} play important roles in intracellular signaling. These two molecules play critical roles in many cell types, including smooth muscle cells and neurons [311, 312]. The frequency and amplitude modulation of Ca^{2+} sparks by contractile and relaxant agents is an important mechanism regulating smooth muscle function [311]. In neurons, voltage-gated Ca^{2+} channels initiate synaptic transmission [313–315].

In the hippocampus, the presence of AC types I and VIII and its sensitivity to Ca^{2+} stimulation implicates AC in mammalian learning and memory, along with hippocampal long-term potentiation. The critical component to this AC interaction is the evidence that increased glutamate NMDA-receptor-mediated Ca^{2+} entry is associated with a cAMP elevation [172]. Through this interaction a network loop connecting cAMP to Ca^{2+} was developed by Cooper *et al.* (Figure **C.1**C).

Both Ca^{2+} and cAMP are also known to oscillate and form cellular microdomains, spatially restricting their signaling feature. cAMP signaling is mediated by the canonical signaling pathway of the α subunits of G-proteins regulating adenylyl cyclase (AC) activation. Adenylyl cyclase is an enzyme that catalyzes the synthesis of cAMP from ATP. On the other hand, the canonical signaling through Ca^{2+} is through the binding of IP_3 to IP_3 receptors on the endoplasmic reticulum (ER), releasing Ca^{2+} from the ER stores. Experiments also show that cAMP and Ca^{2+} oscillate and regulate each other through stimulation or inhibition of specific AC isoforms. In some cases, protein kinase C (PKC), Ca^{2+}, and $G_{\beta\gamma}$ subunits are thought to stimulate or inhibit specific AC isoforms more effectively than the G_{α} unit. Specifically, the stimulation of ACs type I, III, and VIII is mediated by calmodulin. The mechanism of action of Ca^{2+} on AC isoforms V and VI (as of the Cooper *et al.* paper in 1995) is unknown and is not performed by calmodulin [172].

The phenomenological model that couples Ca^{2+} and cAMP dynamics was first described in [172]. We use this model to show how the methods described above can be extended to a system containing more than two components. This model can also be expanded to the heart as they express types II, III, IV, V, VI, VII, and IX AC. Since types V and VI can be inhibited by Ca^{2+}, a larger reaction network can be created using all AC isoforms and Ca^{2+} and cAMP microdomains can be analyzed. These additional interactions may be neccesary for fine tuning of excitation-contraction coupling [265]. The dynamical system for a four component Ca^{2+}-cAMP

network shown in Figure **C.1**(C) is given by:

$$\frac{d[x]}{dt} = a[w] - b[x], \qquad \frac{d[y]}{dt} = c - d[y], \qquad \frac{d[z]}{dt} = e[y] - f[z], \qquad \frac{d[w]}{dt} = h - g[w] \tag{C.16}$$

$$c = c_m \frac{x^{N1}}{x^{N_1} + K_1^{N_1}}, \qquad g = g_m \frac{z^{N_2}}{z^{N_2} + K_2^{N_2}}$$

where x is the cAMP concentration, y is the number of available active channels, z is the free cytosolic Ca^{2+} concentration, w is the available AC. The stimulus through G-protein is modeled through the parameter a. The non linear terms c and g (Eq. **C.17**) are Hill coefficients used to model the cooperative binding interactions of cAMP to channels, as c, and Ca^{2+} to AC, as g. update rest of parameters.

Well mixed model

For the well-mixed system, with initial conditions $x_i = 1$, $y_i = 0.05$, $z_i = 0.1$, $w_i = 0.5$ oscillatory kinetics were observed (Figure **C.5**). Initial conditions were chosen by Cooper et al [172] such that $\frac{dy}{dt} = \frac{dz}{dt} = \frac{dw}{dt} = 0$ at time 0. The nature of the oscillations depend on the value of a; for $a = 5$ (Figure **C.5**A), we obtain damped oscillations and for $a = 2$, we obtain stable oscillations (Figure **C.5**B). In order to understand this system, we first analyze the ODE model. For the system shown in Eq. **C.16**, there exists only one steady state denoted (x^*,y^*,z^*,w^*). Analytic methods become rather complicated, and therefore we used MATLAB's *fsolve* function to calculate this steady state. Using fsolve, we approximate the critical point by finding the point where all functions equal 0, up to a determined tolerance. This is therefore an iterative method for the minimization of all of the function sums. To assess the stability of this state we consider

the Jacobian matrix given by

$$
J = \begin{pmatrix}
-b & 0 & 0 & a \\
c m \dfrac{N_1 K_1^{N_1} x^{N_1-1}}{\left(x^{N_1}+K_1^{N_1}\right)^2} & -d & 0 & 0 \\
0 & e & -f & 0 \\
0 & 0 & -g m \dfrac{N_2 K_2^{N_2} z^{N_2-1}}{\left(z^{N_2}+K_2^{N_2}\right)^2} w & -g m \dfrac{z^{N_2}}{z^{N_2}+K_2^{N_2}}
\end{pmatrix}
\tag{C.17}
$$

For this Jacobian, the criteria for oscillations around the fixed point are the presence of a purely imaginary eigenvalue (the real part is zero). The change from a negative real eigenvalue to a purely imaginary eigenvalue, in Figure **C.6**(a), hints the presence of a Hopf bifurcation. We should note that this condition is not sufficient to characterize the oscillatory nature of the solution, since the Jacobian only considers the first order effects and oscillations exist in the second-order space. For larger systems, and when using numerical tools, it is important to look for real parts around zero rather than exactly zero [267, 269]. We refer the reader to [269] for expanded analysis of Taylor series. To better show second order stability we create a bifurcation plot (Figure **C.6**(c)). In order to create this figure the local maximas of cAMP were recorded as the system underwent a Runge-Kutta 4th order code, these points are then plotted across the scanned parameter [263]. These points then correspond with the highest value of cAMP in each cycle. For this system, if the dots converge to a single point the solution will remain stable. Bifurcation plots typically are used to analyze complex behaviors in mathematical solutions, such as $x_{t+1} = x_t + r x_t (1 - x_t)$ which exhibits bounded chaotic solutions for certain parameters [316].

The stability of the system's oscillatory kinetics can be described as a function of a as shown in Figure **C.6**(a). Although some of the eigenvalues have negative real parts (Figure **C.6**(b)) the largest real valued eigenvalue dominates the system's stability. From the analysis of the Jacobian and bifurcation plot, we then expect to see a limit cycle in the range $0.43 \le a \le 4.6$, which is exactly what is observed in the numerical simulations of the ODEs (Eq. **C.16**) We

therefore conclude that the system experiences a Hopf bifurcation as it moves from a single stable point to a stable limit cycle. A simplified model showing how to analytically solve for a bifurcation and test for the regimes in a 3 component model can be seen in Wilhelm *et al.* [317]

1-D spatial model

What happens to the stability of this oscillatory system in the presence of diffusion? To study the effect of diffusion, we now characterize the stability of the steady states of the well-mixed system in a spatially extended model. As in the previous sections, we utilize the modified Jacobian to find spatial component effects.

$$
J = \begin{pmatrix} -b - D_x k^2 & 0 & 0 & a \\ c_m \dfrac{N_1 K_1^{N_1} x^{N_1-1}}{\left(x^{N_1}+K_1^{N_1}\right)^2} & -d - D_y k^2 & 0 & 0 \\ 0 & e & -f - D_z k^2 & 0 \\ 0 & 0 & -g_m \dfrac{N_2 K_2^{N_2} z^{N_2-1}}{\left(z^{N_2}+K_2^{N_2}\right)^2} w & -g_m \dfrac{z^{N_2}}{z^{N_2}+K_2^{N_2}} - D_w k^2 \end{pmatrix}
\tag{C.18}
$$

Diffusive constants of cAMP and Ca^{2+} were taken to be 444 $\mu m^2/s$ [318] and 530 $\mu m^2/s$ [319]. Since the ion channel and AC are membrane-bound components, their diffusion constants were assumed to be 0.1 $\mu m^2/s$. The diffusion constants were chosen based on biological relevance [318,319]. To analyze the modified Jacobian, we set the model value of $a = 2$ and the wavenumber k (Figure **C.6**(d) and(e)). We can see that a spatial effect possibly exists for very low values of k and a. This is due to the fact that diffusion stabilizes the Jacobian. Regardless of the value of diffusion, the Jacobian has negative eigenvalues and k only serves to spatially stabilize the system.

To verify that this was indeed the case, we conducted numerical simulations for the

reaction-diffusion system; results are shown in Figure **C.5**(c)-(f). The system was initialized with the initial condition $u_0 = 2R[x_i \; y_i \; z_i \; w_i]$ where, R, is a random number between 0 and 1. This puts the mean of all values across space at the well mixed starting condition. System boundary conditions were set as no flux and it was assumed at all points in the system there is a membrane/cytosol interface. We observe that the oscillations for the different species are maintained across time (vertical axis) but no change in observed in spatial dimension (horizontal axis).

C.5.4 Key take-aways

From our analysis of a four-component model for Ca^{2+}-cAMP signaling, we observe a few important characteristics of the system.

1. **Size sometimes doesn't matter**: Within the Cooper model there is no spatial effect, and even at very small k values or large system sizes, this spatial effect is minimal at under 1% when compared against the maximum spatial value. No sustained spatial patterning occurs as this gradient is left over from the randomized starting condition. Within models there does not have to exist a spatial gradient, especially when only one stable point exists as it will always settle around that point (assuming it is not unstable).

2. **History matters**: Random perturbations will start a limit cycle even in the inactive "a=1" state, a value inferred from initial conditions such that it accounts for the steady state history of the system (pre-stimulus). Since in the "a=1" case only one unstable point exists, there may be improper system control and/or chosen kinetic rates may be incorrect if this behavior is not expected. Initial conditions must satisfy the system's history, because the space exists before stimulation and must satisfy these basal (pre-stimulus) rates.

3. **Oscillations and diffusion**: Characterizing oscillations through imaginary eigenvalues

in the Jacobian can characterize undamped, damped, and unstable kinetics. Doing variations across parameters of interest allows the user to find when the system's oscillatory behavior changes providing a powerful tool to describe parameters and conditions for these occurrences.

C.6   Conclusions and Perspectives

Mathematical modeling has served to complement experiment to further our understanding of biological systems. Recent experimental advances in knowledge of these systems have allowed us to construct more and more complex models and our knowledge of the spatial organization of the cell has made us increasingly aware of the structured nature of the cellular environment in which information transfer through signal transduction takes place.

Despite this knowledge, biological models often neglect this structure and consider biological networks in a homogeneous spatial environment. These purely kinetic models are computationally more tractable, but can fail to capture the biological reality. However, incorporating spatial structure into these mathematical models leads to challenging mathematical analyses. In particular, for systems involving spatial patterning, the behavior of the system can vary widely with parameter choice. Complementing the simulation strategies with analysis methods can help us identify the parameter space in which interesting or unexpected behavior can be observed. Above, we have outlined the steps for a comprehensive analytic treatment of spatial structure arising from reaction-diffusion models.

We should note that numerical schemes for solving PDEs have been developed over the last few years [320–322]. These tools complement the analysis of reaction-diffusion systems in cell signaling, particularly for large systems where analytical treatment is not possible. Using three distinct examples (Turing mechanism, wave-pinning, and second-messenger signaling),

we have summarized a tutorial for stability analysis of reaction-diffusion models. We expect that a systems biologist interested in this topic will find this tutorial as a helpful starting point to conduct such analyses.

A challenge or perhaps, an opportunity for the future, is studying reaction-diffusion systems with growing domains. Such systems arise in cases of cell membrane deformation coupled with composition variation on the membrane [323], cell motility [324, 325], and even in subcompartments of neurons such as dendritic spines [326]. These are cases where only numerical or computational methods provide the framework to study the problem at hand and the development of computational tools and their application to biological problems, and obtaining qualitative and quantitative research are areas of ongoing research in many groups including ours.

Acknowledgements

Appendix **C**, in full, is a reprint of the material as it appears in M. C. Getz, J. A. Nirody, and P. Rangamani. Stability analysis in spatial modeling of cell signaling. 10(1):e1395. eprint: https://onlinelibrary.wiley.com/doi/pdf/10.1002/wsbm.1395. The dissertation author was the primary author of this material.

Figure C.3: Steady state behavior for the wave pinning polarization (WPP) model. For all of the above plots, we chose: $\gamma = 1, k_{\text{off}} = 1, K = 1, p = 2.8, k_0 = 0.03$ and vary around p, the average amount of total protein, and k_0, the basal activation rate. (a) The nullclines show the intersection of $f(a,u) = 0$ and $g(a,u) = 0$ and the three steady states at the chosen parameters. (b) Variations of k_0 at p=2.5, (c) Variations of k_0 at p=2.7, (d) Variations of k_0 at p=3. The two stable steady states a_1^* and a_3^* are shown as solid blue and green lines, respectively; the unstable steady state a_2^* is shown as a dashed line. For a range of k_0, all three steady states exist and are real-valued; this region is shaded in red; this range increases with p, eventually resulting in an *irreversible* system response when it reaches $k_0 = 0$. (e) Parameter space topology for the full partial differential equation (PDE) model when $D_U = 10\mu m^2 \text{second}^{-1}$ and $D_A = 0.1\mu m^2 \text{second}^{-1}$. The region of linear instability is shown shaded in orange for wavenumber $k = 0.2 \ \mu m^{-1}$. This corresponds to a perturbation of length $L = \frac{2\pi}{k} \approx 30\mu m$. Smaller values of k result in an expansion of the linear instability region; larger values of k result in the region shrinking. An additional domain is shown shaded in blue, in which front-like solutions are supported when given a sufficiently strong (or spatially graded) perturbation. The parameter choice made by Mori *et al.* (purple point) lies in this region.

190
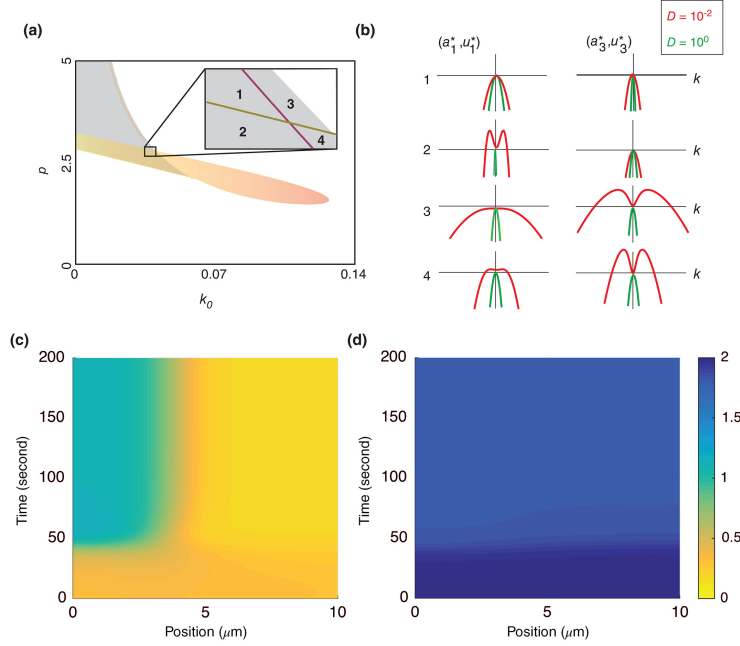
Figure C.4: Examination of the rise of Turing patterns by loss of stability given critical wave numbers k. (a) A small segment of the parameter space is highlighted for the full spatial WPP model, showing regions where neither (region 1), one (regions 2 and 3), or both (region 4) of the equilibrium points become unstable. (b) An illustration of the loss of the linearly instability regime as D approaches 1. Plots show the magnitude of the real part of the rightmost eigenvalue for both equilibria within each of the regions highlighted in (a). Plots are shown for $k \in [-1, 1]$. When $D = 10^{-2}$, corresponding to the localization of the active form to the membrane, a finite range of critical wavenumbers is observed; this range disappears when $D = 1$. Simulations of Eq. **C.12** were conducted in MATLAB's 1D PDE solver *pdepe*. The parameters chosen, from Mori *et al.*: $k_0 = 0.067, K = 1, \gamma = 1, k_{off} = 1, D_a = 0.1, D_u = 10$ for a system size for L=10 μm. A gradient from the back to the front of the system can be seen by the concentrations of a (c) and u (d). Initial conditions were set as the basal solution of (a_1^*, u_1^*), to induce the gradient a_1^* was set as $2a_1^*R$ where R is a random number between 0 and 1.
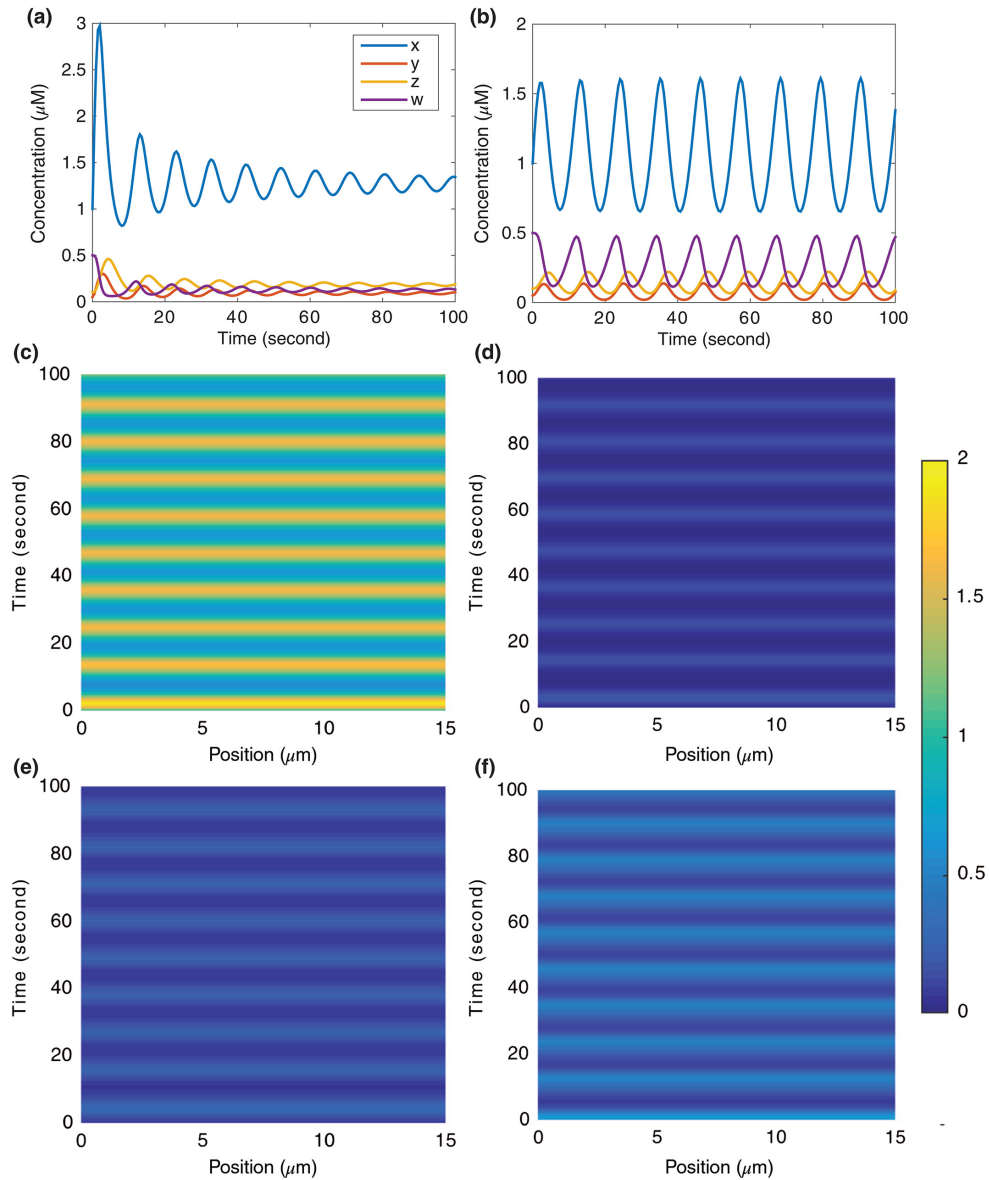
Figure C.5: Well mixed results for the Cooper model showing damped oscillations (a) $a = 5$ and a stable limit cycle (b) $a = 2$. Species are represented as $x =$ cAMP, $y =$ active channels, $z =$ Ca^{2+}, $w =$ AC. (c)–(f) Partial differential equation (PDE) simulation results of the Cooper model, notice no spatial effects exist and the components only oscillate with time. The results show the well mixed model is recovered and the concentrations are spatially even. Panel (c) shows the concentration of cAMP, panel (d) shows the concentration of active channels, panel (e) shows the concentration of Ca^{2+}, and panel (f) shows the concentration of active AC.
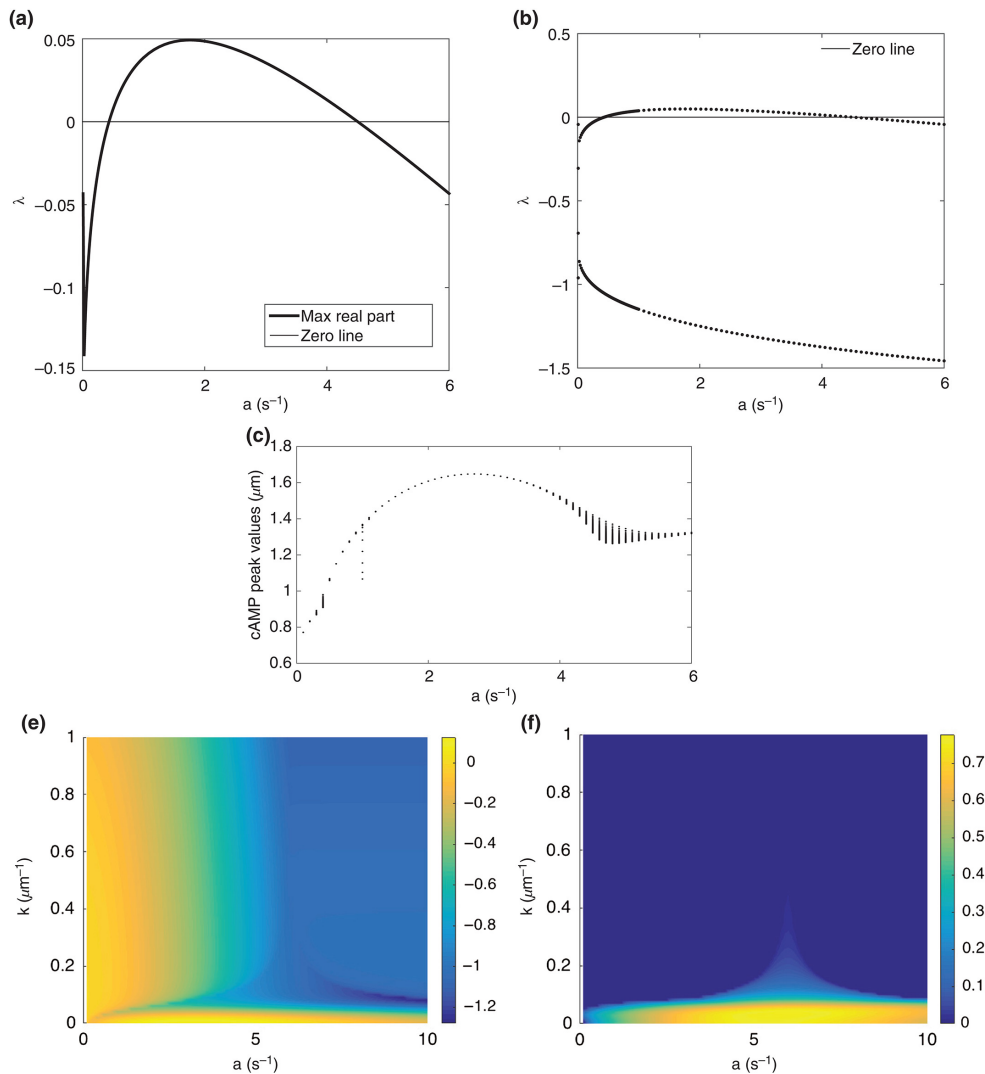
Figure C.6: Stability of the Ca^{2+} - cAMP system across the parameter a. λ denotes the eigenvalue of the system, negative values are stable and positive values should be unstable. The system's second order influences stabilize the kinetics keeping the system from going unstable at the low positive eigenvalues and making the system always stable. Panel (a) shows the maximum real eigenvalue, panel (b) shows all four eigenvalue solutions; there exists two conjugate pairs. panel (c) shows the bifurcation plot showing the system is always stable across a as the peaks all converge to one point. We expect to see a limit cycle in the range $0.43 \leq a \leq 4.6$. The higher the real eigenvalue the larger the amplitude of the kinetic oscillations. (d) and (e) Stability across wavenumber (k) showing the maximum real eigenvalue (d) and the maximum imaginary eigenvalue (e). The system quickly heads toward a stable non-oscillatory solution, indicating that no spatial effects through spatial instability are possible within our parameter space.

193

Appendix D

Stability analysis of a bulk-surface reaction model for membrane-protein clustering

Lucas M. Stolerman[1]* **Michael Getz**[5]* **Stefan G. Llewellyn Smith**[1,2] **Michael Holst**[3,4] **Padmini Rangamani**[1]**

[1]Department of Mechanical and Aerospace Engineering, University of California, San Diego, La Jolla CA 92093-0411

[2]Scripps Institution of Oceanography, University of California, San Diego, La Jolla, CA 92093-0213

[3]Department of Mathematics, University of California, San Diego, La Jolla, CA 92093-0112

[4]Department of Physics, University of California, San Diego, La Jolla, CA 92093-0424

[5] Chemical Engineering Graduate Program, University of California, San Diego, La Jolla, CA 92093-0424

* Both these authors contributed equally **To whom correspondence should be addressed. e-mail: prangamani@ucsd.edu

Protein aggregation on the plasma membrane (PM) is of critical importance to many cellular processes such as cell adhesion, endocytosis, fibrillar conformation, and vesicle transport. Lateral diffusion of protein aggregates or clusters on the surface of the PM plays an important role in governing their heterogeneous surface distribution. However, the stability behavior of the surface distribution of protein aggregates remains poorly understood. Therefore, understanding the spatial patterns that can emerge on the PM solely through protein-protein interaction, lateral diffusion, and feedback is an important step towards a complete description of the mechanisms behind protein clustering on the cell surface. In this work, we investigate the pattern formation of a reaction-diffusion model that describes the dynamics of a system of ligand-receptor complexes. The purely diffusive ligand in the cytosol can bind receptors in the PM, and the resultant ligand-receptor complexes not only diffuse laterally but can also form clusters resulting in different oligomers. Finally, the largest oligomers recruit ligands from the cytosol using positive feedback. From a methodological viewpoint, we provide theoretical estimates for diffusion-driven instabilities of the protein aggregates based on the Turing mechanism. Our main result is a threshold phenomenon, in which a sufficiently high recruitment of ligands promotes the input of new monomeric components and consequently drives the formation of a single-patch spatially heterogeneous steady-state.

D.1   Introduction

Biological membranes are unique two-dimensional structures that separate cellular contents from the extracellular environment and regulate the transport of material into and out of the cell [327,328]. In addition to lipids and carbohydrates, these membranes contain a large proportion of proteins, the composition of which depends on the cell type [328–332]. One of the interesting features of membrane proteins is their ability to form clusters on the cell surface [333–335]. This clustering of proteins on the plasma membrane (PM) results in a spatial heterogeneity in the distribution of protein densities. Many factors can induce such a spatial heterogeneity, including lateral diffusion, physical barriers from the cytoskeleton [336], lipid raft affinity [337], and curvature differences along the membrane [334]. The formation of protein clusters is intimately related to various cellular phenomena such as polarization, membrane depolarization, receptor signaling, enzyme activity, and cytoskeletal regulation [214, 262, 338–341].

A particular example of proteins forming clusters on the membrane is well-elucidated by amyloid-β aggregation/fibrillation in the context of Alzheimer's disease. It is thought that amyloid-β can become cytotoxic when it aggregates on the membrane at high levels [342]. Biophysical measurements show that amyloid-β aggregates become more stable when oligomerized (i.e, when it forms molecular components from repeating units) on the membrane surface [343, 344] and also can destabilize certain membrane compositions [345]. It is also thought that membrane components such as cholesterol may initiate aggregation of amyloid-β, which may then be bolstered by a yet-unidentified secondary feedback mechanism [346]. In general, the aggregation of proteins on the membrane surface appears to be a common mechanism for fibrillar protein aggregation and aggregate propagation in a variety of neurodegenerative diseases [347, 348]. In addition to amyloid-β, surface receptors such as α-amino-3-hydroxy-5-methyl-4-isoxazolepropionic acid receptor (AMPAR) [349, 350] and membrane-bound kinases such as

Fyn [351] are known to cluster on the membrane; these clusters have been implicated in neuronal functioning in physiology [214, 337] and disease [342, 345].

One of the open questions in the field of protein aggregations is the role of the spatial organization of membrane proteins due to bulk-surface reactions and feedback mechanisms. Mathematical modeling has provided substantial insight into the geometric coupling of bulk-surface reaction-diffusion systems [98, 352, 353], including wave-pinning formulations [262, 354], spatial patterning [355, 356], and generalized stability analysis [357–359]. From a modeling perspective, several authors have proposed the classical Smoluchowski coagulation model [360, 361] as a suitable candidate for describing protein aggregation. The system of differential equations in the Smoluchowski model deserves attention as it accounts for the changes in concentration of interacting molecules with different sizes. These molecules can thus reversibly aggregate according to a given *aggregation kernel*. In the recent past, the use of such kernels [362, 363] allowed a successful combination of experimental measurements with computational predictions. These models performed well in terms of comparisons to data and estimation of kinetic parameters such as the aggregation time and the asymptotic cluster distribution. However, by using the original Smoluchowski systems of ordinary differential equations (ODEs), these studies lack descriptions of the spatial protein organization, which can be crucial for the understanding of many cellular processes. To overcome this limitation, one can explicitly consider molecular diffusion and use systems of partial differential equations (PDEs), as has been done in the amyloid-β aggregation models [364–366]. These studies have provided detailed theoretical estimates in terms of boundary conditions and homogenization tools. However, they have restricted the spatial scale to a small three-dimensional region of cerebral tissue and do not describe intracellular phenomena. There is thus a need for mathematical models of protein aggregation in the PM with proper spatial description to account for the numerous cellular processes that occur due to heterogeneous protein distribution.

In this work, our primary goal was to investigate the emergence of spatially heterogeneous steady-state profiles of membrane protein aggregates to identify how feedback between cytosolic and membrane components can drive pattern formation on the membrane. To this end, we merged the concept of bulk-surface reaction-diffusion systems with the Smoluchowski approach to introduce a new bulk-surface model for membrane protein clustering (Figure D.1 (A)). The model equations describe a purely diffusive ligand in the cytosol, which then undergoes membrane binding without any cytosolic aggregation. The resultant membrane-bound protein can diffuse laterally and also form clusters with different oligomeric sizes. Finally, the oligomers of maximum size can further recruit more cytosolic proteins, resulting in a positive feedback for the membrane protein aggregates and stabilization of the oligomers [343, 346]. Following the approach of Ratz and Roger [358, 359], we then analyzed the model for diffusion-driven instabilities using the classical Turing mechanisms. We found these interactions allow diffusion-driven instabilities and pattern formation in the absence of a sustained localized stimulus.

In what follows, we present the model assumptions and derivation in Appendix D.2, the mathematical analysis including stability analysis in Appendix D.3, and conclude with numerical simulations (Appendix D.4) and a discussion (Appendix D.5) about our findings in the context of amyloid-β and clustering of other membrane proteins.

D.2   Model Development

Here we present our bulk-surface reaction-diffusion model for protein aggregation, including feedback. We describe our assumptions (Appendix D.2.1) and the governing equations (Appendix D.2.2) in detail. In Appendix D.2.3, we prove that the total mass of the system is conserved over time, and in Appendix D.2.4, we non-dimensionalize the model. Finally, in section Appendix D.2.5, we perform the system's reduction when the cytosolic diffusion goes to infinity, following the mathematical approach of Ratz and Roger [358, 359].
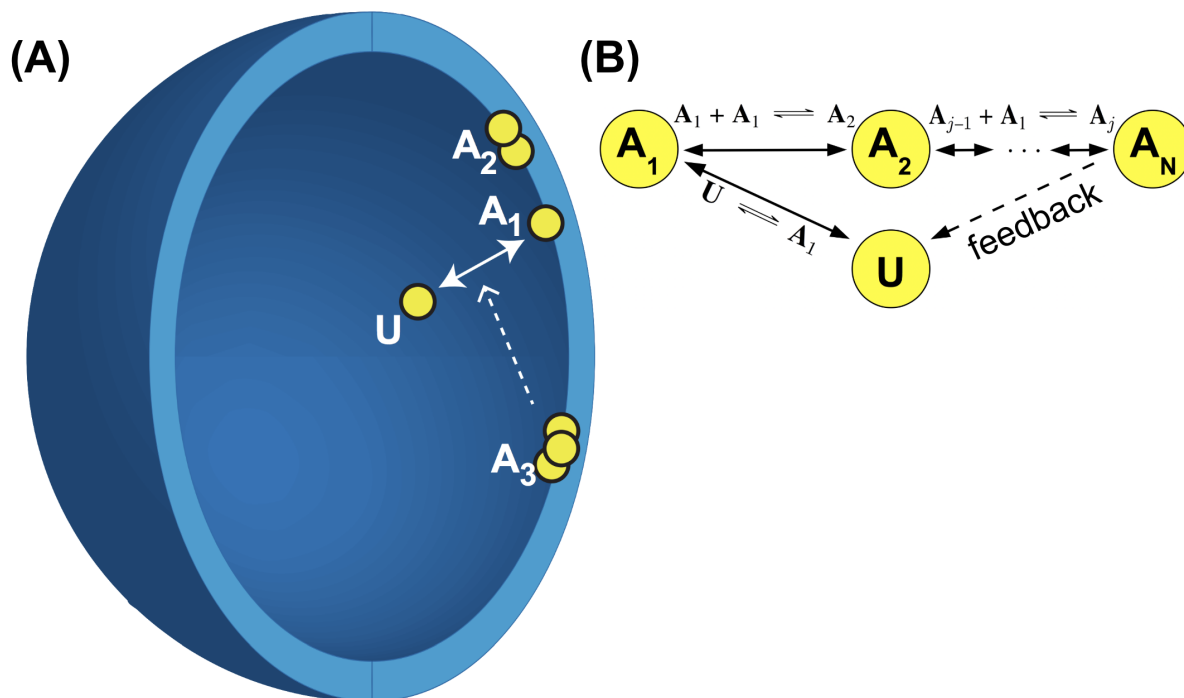
Figure D.1: **A bulk-surface compartmental model for protein aggregation.** (A) As proteins approach the surface they can associate and then oligomerize. This oligomerization then drives further membrane association of monomers. In this figure, we assume that the maximum oligomer size is three and the arrows represent a state change of U to A_1; the dotted line shows the 'catalytic' feedback of A_3 to U and A_1. (B) A detailed diagram of all chemical reactions for an arbitrary maximum oligomer size N.

D.2.1 Assumptions

In our system, we assume that **U** represents the volume component, which can freely diffuse in the cytoplasm. Upon binding to the plasma membrane, it forms a surface monomer component $\mathbf{A}_1$. The $\mathbf{A}_1$ molecules laterally diffuse in the membrane and form the oligomeric components $\mathbf{A}_j$. Here, j denotes the number of $\mathbf{A}_1$ molecules in the oligomer, which is at most $N \in \mathbb{N}$. In terms of chemical reactions, $\mathbf{U} \xrightleftharpoons{f} \mathbf{A}_1$ denotes the binding of the cytosolic component to the plasma membrane with a reaction flux f. The subsequent oligomerization at the membrane is described by

$$\mathbf{A}_{j-1} + \mathbf{A}_1 \rightleftharpoons \mathbf{A}_j \quad \text{for} \quad j = 2, 3, ..., N.$$
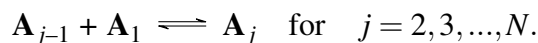
We also assume that the flux term f describes ligand binding/unbinding to the cell surface, where the binding term will be linearly proportional to the concentrations of **U** in the cytosol and $\mathbf{A}_N$ in the plasma membrane. In Figure **D.1** (B), we illustrate the reactions taking place in our system: the exchange between cytosolic and membrane-bound monomer, the formation of dimers, the general oligomerization reactions, and the positive feedback. The oligomerization process is modeled as a particular version of the reversible Smoluchowski model for aggregation dynamics [367]. We also assume that the oligomerization process occurs only by monomer attachment in the mass action regime. Moreover, to keep the analysis tractable, we do not consider any cooperativity term such as Hill's function [368]: the rate at which the different oligomers are formed is independent of their size.

D.2.2 Governing equations

We represent the cellular domain as the bounded region Ω with smooth boundary $\Gamma = \partial\Omega$. We define the concentrations $u(x,t) : \Omega(0, \mathcal{T}] \rightarrow \mathbb{R}$ for the volume component and $a_j(x,t) : \Gamma \times (0, \mathcal{T}] \rightarrow \mathbb{R}$ for the membrane oligomeric components, where x and t represent the location

and time, respectively. The molecular mechanisms underlying membrane protein aggregation and stabilization are quite complex. However, from a feedback standpoint, the so-called "rich gets richer" phenomenon seems to be prevalent in various systems, especially in the context of amyloid fibrillation [369–375]. Therefore, we propose a mathematically tractable *feedback term* to represent this complex mechanism. The flux term is thus defined as

$$f(u, a_1, a_N) = (k_0 + k_b a_N)u - k_d a_1 \tag{D.1}$$

for k_0, k_b and k_d positive constants, where k_0 is the basal binding rate, k_b is the rate of A_N-dependent binding rate, and k_d is the unbinding rate from the membrane into the cytosol. Then the governing equations for the spatiotemporal evolution of the different components are given by

$$\partial_t u = D_u \nabla^2 u \tag{D.2}$$

$$\partial_t a_1 = D_1 \Delta a_1 + (k_0 + k_b a_N)u - k_d a_1 - 2k_m a_1^2 + 2k_2 a_2$$

$$- k_g a_1 \left(\sum_{l=2}^{N-1} a_l \right) + \sum_{j=3}^{N} k_j a_j \tag{D.3}$$

$$\partial_t a_2 = D_2 \Delta a_2 + k_m a_1^2 - k_g a_1 a_2 - k_2 a_2 + k_3 a_3 \tag{D.4}$$

$$\partial_t a_j = D_j \Delta a_j + k_g a_1 a_{j-1} - k_g a_1 a_j - k_j a_j + k_{j+1} a_{j+1}, \quad j = 3, \ldots, N-1 \tag{D.5}$$

$$\partial_t a_N = D_N \Delta a_N + k_g a_1 a_{N-1} - k_N a_N \tag{D.6}$$

Here, ∇^2 and Δ represent the Laplace and Laplace-Beltrami operators, respectively. The parameter k_m represents the rate at which monomers bind to form dimers. The rate k_g at which the oligomers of size greater than two are formed is assumed to be the same for all oligomerization reactions. Finally, k_j represent the rates at which the oligomeric components of size j will release a single monomer. The boundary condition for a is periodic since the domain is closed and the boundary condition for u is given by

$$-D_u \left(\mathbf{n} \cdot \nabla u \right) \Big|_{x \in \Gamma} = (k_0 + k_b a_N)u - k_d a_1 \tag{D.7}$$

as a balance of the diffusive flux and the reaction rate at the membrane. All parameters and variables are non-negative real numbers.

D.2.3 Mass conservation

Let n_X denote the number of molecules of the component X. For a closed system, we know that the total number of single molecules must be given by

$$n_U + n_{A_1} + 2n_{A_2} + ... + Nn_{A_N}$$

since each A_j oligomer must have exactly j molecules of A_1. From this fact, we define the total mass of the system, which accounts for spatial compartments (bulk and surface) and the different molecular size distributions. This is the content of the following.

Proposition D.2.1. *Let u, a_1, a_2,..., a_N be solutions of* (**D.2**)–(**D.7**). *Then the quantity*

$$M(t) := \int_\Omega u(x,t)dx + \sum_{j=1}^N \left\{ j \cdot \int_\Gamma a_j(x,t)ds \right\} \tag{D.8}$$

represents the total mass of the system and is conserved over time, i.e, $M(t) = M_0 \quad \forall t \geq 0$. In this case, M_0 denotes the initial mass which is given by $M_0 = \int_\Omega u(x,0)dx + \sum_{j=1}^N \left\{ j \cdot \int_\Gamma a_j(x,0)ds \right\}$

Proof. By taking the time derivative of $M(t)$, and assuming u and a_j are $\mathcal{C}^2$ solutions for (**D.2**)–(**D.7**), we have

$$\frac{d}{dt}M = \int_\Omega \partial_t u dx + \sum_{j=1}^N \left\{ j \cdot \int_\Gamma \partial_t a_j ds \right\}$$

For the integral $\int_\Omega \partial_t u dx$, we apply the divergence theorem and substitute Eq. (**D.7**) to obtain

$$\int_\Omega \partial_t u dx = D_u \int_\Omega \nabla^2 u dx$$
$$= D_u \int_\Gamma (\nabla u \cdot \mathbf{n}) ds$$
$$= -\int_\Gamma [(k_0 + k_b a_N)u - k_d a_1] ds$$

For the summation of surface integrals $\sum_{j=1}^{N} \left\{ j \cdot \int_{\Gamma} \partial_t a_j ds \right\}$, we substitute the governing equations to obtain

$$\sum_{j=1}^{N} \left\{ j \cdot \int_{\Gamma} \partial_t a_j ds \right\}$$

$$= \int_{\Gamma} \left[D_1 \Delta a_1 + (k_0 + k_b a_N) u - k_d a_1 - 2 k_m a_1^2 + 2 k_2 a_2 - k_g a_1 \left(\sum_{l=2}^{N-1} a_l \right) + \sum_{j=3}^{N} k_j a_j \right] ds$$

$$\quad + \int_{\Gamma} \left[2 \cdot D_2 \Delta a_2 + 2 \cdot \left\{ k_m a_1^2 - k_g a_1 a_2 - k_2 a_2 + k_3 a_3 \right\} \right] ds$$

$$\quad + \sum_{j=3}^{N-1} \int_{\Gamma} \left[j \cdot D_j \Delta a_j + j \cdot \left\{ k_g a_1 a_{j-1} - k_g a_1 a_j - k_j a_j + k_{j+1} a_{j+1} \right\} \right] ds$$

$$\quad + \int_{\Gamma} N \cdot \left[D_N \Delta a_N \right] + N \cdot \left\{ k_g a_1 a_{N-1} - k_N a_N \right\} \right] ds$$

$$= \sum_{j=1}^{N} j D_j \cdot \int_{\Gamma} \Delta a_j ds + \int_{\Gamma} (k_0 + k_b a_N) u - k_d a_1 ds$$

$$= \int_{\Gamma} ((k_0 + k_b a_N) u - k_d a_1) \, ds$$

where the last equality comes from the fact that $\int_{\Gamma} \Delta a_j ds = 0$ as a consequence of the First Green's Theorem [376]. We therefore have

$$\frac{d}{dt} M = \int_{\Omega} \partial_t u dx + \sum_{j=1}^{N} \left\{ j \cdot \int_{\Gamma} \partial_t a_j ds \right\} = 0,$$

from which we conclude that $M(t) = M(0) =: M_0$ for all $t \geq 0$ $\qquad\square$

The mass conservation property for bulk-surface reaction-diffusion models has been established in different contexts [354, 358]. However, to the best of our knowledge, it has never been identified in the context of oligomerization reactions.

D.2.4 Non-dimensionalization

We introduce a non-dimensional version of the system that allows a convenient qualitative interpretation independent of the actual system size, but instead through the ratio of kinetic parameters to the diffusion contributions. We follow the approach in [358, 359] and define

$U, A_1, A_2, ..., A_N$ be the dimensional concentration quantities where $[U] = \text{mol}/\mu m^3$ and $[A] = \text{mol}/\mu m^2$ for $j = 1, ..., N$. We also define L and T as the spatial and temporal quantities, where $[L] = \mu m$ and $[T] = s$. We then introduce the non-dimensional variables

$$\hat{u} = \frac{u}{U}, \quad \hat{a}_j = \frac{a_j}{A_j} \quad (j = 1, ..., N), \quad \hat{t} = \frac{t}{T}, \quad \text{and} \quad \hat{x} = \frac{x}{L},$$

which lead to the transformed domains $\hat{\Omega} := \{ \zeta \in \mathbb{R}^3 | \zeta L \in \Omega \}$ and $\hat{\Gamma} = \partial \hat{\Omega}$. By denoting $\hat{\nabla}, \hat{\nabla}^2$, and $\hat{\Delta}$ as the dimensionless gradient, Laplace, and Laplace-Beltrami operators, respectively, and using

$$\nabla = \frac{1}{L} \hat{\nabla}, \quad \nabla^2 = \frac{1}{L^2} \hat{\nabla}^2, \quad \Delta = \frac{1}{L^2} \hat{\Delta},$$

we can apply the chain rule and rewrite the system (**D.2**)–(**D.6**) in the form

$$\frac{U}{T} \frac{\partial \hat{u}}{\partial \hat{t}} = D_u \frac{U}{L^2} \hat{\nabla}^2 \hat{u}, \quad \hat{x} \in \hat{\Omega}, \tag{D.9}$$

$$\frac{A_1}{T} \frac{\partial \hat{a}_1}{\partial \hat{t}} = \frac{D_1 A_1}{L^2} \hat{\Delta} \hat{a}_1 + k_d A_1 \left\{ \left(\frac{k_0 U}{k_d A_1} + \frac{k_b A_N U}{k_d A_1} \hat{a}_N \right) \hat{u} - \hat{a}_1 - 2 \frac{k_m A_1}{k_d} \hat{a}_1^2 + 2 \frac{k_2 A_2}{k_d A_1} \hat{a}_2 \right.$$
$$\left. - \hat{a}_1 \left(\sum_{l=2}^{N-1} \frac{A_j k_g}{k_d} \hat{a}_j \right) + \sum_{j=3}^{N} \frac{k_j A_j}{k_d A_1} \hat{a}_j \right\}, \quad \hat{x} \in \hat{\Gamma}, \tag{D.10}$$

$$\frac{A_2}{T} \frac{\partial \hat{a}_2}{\partial \hat{t}} = \frac{D_2 A_2}{L^2} \hat{\Delta} \hat{a}_2 + k_d A_1 \left(\frac{k_m A_1}{k_d} \hat{a}_1^2 - \frac{k_2 A_2}{k_d A_1} \hat{a}_2 - \frac{k_g A_2}{k_d} \hat{a}_1 \hat{a}_2 + \frac{k_3 A_3}{k_d A_1} \hat{a}_3 \right), \quad \hat{x} \in \hat{\Gamma}, \tag{D.11}$$

$$\frac{A_j}{T} \frac{\partial \hat{a}_j}{\partial \hat{t}} = \frac{D_j A_j}{L^2} \hat{\Delta} \hat{a}_j + k_d A_1 \left(\frac{k_g A_{j-1}}{k_d} \hat{a}_1 \hat{a}_{j-1} - \frac{k_j A_j}{k_d A_1} \hat{a}_j - \frac{k_g A_j}{k_d} \hat{a}_1 \hat{a}_j + \frac{k_{j+1} A_{j+1}}{k_d A_1} \hat{a}_{j+1} \right),$$
$$\hat{x} \in \hat{\Gamma}, j = 3, ..., N \tag{D.12}$$

$$\frac{A_N}{T} \frac{\partial \hat{a}_N}{\partial \hat{t}} = \frac{D_N A_N}{L^2} \hat{\Delta} \hat{a}_N + k_d A_1 \left(\frac{k_g A_{N-1}}{k_d} \hat{a}_1 \hat{a}_{N-1} - \frac{k_N A_N}{k_d A_1} \hat{a}_N \right), \quad \hat{x} \in \hat{\Gamma}. \tag{D.13}$$

The boundary conditions in (**D.7**) can be rewritten as

$$-\frac{D_u U}{L} (\mathbf{n} \cdot \nabla \hat{u}) \Big|_{x \in \Gamma} = k_d A_1 \left\{ \left(\frac{k_0 U}{k_d A_1} + \frac{k_b A_N}{k_d A_1} \hat{a}_N \right) \hat{u} - \hat{a}_1 \right\}. \tag{D.14}$$

Since $R > 0$, we can define the characteristic concentrations U and A_j by dividing the

total mass of the system per total volume and surface area, respectively. We also define the characteristic time with respect to the diffusion D_1 of the monomeric component across the cellular surface. Formally, we define

$$U = \frac{M_0}{R \cdot |\Gamma|}, \quad A_j = \frac{M_0}{|\Gamma|} \quad \text{for} \quad j = 1, 2, \ldots, N, \quad T = \frac{R^2}{D_1}, \quad L = R, \tag{D.15}$$

and the dimensionless parameters

$$\hat{k}_0 = \frac{k_0 U}{k_d A_1}, \quad \hat{k}_b = \frac{k_b A_N U}{k_d A_1}, \quad \hat{k}_m = \frac{k_m A_1}{k_d}, \quad \hat{k}_j = \frac{k_j A_j}{k_d A_1} \quad (j = 2, \ldots, N),$$

$$\hat{k}_g = \frac{k_g A_j}{k_d} \quad (j = 2, \ldots, N-1), , \quad \gamma = \frac{k_d R^2}{D_1}, \quad \tilde{D} = \frac{D_u}{D_1}, \quad d_j = \frac{D_j}{D_1} \quad (j = 2, \ldots, N).$$

As a result, (**D.9**) can be written as

$$\frac{\partial \hat{u}}{\partial \hat{t}} = \tilde{D} \hat{\nabla}^2 \hat{u}, \tag{D.16}$$

for $\hat{x} \in \hat{\Omega}$ with boundary condition

$$-\tilde{D} \left(\mathbf{n} \cdot \hat{\nabla} \hat{u} \right) \Big|_{x \in \Gamma} = \gamma \left\{ \left[\hat{k}_0 + \hat{k}_b \hat{a}_N \right] \hat{u} - \hat{a}_1 \right\}. \tag{D.17}$$

for $\hat{x} \in \hat{\Gamma}$. Finally, for the surface components, (**D.10**)–(**D.13**) can be written as

$$\frac{\partial \hat{a}_1}{\partial \hat{t}} = \hat{\Delta} \hat{a}_1 + \gamma \left\{ \left[\hat{k}_0 + \hat{k}_b \hat{a}_N \right] \hat{u} - \hat{a}_1 - 2 \hat{k}_m \hat{a}_1^2 + 2 \hat{k}_2 \hat{a}_2 \right.$$

$$\left. - \hat{k}_g \hat{a}_1 \left(\sum_{l=2}^{N-1} \hat{a}_j \right) + \sum_{j=3}^{N} \hat{k}_j \hat{a}_j \right\}, \tag{D.18}$$

$$\frac{\partial \hat{a}_2}{\partial \hat{t}} = d_2 \hat{\Delta} \hat{a}_2 + \gamma \left(\hat{k}_m \hat{a}_1^2 - \hat{k}_2 \hat{a}_2 - \hat{k}_g \hat{a}_1 \hat{a}_2 + \hat{k}_2 \hat{a}_3 \right), \tag{D.19}$$

$$\frac{\partial \hat{a}_j}{\partial \hat{t}} = d_j \hat{\Delta} \hat{a}_j + \gamma \left(\hat{k}_g \hat{a}_1 \hat{a}_{j-1} - \hat{k}_j \hat{a}_j - \hat{k}_g \hat{a}_1 \hat{a}_j + \hat{k}_{j+1} \hat{a}_{j+1} \right), \quad j = 3, \ldots, N \tag{D.20}$$

$$\frac{\partial \hat{a}_N}{\partial \hat{t}} = d_N \hat{\Delta} \hat{a}_N + \gamma \left(\hat{k}_g \hat{a}_1 \hat{a}_{N-1} - \hat{k}_N \hat{a}_N \right). \tag{D.21}$$

D.2.5 System Reduction when $D_u \to \infty$

We further reduce our system by assuming the limit of rapid cytosolic diffusion, which has been experimentally observed for chemotaxis in amoebae [304], membrane-associated PH$_{\delta 1}$ molecules [377], and several other studies [259, 303, 378–383]. From a modelling perspective, this assumption has also been extensively explored, especially in the context of cell polarization [262, 354, 358, 384]. The resulting system is uniquely defined on the membrane surface, and the bulk variable u will be represented by an integral operator also called a *non-local functional*. Our approach closely follows the work of Ratz and Roger [358, 359], though our system can be N-dimensional in principle. Formally, if we assume $D_u \to \infty$ and if the initial concentration of $\hat{u}$ is constant over $\hat{\Omega}$, then $\hat{u}$ no longer depends on space and $u = u(t)$. Therefore, the mass conservation law given by (**D.8**) implies

$$\hat{u}(t)|\hat{\Omega}| + \sum_{j=1}^{N}\left\{ j \cdot \int_{\hat{\Gamma}} \hat{a}_j ds \right\} = \mathcal{M}_0 \tag{D.22}$$

where $\mathcal{M}_0 = \hat{u}(0)|\hat{\Omega}| + \sum_{j=1}^{N}\left\{ j \cdot \int_{\hat{\Gamma}} \hat{a}_j(s,0)ds \right\}$ is the total mass of the dimensionless system. We then define the non-local functional

$$\mathcal{U}[\hat{a}_1, \hat{a}_2, ..., \hat{a}_N](t) := \frac{1}{|\hat{\Omega}|}\left[\mathcal{M}_0 - \sum_{j=1}^{N}\left\{ j \cdot \int_{\hat{\Gamma}} \hat{a}_j ds \right\} \right]$$

as in [358, 359]. Finally, we drop all the hats to obtain the reduced system

$$\frac{\partial a_1}{\partial t} = \Delta a_1 + \gamma \mathcal{F}_1(a_1, a_2 ..., a_N) \tag{D.23}$$

$$\frac{\partial a_j}{\partial t} = d_j \Delta a_j + \gamma \mathcal{F}_j(a_1, a_2 ..., a_N), \quad j = 2, ..., N \tag{D.24}$$

where

$$\mathcal{F}_1 = [k_0 + k_b a_N]\,\mathcal{U}[a_1, a_2, ..., a_N] - a_1 - 2k_m a_1^2 + 2k_2 a_2 - k_g a_1 \left(\sum_{l=2}^{N-1} a_j\right) + \sum_{j=3}^{N} k_j a_j,$$

$$\mathcal{F}_2 = k_m a_1^2 - k_2 a_2 - k_g a_1 a_2 + k_2 a_3,$$

$$\mathcal{F}_j = k_g a_1 a_{j-1} - k_j a_j - k_g a_1 a_j + k_{j+1} a_{j+1}, \quad j = 3, \ldots, N$$

$$\mathcal{F}_N = k_g a_1 a_{N-1} - k_N a_N.$$

In the next sections, we will provide analytical estimates and numerical simulations to analyze the stability properties of the reduced system (**D.23**)–(**D.24**).

D.3 Mathematical Analysis

Obtaining the mathematical conditions for the existence of diffusion-driven instabilities is a crucial step for understanding the origin of heterogeneous steady-state solutions [263, 270]. For membrane proteins, it has been experimentally observed that a heterogeneous distribution of protein density accounts for several processes that ensure proper cell function, such as receptor signaling, membrane polarization/depolarization, and calcium channels activity [214, 339, 340] . For this reason, establishing the precise role of the lateral diffusion in the generation of such heterogeneity is an important step towards a comprehensive description of pattern formation in the cellular surface.

In this section, we present the mathematical framework for investigating diffusion-driven instabilities in the system (**D.23**)–(**D.24**). We establish conditions that guarantee the existence and uniqueness of homogeneous steady-states, or the conditions for having multiple steady-states. We also present a characterization for the Jacobian Matrix in the case of homogeneous perturbations. For the non-homogeneous case, the linearization of the non-local functional yields a different Jacobian matrix, and a family of ordinary differential equations is derived to analyze the stability

in terms of the eigenfunctions of the Laplace-Beltrami operator. We then apply our framework in the case $N = 2$, where we obtain a necessary condition for diffusion-driven instabilities. We start with the characterization of the homogeneous steady-states.

D.3.1 Homogeneous steady-states

The homogeneous solutions of (**D.23**)–(**D.24**) satisfy the ODE system

$$\frac{da_j}{dt} = \gamma \mathcal{F}_j(a_1, a_2 \ldots, a_N) \quad j = 1, \ldots, N$$

and the steady-states in this case are given by $\mathbf{a}^* = (a_1^*, a_2^*, a_3^*, \ldots, a_N^*)$ such that

$$\mathcal{F}_j(\mathbf{a}^*) = 0$$

for all $j = 1, \ldots, N$. From $\mathcal{F}_N(\mathbf{a}^*) = 0$, we obtain $a_N^* = \frac{k_g a_1^* a_{N-1}^*}{k_N}$ and, proceeding recursively, it is easy to show that

$$a_j^* = \frac{k_g a_1^* a_{j-1}^*}{k_j} \quad \text{for} \quad j = 3, \ldots, N, \quad \text{and} \quad a_2^* = \frac{k_m (a_1^*)^2}{k_2}. \tag{D.25}$$

Hence $a_j^* = C_j (a_1^*)^j$ where $C_1 = 1$ and

$$C_j = \left(\prod_{i=3}^{j} \frac{k_g}{k_j} \right) \left(\frac{k_m}{k_2} \right) \quad \text{for} \quad j = 2, \ldots, N.$$

Thus from $\mathcal{F}_1(\mathbf{a}^*) = 0$, we must have

$$a_1^* = [k_0 + k_b\, a_N^*] \frac{1}{|\Omega|} \left[\mathcal{M}_0 - |\Gamma| \sum_{j=1}^{N} j \cdot a_j^* \right]$$

$$= \left[k_0 + k_b\, C_N (a_1^*)^N \right] \frac{1}{|\Omega|} \left[\mathcal{M}_0 - |\Gamma| \sum_{j=1}^{N} j \cdot C_j (a_1^*)^j \right]. \tag{D.26}$$

By multiplying both sides by $|\Omega|$ and rearranging the $(a_1^*)^j$ terms, we can define the

polynomial

$$\mathcal{P}_N(\alpha) = -k_0 \mathcal{M}_0 \, + \, (|\Omega| \, + \, k_0|\Gamma|)\,\alpha \, + \, k_0|\Gamma| \left(\sum_{j=2}^{N-1} jC_j\alpha^j \right)$$

$$+ \, C_N \left(k_0|\Gamma|N - \mathcal{M}_0 k_b\right)\alpha^N \, + \, k_b|\Gamma|C_N \left(\sum_{j=1}^{N} jC_j\alpha^{N+j} \right), \qquad \text{(D.27)}$$

where the roots of $\mathcal{P}_N$ are the steady-state values a_1^*. We then observe that the coefficient of α^N is a non-negative number if and only if

$$k_0|\Gamma|N - \mathcal{M}_0 k_b \geq 0,$$

which in this case implies that $\mathcal{P}_N(\alpha)$ has a unique positive root and therefore that the system has a unique steady-state. This is the case when $k_b = 0$, which means that the largest oligomers do not promote ligand binding in the plasma membrane. On the other hand, if $k_0|\Gamma|N - \mathcal{M}_0 k_b < 0$, then multiple steady-states could exist.

D.3.2   Linear Stability Analysis

Linear stability is a traditional concept from the theory of dynamical systems that treat the study of the local behavior near a steady-state solution. The term "linear" stands for the analysis of the linear approximation of a nonlinear system, which can be sufficient to determine if a steady-state is stable or unstable. In the case of a system of ODEs, the analysis is carried out by evaluating the eigenvalues of the so-called Jacobian matrix. A similar analysis can be done in the context of reaction-diffusion systems of PDEs with the analysis of the eigenvectors of the Laplace operator. A major contribution in this field is due to Alan Turing in the classic paper *"The Chemical Basis of Morphogenesis"* [270]. Turing established the notion of diffusion-driven instabilities and was the first to connect this mathematical idea with the formation of spatially heterogeneous patterns. In what follows, we first analyze the homogeneous perturbations of the steady-states by describing the Jacobian matrix of the system. Then we define the conditions for

diffusion-driven instabilities in our system (**D.23**)–(**D.24**).

Homogeneous perturbations

In this section, we investigate the linear stability of the steady-states $\mathbf{a}^*$ against spatially homogeneous perturbations, that is in the absence of diffusion. Our study is an N-dimensional version of the approach taken in [358, 359] for a GTPase cycling model. We need to compute the eigenvalues λ of the Jacobian matrix

$$\mathcal{J}[\mathbf{a}^*] = \gamma \left[\frac{\partial \mathcal{F}_j^*}{\partial a_i} \right]_{1 \leq i,j \leq N}$$

for $\mathcal{F}_j$ defined in (**D.23**) and (**D.24**). If all the eigenvalues of $\mathcal{J}[\mathbf{a}^*]$ have negative real parts, then the steady-state is called linearly stable [267]. That means that local perturbations will converge to the steady-state.

On the other hand, if at least one of the eigenvalues has a positive real part, then it is called linearly unstable, in which local perturbations will lead the system away from the steady-state. The next proposition generally characterizes $\mathcal{J}[\mathbf{a}^*] - \lambda \mathbf{I}$.

Proposition D.3.1. *The matrix $\mathcal{J}[a^*] - \lambda I$ can be written in the form*

$$\begin{bmatrix} w_0 - \lambda & \boldsymbol{w} \\ \boldsymbol{v} & H - \lambda \boldsymbol{I} \end{bmatrix}$$

where w_0 and λ are real numbers, $\boldsymbol{w} \in \mathbb{R}^{N-1}$ is a row vector, $\boldsymbol{v} \in \mathbb{R}^{N-1}$ is a column vector, and H is a $(N-1) \times (N-1)$ tridiagonal matrix.

Proof. We will first calculate $\frac{\partial \mathcal{F}_j^*}{\partial a_i}$ for $i, j = 1, 2, \ldots, N$. For $j = 1$ we obtain

$$\frac{\partial \mathcal{F}_1^*}{\partial a_1} = -\frac{|\Gamma|(k_0 + k_b a_N^*)}{|\Omega|} - 1 - 4k_m a_1^* - \sum_{l=2}^{N-1} k_g a_l^*,$$

$$\frac{\partial \mathcal{F}_1^*}{\partial a_2} = -2\frac{|\Gamma|(k_0 + k_b a_N^*)}{|\Omega|} - k_g a_1^* + 2k_2,$$

$$\frac{\partial \mathcal{F}_1^*}{\partial a_i} = -i\frac{|\Gamma|(k_0 + k_b a_N^*)}{|\Omega|} - k_g a_1^* + k_i \quad \text{for} \quad i = 3, 4, \ldots, N-1,$$

$$\frac{\partial \mathcal{F}_1^*}{\partial a_N} = -N\frac{|\Gamma|(k_0 + k_b a_N^*)}{|\Omega|} + \frac{k_b}{|\Omega|}\left(\mathcal{M}_0 - |\Gamma|\sum_{j=1}^{N} j \cdot a_j^*\right) + k_N.$$

Now for $j = 2$, we have

$$\frac{\partial \mathcal{F}_2^*}{\partial a_1} = 2k_m a_1^* - k_g a_2^*, \quad \frac{\partial \mathcal{F}_2^*}{\partial a_2} = -k_g a_1^* - k_2, \quad \frac{\partial \mathcal{F}_2^*}{\partial a_3} = k_3 \quad \frac{\partial \mathcal{F}_2^*}{\partial a_i} = 0, \quad i = 4, 5, \ldots, N$$

and for $j = 3$ to $j = N - 1$, we obtain

$$\frac{\partial \mathcal{F}_j^*}{\partial a_1} = k_g a_{j-1}^* - k_g a_j^*, \quad \frac{\partial \mathcal{F}_j^*}{\partial a_{j-1}} = k_g a_1^*, \quad \frac{\partial \mathcal{F}_j^*}{\partial a_j} = -k_g a_1^* - k_j, \quad \frac{\partial \mathcal{F}_j^*}{\partial a_{j+1}} = k_{j+1},$$

and

$$\frac{\partial \mathcal{F}_j^*}{\partial a_i} = 0,$$

otherwise, and finally for $j = N$,

$$\frac{\partial \mathcal{F}_N^*}{\partial a_1} = k_g a_{N-1}^*, \quad \frac{\partial \mathcal{F}_N^*}{\partial a_2} = k_g a_1^*, \quad \frac{\partial \mathcal{F}_N^*}{\partial a_N} = -k_N, \quad \text{and} \quad \frac{\partial \mathcal{F}_N^*}{\partial a_i} = 0 \quad \text{otherwise.}$$

We then define $\mathcal{J}_{ij}^* := \gamma \frac{\partial \mathcal{F}_j^*}{\partial a_i}$, $w_0 := \mathcal{J}_{11}^* - \lambda$, the vectors $\mathbf{v}, \mathbf{w} \in \mathbb{R}^{N-1}$ such that

$$\mathbf{v} = (\mathcal{J}_{21}^* \ \mathcal{J}_{31}^* \cdots \mathcal{J}_{N1}^*)^T \quad \text{and} \quad \mathbf{w} = (\mathcal{J}_{12}^* \ \mathcal{J}_{13}^* \cdots \mathcal{J}_{1N}^*)$$

and

$$H = \begin{bmatrix} \mathcal{I}_{22}^* - \lambda & \mathcal{I}_{23}^* & 0 & \cdots & 0 & 0 & 0 \\ \mathcal{I}_{32}^* & \mathcal{I}_{33}^* - \lambda & \mathcal{I}_{34}^* & \cdots & 0 & 0 & 0 \\ \vdots & \vdots & \vdots & \vdots & \vdots & \vdots & \vdots \\ 0 & 0 & 0 & \cdots & \mathcal{I}_{N-1N-2}^* & \mathcal{I}_{N-1N-1}^* - \lambda & \mathcal{I}_{N-1N}^* \\ 0 & 0 & 0 & \cdots & 0 & \mathcal{I}_{NN-1}^* & \mathcal{I}_{NN}^* - \lambda \end{bmatrix}_{(N-1)\times(N-1)}$$

which proves the proposition. $\qquad\square$

Non-homogeneous perturbations

We now consider a perturbation of the form $\mathbf{a}_s = (a_{s,1}, a_{s,2}, ..., a_{s,N})$ for $s \in (-1,1)$ of the homogeneous steady-state $\mathbf{a}^*$ in the direction of $\Phi = (\varphi_1, \varphi_2, ..., \varphi_N)$, for non-homogeneous $\varphi_j : \Gamma \times (0, T) \to \mathbb{R}$. Thus for each component, we assume

$$a_{s,j}|_{s=0} = a_j^* \quad \text{and} \quad \left. \frac{\partial a_{s,j}}{\partial s} \right|_{s=0} = \varphi_j,$$

so we may write the linear approximation $a_{s,j} \approx a_j^* + s\varphi_j$ for $j = 1, \ldots, N$

$$a_{s,j} = a_j^* + s\, \varphi_j(x,t).$$

In particular, the linearization of the non-local functional yields $\mathcal{U}[\mathbf{a}_s] \approx \mathcal{U}[\mathbf{a}^*] + s\left(\frac{d}{ds}\big|_{s=0} \mathcal{U}[\mathbf{a}_s]\right)$ where

$$\left(\left. \frac{d}{ds} \right|_{s=0} \mathcal{U}[\mathbf{a}_s] \right) = -\sum_{j=1}^{N} \left. \frac{d}{ds} \right|_{s=0} \int_{\Gamma} a_{s,j} ds = -\sum_{j=1}^{N} \int_{\Gamma} \varphi_j ds. \qquad (D.28)$$

Since we assume that $\varphi_j \in L^2(\Gamma)$ are orthogonal to the constant perturbations, which were analyzed in the previous section, we now consider

$$\int_{\Gamma} \varphi_j ds = 0 \quad \text{for} \quad j = 1, \ldots, N,$$

which leads to a linearized system with a constant input $\mathcal{U}[\mathbf{a}_s](t) = \mathcal{U}[\mathbf{a}^*]$. For the approximation

of the component a_1, we thus have

$$\partial_t \varphi_1 = \Delta \varphi_1 + \sum_{j=1}^{N} \tilde{\mathcal{J}}_{1,j}(\mathbf{a}^*)\varphi_j, \qquad (D.29)$$

where

$$\tilde{\mathcal{J}}_{1,1} = -\gamma \left\{ 1 + 4k_m a_1^* + k_g \left(\sum_{l=2}^{N-1} a_l^* \right) \right\}, \quad \tilde{\mathcal{J}}_{1,2}(\mathbf{a}^*) = \gamma(2k_2 - k_g a_1^*),$$

$$\tilde{\mathcal{J}}_{1,j}(\mathbf{a}^*) = \gamma(k_j - k_g a_j^*), \quad j = 3, \ldots, N-1, \quad \text{and} \quad \tilde{\mathcal{J}}_{1,N}(\mathbf{a}^*) = \gamma(k_N + k_b \, \mathcal{U}[\mathbf{a}^*]).$$

The other terms of the Jacobian matrix remain the same as in the case of the homogeneous perturbations, so we omit the explicit calculations. In vector notation, we can then write the linearized system in the form

$$\partial_t \Phi = \mathbf{D}\Delta\Phi + \tilde{\mathcal{J}}(\mathbf{a}^*)\Phi, \qquad (D.30)$$

where $\mathbf{D}$ is a diagonal matrix such that $\mathbf{D}_{jj} = d_j$ where $d_1 = 1$ and $\tilde{\mathcal{J}}(\mathbf{a}^*)$ is the modified Jacobian matrix. We then define $\mathbb{N}_0 := \mathbb{N} \cup \{0\}$ and consider $(\omega_l)_{l \in \mathbb{N}_0} \subset L^2(\Gamma)$, an orthonormal basis of infinitely smooth eigenfunctions of the Laplace-Beltrami operator, i.e,

$$-\Delta\omega_l = \eta_l \omega_l. \quad \text{where} \quad 0 = \eta_0 < \eta_1 \leq \eta_2 \leq \cdots.$$

In the case where Γ is the unitary sphere $\mathbb{S}^2$ parametrized by the angles $\phi \in [0, 2\pi)$ and $\theta \in [0, \pi)$, the eigenfunctions have the closed form

$$\cos(m\phi)P_k^m(\cos(\theta)) \quad \text{and} \quad \sin(m\phi)P_k^m(\cos(\theta))$$

where $k \geq 0$, $0 \leq m \leq k$ and $P_k^m(t)$ are the so-called *associated Legendre function* (see references [385, 386] for details).

Then for each $j = 1, \ldots, N$ we can express each component φ_j as a linear combination

$$\varphi_j = \alpha_{j0} \, \omega_0 + \sum_{i \in \mathbb{N}} \alpha_{jl} \, \omega_l$$

213

where $\alpha_{jl} = \alpha_{jl}(t)$ for $l \in \mathbb{N}_0$. Using vector notation, we can define the quantity $\mathcal{A}_l = (\alpha_{1l}, \alpha_{2l}, \ldots, \alpha_{Nl})^T$ such that

$$\Phi = \mathcal{A}_0 \, \omega_0 + \sum_{l \in \mathbb{N}} \mathcal{A}_i \, \omega_l(x).$$

By substituting the above expansion in (**D.30**), we obtain the linear ODE system

$$\frac{d\mathcal{A}_l}{dt} = \left[-\eta_l \mathbf{D} + \gamma \tilde{\mathcal{J}}(\mathbf{a}^*) \right] \mathcal{A}_l \quad \text{for} \quad l = 0, 1, 2, \ldots \tag{D.31}$$

and diffusion-driven instabilities occur if the above system is unstable for some $l \in \mathbb{N}_0$. This is true when at least one eigenvalue λ of the matrix $-\eta_l \mathbf{D} + \tilde{\mathcal{J}}(\mathbf{a}^*)$ has a positive real part. Therefore our target quantity is the so-called *dispersion relation*

$$h(l) := \max\left(\text{Re}(\lambda(\eta_l)) \right), \tag{D.32}$$

where $\text{Re}(z)$ denotes the real part of a complex number z. Finally, the characteristic polynomials $p_l(\lambda) := \det(\lambda \mathbf{I} - \gamma \tilde{\mathcal{J}}(\mathbf{a}^*) + \eta_l \mathbf{D})$ can be written in the form

$$p_l(\lambda) = \lambda^N + b_{l,N-1} \lambda^{N-1} + \ldots + b_{l,0}$$

where $b_{l,0} = \det(-\gamma \tilde{\mathcal{J}}(\mathbf{a}^*) + \eta_l \mathbf{D})$. Therefore, if $b_{l,0} < 0$ for some $l \in \mathbb{N}$, and since $p_l(\tilde{\lambda}) > 0$ for $\tilde{\lambda}$ sufficiently large ($p_l(\lambda) \to \infty$ as $\lambda \to \infty$), the intermediate value theorem ensures that p_l has a positive root in $[0, \tilde{\lambda}]$ and therefore $h(l) > 0$.

D.3.3 Special Case $N = 2$: Necessary Conditions for Diffusion-Driven Instabilities

We now fix $N = 2$ and analyze the conditions for diffusion-driven instabilities. The equations are given by

$$\partial_t a_1 = \Delta a_1 + \gamma \left\{ \frac{(k_0 + k_b a_2)}{|\Omega|} \left[\mathcal{M}_0 - \int_\Gamma (a_1 + 2a_2) \, ds \right] - a_1 - 2k_m a_1^2 + 2k_2 a_2 \right\} \tag{D.33}$$

$$\partial_t a_2 = d_2 \Delta a_2 + \gamma \left\{ k_m a_1^2 - k_2 a_2 \right\}. \tag{D.34}$$

and describe the simplest case where a reversible *dimerization* (formation of oligomers of size two) occurs on the plasma membrane. Dimerization in the cellular surface is a key factor in regulation and takes place for numerous molecules, such as ion channels [387], receptor tyrosine kinases (RTKs) [338, 388], and K-ras GTPases [389]. From a mathematical perspective, the case $N = 2$ is more tractable, and therefore can potentially give some insight into the mechanisms of pattern formation in our model. On the other hand, even this simple case differs substantially from the previous work of Ratz and Roger [358, 359, 390], since we only assume reversible mass-action instead of Michaelis-Menten kinetics, and also because of the particular positive feedback (Eq. **D.1**) that has not been considered in previous studies.

We provide a necessary condition in a particular case where the system admits a unique spatially homogeneous steady-state. We prove that the system does not exhibit diffusion-driven instabilities provided that k_b is sufficiently small. In biological terms, the following result states that if the A_N-dependent binding rate of monomers to the membrane is low enough, which can be interpreted as a small influence of the largest oligomers in the binding process, then diffusive effects will dominate, and no protein-distribution heterogeneity will form on the cellular surface.

Theorem D.3.1. *Suppose $k_b \geq 0$ is such that*

$$k_b \leq \frac{2}{\mathcal{M}_0} \min \left\{ k_0 |\Gamma|, \frac{d_2 \eta_i |\Omega|}{\gamma} \right\}$$

for all $i \in \mathbb{N}$. Then the system admits a unique steady-state and no diffusion-driven instability exists.

Proof. Let $\mathbf{a}^* = (a_1^*, a_2^*)$ be the spatially-homogeneous steady $\mathbf{a}^* = (a_1^*, a_2^*)$, which is obtained when $a_2^* = \frac{k_m(a_1^*)^2}{k_2}$ and a_1^* is a solution of $\mathcal{P}_2(\alpha) = 0$, where

$$\mathcal{P}_2(\alpha) = -k_0 \mathcal{M}_0 + (|\Omega| + k_0|\Gamma|)\alpha + \frac{k_m}{k_2}(2k_0|\Gamma| - \mathcal{M}_0 k_b)\alpha^2$$
$$+ k_b|\Gamma|\frac{k_m}{k_2}\alpha^3 + 2\left(\frac{k_m}{k_2}\right)^2 k_b|\Gamma|\alpha^4.$$

Now since $k_b \leq \frac{2k_0|\Gamma|}{\mathcal{M}_0}$, we have $2k_0|\Gamma| - \mathcal{M}_0 k_b \geq 0$ and therefore $\mathcal{P}_2$ has only non-negative coefficients except $-k_0\mathcal{M}_0$, which implies that $\mathcal{P}_2(\alpha)$ strictly increases for $\alpha \geq 0$. On the other hand,
then ensures that the system admits a unique positive steady-state in $[0, \tilde{\alpha}]$. The Jacobian matrix with respect to homogeneous perturbations is then given by

$$\mathcal{J}[\mathbf{a}^*] = \gamma \begin{bmatrix} -1 - 4a_1^* k_m - \frac{|\Gamma|}{|\Omega|}\left(\frac{k_b k_m (a_1^*)^2}{k_2} + k_0\right) & 2a_1^* k_m \\ 2k_2 + \frac{k_b}{|\Omega|}\left[\mathcal{M}_0 - \left(\frac{2k_m(a_1^*)^2}{k_2} + a_1^*\right)|\Gamma|\right] - \frac{2|\Gamma|}{|\Omega|}\left(\frac{k_b k_m (a_1^*)^2}{k_2} + k_0\right) & -k_2 \end{bmatrix}$$

with a second-order characteristic polynomial $p(\lambda) = \det(\lambda\mathbf{I} - \mathcal{J}[\mathbf{a}^*])$ given by $p(\lambda) = \lambda^2 + b\lambda + c$, where

$$b = \gamma\left(\frac{(a_1^*)^2|\Gamma|k_b k_m}{k_2|\Omega|} + 4a_1^* k_m + \frac{|\Gamma|k_0}{|\Omega|} + k_2 + 1\right) > 0$$

and

$$c = \gamma^2\left(\frac{8(a_1^*)^3|\Gamma|k_b k_m^2}{k_2|\Omega|} + \frac{3(a_1^*)^2|\Gamma|k_b k_m}{|\Omega|} + \frac{2a_1^* k_m}{|\Omega|}(2|\Gamma|k_0 - k_b\mathcal{M}_0) + \frac{|\Gamma|k_0 k_2}{|\Omega|} + k_2\right)$$

is also positive because $2k_0|\Gamma| - \mathcal{M}_0 k_b \geq 0$. From that we conclude that both eigenvalues

$$\lambda = \frac{-b \pm \sqrt{b^2 - 4c}}{2}$$

must have real negative parts and therefore the steady-states are linearly stable. We then perform a similar argument for non-homogeneous perturbations. From (**D.29**), we obtain the modified

Jacobian matrix $\tilde{\mathcal{J}}(\mathbf{a}^*)$, and for a given $l \in \mathbb{N}_0$, we have

$$\tilde{\mathcal{J}}(\mathbf{a}^*) - \eta_l \mathbf{D} = \begin{bmatrix} -\gamma(1 + 4a_1^* k_m) - \eta_l & \gamma\left\{2k_2 + \frac{k_b}{|\Omega|}\left[\mathcal{M}_0 - |\Gamma|\left(\frac{2k_m(a_1^*)^2}{k_2} + a_1^*\right)\right]\right\} \\ 2\gamma\, a_1^*\, k_m & -\gamma\, k_2 - d_2\eta_l \end{bmatrix}$$

with characteristic polynomials $p_l(\lambda) := \det(\lambda \mathbf{I} - \gamma\tilde{\mathcal{J}}(\mathbf{a}^*) + \eta_l \mathbf{D})$ given by the quadratics $p_l(\lambda) = \lambda^2 + b_l\lambda + c_l$, where

$$b_l = \gamma\left(4a_1^* k_m + k_2 + 1\right) + \eta_l(d_2 + 1) > 0$$

and

$$c_l = \left[d_2\eta_l^2 + \gamma\eta_l(d_2 + k_2) + \gamma^2 k_2\right] + 2\,\gamma k_m\, a_1^*\left(2d_2\eta_l - \frac{\gamma k_b \mathcal{M}_0}{|\Omega|}\right)$$
$$+ \frac{2\gamma^2(a_1^*)^2|\Gamma|k_b k_m}{|\Omega|}\left(1 + \frac{2a_1^* k_m}{k_2}\right)$$

In the case $l \in \mathbb{N}$, the c_l terms are also positive, since we assume

$$k_b \leq \frac{2d_2\eta_l|\Omega|}{\gamma\mathcal{M}_0} \iff 2d_2\eta_l - \frac{\gamma k_b \mathcal{M}_0}{|\Omega|} \geq 0 \quad \forall i \in \mathbb{N},$$

and in this case the $p_l(\lambda)$ have no roots with positive real parts. In the case $l = 0$, we know that $\eta_0 = 0$, but the modified matrix $\tilde{\mathcal{J}}(\mathbf{a}^*)$ yields a different linearized system. Thus we have to analyze the stability of the linear equation given in (**D.31**) in the case where $l = 0$, i.e,

$$\frac{d\mathcal{A}_0}{dt} = \left[\gamma\tilde{\mathcal{J}}(\mathbf{a}^*)\right]\mathcal{A}_0$$

with characteristic polynomial $p_0(\lambda) = \lambda^2 + b_0\lambda + c_0$ where

$$b_0 = \gamma\left(4a_1^* k_m + k_2 + 1\right) > 0$$

and

$$c_0 = \gamma^2\left\{k_2 - 2k_m\, a_1^*\left(\frac{k_b \mathcal{M}_0}{|\Omega|}\right) + \frac{2(a_1^*)^2|\Gamma|k_b k_m}{|\Omega|}\left(1 + \frac{2a_1^* k_m}{k_2}\right)\right\}$$
$$= \gamma^2\left\{k_2 - \frac{2k_m k_b a_1^*}{|\Omega|}\left[\mathcal{M}_0 - |\Gamma|\left(a_1^* + 2\frac{(a_1^*)^2 k_m}{k_2}\right)\right]\right\}. \tag{D.35}$$

We now verify that $c_0 \geq 0$. In fact, from (**D.26**) when $N = 2$, we obtain

$$\frac{1}{|\Omega|} \left[\mathcal{M}_0 - |\Gamma| \left(a_1^* + 2 \frac{(a_1^*)^2 k_m}{k_2} \right) \right] = \frac{k_2 a_1^*}{\left[k_0 k_2 + k_b (a_1^*)^2 k_m \right]},$$

and therefore by substituting the above equation on (**D.35**) and using that $a_2^* = \frac{k_m}{k_2}(a_1^*)^2$, we obtain

$$c_0 = \gamma^2 k_2 \left\{ 1 - 2 \frac{a_2^*}{\left[\frac{k_0}{k_b} + a_2^* \right]} \right\}.$$

Finally, the hypothesis gives us $\frac{k_0}{k_b} \geq \frac{\mathcal{M}_0}{2|\Gamma|}$ and by using $\mathcal{M}_0 - 2|\Gamma| a_2^* \geq 0$ (total mass of a_2 at steady-state does not exceeds the total mass of the system) we obtain $\frac{\mathcal{M}_0}{2|\Gamma|} \geq a_2^*$ and therefore

$$\frac{a_2^*}{\left[\frac{k_0}{k_b} + a_2^* \right]} \leq \frac{1}{2}$$

from which we conclude that $c_0 \geq 0$. Therefore, the steady-state is stable against non-constant perturbations.

$\square$

D.4   Numerical Simulations

We perform numerical simulations to complete our mathematical analysis. In section **D.3**, we established the mathematical framework for investigating the existence of diffusion-driven instabilities and obtained a necessary condition in the case $N = 2$. However, no sufficient conditions were explored, and no further analysis was done for $N > 2$. For this reason, we complete our analysis by searching for linear instabilities in the parameter space and analyzing the single-patch steady-state that forms when the parameters lie in the instability regions. In terms of biological motivation, our analytical estimates provided no conditions that guarantee the formation of spatial-patterns, which in turn are known to exist in the plasma membrane in various contexts. Therefore, we can use numerical simulations to obtain heterogeneous patterns

and analyze their spatial properties.

We start the section by analyzing the parameter regions of bistability (Appendix D.4.1). Then we investigate whether the stable steady-states become linearly unstable under non-homogeneous perturbations (Appendix D.4.2). From the linear instability analysis, we obtain the *single-patch* non-homogeneous steady-state (Appendix D.4.3). Finally, we study the temporal dynamics of pattern formation (Appendix D.4.4) and the single-patch dependence on the cell radius (Appendix D.4.5). The numerical simulations were implemented in Matlab R2018a and Comsol Multiphysics 5.4. In subsections **D.7.1** and **D.7.1** in the Electronic Supplementary Material (ESM), we provide the numerical details of our simulations.

D.4.1 Bistability under homogeneous perturbations

We begin by computing the homogeneous steady-states $\mathbf{a}^*$ and the corresponding eigenvalues of the Jacobian matrix $\mathcal{J}[\mathbf{a}^*]$ under homogeneous perturbations (cf. Appendix D.3.2). We then explore the parameter regions of bistability where the system admits three steady-states, two of them stable and one unstable. In the case $N = 2$, we obtain regions of bistability by change the basal binding rate k_0 and the A_2-dependent binding rate k_b (Figure D.2). For $k_0 = 0.015$, three steady-state values for a_1^* emerge depending on k_b (Figure D.2 (A)). When k_0 also changes, we obtain both a *bistability region* (dark-gray) and a *single steady-state region* (light-gray) (Figure D.2 (B)). A colored (red,black, and blue) vertical line represents the region from Figure D.2 (A). Other parameter choices also lead to bistability regions (see Figure D.8 (A) for $N = 2$ and Figure D.9 (A) for $N = 3$ in the (ESM)).

D.4.2 Linear instability under non-homogeneous perturbations

In this section, we numerically investigate which parameter values promote linear instability under non-homogeneous perturbations. We fix an eigenmode index $l \geq 1$ to explore
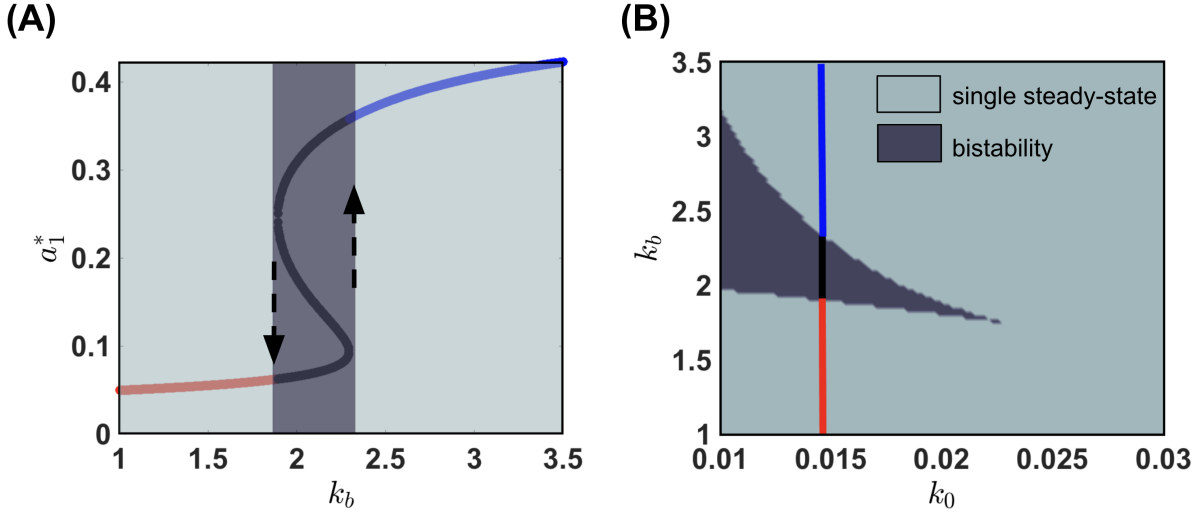
Figure D.2: **Steady-states and Parameter Regions for Bistability** ($N = 2$). (A) The value of $k_0 = 0.015$ is fixed, while k_b ranges from 1 to 3.5. We then compute the steady-states, which are the solution of (**D.26**). The single steady-state branches are shown in red and blue, respectively, while the bistable branch is shown in black. The dark-grey rectangle illustrates the emergence of bistability, and the dashed black arrows indicate the stable steady-states. (B) Bistability region for $k_0 \in [0.01, 0.03]$ with $k_0 = 0.015$ marked. The dark gray region contains the k_b values for which the system admits a bistability region. The single steady-state regions are indicated in light-gray. Remaining fixed parameters: $R = 1$, $\Gamma = 4\pi$, $\Omega = \frac{3}{4}\pi$, $\mathcal{M}_0 = \Gamma$, $k_m = 1$, and $k_2 = 1$.

diffusion-driven instabilities, and let $\mathbf{a}^*$ be a stable steady-state under homogeneous perturbations. We can thus compute the dispersion relation $h(l)$ (Eq. (**D.32**)) defined in Appendix D.3.2 by calculating the roots of the characteristic polynomials $p_l(\lambda)$. This step was done using the function *eig* in Matlab R2018a (see subsection **D.7.1** in the ESM for further details on our Matlab simulations). If $h(l) < 0$, the steady-state remains stable in the direction of the chosen eigenmode. In this case, the analysis is inconclusive, since we would also need to determine the stability for the other eigenmodes. If $h(l) > 0$, the steady-state becomes unstable for the chosen eigenmode, and this is sufficient to ensure a diffusion-driven instability [391]. The case $h(l) = 0$ usually requires higher-order analysis, so we will not consider it in the context of linear stability.

Given a fixed eigenmode index l, we can then divide the parameter space into four regions. We will call them Regions 0, 1, 2, and 3, where the numbers reflect the exact number of unstable steady-states (Figure D.3 (A) for $N = 2$ and (B) for $N = 3$). More precisely, we define:

- **Region 0**: The single steady-state region where $h(l) < 0$; There are no unstable steady-states.

- **Region 1**: The single steady-state region where $h(l) > 0$; There is only <u>one</u> unstable steady-state.

- **Region 2**: The bistability region where $h(l) > 0$ for only one stable steady-state; a total of <u>two</u> unstable steady-states.

- **Region 3**: The bistability region where $h(l) > 0$ for both stable steady-state; a total of <u>three</u> unstable steady-states.

The stability analysis in Region 0 is more subtle and requires further analysis since the stability criterion needs to be fulfilled for all eigenmodes. However, at least for $N = 2$, Theorem D.3.1 ensures that the system remains stable for sufficiently small k_b, which appears to be consistent with the numerical predictions. For higher k_b values, the instabilities emerge in the bistability region (Regions 2 and 3) and also in the single steady-state Regions 0 and 1. We obtain a similar result for $N = 3$ (Figure D.3 (B)). However, it should be noticed that the k_b values promoting linear instabilities are higher (see *y*-axis ranging from 4 to 14) compared with the case $N = 2$. Regions 0, 1, 2, and 3 can be found with other parameter choices (see Figure D.8 (B) for $N = 2$ and Figure D.9 (B) for $N = 3$ in the ESM).

Region 1 is known as a *Turing-type instability region* [263, 270], where the system may converge to a spatially non-homogeneous steady-state. We analyze this region when we increase both k_0 and k_b ranges for different values of the diffusion coefficient d_2 (Figure D.4 (A)). As d_2 decreases, Region 1 increases, which illustrates how the system becomes unstable as the discrepancies between diffusion become higher. A similar phenomenon occurs as we increase the dimensionless parameter γ, also referred to as the *Damköhler number* [392], which is the rate of membrane dissociation of monomers compared to their diffusivity. Increasing γ allows a
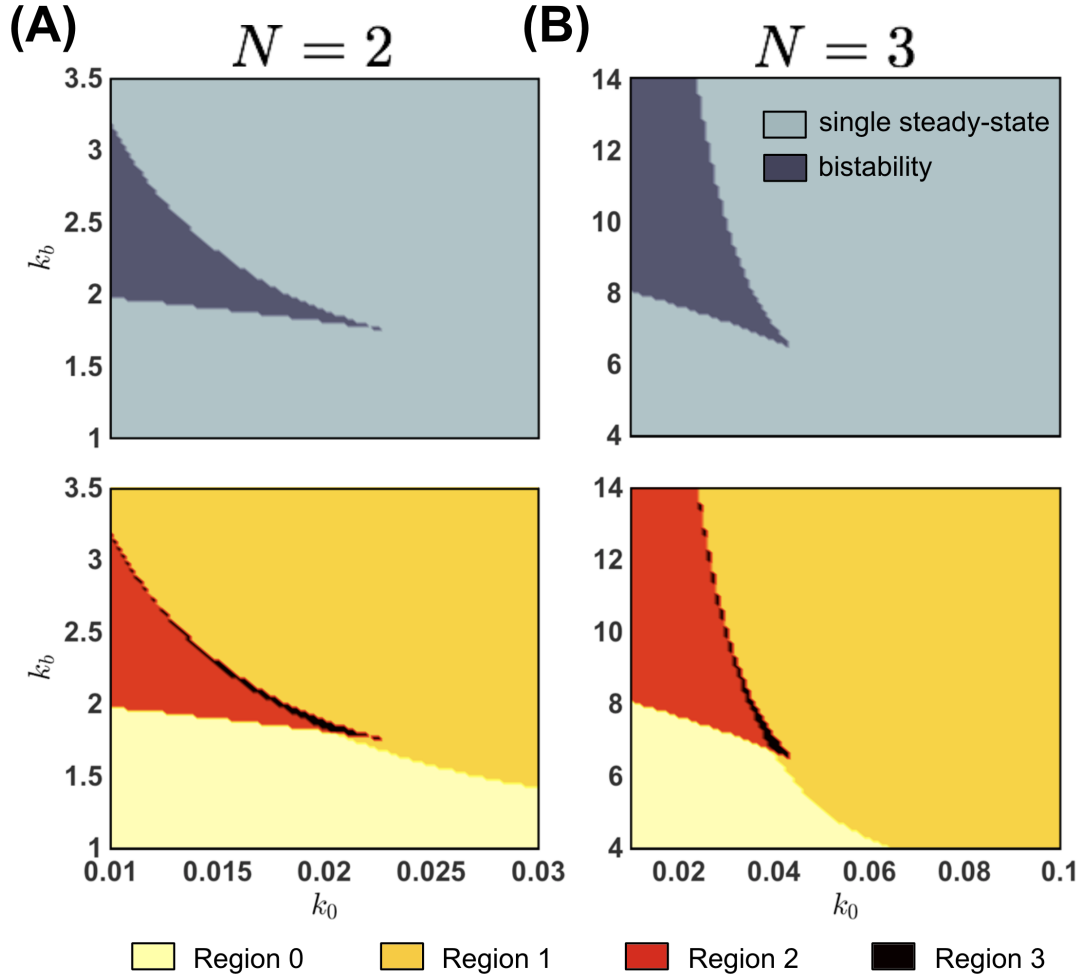
Figure D.3: **Parameter Regions of Bistability and Linear Instability** ($N = 2$ **and** $N = 3$) We scan the reaction rates for different parameter values. In the top, the parameter regions in the $k_0 \times k_b$ plane where the system exhibits bistability under homogeneous perturbations. In the bottom, Regions 0, 1, 2, and 3 divide the $k_0 \times k_b$ plane according to the number of unstable steady-states under non-homogeneous perturbations for the eigenmode $l = 1$ (see text for details). (A) $N = 2$, $d_2 = 0.1$, $\gamma = 1000$. (B) $N = 3$, $d_2 = d_3 = 0.1$, $\gamma = 1000$. The k_b values that promote linear instability are significantly higher for $N = 3$ compared to the case $N = 2$. Remaining fixed parameters: $R = 1$, $\Gamma = 4\pi$, $\Omega = \frac{3}{4}\pi$, $\mathcal{M}_0 = \Gamma$, $k_2 = k_3 = 1$, and $k_m = k_g = 1$.
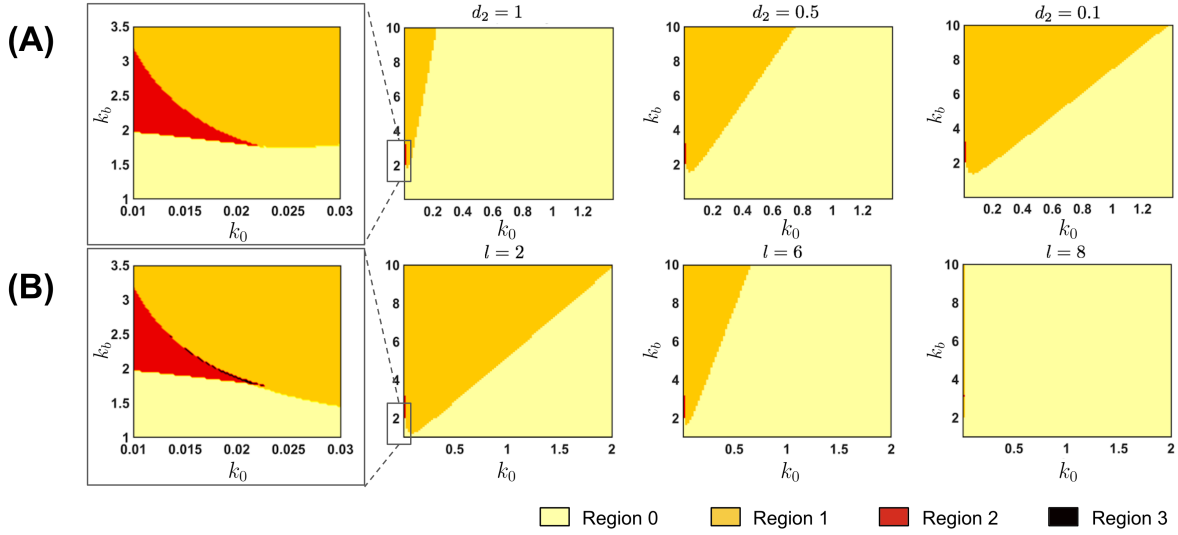
Figure D.4: **Changing the diffusion coefficient and the eigenmode of the Laplace-Beltrami operator for** $N = 2$. (A) For $d_2 = 1$, we show a zoomed plot of the interface of the Regions 1 and 2. Most of the (k_0, k_b) in the rectangle $[0.01, 1.4] \times [1, 10]$ belongs to the Region 0, where the system is stable under non-homogeneous perturbations. However, by decreasing d_2 to 0.5 and further to 0.1, the Region 1 (in orange) significanly increases, which means that the system exhibits a larger instability region for lower d_2 values. In this figure, we fix $\gamma = 10$ and $l = 1$ as the eigenmode index. (B) Linear instability Region 1 for eigenmode index values $l = 2$, 6, and 8. For $l = 2$, the system is unstable under non-homogeneous perturbations for most (k_0, k_b) values above the diagonal of the rectangle $[0.01, 2] \times [1, 10]$. As l increases, Region 1 (in orange) significantly decreases. Therefore, we can analyze the instability of the system by exploring only the first eigenmode, since Region 1 does not expand as l increases. In this figure, we fix $\gamma = 100$ and $d_2 = 0.1$. Remaining fixed parameters: $R = 1$, $\Gamma = 4\pi$, $\Omega = \frac{3}{4}\pi$, $\mathcal{M}_0 = \Gamma$, $k_2 = 1$, and $k_m = 1$.

higher dominance of the reaction flux over diffusion effects [393], and thus a larger unstable space tends to occur (Figure D.10). On the other hand, as the eigenmode index l increases, Region 1 significantly decreases (Figure D.4 (B)). We exhibit the results for $l = 2$, $l = 6$, and $l = 8$. Such a decrease implies that the Regions 1 for the higher eigenmodes ($l > 1$) are contained in the Region 1 for the first eigenmode ($l = 1$). For this reason, to determine the whole instability region in this case (which is the union of Regions 1 for all eigenmodes), it is sufficient to consider Region 1 for $l = 1$.

D.4.3 The emergence of the single-patch non-homogeneous steady-state

In this section, we investigate the spatio-temporal behavior of our system by numerically integrating the dimensionless equations. We consider a spherical domain of radius $R = 1$ and, as in the previous sections, we fix $N = 2$ or $N = 3$. We avoid solving the surface system (**D.23**)–(**D.24**) due to the numerical complexity of the non-local functional. Instead, we solve the dimensionless bulk-surface equations (**D.16**)–(**D.21**) (dropping all the hats) for an extremely high cytosolic diffusion ($\tilde{D} = 10^8$) on (**D.16**). In this way, our resulting system can be seen as an approximation of the reduced system when $\tilde{D} \to \infty$. We randomly perturbed the homogeneous steady-states by considering a small number $\varepsilon > 0$ as the perturbation magnitude and a family $\{\xi(x)\}_{x \in \Gamma}$ of independent random variables uniformly distributed between -1 and 1. In the case where $N = 2$, we define the surface initial conditions

$$a_1(x,0) := a_1^* + \varepsilon\, \xi(x) \quad \text{and} \quad a_2(x,0) := a_2^* - \frac{1}{2}\varepsilon\, \xi(x) \tag{D.36}$$

for $x \in \Gamma$, where the $\frac{1}{2}$ accounts for mass conservation (see (**D.22**)). For the volume component, we define $u(x,0) := u^*$, for $x \in \Omega$, where $u^* = \frac{1}{|\Omega|}\left[\mathcal{M}_0 - |\Gamma|(a_1^* + 2a_2^*)\right]$ also because of the mass conservation property. For $N = 3$ we define a_1^* as in (**D.36**), $a_j(x,0) := a_j^* - \frac{1}{5}\varepsilon\, \xi(x)$ for $j = 2$ and $j = 3$, and $u^* = \frac{1}{|\Omega|}\left[\mathcal{M}_0 - |\Gamma|(a_1^* + 2a_2^* + 3a_3^*)\right]$.

Remark D.4.1. *The element $(a_1^*, a_2^*, ..., a_N^*)$ is a homogeneous steady-state of the system (**D.23**)–(**D.24**) if and only if $(a_1^*, a_2^*, ..., a_N^*, u^*)$ is a homogeneous steady-state of the system (**D.16**)–(**D.21**) provided that*

$$u^* = \frac{1}{|\Omega|}\left[\mathcal{M}_0 - |\Gamma|(a_1^* + 2a_2^* + .. + Na_N^*)\right]$$

From the remark above, we can obtain the steady-states of the reduced system (**D.23**)–(**D.24**). Then we can numerically integrate the bulk-surface PDE system (**D.16**)–(**D.21**) using the perturbation scheme described above. In order to associate the parameter regions that lead to instabilities with the formation of spatial patterns, we select four (k_0, k_b) values in the four
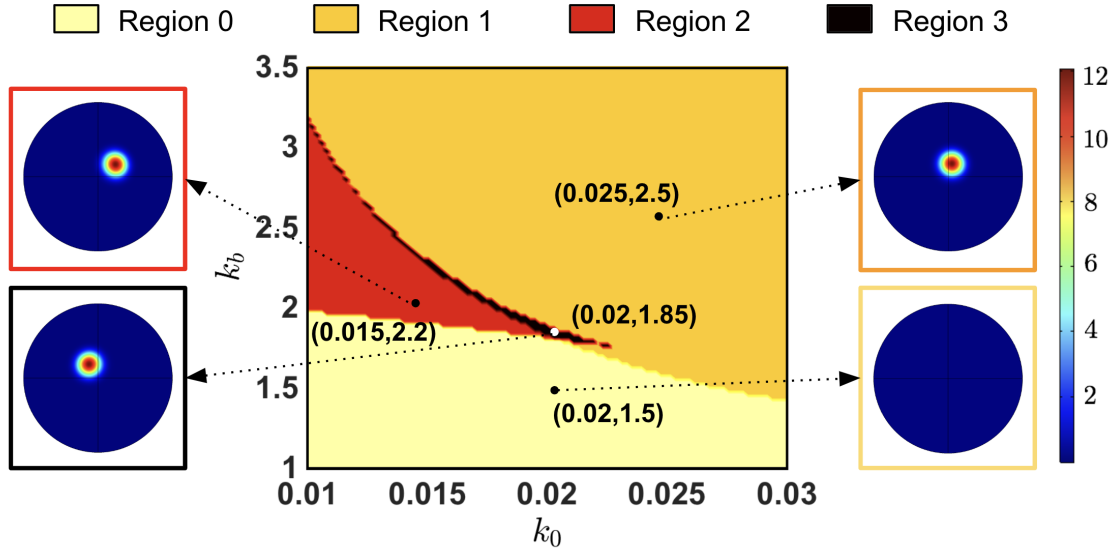
Figure D.5: **Linear Instability and Pattern Formation** ($N = 2$). We exhibit the stability analysis colormap for eigenmode index $l = 1$ and the final spatial profile of the a_1 component. We consider four (k_0, k_b) values from Regions 0, 1, 2, and 3, which are colored in light-yellow, orange, red or black, respectively. For Regions 1, 2, and 3, we observe the emergence of a single-patch spatially heterogeneous steady-state which is consistent across parameter regions in terms of its circular shape and concentration gradient. For Region 0, we do not observe a pattern formation for this particular eigenmode. In this figure, $d_2 = 0.1$, $\gamma = 1000$, $k_m = k_2 = 1$. steady-state values. Region 0: $a_1^* = 0.0812$, $a_2^* = 0.0066$, $u^* = 2.7168$. Region 1: $a_1^* = 0.3817$, $a_2^* = 0.1457$, $u^* = 0.9806$. Region 2: $a_1^* = 0.2759$, $a_2^* = 0.0761$, $u^* = 1.7155$. Region 3: $a_1^* = 0.1107$, $a_2^* = 0.0123$, $u^* = 2.5942$. Remaining fixed parameters: $R = 1$, $\Gamma = 4\pi$, $\Omega = \frac{3}{4}\pi$, $\mathcal{M}_0 = \Gamma$, $k_2 = 1$, $k_m = 1$.

Regions 0, 1, 2, and 3 (Figure D.5). We fix $N = 2$ and the eigenmode index $l = 1$. For each choice of (k_0, k_b), we integrate the system (**D.16**)–(**D.21**) to its final state by perturbing a homogeneous steady-state. We then plot the result for the a_1 component and visually inspect the results. For (k_0, k_b) in Regions 1, 2, and 3, (colored in orange, red or black, respectively), a *single-patch* spatially heterogeneous steady-state emerges. On the other hand, when (k_0, k_b) belong to Region 0, in which the system is stable for the eigenmode index $l = 1$, the system converges to its homogeneous steady-state. This result indicates that the single-patch pattern is consistent across parameter choices in Regions 1, 2, and 3, once it remains unchanged in its circular shape and gradient of concentrations. Figure D.11 in the ESM shows a similar result in the case $N = 3$.

D.4.4 Temporal evolution and pattern formation

In this section, we further investigate the temporal evolution of the system. We consider $N = 2$ and $(k_0, k_b) = (0.025, 2.5)$ which belongs to Region 1 (see Figure D.5). We then observe the spatial distribution of a_1 for different times (Figure D.6 (A)). At $t = 0$, We apply a random perturbation of magnitude $\varepsilon = 10^{-10}$ around the unique homogeneous steady-state that is unstable under non-homogeneous perturbations. The system then smooths due to diffusion and the small random peaks continuously coalesce and react, until a few large domains emerge at $t = 0.099$. At $t = 0.114$ and $t = 0.119$, multiple patches of higher a_1 concentration emerge. The feedback term (Eq. (**D.1**)) then plays its role, once the higher a_2 concentration location promotes the recruitment of more cytosolic component. This leads to the formation of the single-patch profile at $t = 0.159$. From that time until the final time ($t = 1$), the spatial configuration only changes in terms of concentration gradients. File F1 in the ESM contains a movie of the simulation shown in Figure D.6 (A) for both monomeric (a_1) and dimeric components (a_2). In Figure D.12 in the ESM, we show a similar result for $N = 3$.

In order to quantify the single-patch size, we quantify the surface area of the high-concentration locations in the spherical domain. For this purpose, we define the function

$$I_{a_j}^{\varepsilon}(t) = \int_{\Gamma} \mathbb{1}_{\{a_j(x,t) > \langle a_j \rangle(t) + \varepsilon\}} ds \tag{D.37}$$

where ε is the perturbation magnitude, j is the index of the oligomeric component, and $\langle a_j \rangle(t) = \int_{\Gamma} a_j ds$ is the average concentration of a_j across the sphere Γ. We then evaluate the evolution of $I_{a_j}^{\varepsilon}(t)$ over time (Figure D.6 (B)). We exhibit the results of a single simulation for $N = 2$ and $N = 3$, and $\varepsilon = 10^{-10}$. At early times, when the concentrations a_j are close to the steady-state a_j^* across the domain, $I_{a_j}^{\varepsilon}(t)$ remains close to 0. Then the combination of diffusion and the feedback term makes the concentration gradients increase in a large portion of the domain, as illustrated in Figure D.6 (A) for $t = 0.099$, $t = 0.114$, and $t = 0.119$. Finally, the formation

of the single-patch promotes the decrease of $I_{a_j}^\varepsilon(t)$, since the area of high concentration tends to be small in comparison with the total surface area. Moreover, the concentration outside the patch tends to be small, which makes the average $\langle a_j \rangle(t)$ assume lower values. Therefore, in the final times, the locations in the sphere where the concentrations remain above the average can be associated with the single patch. For this reason, we define the *single-patch area*

$$\mathcal{S}_{a_j}^\varepsilon := I_{a_j}^\varepsilon(t_f),$$

where t_f is the final simulation time. In this work, we avoid an analytical treatment for the functions $I_{a_j}^\varepsilon(t)$. In particular, we base our definition of the single-patch area $\mathcal{S}_{a_j}^\varepsilon$ on visual inspection of the curves in Fig 6(B): for $N = 2$ and $N = 3$, the quantities $I_{a_1}^\varepsilon(t)$ converge to a final value after a transient increase and subsequent decrease in time. Thus we assume that this final value gives a good estimate of the single-patch area as a function ε. In Figure D.13 in the ESM, we illustrate how the percentage of $\mathcal{S}_{a_j}^\varepsilon$ with respect to the total surface area does not change significantly as ε changes. We also observe that $I_{a_1}^\varepsilon > I_{a_2}^\varepsilon$ for all times in the case where $N = 2$, and also $I_{a_1}^\varepsilon > I_{a_2}^\varepsilon > I_{a_3}^\varepsilon$ in the case where $N = 3$. We conclude that $\mathcal{S}_{a_1}^\varepsilon > \mathcal{S}_{a_2}^\varepsilon$ (for $N = 2$) and $\mathcal{S}_{a_1}^\varepsilon > \mathcal{S}_{a_2}^\varepsilon > \mathcal{S}_{a_3}^\varepsilon$ (for $N = 3$). In order to better visualize this area shrinking as the oligomer size increases, we plot the final normalized concentration profiles (Figure D.6 (C)). Given the arc-length parametrization of a geodesic curve crossing the single-patch region, the concentration distributions become tighter for a_2 compared to a_1 in the case $N = 2$. The inset plot shows the non-normalized concentrations, where we see that $a_2 > a_1$ in the single-patch location. A similar phenomenon occurs for $N = 3$: the distribution and maximum value of a_j becomes tighter and larger as j increases from 1 to 3.

D.4.5 Change of the cell radius and single-patch area

We investigate how the single-patch area of a spherical cell depends on its radius R. From the non-dimensionalization of the bulk-surface system (see Appendix D.2.4), we defined
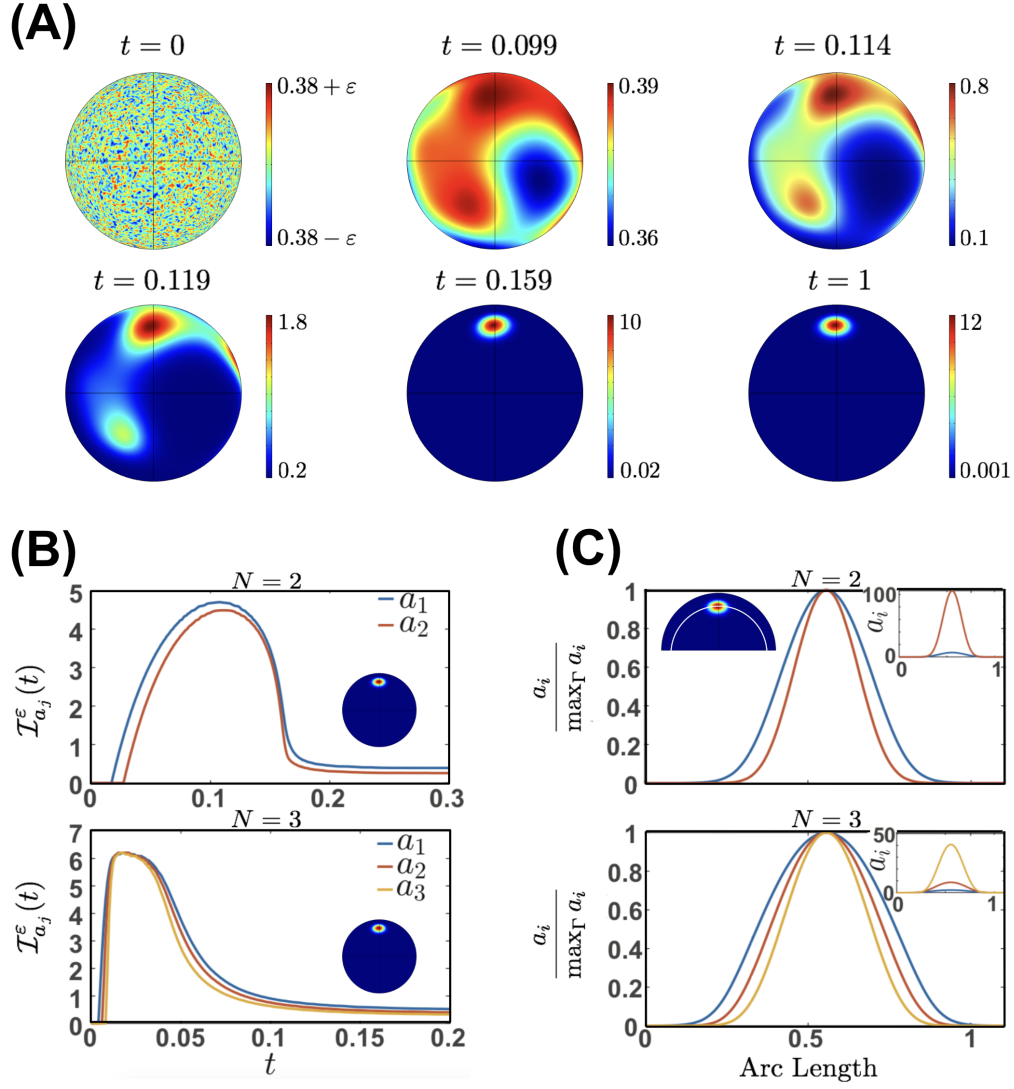
Figure D.6: **Temporal evolution and pattern formation** (A) Spatial distribution of the monomeric component (a_1) at different non-dimensional times. At $t = 0$, a random perturbation of magnitude $\varepsilon = 10^{-10}$ is applied to the unstable homogeneous steady-state. At $t = 0.099$, a small gradient emerges until $t = 0.114$, and at $t = 0.119$, the high-concentration domains begin to coalesce. At $t = 0.159$, the system converges to the single-patch profile. Finally, at $t = 1$, we show the single-patch steady-state with a final concentration gradient from 0.001 to 12 a.u. In this figure, we consider $N = 2$, $k_0 = 0.025$, and $k_b = 2.5$ such that a single steady-state becomes unstable under non-homogeneous perturbations ((k_0, k_b) belongs to Region 1 in Figure D.5). The steady-state is given by $a_1^* = 0.3817$, $a_2^* = 0.1457$, and $u^* = 0.9806$. A supplemental movie for panel (A) can be found in supplemental file F1. Remaining fixed parameters: $R = 1$, $\Gamma = 4\pi$, $\Omega = \frac{3}{4}\pi$, $\mathcal{M}_0 = \Gamma$, $k_2 = 1$, $k_m = 1$. (B) Evolution of $(I_{a_j}^\varepsilon)(t)$ that gives the single-patch area $\mathcal{S}_{a_j}^\varepsilon$ for $N = 2$ and $N = 3$ (see text for details). Inset: a single-patch final configuration. Parameter values: $R = 1$, $\gamma = 1000$, $d_2 = d_3 = 0.1$, $k_0 = 0.016$, $k_m = 1$, and $k_2 = 0.44$. Top: $N = 2$, $k_b = 1$. Bottom: $N = 3$, $k_b = 10$, $k_g = k_m$, $k_3 = k_2$. Initial conditions: $a_1(0) = 0.0918$, $a_2(0) = 0.0191$, $a_3(0) = 0$, $u(0) = 2.6099$. (C) For $N = 2$ and $N = 3$, we plot the final normalized a_j concentrations on a geodesic curve parametrized by arc-length. As the oligomer index j increases, the distribution and maximum value of a_j becomes tighter and higher (inset), respectively.

the characteristic quantities (**D.15**). In order to move through a dimensional system, we define the dimensionless parameters as depending on R to preserve a constant volume concentration. Therefore, we assume a constant U such that $\mathcal{M}_0 \propto R^3$, making the dimensionless parameters functions of R. For this reason, each choice of R will lead to a different solution of the non-dimensional system (**D.16**)–(**D.21**). In particular, it will also change the non-dimensional single-patch area $\mathcal{S}_{a_j}^{\varepsilon}$. We show the results for R ranging from 0.5 to 5 and two different parameters (Figure D.7):

$$\text{area percentage} = \frac{\mathcal{S}_{a_j}^{\varepsilon}}{4\pi} \times 100 \quad \text{and} \quad \text{dimensional area} = \mathcal{S}_{a_j}^{\varepsilon} R^2.$$

For $N = 2$ and $N = 3$, we provide the same total volume concentration for the system. For clarity, in this section we will refer to the non-dimensional system with the hat (^) notation. We define the initial conditions as a linear ramp of slope ε around the steady-state

$$\hat{a}_1(x,0) = \hat{a}_1^* + \varepsilon \hat{x}_1 \quad \text{and} \quad \hat{a}_2(x,0) = \hat{a}_2^* - \frac{1}{2} \varepsilon \hat{x}_1,$$

where $\hat{x} = (\hat{x}_1, \hat{x}_2, \hat{x}_3) \in \hat{\Gamma}$ and $\hat{x}_1$ is the position with the sphere centered in the origin. In the case $N = 3$, we assumed $a_3^* = 0$. See Figure D.7 caption for details on the parameter choices. We then observe the same phenomena: the dimensional area (fig. D.7 red; open circles) increases approximately linearly with R. On the other hand, the area percentage (fig. D.7 black; closed circles) decreases with R. We can then conclude that although the dimensional area of clusters increases, the additional spherical area changes at a much faster rate since the area percentage varies with $\approx \frac{1}{R}$. The effect of N on single-patch area shows both dimensional area and area percentage are higher for $N = 3$ (fig. D.7(B)) in comparison with $N = 2$ (fig. D.7(A)).
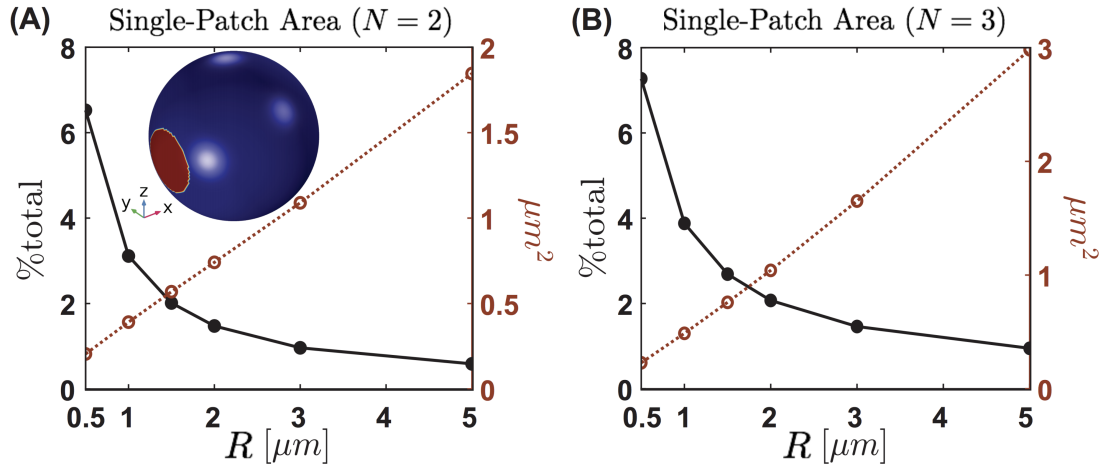
Figure D.7: **Change of the cell radius and single-patch area.** We quantify the percentage of the total area and the dimensional area (see text for details), for various radii R ranging from 0.5 to 5. The R value was changed in the non-dimensional system with a fixed concentration (U) through variations in Γ, γ, A, $\hat{k}_0$, $\hat{k}_m$, and $\hat{k}_g$ (see equations **D.16 – D.21**). (A) We quantify the Patch size for the $N = 2$ case (red; open circles), then normalized against the total area of the sphere (black; closed circles). As the radius increases, the patch size increases approximately linearly, but the percent area decreases rapidly. (B) The same simulation for $N = 3$. As the radius increases the patch size increases, but the total percent area still decreases. Between cases, we observe the same general qualitative properties for single-patch area percentage and dimensional area. The major differences arise in the absolute values, as $N = 3$ creates larger patches. In these simulations, $\varepsilon = 0.01a_2^*$, $a_1^* = 0.0981$, $a_2^* = 0.0191$, $a_3^* = 0$, $u^* = 2.6099$. Parameter values: $d_2 = d_3 = 0.1$, $\tilde{D} = 10^8$, $\hat{k}_0 = \frac{0.016}{R}$, $\tilde{k}_b = 10$, $\hat{k}_g = \hat{k}_m = R$, $\hat{k}_3 = \hat{k}_2 = 0.44$, $\gamma = 1000R^2$.

D.5   Discussion

Protein heterogeneity in the PM is of critical importance to cellular functions. Many factors influence this heterogeneity, including membrane composition, protein-protein interaction, phase separation, lateral diffusion, and possible feedback, resulting in the formation of spatial patterns [333–335]. For this reason, understanding the interplay of aggregation kinetics, lateral diffusion, and feedback in the formation of spatial patterns is an essential step towards developing a complete description of the mechanisms behind protein clustering on the cell surface. In this work, we developed a bulk-surface model for protein aggregation with positive feedback that exhibits a spatially heterogeneous single-patch steady-state. To the best of our knowledge, this is the first modeling attempt that merges the reaction-diffusion version of classical Smoluchowski dynamics with the modern bulk-surface geometrical setup.

A major result from our model is the role played by the feedback term $k_b\, a_N$ in the boundary conditions (**D.1**). If k_b is low enough, the steady-state distribution is spatially uniform, and no protein heterogeneity exists. For $N = 2$, we formally proved such a result (Theorem D.3.1), and for $N = 3$, we used numerical simulations to observe a similar phenomenon. In particular, in the total absence of feedback ($k_b = 0$), we observed that spatial heterogeneity is not achievable when we only considered protein-protein interaction. On the other hand, if k_b is sufficiently high, we observed the emergence of linear instability and therefore patterning on the cellular surface. Experimental observations have shown that membrane proteins do organize in a spatially heterogeneous fashion [349–351]. However, the molecular mechanisms are still being investigated experimentally. The feedback mechanism we proposed here can also be interpreted in purely biological terms. The largest oligomers recruit ligands from the cytosol, which form ligand-receptor monomers. If the rate of recruitment of monomers is low, diffusive effects dominate, and the configuration of the system is homogeneous in space. On the other hand, a higher rate promotes a significant influx of new monomeric components. Then, continued oligomerization

generates higher concentrations of the largest components, which closes the positive feedback loop and drives pattern formation. The largest oligomers can thus be interpreted as self-activators of pattern formation. For this reason, our mechanism of pattern formation can be related to the classical Turing framework, where self-activation is required to generate spatial patterns [270,394]. Another interesting aspect of our model is the absence of an explicit description of cooperative binding. For the wave-pinning model [262, 299, 354], cooperativity is included with a Hill function, which accounts for the positive feedback. In contrast, our oligomerization reactions assume only mass-action kinetics, which seems to be insufficient for pattern formation without the feedback term.

Bistable systems are well known to promote diffusion-driven instabilities in the context of cell polarization [395, 396]. For the wave-pinning model [262, 299, 354], the structure of the Hill function is responsible for bistability. Other studies followed a similar approach, using a particular choice of reaction flux that is naturally associated with a bistable regime [397, 398]. In our model, bistability emerges by the combination of two key ingredients: positive feedback and mass conservation. This observation becomes clear as we carefully inspect the steady-state analysis of the reduced system (cf. Appendix D.3.1). First, the equilibrium of the oligomerization reactions (driven only by mass action kinetics) provides the distribution across the different surface components. Then, the input from the non-local functional comes into play, as a consequence of the boundary conditions and mass conservation. The non-local functional at steady-state provides an extra equation, which gives the equilibrium solutions for the monomeric component. The particular contribution of the feedback comes from the coefficient $C_N \left(k_0 |\Gamma| N - \mathcal{M}_0 k_b \right) \alpha^N$ of the polynomial $\mathcal{P}_N(\alpha)$. If the coefficient is negative, then the existence of three roots, and therefore three steady-states, is achievable. In this case, we can compute their stability under homogeneous perturbations and verify bistability.

Under non-homogeneous perturbations, one or two stable steady-states may become

unstable, and the system undergoes a diffusion-driven instability. Even more impressive is the emergence of a linear instability parameter region, called Region 1 in this study, when the system admits a single steady-state that becomes unstable. We note that in Getz et al. [399], the authors were able to find a region of linear instability for the Wave-Pinning model that is comparable with our Region 1. While the authors briefly discussed the changes in that parameter region for different wave-numbers, here we explicitly showed that the leading eigenmode exhibits a region of instability that shrinks as the eigenmode index increases. Such instability in the lower modes, which are associated with the smallest positive eigenvalues of the Laplace-Beltrami operator, has been often related to a single-patch steady-state pattern [390, 400], which is confirmed for our system.

The single-patch steady-state consistently appears for parameter values corresponding to the different instability regions (called as Regions 0, 1,2 and 3). Goryachev et al. [400] found a similar spatial profile for the Cdc42 GTPase cycle, where the influx of new cytoplasmic components maintained the cluster steady-state and compensated for its lateral diffusion. A similar phenomenon seems to happen in our system. An allegory that explains the stable existence of such heterogeneous steady-states is the so-called "rich gets richer" competition [401]. In this case, larger domains outcompete the smaller until only one stable domain arises. Our hypothesis about the existence of the single-patch is based on the role of the positive feedback term. We assume that the presence of high concentrations of the largest oligomer promotes ligand binding onto the PM in a linear fashion, without any saturation mechanism or steric effects. As in [400], this assumption seems to account for a resource competition that excludes the possibility of multiple patches. In cells, multiple patches of protein aggregates are observed [402]. The number and size of these aggregates often depend on the particular experimental condition and the membrane composition. Modeling such observations will require the development of a more thermodynamically detailed model.

Based on the insights from our model, we identify future research directions that will enhance studies such as ours. In the current formulation, we lack a formal explanation for the emergence and robustness of the single patch steady-state. The spatial aspects of the model render such analysis hard, but it may be possible to obtain a formal proof by considering a one-dimensional version of our system as in [262]. Another interesting quantity to be computed in future studies is the so-called *amplitude of the pattern*, for which a formal calculation was recently developed [403]. Additionally, the mathematical challenge for a theoretical stability result lies in the increasing complexity of the system as N increases. In this case, we have relied on numerical simulations for $N = 3$ to identify the threshold phenomenon for diffusion-driven instabilities. However, future efforts in this direction could open up new mathematical avenues for stability analysis of increasingly complex systems. Regarding the parameter choices, it's important to acknowledge that our parameters were not informed by data. Instead, in this work we focused on establishing the dimensionless parameter spaces that yield linear instabilities within the Turing approach. In a different direction, future efforts will be devoted to adapting our system to specific biological problems. Finally, including the role of curvature and cytosolic diffusion in the formation of membrane protein aggregates would bring us closer to analyses of biological and biophysical systems. These are topics of ongoing studies in our group.

D.6   Acknowledgments

D.7   Electronic Supplementary Material

D.7.1   Details regarding the numerical simulations

Matlab simulations

For computing the roots of the polynomials $P_N(\alpha)$ (Eq. **D.27**), which are the steady-state values for the monomeric component a_1^*, we applied the Matlab R2018a functions *sym2poly* and *roots*. Function *sym2poly* converts a symbolic polynomial into a vector with the corresponding polynomial coefficients. We then use the function *roots*, which computes the polynomial roots. For the eigenvalues of the Jacobian matrices $\mathcal{J}[\mathbf{a}^*]$ and $\tilde{\mathcal{J}}(\mathbf{a}^*)$ (defined in sections **D.3.2** and **D.3.2**, respectively), we used the function *eig* that gives the eigenvalues of a matrix.

Comsol simulations

The system runs using the MUltifrontal Massively Parallel sparse direct Solver (MUMPS) algorithm [404] to solve the Finite Element Method (FEM) problem in COMSOL Multiphysics 5.4(R). As long as the problem is well conditioned (i.e. no long edges/sharp interfaces) the direct method used should not matter as all algorithms will converge to the same solution. Other direct solvers available are PARDISO and SPOOLES. A tetrahedral mesh was used for better accuracy and adaptability at the spherical interface. For faster conversion of the solution, multiple mesh sizes were utilized. In what follows, we prescribe the details of our numerical simulations:

- Version: 5.4

- Algorithm : MUMPS

- Tolerance: Physics controlled

- Max iterations to reach tolerance: 10

- Mesh size : Automated free tetrahedral mesh generation with constraints:

- <u>Volume</u>: Max: 0.3, Min: 0.056, Max growth rate: 1.6, Curvature factor: 0.7, Resolution of narrow regions: 0.4.

- <u>Surface</u>: Max: 0.05, Min: 8E-4, Max growth rate: 1.3, Curvature factor: 0.2, Resolution of narrow regions: 1.

- <u>Boundary Layer</u>: BL: 8, stretching factor: 1.2, Automatic thickness.
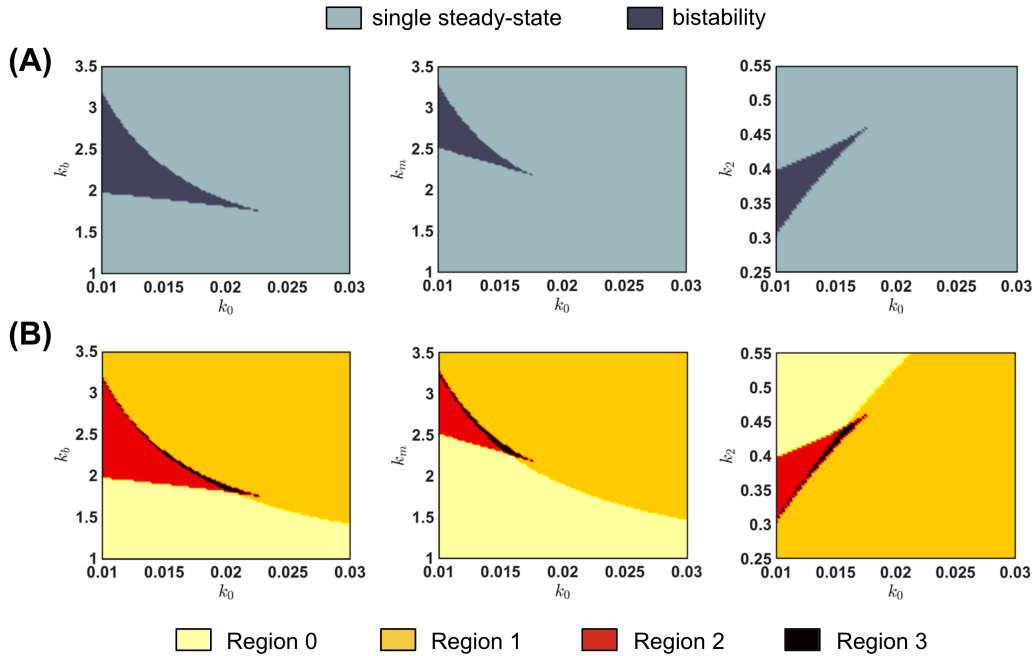
Figure D.8: **Parameter Regions of Bistability and Linear Instability** ($N = 2$)**.** We scan the reaction rates for different parameter values. (A) regions where the well-mixed system exhibits bistability. (B) The corresponding Regions 0, 1, 2, and 3 (see section **D.4.2** of the manuscript for details). In the figure, we fixed $d_2 = 0.1$, $\gamma = 1000$, and eigenmode index $l = 1$. Remaining fixed parameters: $R = 1$, $\Gamma = 4\pi$, $\Omega = \frac{3}{4}\pi$, $\mathcal{M}_0 = \Gamma$, $k_2 = 1$, and $k_m = 1$ (when not varying)
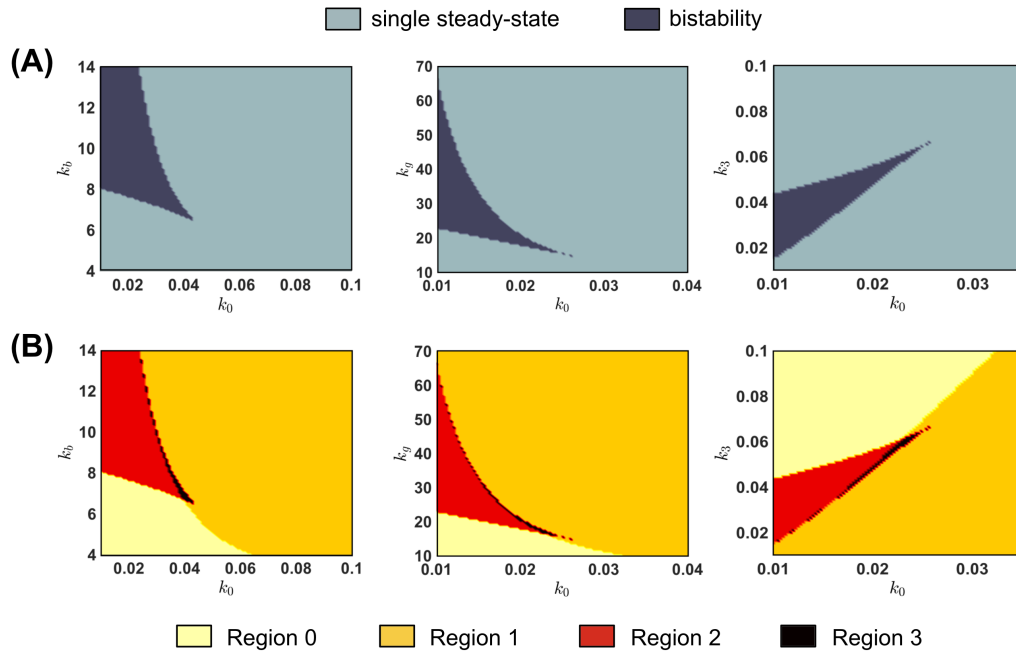
Figure D.9: **Parameter Regions of Bistability and Linear Instability** ($N = 3$). We scan the reaction rates for different parameter values. (A) regions where the well-mixed system exhibits bistability. (B) The corresponding Regions 0, 1, 2, and 3 (see manuscript for details). In the figure, we fixed $d_2 = d_3 = 0.1$, $\gamma = 1000$, and eigenmode index $l = 1$. Remaining fixed parameters: $R = 1$, $\Gamma = 4\pi$, $\Omega = \frac{3}{4}\pi$, $\mathcal{M}_0 = \Gamma$,$k_2 = k_3 = 1$, and $k_m = k_g = 1$ (when not varying).
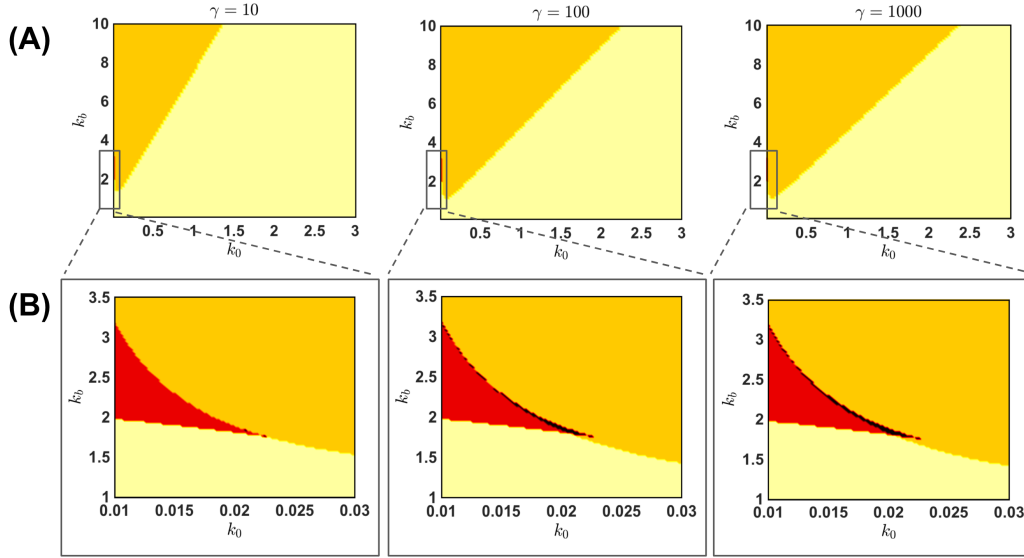
Figure D.10: **Changing the dimensionless parameter** γ ($N = 2$). (A) Changing the reaction parameter γ for a wider range of k_0 and k_b allow us to observe instability regions in the single steady-state regime that are considerably larger than the union of Regions 2 and 3. We observe an increase of Region 1 as γ increases. (B) A zoom on Region 2 and 3 shows little differences among the profiles, except for $\gamma = 10$, where the Region 3 is significantly reduced. In this figure, we consider $d_2 = 0.1$ and eigenmode $l = 1$. Remaining fixed parameters: $R = 1$, $\Gamma = 4\pi$, $\Omega = \frac{3}{4}\pi$, $\mathcal{M}_0 = \Gamma$, $k_2 = 1$, and $k_m = 1$.
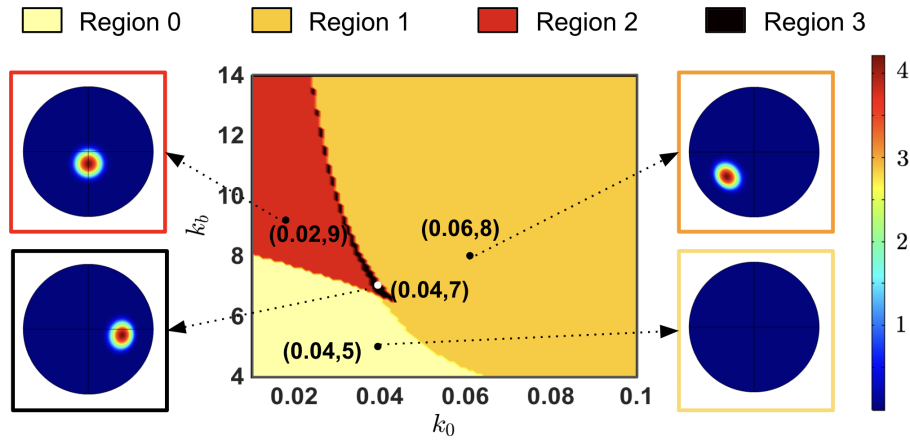
Figure D.11: **Linear Instability and Pattern Formation** ($N = 3$). We exhibit the stability analysis colormap for eigenmode index $l = 1$ and the final spatial profile of the a_1 component. We consider four (k_0, k_b) values from Regions 0, 1, 2, and 3, which are colored in light-yellow, orange, red, or black, respectively. For Regions 1, 2, and 3, we observe the emergence of a single-patch spatially heterogeneous steady-state, which is consistent across parameter regions in terms of its circular shape and concentration gradient. For Region 0, we do not observe a pattern formation for this particular eigenmode. In the figure, we fixed $d_2 = d_3 = 0.1$, $\gamma = 1000$, eigenmode index $l = 1$, $k_m = k_g = k_2 = k_3 = 1$. steady-state values. Region 0: $a_1^* = 0.1251$, $a_2^* = 0.0157$, $a_3^* = 0.002$, $u^* = 2.513$, Region 1: $a_1^* = 0.3439$, $a_2^* = 0.1183$, $a_3^* = 0.0407$, $u^* = 0.8922$. Region 2: $a_1^* = 0.3442$, $a_2^* = 0.1185$, $a_3^* = 0.0408$, $u^* = 0.8892$. Region 3: $a_1^* = 0.1598$, $a_2^* = 0.0255$, $a_3^* = 0.0041$, $u^* = 2.3306$. Remaining fixed parameters: $R = 1$, $\Gamma = 4\pi$, $\Omega = \frac{3}{4}\pi$, $\mathcal{M}_0 = \Gamma$, $k_2 = k_3 = 1$, $k_m = k_g = 1$.
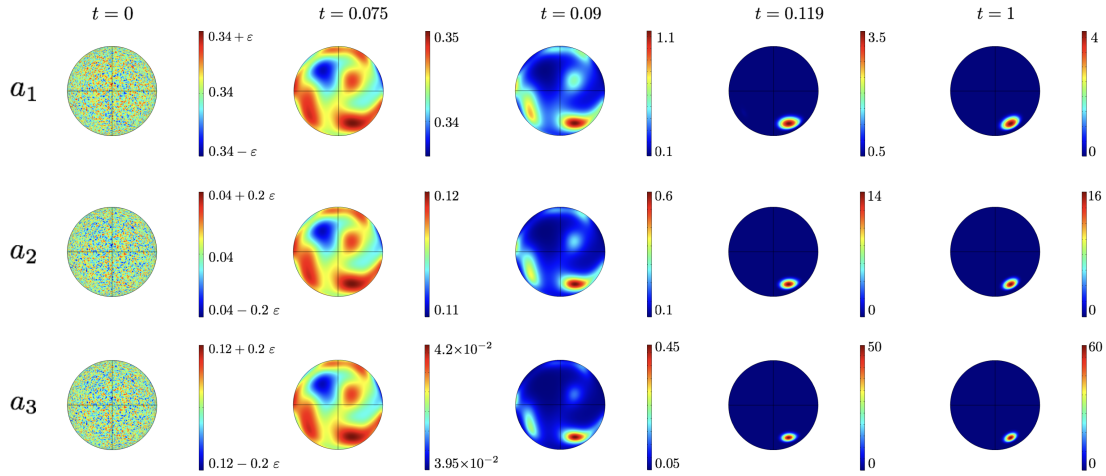
Figure D.12: **Temporal Evolution and pattern formation** ($N = 3$). Spatial distribution of the three components (a_1, a_2, and a_3) at different non-dimensional times. At $t = 0$, a random perturbation of magnitude $\varepsilon = 10^{-10}$ is applied to the unstable homogeneous steady-state. At $t = 0.075$, a small gradient emerges. At $t = 0.09$, multiple patches can be seen and at $t = 0.119$ the system exhibits the single-patch profile. Finally, at $t = 1$, we show the single-patch steady-state. In the figure, we fixed $d_2 = d_3 = 1$, $\gamma = 1000$, $k_m = k_g = k_2 = k_3 = 1$, $k_0 = 0.06$, $k_b = 8$ (Region 1). The steady-state is given by $a_1(0) = 0.3439$, $a_2(0) = 0.1183$, $a_3(0) = 0.0407$, and $u(0) = 0.8922$. Remaining fixed parameters: $R = 1$, $\Gamma = 4\pi$, $\Omega = \frac{3}{4}\pi$,

Appendix **D**, in full, is a reprint of the material as it appears in L. M. Stolerman, M. Getz, S. G. L. Smith, M. Holst, and P. Rangamani. Stability Analysis of a Bulk–Surface Reaction Model for Membrane Protein Clustering. 82(2):30. The dissertation author was the co-first author of this material.

Single-Patch Area ($N = 2$)
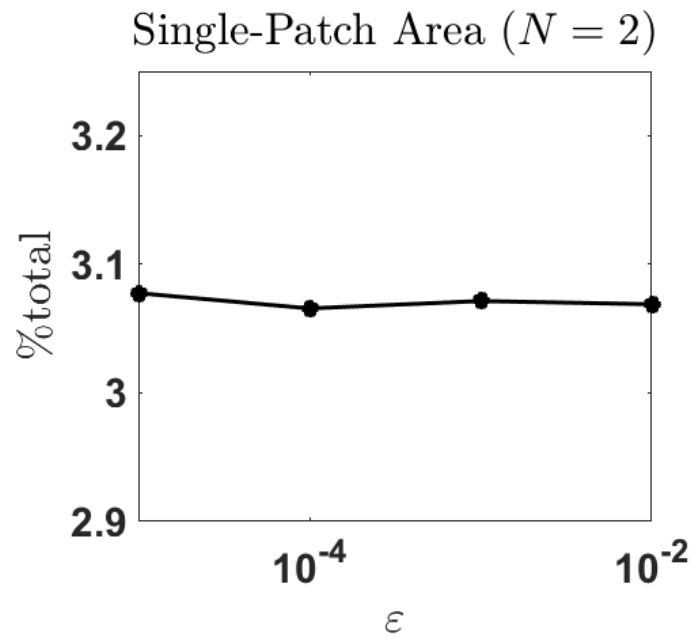
Figure D.13: **Single-patch area and perturbation magnitude** We plot the percentage of $\mathcal{S}_{a_j}^{\varepsilon}$ with respect to the total surface area. We observe that such quantity does not change significantly as ε changes. In this figure, we assume $R = 1$, $d_2 = 0.1$, $k_0 = 0.016$, $k_b = k_m = 1$, $k_2 = 0.44$, $a_1(0) = 0.918$, $a_2(0) = 0.0191$, $\gamma = 1000$, $N = 2$, and $u(0) = 2.6099$

Bibliography

[1] J. A. Beavo and L. L. Brunton. Cyclic nucleotide research – still expanding after half a century. *Nature Reviews. Molecular Cell Biology*, 3(9):710–718, 2002.

[2] A. C. Newton, M. D. Bootman, and J. D. Scott. Second Messengers. *Cold Spring Harbor Perspectives in Biology*, 8(8), 2016.

[3] P. Sassone-Corsi. The cyclic AMP pathway. *Cold Spring Harbor Perspectives in Biology*, 4(12), 2012.

[4] D. E. Clapham. Calcium signaling. 131(6):1047–1058.

[5] K. L. Pierce, R. T. Premont, and R. J. Lefkowitz. Seven-transmembrane receptors. *Nature Reviews Molecular Cell Biology*, 3(9):639–650, 2002.

[6] S. J. MacKenzie, G. S. Baillie, I. McPhee, C. MacKenzie, R. Seamons, T. McSorley, J. Millen, M. B. Beard, G. van Heeke, and M. D. Houslay. Long PDE4 cAMP specific phosphodiesterases are activated by protein kinase A-mediated phosphorylation of a single serine residue in Upstream Conserved Region 1 (UCR1). *British Journal of Pharmacology*, 136(3):421–433, 2002.

[7] K. S. Murthy, H. Zhou, and G. M. Makhlouf. PKA-dependent activation of PDE3A and PDE4 and inhibition of adenylyl cyclase V/VI in smooth muscle. *American Journal of Physiology. Cell Physiology*, 282(3):C508–517, 2002.

[8] C. Sette and M. Conti. Phosphorylation and activation of a cAMP-specific phosphodiesterase by the cAMP-dependent protein kinase. Involvement of serine 54 in the enzyme activation. *The Journal of Biological Chemistry*, 271(28):16526–16534, 1996.

[9] J. Tremblay, B. Lachance, and P. Hamet. Activation of cyclic GMP-binding and cyclic AMP-specific phosphodiesterases of rat platelets by a mechanism involving cyclic AMP-

dependent phosphorylation. *Journal of Cyclic Nucleotide and Protein Phosphorylation Research*, 10(4):397–411, 1985.

[10] G. Dupont, L. Combettes, G. S. Bird, and J. W. Putney. Calcium oscillations. 3(3).

[11] O. Dyachok, Y. Isakov, J. Sagetorp, and A. Tengholm. Oscillations of cyclic AMP in hormone-stimulated insulin-secreting beta-cells. 439(7074):349–352.

[12]

[13] A. B. Parekh. Decoding cytosolic Ca2$^+$ oscillations. 36(2):78–87.

[14] Q. Ni, A. Ganesan, N.-N. Aye-Han, X. Gao, M. D. Allen, A. Levchenko, and J. Zhang. Signaling diversity of PKA achieved via a Ca2+-cAMP-PKA oscillatory circuit. *Nature Chemical Biology*, 7(1):34–40, 2011.

[15] A. Tengholm. Cyclic AMP dynamics in the pancreatic β-cell. 117(4):355–369.

[16] R. Nesher, E. Anteby, M. Yedovizky, N. Warwar, N. Kaiser, and E. Cerasi. Beta-cell protein kinases and the dynamics of the insulin response to glucose. 51 Suppl 1:S68–73.

[17] P. Rorsman and F. M. Ashcroft. Pancreatic β-Cell Electrical Activity and Insulin Secretion: Of Mice and Men. 98(1):117–214.

[18] M. A. White and R. G. Anderson. Signaling Networks in Living Cells. 45(1):587–603. _eprint: https://doi.org/10.1146/annurev.pharmtox.45.120403.095807.

[19] F. D. Smith and J. D. Scott. Signaling complexes: Junctions on the intracellular information super highway. 12(1):R32–40.

[20] O. H. Petersen. Calcium signal compartmentalization. 35(2):177–182.

[21] D. Calebiro and I. Maiellaro. cAMP signaling microdomains and their observation by optical methods. 8.

[22] M. D. Stern. Buffering of calcium in the vicinity of a channel pore. 13(3):183–192.

[23] J. Hanoune and N. Defer. Regulation and Role of Adenylyl Cyclase Isoforms. 41(1):145–174. _eprint: https://doi.org/10.1146/annurev.pharmtox.41.1.145.

[24] A. T. Bender and J. A. Beavo. Cyclic nucleotide phosphodiesterases: Molecular regulation to clinical use. *Pharmacological Reviews*, 58(3):488–520, 2006.

[25] C. Lohse, A. Bock, I. Maiellaro, A. Hannawacker, L. R. Schad, M. J. Lohse, and W. R. Bauer. Experimental and mathematical analysis of cAMP nanodomains. 12(4):e0174856.

[26] N. Musheshe, M. Schmidt, and M. Zaccolo. cAMP: From Long-Range Second Messenger to Nanodomain Signalling. 39(2):209–222.

[27] J. J. Saucerman, E. C. Greenwald, and R. Polanowska-Grabowska. Mechanisms of cyclic AMP compartmentation revealed by computational models. 143(1):39–48.

[28] P. Tagliaferri, D. Katsaros, T. Clair, S. Ally, G. Tortora, L. Neckers, B. Rubalcava, Z. Parandoosh, Y.-a. Chang, G. R. Revankar, G. W. Crabtree, R. K. Robins, and Y. S. Cho-Chung. Synergistic Inhibition of Growth of Breast and Colon Human Cancer Cell Lines by Site-selective Cyclic AMP Analogues. *Cancer Research*, 48(6):1642–1650, 1988.

[29] N. Dumaz, R. Hayward, J. Martin, L. Ogilvie, D. Hedley, J. A. Curtin, B. C. Bastian, C. Springer, and R. Marais. In melanoma, RAS mutations are accompanied by switching signaling from BRAF to CRAF and disrupted cyclic AMP signaling. *Cancer Research*, 66(19):9483–9491, 2006.

[30] M. J. Boucher, C. Duchesne, J. Lainé, J. Morisset, and N. Rivard. cAMP protection of pancreatic cancer cells against apoptosis induced by ERK inhibition. *Biochemical and Biophysical Research Communications*, 285(2):207–216, 2001.

[31] A. M. Fajardo, G. A. Piazza, and H. N. Tinsley. The role of cyclic nucleotide signaling pathways in cancer: Targets for prevention and treatment. *Cancers*, 6(1):436–458, 2014.

[32] D. Filmore. It's a GPCR world. *Modern drug discovery*, 7(11):24–28, 2004.

[33] P. Pantziarka, V. Sukhatme, S. Crispino, G. Bouche, L. Meheus, and V. P. Sukhatme. Repurposing drugs in oncology (ReDO)—selective PDE5 inhibitors as anti-cancer agents. *ecancermedicalscience*, 12, 2018.

[34] I. Barone, C. Giordano, D. Bonofiglio, S. Andò, and S. Catalano. Phosphodiesterase type 5 and cancers: Progress and challenges. *Oncotarget*, 8(58):99179–99202, 2017.

[35] P. Ghosh. The stress polarity pathway: AMPK 'GIV'-es protection against metabolic insults. *Aging*, 9(2):303–314, 2017.

[36] F. J. Alenghat, J. D. Tytell, C. K. Thodeti, A. Derrien, and D. E. Ingber. Mechanical control of cAMP signaling through integrins is mediated by the heterotrimeric Gαs protein. *Journal of cellular biochemistry*, 106(4):529–538, 2009.

[37] H. Poppleton, H. Sun, D. Fulgham, P. Bertics, and T. B. Patel. Activation of G by the Epidermal Growth Factor Receptor Involves Phosphorylation. *Journal of Biological Chemistry*, 271(12):6947–6951, 1996.

[38] P. Burke, K. Schooler, and H. S. Wiley. Regulation of Epidermal Growth Factor Receptor Signaling by Endocytosis and Intracellular Trafficking. *Molecular Biology of the Cell*, 12(6):1897–1910, 2001.

[39] B. N. Kholodenko, O. V. Demin, G. Moehren, and J. B. Hoek. Quantification of Short Term Signaling by the Epidermal Growth Factor Receptor. *Journal of Biological Chemistry*, 274(42):30169–30181, 1999.

[40] A. O. Beas, V. Taupin, C. Teodorof, L. T. Nguyen, M. Garcia-Marcos, and M. G. Farquhar. Gαs promotes EEA1 endosome maturation and shuts down proliferative signaling through interaction with GIV (Girdin). *Molecular Biology of the Cell*, 23(23):4623–4634, 2012.

[41] P. Ghosh, A. O. Beas, S. J. Bornheimer, M. Garcia-Marcos, E. P. Forry, C. Johannson, J. Ear, B. H. Jung, B. Cabrera, J. M. Carethers, and M. G. Farquhar. A Gαi–GIV Molecular Complex Binds Epidermal Growth Factor Receptor and Determines Whether Cells Migrate or Proliferate. *Molecular Biology of the Cell*, 21(13):2338–2354, 2010.

[42] V. Gupta, D. Bhandari, A. Leyme, N. Aznar, K. K. Midde, I.-C. Lo, J. Ear, I. Niesman, I. López-Sánchez, J. B. Blanco-Canosa, M. von Zastrow, M. Garcia-Marcos, M. G. Farquhar, and P. Ghosh. GIV/Girdin activates Gαi and inhibits Gαs via the same motif. *Proceedings of the National Academy of Sciences*, 113(39):E5721–E5730, 2016.

[43] C. Lin, J. Ear, K. Midde, I. Lopez-Sanchez, N. Aznar, M. Garcia-Marcos, I. Kufareva, R. Abagyan, and P. Ghosh. Structural basis for activation of trimeric Gi proteins by multiple growth factor receptors via GIV/Girdin. *Molecular Biology of the Cell*, 25(22):3654–3671, 2014.

[44] C. Lin, J. Ear, Y. Pavlova, Y. Mittal, I. Kufareva, M. Ghassemian, R. Abagyan, M. Garcia-Marcos, and P. Ghosh. Tyrosine Phosphorylation of the Guanine Nucleotide Exchange Factor GIV Promotes Activation of PI3K During Cell Migration. *Science signaling*, 4(192):ra64, 2011.

[45] G. S. Ma, N. Aznar, N. Kalogriopoulos, K. K. Midde, I. Lopez-Sanchez, E. Sato, Y. Dunkel, R. L. Gallo, and P. Ghosh. Therapeutic effects of cell-permeant peptides that activate G proteins downstream of growth factors. *Proceedings of the National Academy of Sciences of the United States of America*, 112(20):E2602–E2610, 2015.

[46] G. S. Ma, I. Lopez-Sanchez, N. Aznar, N. Kalogriopoulos, S. Pedram, K. Midde, T. P.

Ciaraldi, R. R. Henry, and P. Ghosh. Activation of G proteins by GIV-GEF is a pivot point for insulin resistance and sensitivity. *Molecular Biology of the Cell*, 26(23):4209–4223, 2015.

[47] K. K. Midde, N. Aznar, M. B. Laederich, G. S. Ma, M. T. Kunkel, A. C. Newton, and P. Ghosh. Multimodular biosensors reveal a novel platform for activation of G proteins by growth factor receptors. *Proceedings of the National Academy of Sciences of the United States of America*, 112(9):E937–946, 2015.

[48] K. Parag-Sharma, A. Leyme, V. DiGiacomo, A. Marivin, S. Broselid, and M. Garcia-Marcos. Membrane Recruitment of the Non-receptor Protein GIV/Girdin (Gα-interacting, Vesicle-associated Protein/Girdin) Is Sufficient for Activating Heterotrimeric G Protein Signaling. *Journal of Biological Chemistry*, 291(53):27098–27111, 2016.

[49] A. Leyme, A. Marivin, and M. Garcia-Marcos. GIV/Girdin (Gα-interacting, Vesicle-associated Protein/Girdin) Creates a Positive Feedback Loop That Potentiates Outside-in Integrin Signaling in Cancer Cells. *The Journal of Biological Chemistry*, 291(15):8269–8282, 2016.

[50] A. Leyme, A. Marivin, L. Perez-Gutierrez, L. T. Nguyen, and M. Garcia-Marcos. Integrins activate trimeric G proteins via the nonreceptor protein GIV/Girdin. *The Journal of Cell Biology*, 210(7):1165–1184, 2015.

[51] I. Lopez-Sanchez, N. Kalogriopoulos, I.-C. Lo, F. Kabir, K. K. Midde, H. Wang, and P. Ghosh. Focal adhesions are foci for tyrosine-based signal transduction via GIV/Girdin and G proteins. *Molecular Biology of the Cell*, 26(24):4313–4324, 2015.

[52] L. Weng, A. Enomoto, H. Miyoshi, K. Takahashi, N. Asai, N. Morone, P. Jiang, J. An, T. Kato, K. Kuroda, T. Watanabe, M. Asai, M. Ishida-Takagishi, Y. Murakumo, H. Nakashima, K. Kaibuchi, and M. Takahashi. Regulation of cargo-selective endocytosis by dynamin 2 GTPase-activating protein girdin. *The EMBO Journal*, 33(18):2098–2112, 2014.

[53] M. Anai, N. Shojima, H. Katagiri, T. Ogihara, H. Sakoda, Y. Onishi, H. Ono, M. Fujishiro, Y. Fukushima, N. Horike, A. Viana, M. Kikuchi, N. Noguchi, S. Takahashi, K. Takata, Y. Oka, Y. Uchijima, H. Kurihara, and T. Asano. A novel protein kinase B (PKB)/AKT-binding protein enhances PKB kinase activity and regulates DNA synthesis. *The Journal of Biological Chemistry*, 280(18):18525–18535, 2005.

[54] A. Enomoto, H. Murakami, N. Asai, N. Morone, T. Watanabe, K. Kawai, Y. Murakumo, J. Usukura, K. Kaibuchi, and M. Takahashi. Akt/PKB regulates actin organization and cell motility via Girdin/APE. *Developmental Cell*, 9(3):389–402, 2005.

246

[55] H. Le-Niculescu, I. Niesman, T. Fischer, L. DeVries, and M. G. Farquhar. Identification and characterization of GIV, a novel Galpha i/s-interacting protein found on COPI, endoplasmic reticulum-Golgi transport vesicles. *The Journal of Biological Chemistry*, 280(23):22012–22020, 2005.

[56] F. Simpson, S. Martin, T. M. Evans, M. Kerr, D. E. James, R. G. Parton, R. D. Teasdale, and C. Wicking. A Novel Hook-Related Protein Family and the Characterization of Hook-Related Protein 1. *Traffic*, 6(6):442–458, 2005.

[57] M. Garcia-Marcos, P. S. Kietrsunthorn, H. Wang, P. Ghosh, and M. G. Farquhar. G Protein Binding Sites on Calnuc (Nucleobindin 1) and NUCB2 (Nucleobindin 2) Define a New Class of Gαi-regulatory Motifs. *The Journal of Biological Chemistry*, 286(32):28138–28149, 2011.

[58] N. Aznar, K. K. Midde, Y. Dunkel, I. Lopez-Sanchez, Y. Pavlova, A. Marivin, J. Barbazán, F. Murray, U. Nitsche, K.-P. Janssen, K. Willert, A. Goel, M. Abal, M. Garcia-Marcos, and P. Ghosh. Daple is a novel non-receptor GEF required for trimeric G protein activation in Wnt signaling. *eLife*, 4:e07091, 2015.

[59] K. K. Midde, N. Aznar, N. Kalogriopoulos, and P. Ghosh. Heterotrimeric G Proteins: Breaking the rules of engagement, space and time. *BioEssays : news and reviews in molecular, cellular and developmental biology*, 38(4):379–393, 2016.

[60] N. A. Kalogriopoulos, S. D. Rees, T. Ngo, N. J. Kopcho, A. V. Ilatovskiy, N. Sun, E. A. Komives, G. Chang, P. Ghosh, and I. Kufareva. Structural basis for GPCR-independent activation of heterotrimeric Gi proteins. *Proceedings of the National Academy of Sciences*, 116(33):16394–16403, 2019.

[61] E. W. Sutherland and T. W. Rall. Fractionation and Characterization of a Cyclic Adenine Ribonucleotide Formed by Tissue Particles. *Journal of Biological Chemistry*, 232(2):1077–1092, 1958.

[62] T. Yoshimasa, D. R. Sibley, M. Bouvier, R. J. Lefkowitz, and M. G. Caron. Cross-talk between cellular signalling pathways suggested by phorbol-ester-induced adenylate cyclase phosphorylation. 327(6117):67–70.

[63] J. I. E. Bruce, S. V. Straub, and D. I. Yule. Crosstalk between cAMP and Ca2+ signaling in non-excitable cells. 34(6):431–444.

[64] T. A. Goraya and D. M. F. Cooper. Ca2+-calmodulin-dependent phosphodiesterase (PDE1): Current perspectives. 17(7):789–797.

[65] N. Aznar, N. Kalogriopoulos, K. K. Midde, and P. Ghosh. Heterotrimeric G protein signaling via GIV/Girdin: Breaking the rules of engagement, space, and time. *BioEssays: News and Reviews in Molecular, Cellular and Developmental Biology*, 38(4):379–393, 2016.

[66] P. Ghosh. The untapped potential of tyrosine-based G protein signaling. 105:99–107.

[67] P. Ghosh. Heterotrimeric G proteins as emerging targets for network based therapy in cancer: End of a long futile campaign striking heads of a Hydra. *Aging*, 7(7):469–474, 2015.

[68] F. J. Lowery and D. Yu. Growth factor signaling in metastasis: Current understanding and future opportunities. *Cancer Metastasis Reviews*, 31(3-4):479–491, 2012.

[69] C. Marty and R. D. Ye. Heterotrimeric G Protein Signaling Outside the Realm of Seven Transmembrane Domain Receptors. 78(1):12–18.

[70] G. S. Ma, N. Aznar, N. Kalogriopoulos, K. K. Midde, I. Lopez-Sanchez, E. Sato, Y. Dunkel, R. L. Gallo, and P. Ghosh. Therapeutic effects of cell-permeant peptides that activate G proteins downstream of growth factors. *Proceedings of the National Academy of Sciences of the United States of America*, 112(20):E2602–E2610, 2015.

[71] B. Schoeberl, C. Eichler-Jonsson, E. D. Gilles, and G. Müller. Computational modeling of the dynamics of the MAP kinase cascade activated by surface and internalized EGF receptors. *Nature Biotechnology*, 20(4):370–375, 2002.

[72] J. A. Berkers, P. M. v. B. en Henegouwen, and J. Boonstra. Three classes of epidermal growth factor receptors on HeLa cells. *Journal of Biological Chemistry*, 266(2):922–927, 1991.

[73] A. R. French, D. K. Tadaki, S. K. Niyogi, and D. A. Lauffenburger. Intracellular Trafficking of Epidermal Growth Factor Family Ligands Is Directly Influenced by the pH Sensitivity of the Receptor/Ligand Interaction. *Journal of Biological Chemistry*, 270(9):4334–4340, 1995.

[74] D. Bhandari, I. Lopez-Sanchez, A. To, I.-C. Lo, N. Aznar, A. Leyme, V. Gupta, I. Niesman, A. L. Maddox, M. Garcia-Marcos, M. G. Farquhar, and P. Ghosh. Cyclin-dependent kinase 5 activates guanine nucleotide exchange factor GIV/Girdin to orchestrate migration–proliferation dichotomy. *Proceedings of the National Academy of Sciences of the United States of America*, 112(35):E4874–E4883, 2015.

[75] J.-P. Vilardaga, F. G. Jean-Alphonse, and T. J. Gardella. Endosomal generation of cAMP in GPCR signaling. *Nature Chemical Biology*, 10(9):700–706, 2014.

[76] M. Garcia-Marcos, P. Ghosh, and M. G. Farquhar. GIV is a nonreceptor GEF for G alpha i with a unique motif that regulates Akt signaling. *Proceedings of the National Academy of Sciences of the United States of America*, 106(9):3178–3183, 2009.

[77] O. Atay and J. M. Skotheim. Spatial and temporal signal processing and decision making by MAPK pathways. *The Journal of Cell Biology*, 216(2):317–330, 2017.

[78] F. Edfors, F. Danielsson, B. M. Hallström, L. Käll, E. Lundberg, F. Pontén, B. Forsström, and M. Uhlén. Gene-specific correlation of RNA and protein levels in human cells and tissues. 12(10):883.

[79] I. Kosti, N. Jain, D. Aran, A. J. Butte, and M. Sirota. Cross-tissue Analysis of Gene and Protein Expression in Normal and Cancer Tissues. 6:24799.

[80] P. Dalerba, T. Kalisky, D. Sahoo, P. S. Rajendran, M. E. Rothenberg, A. A. Leyrat, S. Sim, J. Okamoto, D. M. Johnston, D. Qian, M. Zabala, J. Bueno, N. F. Neff, J. Wang, A. A. Shelton, B. Visser, S. Hisamori, Y. Shimono, M. van de Wetering, H. Clevers, M. F. Clarke, and S. R. Quake. Single-cell dissection of transcriptional heterogeneity in human colon tumors. 29(12):1120–1127.

[81] J. D. Violin, L. M. DiPilato, N. Yildirim, T. C. Elston, J. Zhang, and R. J. Lefkowitz. Beta2-adrenergic receptor signaling and desensitization elucidated by quantitative modeling of real time cAMP dynamics. 283(5):2949–2961.

[82] R. Irannejad, J. C. Tomshine, J. R. Tomshine, M. Chevalier, J. P. Mahoney, J. Steyaert, S. G. F. Rasmussen, R. K. Sunahara, H. El-Samad, B. Huang, and M. von Zastrow. Conformational biosensors reveal GPCR signalling from endosomes. *Nature*, 495(7442):534–538, 2013.

[83] I. Amit, R. Wides, and Y. Yarden. Evolvable signaling networks of receptor tyrosine kinases: Relevance of robustness to malignancy and to cancer therapy. *Molecular Systems Biology*, 3, 2007.

[84] I. Amit, A. Citri, T. Shay, Y. Lu, M. Katz, F. Zhang, G. Tarcic, D. Siwak, J. Lahad, J. Jacob-Hirsch, N. Amariglio, N. Vaisman, E. Segal, G. Rechavi, U. Alon, G. B. Mills, E. Domany, and Y. Yarden. A module of negative feedback regulators defines growth factor signaling. *Nature Genetics*, 39(4):503–512, 2007.

[85] J. C. Doyle and M. Csete. Architecture, constraints, and behavior. *Proceedings of the National Academy of Sciences*, 108(Supplement 3):15624–15630, 2011.

[86] H. Kitano. Cancer as a robust system: Implications for anticancer therapy. *Nature Reviews. Cancer*, 4(3):227–235, 2004.

[87] S. Iadevaia, L. K. Nakhleh, R. Azencott, and P. T. Ram. Mapping network motif tunability and robustness in the design of synthetic signaling circuits. *PloS One*, 9(3):e91743, 2014.

[88] Z. Liang, J. Zhang, X. Zeng, J. Gao, S. Wu, and T. Liu. Relationship between EGFR expression, copy number and mutation in lung adenocarcinomas. 10:376.

[89] R. I. Nicholson, J. M. Gee, and M. E. Harper. EGFR and cancer prognosis. 37 Suppl 4:S9–15.

[90] H. S. Park, M. H. Jang, E. J. Kim, H. J. Kim, H. J. Lee, Y. J. Kim, J. H. Kim, E. Kang, S.-W. Kim, I. A. Kim, and S. Y. Park. High EGFR gene copy number predicts poor outcome in triple-negative breast cancer. 27(9):1212–1222.

[91] G. Selvaggi, S. Novello, V. Torri, E. Leonardo, P. De Giuli, P. Borasio, C. Mossetti, F. Ardissone, P. Lausi, and G. V. Scagliotti. Epidermal growth factor receptor overexpression correlates with a poor prognosis in completely resected non-small-cell lung cancer. 15(1):28–32.

[92] J. S. Park, H. S. Kim, Y. S. Bae, J.-H. Cheong, S. Y. Rha, S. H. Noh, and H. Kim. Prognostic significance and frequency of EGFR expression and amplification in surgically resected advanced gastric cancer. 46(6):507–516.

[93] Z. Jiang, C. Li, F. Li, and X. Wang. EGFR gene copy number as a prognostic marker in colorectal cancer patients treated with cetuximab or panitumumab: A systematic review and meta analysis. 8(2):e56205.

[94] P. Llovet, J. Sastre, J. S. Ortega, I. Bando, M. Ferrer, P. García-Alfonso, O. Donnay, A. Carrato, A. Jiménez, E. Aranda, A. León, C. Grávalos, J. C. Cámara, J. Feliú, B. Sanchíz, T. Caldés, and E. Díaz-Rubio. Prognostic Value of BRAF, PI3K, PTEN, EGFR Copy Number, Amphiregulin and Epiregulin Status in Patients with KRAS Codon 12 Wild-Type Metastatic Colorectal Cancer Receiving First-Line Chemotherapy with Anti-EGFR Therapy. 19(6):397–408.

[95] D. G. McEwan, V. G. Brunton, G. S. Baillie, N. R. Leslie, M. D. Houslay, and M. C. Frame. Chemoresistant KM12C colon cancer cells are addicted to low cyclic AMP levels

in a phosphodiesterase 4-regulated compartment via effects on phosphoinositide 3-kinase. *Cancer Research*, 67(11):5248–5257, 2007.

[96] M. G. Waugh. Phosphatidylinositol 4-kinases, phosphatidylinositol 4-phosphate and cancer. *Cancer Letters*, 325(2):125–131, 2012.

[97] R. Savai, S. S. Pullamsetti, G.-A. Banat, N. Weissmann, H. A. Ghofrani, F. Grimminger, and R. T. Schermuly. Targeting cancer with phosphodiesterase inhibitors. *Expert Opinion on Investigational Drugs*, 19(1):117–131, 2010.

[98] P. Rangamani, A. Lipshtat, E. U. Azeloglu, R. C. Calizo, M. Hu, S. Ghassemi, J. Hone, S. Scarlata, S. R. Neves, and R. Iyengar. Decoding information in cell shape. *Cell*, 154(6):1356–1369, 2013.

[99] P. Rangamani and R. Iyengar. Modelling spatio-temporal interactions within the cell. *Journal of Biosciences*, 32(1):157–167, 2007.

[100] R. N. Gutenkunst, J. J. Waterfall, F. P. Casey, K. S. Brown, C. R. Myers, and J. P. Sethna. Universally Sloppy Parameter Sensitivities in Systems Biology Models. *PLOS Computational Biology*, 3(10):e189, 2007.

[101] T. Friedlander, A. E. Mayo, T. Tlusty, and U. Alon. Evolution of Bow-Tie Architectures in Biology. *PLoS Computational Biology*, 11(3), 2015.

[102] I. López-Sánchez, M. Garcia-Marcos, Y. Mittal, N. Aznar, M. G. Farquhar, and P. Ghosh. Protein kinase C-theta (PKCθ) phosphorylates and inhibits the guanine exchange factor, GIV/Girdin. *Proceedings of the National Academy of Sciences of the United States of America*, 110(14):5510–5515, 2013.

[103] U. S. Bhalla and R. Iyengar. Emergent Properties of Networks of Biological Signaling Pathways. *Science*, 283(5400):381–387, 1999.

[104] P. Rangamani and R. Iyengar. Modelling cellular signalling systems. *Essays in Biochemistry*, 45:83–94, 2008.

[105] B. M. Slepchenko, J. C. Schaff, I. Macara, and L. M. Loew. Quantitative cell biology with the Virtual Cell. 13(11):570–576.

[106] L. M. Loew and J. C. Schaff. The Virtual Cell: A software environment for computational cell biology. *Trends in Biotechnology*, 19(10):401–406, 2001.

[107] C. V. Falkenberg, M. L. Blinov, and L. M. Loew. Pleomorphic ensembles: Formation of large clusters composed of weakly interacting multivalent molecules. 105(11):2451–2460.

[108] P. J. Michalski and L. M. Loew. CaMKII activation and dynamics are independent of the holoenzyme structure: An infinite subunit holoenzyme approximation. 9(3):036010.

[109] P. Mendes, S. Hoops, S. Sahle, R. Gauges, J. Dada, and U. Kummer. Computational modeling of biochemical networks using COPASI. 500:17–59.

[110] A. Varma, M. Morbidelli, and H. Wu. *Parametric Sensitivity in Chemical Systems*. Cambridge University Press.

[111] B. P. Ingalls and H. M. Sauro. Sensitivity analysis of stoichiometric networks: An extension of metabolic control analysis to non-steady state trajectories. 222(1):23–36.

[112] I. Lopez-Sanchez, Y. Dunkel, Y.-S. Roh, Y. Mittal, S. De Minicis, A. Muranyi, S. Singh, K. Shanmugam, N. Aroonsakool, F. Murray, S. B. Ho, E. Seki, D. A. Brenner, and P. Ghosh. GIV/Girdin is a central hub for profibrogenic signalling networks during liver fibrosis. *Nature Communications*, 5:4451, 2014.

[113] R. N. Jorissen, P. Gibbs, M. Christie, S. Prakash, L. Lipton, J. Desai, D. Kerr, L. A. Aaltonen, D. Arango, M. Kruhøffer, T. F. Orntoft, C. L. Andersen, M. Gruidl, V. P. Kamath, S. Eschrich, T. J. Yeatman, and O. M. Sieber. Metastasis-Associated Gene Expression Changes Predict Poor Outcomes in Patients with Dukes Stage B and C Colorectal Cancer. 15(24):7642–7651.

[114] S. Laibe, A. Lagarde, A. Ferrari, G. Monges, D. Birnbaum, and a. t. C. P. Olschwang, Sylviane. A Seven-Gene Signature Aggregates a Subgroup of Stage II Colon Cancers with Stage III. 16(10):560–565.

[115] J. J. Smith, N. G. Deane, F. Wu, N. B. Merchant, B. Zhang, A. Jiang, P. Lu, J. C. Johnson, C. Schmidt, C. E. Bailey, S. Eschrich, C. Kis, S. Levy, M. K. Washington, M. J. Heslin, R. J. Coffey, T. J. Yeatman, Y. Shyr, and R. D. Beauchamp. Experimentally derived metastasis gene expression profile predicts recurrence and death in patients with colon cancer. 138(3):958–968.

[116] M. Thorsteinsson, L. T. Kirkeby, R. Hansen, L. R. Lund, L. T. Sørensen, T. A. Gerds, P. Jess, and J. Olsen. Gene expression profiles in stages II and III colon cancers: Application of a 128-gene signature. 27(12):1579–1586.

[117] D. Sahoo, D. L. Dill, A. J. Gentles, R. Tibshirani, and S. K. Plevritis. Boolean implication networks derived from large scale, whole genome microarray datasets. 9(10):R157.

252

[118] M. Getz, L. Swanson, D. Sahoo, P. Ghosh, and P. Rangamani. A predictive computational model reveals that GIV/Girdin serves as a tunable valve for EGFR-stimulated Cyclic AMP Signals. *Molecular Biology of the Cell*, pages mbc.E18–10–0630, 2019.

[119] I. Amit, R. Wides, and Y. Yarden. Evolvable signaling networks of receptor tyrosine kinases: Relevance of robustness to malignancy and to cancer therapy. *Molecular Systems Biology*, 3:151, 2007.

[120] R. Hepp, L. Tricoire, E. Hu, N. Gervasi, D. Paupardin-Tritsch, B. Lambolez, and P. Vincent. Phosphodiesterase type 2 and the homeostasis of cyclic GMP in living thalamic neurons. *Journal of Neurochemistry*, 102(6):1875–1886, 2007.

[121] L. R. V. Castro, N. Gervasi, E. Guiot, L. Cavellini, V. O. Nikolaev, D. Paupardin-Tritsch, and P. Vincent. Type 4 Phosphodiesterase Plays Different Integrating Roles in Different Cellular Domains in Pyramidal Cortical Neurons. *The Journal of Neuroscience*, 30(17):6143–6151, 2010.

[122] M. D. Houslay and G. Milligan. Tailoring cAMP-signalling responses through isoform multiplicity. *Trends in Biochemical Sciences*, 22(6):217–224, 1997.

[123] M. Kirschner and J. Gerhart. Evolvability. *Proceedings of the National Academy of Sciences*, 95(15):8420–8427, 1998.

[124] K. Oda, Y. Matsuoka, A. Funahashi, and H. Kitano. A comprehensive pathway map of epidermal growth factor receptor signaling. *Molecular Systems Biology*, 1:2005.0010, 2005.

[125] B. D. Coleman, A. Marivin, K. Parag-Sharma, V. DiGiacomo, S. Kim, J. S. Pepper, J. Casler, L. T. Nguyen, M. R. Koelle, and M. Garcia-Marcos. Evolutionary Conservation of a GPCR-Independent Mechanism of Trimeric G Protein Activation. *Molecular Biology and Evolution*, 33(3):820–837, 2016.

[126] R. Thomas and Z. Weihua. Rethink of EGFR in Cancer With Its Kinase Independent Function on Board. *Frontiers in Oncology*, 9, 2019.

[127] V. Follin-Arbelet, P. O. Hofgaard, H. Hauglin, S. Naderi, A. Sundan, R. Blomhoff, B. Bogen, and H. K. Blomhoff. Cyclic AMP induces apoptosis in multiple myeloma cells and inhibits tumor development in a mouse myeloma model. *BMC Cancer*, 11(1):301, 2011.

[128] A. J. Gooding and W. P. Schiemann. Harnessing protein kinase A activation to induce mesenchymal-epithelial programs to eliminate chemoresistant, tumor-initiating breast cancer cells. *Translational cancer research*, 5(Suppl 2):S226–S232, 2016.

[129] K. Murata, T. Sudo, M. Kameyama, H. Fukuoka, M. Mukai, Y. Doki, Y. Sasaki, O. Ishikawa, Y. Kimura, and S. Imaoka. Cyclic AMP specific phosphodiesterase activity and colon cancer cell motility. *Clinical & Experimental Metastasis*, 18(7):599–604, 2000.

[130] Y. Ou, X. Zheng, Y. Gao, M. Shu, T. Leng, Y. Li, W. Yin, W. Zhu, Y. Huang, Y. Zhou, J. Tang, P. Qiu, G. Yan, J. Hu, H. Ruan, and H. Hu. Activation of cyclic AMP/PKA pathway inhibits bladder cancer cell invasion by targeting MAP4-dependent microtubule dynamics. *Urologic Oncology*, 32(1):47.e21–28, 2014.

[131] D. R. Perez, Y. Smagley, M. Garcia, M. B. Carter, A. Evangelisti, K. Matlawska-Wasowska, S. S. Winter, L. A. Sklar, and A. Chigaev. Cyclic AMP efflux inhibitors as potential therapeutic agents for leukemia. *Oncotarget*, 7(23):33960–33982, 2016.

[132] N. P. Zimmerman, I. Roy, A. D. Hauser, J. M. Wilson, C. L. Williams, and M. B. Dwinell. Cyclic AMP regulates the migration and invasion potential of human pancreatic cancer cells. *Molecular Carcinogenesis*, 54(3):203–215, 2015.

[133] K. Midde, N. Sun, C. Rohena, L. Joosen, H. Dhillon, and P. Ghosh. Single-Cell Imaging of Metastatic Potential of Cancer Cells. *iScience*, 10:53–65, 2018.

[134] L. Yu, Y. Sun, J. Li, Y. Wang, Y. Zhu, Y. Shi, X. Fan, J. Zhou, Y. Bao, J. Xiao, K. Cao, and P. Cao. Silencing the Girdin gene enhances radio-sensitivity of hepatocellular carcinoma via suppression of glycolytic metabolism. *Journal of Experimental & Clinical Cancer Research*, 36(1):110, 2017.

[135] Y.-J. Zhang, A.-J. Li, Y. Han, L. Yin, and M.-B. Lin. Inhibition of Girdin enhances chemosensitivity of colorectal cancer cells to oxaliplatin. *World Journal of Gastroenterology*, 20(25):8229–8236, 2014.

[136] W. Wang, Y. Li, J. Y. Zhu, D. Fang, H.-F. Ding, Z. Dong, Q. Jing, S.-B. Su, and S. Huang. Triple negative breast cancer development can be selectively suppressed by sustaining an elevated level of cellular cyclic AMP through simultaneously blocking its efflux and decomposition. *Oncotarget*, 7(52):87232–87245, 2016.

[137] H. Wang, T. Misaki, V. Taupin, A. Eguchi, P. Ghosh, and M. G. Farquhar. GIV/girdin links vascular endothelial growth factor signaling to Akt survival signaling in podocytes independent of nephrin. *Journal of the American Society of Nephrology: JASN*, 26(2):314–327, 2015.

[138] T. Nagamatsu, H. Imai, M. Yokoi, T. Nishiyama, Y. Hirasawa, T. Nagao, and Y. Suzuki. Protective Effect of Prostaglandin EP4-Receptor Agonist on Anti-glomerular Basement Mem-

brane Antibody-Associated Nephritis. *Journal of Pharmacological Sciences*, 102(2):182–188, 2006.

[139] T. Nagamatsu, T. Nishiyama, I. Goto, T. Nagao, and Y. Suzuki. Adenosine 3', 5' cyclic monophosphate attenuates the production of fibronectin in the glomeruli of anti-glomerular basement membrane antibody-associated nephritic rats. *British Journal of Pharmacology*, 140(7):1245–1251, 2003.

[140] E. Shimizu, Y. Kobayashi, Y. Oki, T. Kawasaki, T. Yoshimi, and H. Nakamura. OPC-13013, a cyclic nucleotide phosphodiesterase type III, inhibitor, inhibits cell proliferation and transdifferentiation of cultured rat hepatic stellate cells. *Life Sciences*, 64(23):2081–2088, 1999.

[141] K. Houglum, K. S. Lee, and M. Chojkier. Proliferation of hepatic stellate cells is inhibited by phosphorylation of CREB on serine 133. *The Journal of Clinical Investigation*, 99(6):1322–1328, 1997.

[142] N. Kawada, T. Kuroki, K. Kobayashi, M. Inoue, and K. Kaneda. Inhibition of myofibroblastic transformation of cultured rat hepatic stellate cells by methylxanthines and dibutyryl cAMP. *Digestive Diseases and Sciences*, 41(5):1022–1029, 1996.

[143] A. Hartung, A.-M. Ordelheide, H. Staiger, M. Melzer, H.-U. Häring, and R. Lammers. The Akt substrate Girdin is a regulator of insulin signaling in myoblast cells. *Biochimica et Biophysica Acta (BBA) - Molecular Cell Research*, 1833(12):2803–2811, 2013.

[144] S.-P. Chai and J. C. Fong. Synergistic induction of insulin resistance by endothelin-1 and cAMP in 3T3-L1 adipocytes. *Biochimica et Biophysica Acta (BBA) - Molecular Basis of Disease*, 1852(10, Part A):2048–2055, 2015.

[145] D. M. Erion, I. D. Ignatova, S. Yonemitsu, Y. Nagai, P. Chatterjee, D. Weismann, J. J. Hsiao, D. Zhang, T. Iwasaki, R. Stark, C. Flannery, M. Kahn, C. M. Carmean, X. X. Yu, S. F. Murray, S. Bhanot, B. P. Monia, G. W. Cline, V. T. Samuel, and G. I. Shulman. Prevention of Hepatic Steatosis and Hepatic Insulin Resistance by Knockdown of cAMP Response Element-Binding Protein. *Cell Metabolism*, 10(6):499–506, 2009.

[146] Y. Kida, B. L. Nyomba, C. Bogardus, and D. M. Mott. Defective insulin response of cyclic adenosine monophosphate-dependent protein kinase in insulin-resistant humans. *The Journal of Clinical Investigation*, 87(2):673–679, 1991.

[147] D. Kirsch, W. Kemmler, and H. U. Häring. Cyclic AMP modulates insulin binding and induces post-receptor insulin resistance of glucose transport in isolated rat adipocytes. *Biochemical and Biophysical Research Communications*, 115(1):398–405, 1983.

[148] D. M. Kirsch, W. Bachmann, and H. U. Häring. Ciglitazone reverses cAMP-induced post-insulin receptor resistance in rat adipocytes in vitro. *FEBS Letters*, 176(1):49–54, 1984.

[149] J. F. Tanti, T. Grémeaux, N. Rochet, E. V. Obberghen, and Y. L. Marchand-Brustel. Effect of cyclic AMP-dependent protein kinase on insulin receptor tyrosine kinase activity. *Biochemical Journal*, 245(1):19–26, 1987.

[150] C. E. Ramirez, H. Nian, C. Yu, J. L. Gamboa, J. M. Luther, N. J. Brown, and C. A. Shibao. Treatment with Sildenafil Improves Insulin Sensitivity in Prediabetes: A Randomized, Controlled Trial. *The Journal of Clinical Endocrinology and Metabolism*, 100(12):4533–4540, 2015.

[151] H. Makino, A. Kanatsuka, T. Suzuki, S. Kuribayashi, N. Hashimoto, S. Yoshida, and M. Nishimura. Insulin Resistance of Fat Cells from Spontaneously Diabetic KK Mice: Analysis of Insulin-sensitive Phosphodiesterase. *Diabetes*, 34(9):844–849, 1985.

[152] T. Kitamura, Y. Kitamura, S. Kuroda, Y. Hino, M. Ando, K. Kotani, H. Konishi, H. Matsuzaki, U. Kikkawa, W. Ogawa, and M. Kasuga. Insulin-Induced Phosphorylation and Activation of Cyclic Nucleotide Phosphodiesterase 3B by the Serine-Threonine Kinase Akt. *Molecular and Cellular Biology*, 19(9):6286–6296, 1999.

[153] Y. Tang, H. Osawa, H. Onuma, T. Nishimiya, M. Ochi, and H. Makino. Improvement in insulin resistance and the restoration of reduced phosphodiesterase 3B gene expression by pioglitazone in adipose tissue of obese diabetic KKAy mice. *Diabetes*, 48(9):1830–1835, 1999.

[154] L. Liu, P. Jiang, D. Cui, J. Du, L. He, J. Yao, and D. Liu. [Expression of Girdin in brain tissues of Alzheimer's disease]. *Zhonghua Bing Li Xue Za Zhi = Chinese Journal of Pathology*, 44(5):301–304, 2015.

[155] M. Martínez, E. Fernández, A. Frank, C. Guaza, M. de la Fuente, and A. Hernanz. Increased cerebrospinal fluid cAMP levels in Alzheimer's disease. *Brain Research*, 846(2):265–267, 1999.

[156] E. van Daalen, C. Kemner, N. E. Verbeek, B. van der Zwaag, T. Dijkhuizen, P. Rump, R. Houben, R. van 't Slot, M. V. de Jonge, W. G. Staal, F. A. Beemer, J. A. S. Vorstman, J. P. H. Burbach, H. K. P. van Amstel, R. Hochstenbach, E. H. Brilstra, and M. Poot. Social responsiveness scale-aided analysis of the clinical impact of copy number variations in autism. *Neurogenetics*, 12(4):315–323, 2011.

[157] S. Hayano, M. Takefuji, K. Maeda, T. Noda, H. Ichimiya, K. Kobayashi, A. Enomoto,

N. Asai, M. Takahashi, and T. Murohara. Akt-dependent Girdin phosphorylation regulates repair processes after acute myocardial infarction. *Journal of Molecular and Cellular Cardiology*, 88:55–63, 2015.

[158] T. Ito, K. Komeima, T. Yasuma, A. Enomoto, N. Asai, M. Asai, S. Iwase, M. Takahashi, and H. Terasaki. Girdin and its phosphorylation dynamically regulate neonatal vascular development and pathological neovascularization in the retina. *The American Journal of Pathology*, 182(2):586–596, 2013.

[159] H. Miyachi, M. Takahashi, and K. Komori. A Novel Approach against Vascular Intimal Hyperplasia Through the Suppression of Girdin. *Annals of Vascular Diseases*, 8(2):69–73, 2015.

[160] Leineweber Kirsten, Böhm Michael, and Heusch Gerd. Cyclic Adenosine Monophosphate in Acute Myocardial Infarction With Heart Failure. *Circulation*, 114(5):365–367, 2006.

[161] M. G. Gold, F. Stengel, P. J. Nygren, C. R. Weisbrod, J. E. Bruce, C. V. Robinson, D. Barford, and J. D. Scott. Architecture and dynamics of an A-kinase anchoring protein 79 (AKAP79) signaling complex. *Proceedings of the National Academy of Sciences*, 108(16):6426–6431, 2011.

[162] S. A. Hinke, M. F. Navedo, A. Ulman, J. L. Whiting, P. J. Nygren, G. Tian, A. J. Jimenez-Caliani, L. K. Langeberg, V. Cirulli, A. Tengholm, M. L. Dell'Acqua, L. F. Santana, and J. D. Scott. Anchored phosphatases modulate glucose homeostasis. 31(20):3991–4004.

[163] D. L. Beene and J. D. Scott. A-kinase anchoring proteins take shape. 19(2):192–198.

[164] E. C. Greenwald and J. J. Saucerman. Bigger, better, faster: Principles and models of AKAP signaling. 58(5):462–469.

[165] K. L. Everett and D. M. F. Cooper. An Improved Targeted cAMP Sensor to Study the Regulation of Adenylyl Cyclase 8 by Ca2+ Entry through Voltage-Gated Channels. 8(9):e75942.

[166] J. Akerboom, N. Carreras Calderón, L. Tian, S. Wabnig, M. Prigge, J. Tolö, A. Gordus, M. B. Orger, K. E. Severi, J. J. Macklin, R. Patel, S. R. Pulver, T. J. Wardill, E. Fischer, C. Schüler, T.-W. Chen, K. S. Sarkisyan, J. S. Marvin, C. I. Bargmann, D. S. Kim, S. Kügler, L. Lagnado, P. Hegemann, A. Gottschalk, E. R. Schreiter, and L. L. Looger. Genetically encoded calcium indicators for multi-color neural activity imaging and combination with optogenetics. 6.

[167] S. Wachten, N. Masada, L.-J. Ayling, A. Ciruela, V. O. Nikolaev, M. J. Lohse, and D. M. F.

Cooper. Distinct pools of cAMP centre on different isoforms of adenylyl cyclase in pituitary-derived GH3B6 cells. 123(1):95–106.

[168] L. R. Landa, M. Harbeck, K. Kaihara, O. Chepurny, K. Kitiphongspattana, O. Graf, V. O. Nikolaev, M. J. Lohse, G. G. Holz, and M. W. Roe. Interplay of Ca2+ and cAMP signaling in the insulin-secreting MIN6 beta-cell line. 280(35):31294–31302.

[169] H. Dou, C. Wang, X. Wu, L. Yao, X. Zhang, S. Teng, H. Xu, B. Liu, Q. Wu, Q. Zhang, M. Hu, Y. Wang, L. Wang, Y. Wu, S. Shang, X. Kang, L. Zheng, J. Zhang, M. Raoux, J. Lang, Q. Li, J. Su, X. Yu, L. Chen, and Z. Zhou. Calcium influx activates adenylyl cyclase 8 for sustained insulin secretion in rat pancreatic beta cells. 58(2):324–333.

[170] N. Defer, M. Best-Belpomme, and J. Hanoune. Tissue specificity and physiological relevance of various isoforms of adenylyl cyclase. 279(3):F400–416.

[171] P. Han, J. Werber, M. Surana, N. Fleischer, and T. Michaeli. The Calcium/Calmodulin-dependent Phosphodiesterase PDE1C Down-regulates Glucose-induced Insulin Secretion. *Journal of Biological Chemistry*, 274(32):22337–22344, 1999.

[172] D. M. Cooper, N. Mons, and J. W. Karpen. Adenylyl cyclases and the interaction between calcium and cAMP signalling. *Nature*, 374(6521):421–424, 1995.

[173] K.-L. Ang and F. A. Antoni. Reciprocal regulation of calcium dependent and calcium independent cyclic AMP hydrolysis by protein phosphorylation. *Journal of Neurochemistry*, 81(3):422–433, 2002.

[174] N. Masada, A. Ciruela, D. A. MacDougall, and D. M. F. Cooper. Distinct Mechanisms of Regulation by Ca2+/Calmodulin of Type 1 and 8 Adenylyl Cyclases Support Their Different Physiological Roles. *Journal of Biological Chemistry*, 284(7):4451–4463, 2009.

[175] N. Masada, S. Schaks, S. E. Jackson, A. Sinz, and D. M. F. Cooper. Distinct Mechanisms of Calmodulin Binding and Regulation of Adenylyl Cyclases 1 and 8. *Biochemistry*, 51(40):7917–7929, 2012.

[176] D. Willoughby, N. Masada, S. Wachten, M. Pagano, M. L. Halls, K. L. Everett, A. Ciruela, and D. M. F. Cooper. AKAP79/150 Interacts with AC8 and Regulates Ca2+-dependent cAMP Synthesis in Pancreatic and Neuronal Systems. 285(26):20328–20342.

[177] D. Willoughby and D. M. F. Cooper. Ca2+ stimulation of adenylyl cyclase generates dynamic oscillations in cyclic AMP. 119(5):828–836.

[178] B. E. Peercy, A. S. Sherman, and R. Bertram. Modeling of Glucose-Induced cAMP Oscillations in Pancreatic β Cells: cAMP Rocks when Metabolism Rolls. 109(2):439–449.

[179] L. E. Fridlyand, M. C. Harbeck, M. W. Roe, and L. H. Philipson. Regulation of cAMP dynamics by Ca2+ and G protein-coupled receptors in the pancreatic beta-cell: A computational approach. 293(6):C1924–1933.

[180] M. Raoux, P. Vacher, J. Papin, A. Picard, E. Kostrzewa, A. Devin, J. Gaitan, I. Limon, M. J. Kas, C. Magnan, and J. Lang. Multilevel control of glucose homeostasis by adenylyl cyclase 8. 58(4):749–757.

[181] M. Conti, D. Mika, and W. Richter. Cyclic AMP compartments and signaling specificity: Role of cyclic nucleotide phosphodiesterases. 143(1):29–38.

[182] G. C. H. Mo, B. Ross, F. Hertel, P. Manna, X. Yang, E. Greenwald, C. Booth, A. M. Plummer, B. Tenner, Z. Chen, Y. Wang, E. J. Kennedy, P. A. Cole, K. G. Fleming, A. Palmer, R. Jimenez, J. Xiao, P. Dedecker, and J. Zhang. Genetically encoded biosensors for visualizing live-cell biochemical activity at super-resolution. 14(4):427–434.

[183] J. Zhang and M. S. Shapiro. Mechanisms and dynamics of AKAP79/150-orchestrated multi-protein signalling complexes in brain and peripheral nerve. *The Journal of Physiology*, 594(1):31–37, 2016.

[184] S. Tajada, C. M. Moreno, S. O'Dwyer, S. Woods, D. Sato, M. F. Navedo, and L. F. Santana. Distance constraints on activation of TRPV4 channels by AKAP150-bound PKCα in arterial myocytes. 149(6):639–659.

[185] A. M. Purkey, K. M. Woolfrey, K. C. Crosby, D. G. Stich, W. S. Chick, J. Aoto, and M. L. Dell'Acqua. AKAP150 Palmitoylation Regulates Synaptic Incorporation of Ca2+-Permeable AMPA Receptors to Control LTP. 25(4):974–987.e4.

[186] T. A. Goraya, N. Masada, A. Ciruela, D. Willoughby, M. A. Clynes, and D. M. F. Cooper. Kinetic properties of Ca2+/calmodulin-dependent phosphodiesterase isoforms dictate intracellular cAMP dynamics in response to elevation of cytosolic Ca2+. 20(2):359–374.

[187] S. R. Agarwal, C. E. Clancy, and R. D. Harvey. Mechanisms Restricting Diffusion of Intracellular cAMP. *Scientific Reports*, 6:19577, 2016.

[188] C. Depry, M. D. Allen, and J. Zhang. Visualization of PKA activity in plasma membrane microdomains. 7(1):52–58.

[189] J. G. Murphy, J. L. Sanderson, J. A. Gorski, J. D. Scott, W. A. Catterall, W. A. Sather,

and M. L. Dell'Acqua. AKAP-anchored PKA maintains neuronal L-type calcium channel activity and NFAT transcriptional signaling. 7(5):1577–1588.

[190] L. E. Fridlyand and L. H. Philipson. Coupling of metabolic, second messenger pathways and insulin granule dynamics in pancreatic beta-cells: A computational analysis. *Progress in Biophysics and Molecular Biology*, 107(2):293–303, 2011.

[191] P. Gilon, M. A. Ravier, J.-C. Jonas, and J.-C. Henquin. Control Mechanisms of the Oscillations of Insulin Secretion In Vitro and In Vivo. 51:S144–S151.

[192] O. Schmitz, B. Brock, M. Hollingdal, C. B. Juhl, and N. Pørksen. High-frequency insulin pulsatility and type 2 diabetes: From physiology and pathophysiology to clinical pharmacology. 28:4S14–20.

[193] M. L. Dell'Acqua, K. E. Smith, J. A. Gorski, E. A. Horne, E. S. Gibson, and L. L. Gomez. Regulation of neuronal PKA signaling through AKAP targeting dynamics. 85(7):627–633.

[194] O. Torres-Quesada, J. E. Mayrhofer, and E. Stefan. The many faces of compartmentalized PKA signalosomes. 37:1–11.

[195] J. L. Thompson and T. J. Shuttleworth. Anchoring protein AKAP79-mediated PKA phosphorylation of STIM1 determines selective activation of the ARC channel, a store-independent Orai channel. 593(3):559–572.

[196] X. Zhang, T. Pathak, R. Yoast, S. Emrich, P. Xin, R. M. Nwokonko, M. Johnson, S. Wu, C. Delierneux, M. Gueguinou, N. Hempel, J. W. Putney, D. L. Gill, and M. Trebak. A calcium/cAMP signaling loop at the ORAI1 mouth drives channel inactivation to shape NFAT induction. 10(1):1971.

[197] D. Willoughby, M. L. Halls, K. L. Everett, A. Ciruela, P. Skroblin, E. Klussmann, and D. M. F. Cooper. A key phosphorylation site in AC8 mediates regulation of Ca2+-dependent cAMP dynamics by an AC8–AKAP79–PKA signalling complex. 125(23):5850–5859.

[198] S. Barg, X. Ma, L. Eliasson, J. Galvanovskis, S. O. Göpel, S. Obermüller, J. Platzer, E. Renström, M. Trus, D. Atlas, J. Striessnig, and P. Rorsman. Fast Exocytosis with Few Ca2+ Channels in Insulin-Secreting Mouse Pancreatic B Cells. 81(6):3308–3323.

[199] E. Renström, L. Eliasson, and P. Rorsman. Protein kinase A-dependent and -independent stimulation of exocytosis by cAMP in mouse pancreatic B-cells. 502(1):105–118.

[200] J. Gao, M. Hirata, A. Mizokami, J. Zhao, I. Takahashi, H. Takeuchi, and M. Hirata.

Differential role of SNAP-25 phosphorylation by protein kinases A and C in the regulation of SNARE complex formation and exocytosis in PC12 cells. 28(5):425–437.

[201] A. Gucek, N. R. Gandasi, M. Omar-Hmeadi, M. Bakke, S. O. Døskeland, A. Tengholm, and S. Barg. Fusion pore regulation by Epac2/cAMP controls cargo release during insulin exocytosis. page 403253.

[202] C. H. Bohrer, X. Yang, X. Weng, B. Tenner, B. Ross, R. Mcquillen, J. Zhang, E. Roberts, and J. Xiao. A Pairwise Distance Distribution Correction (DDC) algorithm for blinking-free super-resolution microscopy. page 768051.

[203] H. Berry. Monte Carlo Simulations of Enzyme Reactions in Two Dimensions: Fractal Kinetics and Spatial Segregation. *Biophysical Journal*, 83(4):1891–1901, 2002.

[204] L. E. Fridlyand and L. H. Philipson. Pancreatic Beta Cell G-Protein Coupled Receptors and Second Messenger Interactions: A Systems Biology Computational Analysis. *PLOS ONE*, 11(5):e0152869, 2016.

[205] B. W. Boras, A. Kornev, S. S. Taylor, and A. D. McCulloch. Using Markov State Models to Develop a Mechanistic Understanding of Protein Kinase A Regulatory Subunit RIα Activation in Response to cAMP Binding. *Journal of Biological Chemistry*, 289(43):30040–30051, 2014.

[206] M. Lai, D. Brun, S. J. Edelstein, and N. L. Novère. Modulation of Calmodulin Lobes by Different Targets: An Allosteric Model with Hemiconcerted Conformational Transitions. *PLOS Computational Biology*, 11(1):e1004063, 2015.

[207] L. E. Fridlyand, N. Tamarina, and L. H. Philipson. Modeling of Ca2+ flux in pancreatic beta-cells: Role of the plasma membrane and intracellular stores. *American Journal of Physiology. Endocrinology and Metabolism*, 285(1):E138–154, 2003.

[208] P.-C. Yang, B. W. Boras, M.-T. Jeng, S. S. Docken, T. J. Lewis, A. D. McCulloch, R. D. Harvey, and C. E. Clancy. A Computational Modeling and Simulation Approach to Investigate Mechanisms of Subcellular cAMP Compartmentation. *PLOS Computational Biology*, 12(7):e1005005, 2016.

[209] S. Gao, H.-y. Wang, and C. C. Malbon. AKAP12 and AKAP5 form higher-order hetero-oligomers. *Journal of Molecular Signaling*, 6(1):8, 2011.

[210] M. Zhang, T. Patriarchi, I. S. Stein, H. Qian, L. Matt, M. Nguyen, Y. K. Xiang, and J. W. Hell. Adenylyl Cyclase Anchoring by a Kinase Anchor Protein AKAP5 (AKAP79/150)

Is Important for Postsynaptic β-Adrenergic Signaling. *Journal of Biological Chemistry*, 288(24):17918–17931, 2013.

[211] C. A. Haselwandter, M. Kardar, A. Triller, and R. A. da Silveira. Self-assembly and plasticity of synaptic domains through a reaction-diffusion mechanism. *Physical Review E*, 92(3):032705, 2015.

[212] F. D. Smith, J. L. Esseltine, P. J. Nygren, D. Veesler, D. P. Byrne, M. Vonderach, I. Strashnov, C. E. Eyers, P. A. Eyers, L. K. Langeberg, and J. D. Scott. Local protein kinase A action proceeds through intact holoenzymes. *Science (New York, N.Y.)*, 356(6344):1288–1293, 2017.

[213] C. A. Haselwandter, M. Calamai, M. Kardar, A. Triller, and R. Azeredo da Silveira. Formation and Stability of Synaptic Receptor Domains. *Physical Review Letters*, 106(23):238104, 2011.

[214] Q. Z. Lao, E. Kobrinsky, Z. Liu, and N. M. Soldatov. Oligomerization of $Ca_v\beta$ subunits is an essential correlate of Ca^{2+} channel activity. *FASEB journal : official publication of the Federation of American Societies for Experimental Biology*, 24(12):5013–5023, 2010.

[215] B. Iooss and P. Lemaître. A Review on Global Sensitivity Analysis Methods. In G. Dellino and C. Meloni, editors, *Uncertainty Management in Simulation-Optimization of Complex Systems: Algorithms and Applications*, Operations Research/Computer Science Interfaces Series, pages 101–122. Springer US, Boston, MA, 2015.

[216] X.-Y. Zhang, M. N. Trame, L. J. Lesko, and S. Schmidt. Sobol Sensitivity Analysis: A Tool to Guide the Development and Evaluation of Systems Pharmacology Models. *CPT: pharmacometrics & systems pharmacology*, 4(2):69–79, 2015.

[217] A. Saltelli, P. Annoni, I. Azzini, F. Campolongo, M. Ratto, and S. Tarantola. Variance based sensitivity analysis of model output. Design and estimator for the total sensitivity index. *Computer Physics Communications*, 181(2):259–270, 2010.

[218] L. Zhao, C. D. Kroenke, J. Song, D. Piwnica-Worms, J. J. H. Ackerman, and J. J. Neil. Intracellular water-specific MR of microbead-adherent cells: The HeLa cell intracellular water exchange lifetime. *NMR in biomedicine*, 21(2):159–164, 2008.

[219] R. Villasenor, H. Nonaka, P. Del Conte-Zerial, Y. Kalaidzidis, and M. Zerial. Regulation of EGFR signal transduction by analogue-to-digital conversion in endosomes. *eLife*, 4, 2015.

[220] L. Foret, J. E. Dawson, R. Villaseñor, C. Collinet, A. Deutsch, L. Brusch, M. Zerial, Y. Kalaidzidis, and F. Jülicher. A General Theoretical Framework to Infer Endosomal

Network Dynamics from Quantitative Image Analysis. *Current Biology*, 22(15):1381–1390, 2012.

[221] D. W. Peterson, D. M. Ando, D. A. Taketa, H. Zhou, F. W. Dahlquist, and J. Lew. No difference in kinetics of tau or histone phosphorylation by CDK5/p25 versus CDK5/p35 in vitro. *Proceedings of the National Academy of Sciences of the United States of America*, 107(7):2884–2889, 2010.

[222] K.-H. Sun, Y. de Pablo, F. Vincent, E. O. Johnson, A. K. Chavers, and K. Shah. Novel Genetic Tools Reveal Cdk5's Major Role in Golgi Fragmentation in Alzheimer's Disease. *Molecular Biology of the Cell*, 19(7):3052–3069, 2008.

[223] R. Dhavan and L.-H. Tsai. A decade of CDK5. *Nature Reviews Molecular Cell Biology*, 2(10):749–759, 2001.

[224] G. N. Patrick, P. Zhou, Y. T. Kwon, P. M. Howley, and L.-H. Tsai. P35, the Neuronal-specific Activator of Cyclin-dependent Kinase 5 (Cdk5) Is Degraded by the Ubiquitin-Proteasome Pathway. *Journal of Biological Chemistry*, 273(37):24057–24064, 1998.

[225] S. Hoops, S. Sahle, R. Gauges, C. Lee, J. Pahle, N. Simus, M. Singhal, L. Xu, P. Mendes, and U. Kummer. COPASI—a COmplex PAthway SImulator. *Bioinformatics*, 22(24):3067–3074, 2006.

[226] S. McLaughlin, J. Wang, A. Gambhir, and D. Murray. PIP(2) and proteins: Interactions, organization, and information flow. *Annual Review of Biophysics and Biomolecular Structure*, 31:151–175, 2002.

[227] S. R. Neves, P. Tsokas, A. Sarkar, E. A. Grace, P. Rangamani, S. M. Taubenfeld, C. M. Alberini, J. C. Schaff, R. D. Blitzer, I. I. Moraru, and R. Iyengar. Cell shape and negative links in regulatory motifs together control spatial information flow in signaling networks. *Cell*, 133(4):666–680, 2008.

[228] C. B. Melsom, Ø. Ørstavik, J.-B. Osnes, T. Skomedal, F. O. Levy, and K. A. Krobert. G i Proteins Regulate Adenylyl Cyclase Activity Independent of Receptor Activation. *PLOS ONE*, 9(9):e106608, 2014.

[229] H. Imamura, K. P. H. Nhat, H. Togawa, K. Saito, R. Iino, Y. Kato-Yamada, T. Nagai, and H. Noji. Visualization of ATP levels inside single living cells with fluorescence resonance energy transfer-based genetically encoded indicators. 106(37):15651–15656.

[230] C. Kim, C. Y. Cheng, S. A. Saldanha, and S. S. Taylor. PKA-I Holoenzyme Structure Reveals a Mechanism for cAMP-Dependent Activation. *Cell*, 130(6):1032–1043, 2007.

[231] J. G. H. Bruystens, J. Wu, A. Fortezzo, A. P. Kornev, D. K. Blumenthal, and S. S. Taylor. PKA RIα Homodimer Structure Reveals an Intermolecular Interface with Implications for Cooperative cAMP Binding and Carney Complex Disease. *Structure*, 22(1):59–69, 2014.

[232] A. A. Alousi, J. R. Jasper, P. A. Insel, and H. J. Motulsky. Stoichiometry of receptor-Gs-adenylate cyclase interactions. *FASEB journal: official publication of the Federation of American Societies for Experimental Biology*, 5(9):2300–2303, 1991.

[233] S. R. Post, R. Hilal-Dandan, K. Urasawa, L. L. Brunton, and P. A. Insel. Quantification of signalling components and amplification in the beta-adrenergic-receptor-adenylate cyclase pathway in isolated adult rat ventricular myocytes. *Biochemical Journal*, 311(Pt 1):75–80, 1995.

[234] D. Cassel, F. Eckstein, M. Lowe, and Z. Selinger. Determination of the turn-off reaction for the hormone-activated adenylate cyclase. *The Journal of Biological Chemistry*, 254(19):9835–9838, 1979.

[235] M. Zorn, K. E. Fladmark, D. Øgreid, B. Jastorff, S. O. Døskeland, and W. R. G. Dostmann. Ala335 is essential for high-affinity cAMP-binding of both sites A and B of cAMP-dependent protein kinase type I. *FEBS Letters*, 362(3):291–294, 1995.

[236] F. Plattner, K. Hayashi, A. Hernández, D. R. Benavides, T. C. Tassin, C. Tan, J. Day, M. W. Fina, E. Y. Yuen, Z. Yan, M. S. Goldberg, A. C. Nairn, P. Greengard, E. J. Nestler, R. Taussig, A. Nishi, M. D. Houslay, and J. A. Bibb. The role of ventral striatal cAMP signaling in stress-induced behaviors. *Nature Neuroscience*, 18(8):1094–1100, 2015.

[237] J. S. Bian, W. M. Zhang, J. M. Pei, and T. M. Wong. The role of phosphodiesterase in mediating the effect of protein kinase C on cyclic AMP accumulation upon kappa-opioid receptor stimulation in the rat heart. *The Journal of Pharmacology and Experimental Therapeutics*, 292(3):1065–1070, 2000.

[238] S. R. Neves. Developing models in Virtual Cell. *Science signaling*, 4(192):tr12, 2011.

[239] T. Bäck and H.-P. Schwefel. An Overview of Evolutionary Algorithms for Parameter Optimization. *Evolutionary Computation*, 1(1):1–23, 1993.

[240] V. Shukla, Y.-L. Zheng, S. K. Mishra, N. D. Amin, J. Steiner, P. Grant, S. Kesavapany, and H. C. Pant. A truncated peptide from p35, a Cdk5 activator, prevents Alzheimer's disease phenotypes in model mice. 27(1):174–186.

[241] P. Wee, H. Shi, J. Jiang, Y. Wang, and Z. Wang. EGF stimulates the activation of EGF receptors and the selective activation of major signaling pathways during mitosis. 27(3):638–651.

[242] R. W. Van Dyke. Heterotrimeric G protein subunits are located on rat liver endosomes. 4(1):1.

[243] B. Zheng, Y. C. Ma, R. S. Ostrom, C. Lavoie, G. N. Gill, P. A. Insel, X. Y. Huang, and M. G. Farquhar. RGS-PX1, a GAP for GalphaS and sorting nexin in vesicular trafficking. 294(5548):1939–1942.

[244] E. R. Siuda, J. G. McCall, R. Al-Hasani, G. Shin, S. Il Park, M. J. Schmidt, S. L. Anderson, W. J. Planer, J. A. Rogers, and M. R. Bruchas. Optodynamic simulation of β-adrenergic receptor signalling. 6:8480.

[245] N. G. Tsvetanova, R. Irannejad, and M. von Zastrow. G protein-coupled receptor (GPCR) signaling via heterotrimeric G proteins from endosomes. 290(11):6689–6696.

[246] T. Sungkaworn, M.-L. Jobin, K. Burnecki, A. Weron, M. J. Lohse, and D. Calebiro. Single-molecule imaging reveals receptor-G protein interactions at cell surface hot spots. 550(7677):543–547.

[247] S. L. Bowman, D. J. Shiwarski, and M. A. Puthenveedu. Distinct G protein-coupled receptor recycling pathways allow spatial control of downstream G protein signaling. 214(7):797–806.

[248] B. G. Nair, B. Parikh, G. Milligan, and T. B. Patel. Gs alpha mediates epidermal growth factor-elicited stimulation of rat cardiac adenylate cyclase. 265(34):21317–21322.

[249] H. Sun, Z. Chen, H. Poppleton, K. Scholich, J. Mullenix, G. J. Weipz, D. L. Fulgham, P. J. Bertics, and T. B. Patel. The juxtamembrane, cytosolic region of the epidermal growth factor receptor is involved in association with alpha-subunit of Gs. 272(9):5413–5420.

[250] B. G. Nair and T. B. Patel. Regulation of cardiac adenylyl cyclase by epidermal growth factor (EGF). Role of EGF receptor protein tyrosine kinase activity. 46(7):1239–1245.

[251] Z. Liu, S. Turan, V. L. Wehbi, J.-P. Vilardaga, and M. Bastepe. Extra-long Gαs Variant XLαs Protein Escapes Activation-induced Subcellular Redistribution and Is Able to Provide Sustained Signaling. *The Journal of Biological Chemistry*, 286(44):38558–38569, 2011.

[252] A. Watts. *Protein-Lipid Interactions*. Elsevier, 1993.

[253] E. M. Griner and M. G. Kazanietz. Protein kinase C and other diacylglycerol effectors in cancer. *Nat Rev Cancer*, 7(4):281–294, 2007.

[254] Y.-W. Wu, L. K. Oesterlin, K.-T. Tan, H. Waldmann, K. Alexandrov, and R. S. Goody.

Membrane targeting mechanism of Rab GTPases elucidated by semisynthetic protein probes. *Nature Chemical Biology*, 6(7):534–540, 2010.

[255] R. D. Malmstrom, A. P. Kornev, S. S. Taylor, and R. E. Amaro. Allostery through the computational microscope: cAMP activation of a canonical signalling domain. *Nature Communications*, 6:7588, 2015.

[256] F. Capuani, A. Conte, E. Argenzio, L. Marchetti, C. Priami, S. Polo, P. P. Di Fiore, S. Sigismund, and A. Ciliberto. Quantitative analysis reveals how EGFR activation and downregulation are coupled in normal but not in cancer cells. *Nature Communications*, 6:7999, 2015.

[257] J. Zhang, C. J. Hupfeld, S. S. Taylor, J. M. Olefsky, and R. Y. Tsien. Insulin disrupts β-adrenergic signalling to protein kinase A in adipocytes. *Nature*, 437(7058):569–573, 2005.

[258] B. S. Donahue and R. F. Abercrombie. Free diffusion coefficient of ionic calcium in cytoplasm. *Cell Calcium*, 8(6):437–448, 1987.

[259] B. N. Kholodenko. Cell-signalling dynamics in time and space. *Nature Reviews. Molecular Cell Biology*, 7(3):165–176, 2006.

[260] J. Meyers, J. Craig, and D. J. Odde. Potential for Control of Signaling Pathways via Cell Size and Shape. *Current Biology*, 16(17):1685–1693, 2006.

[261] S. Kondo and T. Miura. Reaction-diffusion model as a framework for understanding biological pattern formation. *Science (New York, N.Y.)*, 329(5999):1616–1620, 2010.

[262] Y. Mori, A. Jilkine, and L. Edelstein-Keshet. Wave-pinning and cell polarity from a bistable reaction-diffusion system. *Biophysical journal*, 94(9):3684–3697, 2008.

[263] J. D. Murray. *Mathematical Biology*. Springer, 2nd corr edition, 1993.

[264] J. E. Ferrell Jr., T. Y.-C. Tsai, and Q. Yang. Modeling the Cell Cycle: Why Do Certain Circuits Oscillate? *Cell*, 144(6):874–885, 2011.

[265] T. Kamide, S. Okumura, S. Ghosh, Y. Shinoda, Y. Mototani, Y. Ohnuki, H. Jin, W. Cai, K. Suita, I. Sato, M. Umemura, T. Fujita, U. Yokoyama, M. Sato, K. Furutani, H. Kitano, and Y. Ishikawa. Oscillation of cAMP and Ca(2+) in cardiac myocytes: A systems biology approach. *The journal of physiological sciences: JPS*, 65(2):195–200, 2015.

[266] S. Wiggins. *Introduction to Applied Nonlinear Dynamical Systems and Chaos*. Number 2 in Texts in Applied Mathematics. Springer, New York, 2nd edition edition, 2003.

[267] S. H. Strogatz. *Nonlinear Dynamics And Chaos: With Applications To Physics, Biology, Chemistry And Engineering*. Westview Press, Reading, Mass, first edition edition edition, 1994.

[268] S. H. Strogatz. *Nonlinear Dynamics and Chaos: With Applications to Physics, Biology, Chemistry, and Engineering*. Westview Press, Boulder, CO, 2 edition edition, 2014.

[269] J. Guckenheimer and P. Holmes. *Nonlinear Oscillations, Dynamical Systems, and Bifurcations of Vector Fields*. Springer, New York, 1st ed. 1983. corr. 6th printing 2002 edition edition, 2002.

[270] A. M. Turing. The Chemical Basis of Morphogenesis. *Philosophical Transactions of the Royal Society of London. Series B, Biological Sciences*, 237(641):37–72, 1952.

[271] H. Meinhardt and A. Gierer. Applications of a Theory of Biological Pattern Formation Based on Lateral Inhibition. *Journal of Cell Science*, 15(2):321–346, 1974.

[272] H. Shoji, A. Mochizuki, Y. Iwasa, M. Hirata, T. Watanabe, S. Hioki, and S. Kondo. Origin of directionality in the fish stripe pattern. *Developmental Dynamics*, 226(4):627–633, 2003.

[273] H. Meinhardt and M. Klingler. A model for pattern formation on the shells of molluscs. *Journal of Theoretical Biology*, 126(1):63–89, 1987.

[274] S. Newman and H. Frisch. Dynamics of skeletal pattern formation in developing chick limb. *Science*, 205(4407):662, 1979.

[275] T. Miura and K. Shiota. TGFbeta2 acts as an "activator" molecule in reaction-diffusion model and is involved in cell sorting phenomenon in mouse limb micromass culture. *Developmental Dynamics: An Official Publication of the American Association of Anatomists*, 217(3):241–249, 2000.

[276] W. Wang, D. Rigueur, and K. M. Lyons. TGFβ Signaling in Cartilage Development and Maintenance. *Birth defects research. Part C, Embryo today : reviews*, 102(1):37–51, 2014.

[277] R. Cagan. Principles of Drosophila Eye Differentiation. *Current topics in developmental biology*, 89:115–135, 2009.

[278] R. Phillips, J. Kondev, J. Theriot, and H. Garcia. *Physical Biology of the Cell*. Garland Science, London : New York, NY, 2 edition edition, 2012.

[279] M. Otsuji, S. Ishihara, C. Co, K. Kaibuchi, A. Mochizuki, and S. Kuroda. A Mass Conserved Reaction–Diffusion System Captures Properties of Cell Polarity. *PLoS Computational Biology*, 3(6), 2007.

[280] A. Varma, K. C. Huang, and K. D. Young. The Min System as a General Cell Geometry Detection Mechanism: Branch Lengths in Y-Shaped Escherichia coli Cells Affect Min Oscillation Patterns and Division Dynamics. *Journal of Bacteriology*, 190(6):2106–2117, 2008.

[281] U. S. Bhalla and R. Iyengar. Emergent properties of networks of biological signaling pathways. *Science (New York, N.Y.)*, 283(5400):381–387, 1999.

[282] S. R. Neves, P. T. Ram, and R. Iyengar. G Protein Pathways. *Science*, 296(5573):1636, 2002.

[283] N. I. Markevich, J. B. Hoek, and B. N. Kholodenko. Signaling switches and bistability arising from multisite phosphorylation in protein kinase cascades. *The Journal of Cell Biology*, 164(3):353, 2004.

[284] W. W. Chen, M. Niepel, and P. K. Sorger. Classic and contemporary approaches to modeling biochemical reactions. *Genes & Development*, 24(17):1861–1875, 2010.

[285] E. U. Azeloglu and R. Iyengar. Signaling networks: Information flow, computation, and decision making. *Cold Spring Harbor Perspectives in Biology*, 7(4):a005934, 2015.

[286] E. Bartocci and P. Lió. Computational Modeling, Formal Analysis, and Tools for Systems Biology. *PLOS Computational Biology*, 12(1):e1004591, 2016.

[287] I. I. Moraru, J. C. Schaff, B. M. Slepchenko, M. Blinov, F. Morgan, A. Lakshminarayana, F. Gao, Y. Li, and L. M. Loew. The Virtual Cell Modeling and Simulation Software Environment. *IET systems biology*, 2(5):352–362, 2008.

[288] J. R. Stiles, D. V. Helden, T. M. Bartol, E. E. Salpeter, and M. M. Salpeter. Miniature endplate current rise times less than 100 microseconds from improved dual recordings can be modeled with passive acetylcholine diffusion from a synaptic vesicle. *Proceedings of the National Academy of Sciences*, 93(12):5747–5752, 1996.

[289] J. Stiles and T. Bartol. Monte Carlo Methods for Simulating Realistic Synaptic Microphys-

iology Using MCell. In *Computational Neuroscience*, Frontiers in Neuroscience. CRC Press, 2000.

[290] R. Kerr, T. Bartol, B. Kaminsky, M. Dittrich, J. Chang, S. Baden, T. Sejnowski, and J. Stiles. Fast Monte Carlo Simulation Methods for Biological Reaction-Diffusion Systems in Solution and on Surfaces. *SIAM Journal on Scientific Computing*, 30(6):3126–3149, 2008.

[291] W. Xiong and J. E. Ferrell. A positive-feedback-based bistable 'memory module' that governs a cell fate decision. *Nature*, 426(6965):460–465, 2003.

[292] C. P. Bagowski and J. E. Ferrell Jr. Bistability in the JNK cascade. *Current Biology*, 11(15):1176–1182, 2001.

[293] A. Nakamasu, G. Takahashi, A. Kanbe, and S. Kondo. Interactions between zebrafish pigment cells responsible for the generation of Turing patterns. *Proceedings of the National Academy of Sciences*, 106(21):8429–8434, 2009.

[294] H. S. Jung, P. H. Francis-West, R. B. Widelitz, T. X. Jiang, S. Ting-Berreth, C. Tickle, L. Wolpert, and C. M. Chuong. Local inhibitory action of BMPs and their relationships with activators in feather formation: Implications for periodic patterning. *Developmental Biology*, 196(1):11–23, 1998.

[295] S. Sick, S. Reinker, J. Timmer, and T. Schlake. WNT and DKK determine hair follicle spacing through a reaction-diffusion mechanism. *Science (New York, N.Y.)*, 314(5804):1447–1450, 2006.

[296] D. Thomas and G. Gellf. Artificial Enzyme Membranes and Enzyme Reactors. In H. H. Weetall and S. Suzuki, editors, *Immobilized Enzyme Technology*, pages 85–98. Springer US, 1975.

[297] J. Seelig. Anisotropic Motion in Liquid Crystalline Structures. In *Spin Labeling*, pages 373–409. Elsevier, 1976.

[298] G. Catalano, J. C. Eilbeck, A. Monroy, and E. Parisi. A mathematical model for pattern formation in biological systems. *Physica D Nonlinear Phenomena*, 3:439–456, 1981.

[299] Y. Mori, A. Jilkine, and L. Edelstein-Keshet. Asymptotic and Bifurcation Analysis of Wave-Pinning in a Reaction-Diffusion Model for Cell Polarization. *SIAM Journal on Applied Mathematics*, 71(4):1401–1427, 2011.

[300] A. Jilkine and L. Edelstein-Keshet. A Comparison of Mathematical Models for Polarization

of Single Eukaryotic Cells in Response to Guided Cues. *PLOS Computational Biology*, 7(4):e1001121, 2011.

[301] G. R. Walther, A. F. M. Marée, L. Edelstein-Keshet, and V. A. Grieneisen. Deterministic versus stochastic cell polarisation through wave-pinning. *Bulletin of Mathematical Biology*, 74(11):2570–2599, 2012.

[302] W. R. Holmes and L. Edelstein-Keshet. Analysis of a minimal Rho-GTPase circuit regulating cell shape. *Physical Biology*, 13(4):046001, 2016.

[303] P. K. Trong, E. M. Nicola, N. W. Goehring, K. V. Kumar, and S. W. Grill. Parameter-space topology of models for cell polarity. *New Journal of Physics*, 16(6):065009, 2014.

[304] M. Postma, L. Bosgraaf, H. M. Loovers, and P. J. M. Van Haastert. Chemotaxis: Signalling modules join hands at front and tail. *EMBO reports*, 5(1):35–40, 2004.

[305] W. R. Holmes. An Efficient, Nonlinear Stability Analysis for Detecting Pattern Formation in Reaction Diffusion Systems. *Bulletin of Mathematical Biology*, 76(1):157–183, 2014.

[306] L. Edelstein-Keshet, W. R. Holmes, M. Zajac, and M. Dutot. From simple to detailed models for cell polarization. *Philosophical Transactions of the Royal Society B: Biological Sciences*, 368(1629), 2013.

[307] M. Raftopoulou and A. Hall. Cell migration: Rho GTPases lead the way. *Developmental Biology*, 265(1):23–32, 2004.

[308] B. Lin, W. R. Holmes, C. J. Wang, T. Ueno, A. Harwell, L. Edelstein-Keshet, T. Inoue, and A. Levchenko. Synthetic spatially graded Rac activation drives cell polarization and movement. *Proceedings of the National Academy of Sciences*, 109(52):E3668–E3677, 2012.

[309] W. R. Holmes, B. Lin, A. Levchenko, and L. Edelstein-Keshet. Modelling Cell Polarization Driven by Synthetic Spatially Graded Rac Activation. *PLOS Computational Biology*, 8(6):e1002366, 2012.

[310] K. Rei, C. D. Nobes, G. Thomas, A. Hall, and D. A. Cantrell. Phosphatidylinositol 3-kinase signals activate a selective subset of Rac/Rho-dependent effector pathways. *Current Biology*, 6(11):1445–1455, 1996.

[311] J. H. Jaggar, V. A. Porter, W. J. Lederer, and M. T. Nelson. Calcium sparks in smooth muscle. *American Journal of Physiology - Cell Physiology*, 278(2):C235–C256, 2000.

[312] W. A. Catterall. Voltage-Gated Calcium Channels. *Cold Spring Harbor Perspectives in Biology*, 3(8):a003947, 2011.

[313] R. W. Tsien, D. Lipscombe, D. V. Madison, K. R. Bley, and A. P. Fox. Multiple types of neuronal calcium channels and their selective modulation. *Trends in Neurosciences*, 11(10):431–438, 1988.

[314] K. Dunlap, J. I. Luebke, and T. J. Turner. Exocytotic Ca2+ channels in mammalian central neurons. *Trends in Neurosciences*, 18(2):89–98, 1995.

[315] W. A. Catterall and A. P. Few. Calcium Channel Regulation and Presynaptic Plasticity. *Neuron*, 59(6):882–901, 2008.

[316] H.-O. Peitgen and P. H. Richter. *The Beauty of Fractals: Images of Complex Dynamical Systems*. Springer, Berlin; Heidelberg u.a., softcover reprint of the original 1st ed. 1986 edition edition, 2012.

[317] T. Wilhelm and R. Heinrich. Smallest chemical reaction system with Hopf bifurcation. *Journal of Mathematical Chemistry*, 17(1):1–14, 1995.

[318] M. Dworkin and K. H. Keller. Solubility and diffusion coefficient of adenosine 3':5'-monophosphate. *Journal of Biological Chemistry*, 252(3):864–865, 1977.

[319] B. S. Donahue and R. F. Abercrombie. Free diffusion coefficient of ionic calcium in cytoplasm. *Cell Calcium*, 8(6):437–448, 1987.

[320] C. N. Angstmann, I. C. Donnelly, B. I. Henry, B. A. Jacobs, T. A. M. Langlands, and J. A. Nichols. From stochastic processes to numerical methods: A new scheme for solving reaction subdiffusion fractional partial differential equations. *Journal of Computational Physics*, 307:508–534, 2016.

[321] M. Razi, P. Attar, and P. Vedula. Numerical Solution of Multidimensional Hyperbolic PDEs Using Defect Correction on Adaptive Grids. *Journal of Scientific Computing*, 69(2):581–609, 2016.

[322] X. Yang. Linear, first and second-order, unconditionally energy stable numerical schemes for the phase field model of homopolymer blends. *Journal of Computational Physics*, 327:294–316, 2016.

[323] K. Oglecka, P. Rangamani, B. Liedberg, R. S. Kraut, and A. N. Parikh. Oscillatory phase separation in giant lipid vesicles induced by transmembrane osmotic differentials. 3:e03695.

[324] Y. Xiong, P. Rangamani, M.-A. Fardin, A. Lipshtat, B. Dubin-Thaler, O. Rossier, M. P. Sheetz, and R. Iyengar. Mechanisms controlling cell size and shape during isotropic cell spreading. *Biophysical journal*, 98(10):2136–2146, 2010.

[325] P. Rangamani, M.-A. Fardin, Y. Xiong, A. Lipshtat, O. Rossier, M. P. Sheetz, and R. Iyengar. Signaling network triggers and membrane physical properties control the actin cytoskeleton-driven isotropic phase of cell spreading. *Biophysical journal*, 100(4):845–857, 2011.

[326] P. Rangamani, M. G. Levy, S. Khan, and G. Oster. Paradoxical signaling regulates structural plasticity in dendritic spines. *Proceedings of the National Academy of Sciences*, 113(36):E5298–E5307, 2016.

[327] J. E. Darnell, H. F. Lodish, D. Baltimore, et al. *Molecular cell biology*, volume 2. Scientific American Books New York, 1990.

[328] W. Stillwell. *An introduction to biological membranes: from bilayers to rafts*. Newnes, 2013.

[329] G. Guidotti. The composition of biological membranes. *Archives of internal medicine*, 129(2):194–201, 1972.

[330] P. L. Yeagle. *The structure of biological membranes*. CRC press, 2011.

[331] P. Albersheim and A. J. Anderson-Prouty. Carbohydrates, proteins, cell surfaces, and the biochemistry of pathogenesis. *Annual Review of Plant Physiology*, 26(1):31–52, 1975.

[332] M. K. Jain, R. C. Wagner, et al. Introduction to biological membranes. 1988.

[333] K. Hashimoto and A. R. Panchenko. Mechanisms of protein oligomerization, the critical role of insertions and deletions in maintaining different oligomeric states. *Proceedings of the National Academy of Sciences*, 107(47):20352–20357, 2010.

[334] L. Johannes, W. Pezeshkian, J. H. Ipsen, and J. C. Shillcock. Clustering on Membranes: Fluctuations and More. *Trends in Cell Biology*, 28(5):405–415, 2018.

[335] I. Ispolatov. Binding properties and evolution of homodimers in protein-protein interaction networks. *Nucleic Acids Research*, 33(11):3629–3635, 2005.

[336] N. Porat-Shliom, O. Milberg, A. Masedunskas, and R. Weigert. Multiple roles for the actin cytoskeleton during regulated exocytosis. *Cellular and molecular life sciences : CMLS*, 70(12):2099–2121, 2013.

[337] J. H. Lorent, B. Diaz-Rohrer, X. Lin, K. Spring, A. A. Gorfe, K. R. Levental, and I. Levental. Structural determinants and functional consequences of protein affinity for membrane rafts. *Nature Communications*, 8(1):1219, 2017.

[338] M. A. Lemmon and J. Schlessinger. Cell signaling by receptor tyrosine kinases. *Cell*, 141(7):1117–1134, 2010.

[339] R. Sleno and T. E. Hébert. Chapter Five - The Dynamics of GPCR Oligomerization and Their Functional Consequences. In A. K. Shukla, editor, *International Review of Cell and Molecular Biology*, volume 338 of *G Protein-Coupled Receptors: Emerging Paradigms in Activation, Signaling and Regulation Part A*, pages 141–171. Academic Press, 2018.

[340] L. Baisamy, N. Jurisch, and D. Diviani. Leucine Zipper-mediated Homo-oligomerization Regulates the Rho-GEF Activity of AKAP-Lbc. *Journal of Biological Chemistry*, 280(15):15405–15412, 2005.

[341] C. P. Chen, S. Posy, A. Ben-Shaul, L. Shapiro, and B. H. Honig. Specificity of cell-cell adhesion by classical cadherins: Critical role for low-affinity dimerization through -strand swapping. *Proceedings of the National Academy of Sciences*, 102(24):8531–8536, 2005.

[342] S. Askarova, X. Yang, and J. C.-M. Lee. Impacts of Membrane Biophysics in Alzheimer's Disease: From Amyloid Precursor Protein Processing to Aβ Peptide-Induced Membrane Changes. *International Journal of Alzheimer's Disease*, 2011, 2011.

[343] B. Sarkar, A. Das, and S. Maiti. Thermodynamically stable amyloid-β monomers have much lower membrane affinity than the small oligomers. *Frontiers in Physiology*, 4:84, 2013.

[344] Y.-J. Zhang, J.-M. Shi, C.-J. Bai, H. Wang, H.-Y. Li, Y. Wu, and S.-R. Ji. Intra-membrane Oligomerization and Extra-membrane Oligomerization of Amyloid-β Peptide Are Competing Processes as a Result of Distinct Patterns of Motif Interplay. *Journal of Biological Chemistry*, 287(1):748–756, 2012.

[345] M. Andreasen, N. Lorenzen, and D. Otzen. Interactions between misfolded protein oligomers and membranes: A central topic in neurodegenerative diseases? *Biochimica et Biophysica Acta (BBA) - Biomembranes*, 1848(9):1897–1907, 2015.

[346] J. Habchi, S. Chia, C. Galvagnion, T. C. T. Michaels, M. M. J. Bellaiche, F. S. Ruggeri, M. Sanguanini, I. Idini, J. R. Kumita, E. Sparr, S. Linse, C. M. Dobson, T. P. J. Knowles, and M. Vendruscolo. Cholesterol catalyses Aβ42 aggregation through a heterogeneous nucleation pathway in the presence of lipid membranes. *Nature Chemistry*, 10(6):673–683, 2018.

[347] B. B. Holmes and M. I. Diamond. Cellular mechanisms of protein aggregate propagation. *Curr. Opin. Neurol.*, 25(6):721–726, 2012.

[348] A. Rawat, R. Langen, and J. Varkey. Membranes as modulators of amyloid protein misfolding and target of toxicity. *Biochim. Biophys. Acta Biomembr.*, 2018.

[349] D. Choquet. Fast AMPAR trafficking for a high-frequency synaptic transmission. *European Journal of Neuroscience*, 32(2):250–260, 2010.

[350] Q. Gan, C. L. Salussolia, and L. P. Wollmuth. Assembly of AMPA receptors: Mechanisms and regulation. *The Journal of Physiology*, 593(Pt 1):39–48, 2015.

[351] P. Padmanabhan, R. Martínez-Mármol, D. Xia, J. Götz, and F. A. Meunier. Frontotemporal dementia mutant Tau promotes aberrant Fyn nanoclustering in hippocampal dendritic spines. *eLife*, 8:e45040, 2019.

[352] E. Frey, J. Halatek, S. Kretschmer, and P. Schwille. Protein pattern formation. In *Physics of Biological Membranes*, pages 229–260. Springer, 2018.

[353] J. Denk, S. Kretschmer, J. Halatek, C. Hartl, P. Schwille, and E. Frey. MinE conformational switching confers robustness on self-organized Min protein patterns. *Proceedings of the National Academy of Sciences*, 115(18):4553–4558, 2018.

[354] D. Cusseddu, L. Edelstein-Keshet, J. A. Mackenzie, S. Portet, and A. Madzvamuse. A coupled bulk-surface model for cell polarisation. *Journal of theoretical biology*, 2018.

[355] W. Giese, M. Eigel, S. Westerheide, C. Engwer, and E. Klipp. Influence of cell shape, inhomogeneities and diffusion barriers in cell polarization models. *Physical biology*, 12(6):066014, 2015.

[356] R. Diegmiller, H. Montanelli, C. B. Muratov, and S. Y. Shvartsman. Spherical caps in cell polarization. *Biophysical journal*, 115(1):26–30, 2018.

[357] A. Madzvamuse, A. H. W. Chung, and C. Venkataraman. Stability analysis and simulations of coupled bulk-surface reaction-diffusion systems. *Proceedings of the Royal Society A: Mathematical, Physical and Engineering Sciences*, 471(2175):20140546–20140546, 2015.

[358] A. Rätz and M. Röger. Turing instabilities in a mathematical model for signaling networks. *Journal of mathematical biology*, 65(6-7):1215–1244, 2012.

[359] A. Rätz. Turing-type instabilities in bulk–surface reaction–diffusion systems. *Journal of Computational and Applied Mathematics*, 289:142–152, 2015.

[360] M. v. Smoluchowski. Versuch einer mathematischen Theorie der Koagulationskinetik kolloider Lösungen. *Zeitschrift für physikalische Chemie*, 92(1):129–168, 1918.

[361] R. L. Drake. A general mathematical survey of the coagulation equation. *Topics in current aerosol research (Part 2)*, 3(Part 2):201–376, 1972.

[362] P. Arosio, S. Rima, M. Lattuada, and M. Morbidelli. Population Balance Modeling of Antibodies Aggregation Kinetics. *The Journal of Physical Chemistry B*, 116(24):7066–7075, 2012.

[363] M. Zidar, D. Kuzman, and M. Ravnik. Characterisation of protein aggregation with the Smoluchowski coagulation approach for use in biopharmaceuticals. *Soft Matter*, 14(29):6001–6012, 2018.

[364] Y. Achdou, B. Franchi, N. Marcello, and M. C. Tesi. A qualitative model for aggregation and diffusion of β-amyloid in Alzheimer's disease. *Journal of mathematical biology*, 67(6-7):1369–1392, 2013.

[365] B. Franchi and S. Lorenzani. From a microscopic to a macroscopic model for Alzheimer disease: two-scale homogenization of the smoluchowski equation in perforated domains. *Journal of Nonlinear Science*, 26(3):717–753, 2016.

[366] M. Bertsch, B. Franchi, N. Marcello, M. C. Tesi, and A. Tosin. Alzheimer's disease: a mathematical model for onset and progression. *Mathematical medicine and biology: a journal of the IMA*, 34(2):193–214, 2016.

[367] J. Bentz and S. Nir. Mass action kinetics and equilibria of reversible aggregation. *Journal of the Chemical Society, Faraday Transactions 1: Physical Chemistry in Condensed Phases*, 77(6):1249–1275, 1981.

[368] J.-P. Changeux, J. Thiéry, Y. Tung, and C. Kittel. On the cooperativity of biological membranes. *Proceedings of the National Academy of Sciences of the United States of America*, 57(2):335, 1967.

[369] E. Chatani and N. Yamamoto. Recent progress on understanding the mechanisms of amyloid nucleation. *Biophysical reviews*, 10(2):527–534, 2018.

[370] R. Crespo, F. A. Rocha, A. M. Damas, and P. M. Martins. A generic crystallization-like model that describes the kinetics of amyloid fibril formation. *Journal of Biological Chemistry*, 287(36):30585–30594, 2012.

[371] S. M. Johnson, S. Connelly, C. Fearns, E. T. Powers, and J. W. Kelly. The transthyretin

amyloidoses: from delineating the molecular mechanism of aggregation linked to pathology to a regulatory-agency-approved drug. *Journal of molecular biology*, 421(2-3):185–203, 2012.

[372] J. T. Jarrett and P. T. Lansbury Jr. Seeding "one-dimensional crystallization" of amyloid: a pathogenic mechanism in alzheimer's disease and scrapie? *Cell*, 73(6):1055–1058, 1993.

[373] S. I. Cohen, M. Vendruscolo, C. M. Dobson, and T. P. Knowles. From macroscopic measurements to microscopic mechanisms of protein aggregation. *Journal of molecular biology*, 421(2-3):160–171, 2012.

[374] P. Arosio, T. P. Knowles, and S. Linse. On the lag phase in amyloid fibril formation. *Physical Chemistry Chemical Physics*, 17(12):7606–7618, 2015.

[375] G. Meisl, J. B. Kirkegaard, P. Arosio, T. C. Michaels, M. Vendruscolo, C. M. Dobson, S. Linse, and T. P. Knowles. Molecular mechanisms of protein aggregation from global fitting of kinetic models. *Nature protocols*, 11(2):252, 2016.

[376] A. van Oosterom. The surface Laplacian operator of the potentials on a bounded volume conductor has a unique inverse. *IEEE transactions on biomedical engineering*, 53(7):1449–1450, 2006.

[377] N. W. Goehring, D. Chowdhury, A. A. Hyman, and S. W. Grill. FRAP analysis of membrane-associated proteins: lateral diffusion and membrane-cytoplasmic exchange. *Biophysical journal*, 99(8):2443–2452, 2010.

[378] S. M. Christensen, H.-L. Tu, J. E. Jun, S. Alvarez, M. G. Triplet, J. S. Iwig, K. K. Yadav, D. Bar-Sagi, J. P. Roose, and J. T. Groves. One-way membrane trafficking of sos in receptor-triggered ras activation. *Nature structural & molecular biology*, 23(9):838, 2016.

[379] G. Adam and M. Delbrück. Reduction of dimensionality in biological diffusion processes. *Structural chemistry and molecular biology*, 198:198–215, 1968.

[380] H. Berg. Em purcell physics of chemoreception. *Biophys J*, 20:193–219, 1977.

[381] M. A. McCloskey and M. Poo. Rates of membrane-associated reactions: reduction of dimensionality revisited. *The Journal of cell biology*, 102(1):88–96, 1986.

[382] J. M. Haugh and D. A. Lauffenburger. Physical modulation of intracellular signaling processes by locational regulation. *Biophysical journal*, 72(5):2014–2031, 1997.

[383] S. M. Abel, J. P. Roose, J. T. Groves, A. Weiss, and A. K. Chakraborty. The membrane

environment can promote or suppress bistability in cell signaling networks. *The Journal of Physical Chemistry B*, 116(11):3630–3640, 2012.

[384] P. K. Trong, E. M. Nicola, N. W. Goehring, K. V. Kumar, and S. W. Grill. Parameter-space topology of models for cell polarity. *New Journal of Physics*, 16(6):065009, 2014.

[385] J. Gallier. Notes on spherical harmonics and linear representations of lie groups. *preprint*, 2009.

[386] R. A. Silverman et al. *Special functions and their applications*. Courier Corporation, 1972.

[387] N. J. Marianayagam, M. Sunde, and J. M. Matthews. The power of two: Protein dimerization in biology. *Trends in Biochemical Sciences*, 29(11):618–625, 2004.

[388] S. Sarabipour and K. Hristova. Mechanism of FGF receptor dimerization and activation. *Nature communications*, 7:10262, 2016.

[389] S. Muratcioglu, T. S. Chavan, B. C. Freed, H. Jang, L. Khavrutskii, R. N. Freed, M. A. Dyba, K. Stefanisko, S. G. Tarasov, A. Gursoy, et al. GTP-dependent K-Ras dimerization. *Structure*, 23(7):1325–1335, 2015.

[390] A. Rätz and M. Röger. Symmetry breaking in a bulk–surface reaction–diffusion model for signalling networks. *Nonlinearity*, 27(8):1805, 2014.

[391] S. Smith and N. Dalchau. Model reduction permits Turing instability analysis of arbitrary reaction-diffusion models. *Journal of the Royal Society Interface*, 15, 2018.

[392] H. S. Fogler. *Elements of Chemical Reaction Engineering (4th Edition)*. Prentice Hall, 4 edition, 2005.

[393] S. Burke and T. Schumann. Diffusion flames. *Industrial & Engineering Chemistry*, 20(10):998–1004, 1928.

[394] A. Gierer and H. Meinhardt. A theory of biological pattern formation. *Kybernetik*, 12(1):30–39, 1972.

[395] W.-J. Rappel and L. Edelstein-Keshet. Mechanisms of cell polarization. *Current opinion in systems biology*, 3:43–53, 2017.

[396] M. Semplice, A. Veglio, G. Naldi, G. Serini, and A. Gamba. A bistable model of cell polarity. *PloS one*, 7(2):e30977, 2012.

[397] C. Beta, G. Amselem, and E. Bodenschatz. A bistable mechanism for directional sensing. *New Journal of Physics*, 10(8):083015, 2008.

[398] S. Alonso and M. Baer. Phase separation and bistability in a three-dimensional model for protein domain formation at biomembranes. *Physical biology*, 7(4):046012, 2010.

[399] M. C. Getz, J. A. Nirody, and P. Rangamani. Stability analysis in spatial modeling of cell signaling. 10(1):e1395. _eprint: https://onlinelibrary.wiley.com/doi/pdf/10.1002/wsbm.1395.

[400] A. B. Goryachev and A. V. Pokhilko. Dynamics of Cdc42 network embodies a Turing-type mechanism of yeast cell polarity. *FEBS letters*, 582(10):1437–1443, 2008.

[401] A. Manor and N. M. Shnerb. Dynamical failure of Turing patterns. *EPL (Europhysics Letters)*, 74(5):837, 2006.

[402] S. Han, M. Kollmer, D. Markx, S. Claus, P. Walther, and M. Fändrich. Amyloid plaque structure and cell surface interactions of β-amyloid fibrils revealed by electron tomography. *Sci. Rep.*, 7:43577, 2017.

[403] Y. Chen and J. Buceta. A non-linear analysis of Turing pattern formation. *PLOS ONE*, 14(8):1–9, 2019.

[404] P. Amestoy, A. Buttari, I. Duff, A. Guermouche, J.-Y. L'Excellent, and B. Uçar. Mumps. *Encyclopedia of Parallel Computing*, pages 1232–1238, 2011.